On the Fragmentation Behavior of Ziegler-Type Catalysts During the Early Stages of α-Olefin Polymerization
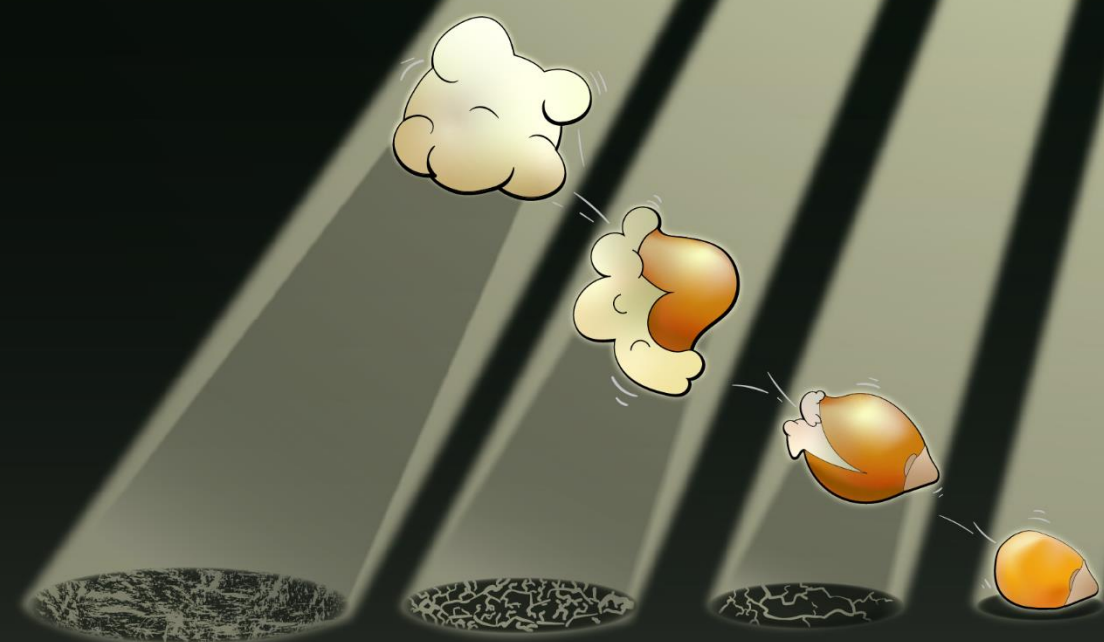
Koen W. Bossers

On the Fragmentation Behavior of Ziegler-Type Catalysts During the Early Stages of α-Olefin Polymerization

Over het Fragmentatiegedrag van Ziegler-Gebaseerde Katalysatoren Tijdens de Vroege Stadia van α-Olefine Polymerisatie

(met een samenvatting in het Nederlands)

Proefschrift

Ter verkrijging van de graad van doctor aan de
Universiteit Utrecht
op gezag van de
rector magnificus, prof.dr. H.R.B.M. Kummeling,
ingevolge het besluit van het college voor promoties
in het openbaar te verdedigen op

maandag 22 november 2021 des middags te 4.15 uur

door

Koen Wynand Bossers

geboren op 26 augustus 1993
te Nieuwegein

Promotor:

Prof. dr. ir. B. M. Weckhuysen

To my grandfather, Jan van Vucht, and my father, Kees Bossers

Table of Contents

Chapter 1. Introduction

In this Chapter, the catalytic polymerization of α-olefins is discussed with an emphasis on what polyolefins are and how they are formed inside the porous framework of these catalyst particles, which ultimately leads to the catalyst breaking up in fragments dispersed throughout the polymer. Furthermore, an outline of the PhD Thesis is provided. The first experimental half of this PhD Thesis is focused on developing a methodology to use synchrotron-based, non-invasive X-ray nano-tomography techniques to study the fragmentation behavior of two sets of industrially relevant, pre-polymerized Ziegler-type polyolefin catalysts in 3-D. In the second experimental half of this PhD Thesis a high atomic weight support matrix based on LaOCl is introduced for both enhanced imaging contrast to study the catalyst fragmentation behavior as well as a good moisture stability with respect to the conventional $MgCl_2$ support matrix. Using this LaOCl framework a spherical cap model system was developed as well as the synthesis of mono-disperse and highly spherical LaOCl bulk particles.

1.1 Polyolefins

Plastics have helped shape modern society in ways similar to how steam machinery were the cradle of the industrial revolution with the exponential population growth as a result [1]. Plastics are found in applications ranging from the preservation of foods beyond what mother nature had initially intended, in furniture, reduce the total weight of automobiles with only minimally compromising impact strength and integrity, the isolation and preservation of electrical currents in cables, protective fibers against ballistic compounds and keeping medical equipment under sterile conditions ready for e.g. surgery [1,2]. Plastics can be categorized as either thermoplastics meaning that they can be shaped indefinitely by remelting the plastic or thermosets meaning that they will harden into their irreversible, final shape [3]. The plastic market is highly diverse and to name just a few includes polyethylene terephthalate, polycarbonate, polystyrene, polytetrafluorethylene, polyvinylchloride, polylactic acid, nylon, poly(methyl methacrylate), polyurethane and polyolefins. These polyolefins are the largest constituent with over 60% volume share of the thermoplastic market, which itself is a gigantic market with over 180 million tonnes produced annually [4-6]. The polyolefin family consists mainly of different types or so-called grades of polyethylene and polypropylene, but also ethylene-propylene rubbers with and without additional diene monomers added and higher α-olefin polymers, such as poly-1-butylene [7,8].

The most simple polyolefin structure is based on the polymerization of ethylene into a linear methylene backbone without any side-chain branching. This type of polyethylene grade is referred to as high-density polyethylene (HDPE). This achieved high density, typically in the range of 0.94-0.96 g/cm^3, is the result of the efficient packing of the linear methylene backbone of the polymer chains in lamellas and leads to a highly crystalline polymer up to roughly 75% [9]. It should be noted here that a 100% crystalline PE isn't feasible as the crystallization degree is limited by the high viscosity of the polymer [10]. As a higher concentration of side-chains are introduced in the methylene backbone, either through the direct incorporation of higher α-olefin co-monomers added in the feedstock, such as 1-hexene and 1-octene or through chain transfer during the polymerization reaction, the crystalline packing of these chains starts to decrease [11]. This results in a lower polyethylene density and hence other polyethylene types, such as medium-density (MDPE), linear low-density (LLDPE), low density (LDPE) and very low-density (VLDPE) polyethylene grades are also available. In Figure 1.1 these different polyethylene types are drawn schematically alongside the density range they fall in. These different polyethylene grades vary in their physico-chemical properties, such as impact strength, tensile strength, melting point, wear and abrasion resistance and processibility, and are therefore found in a large range of applications [12].
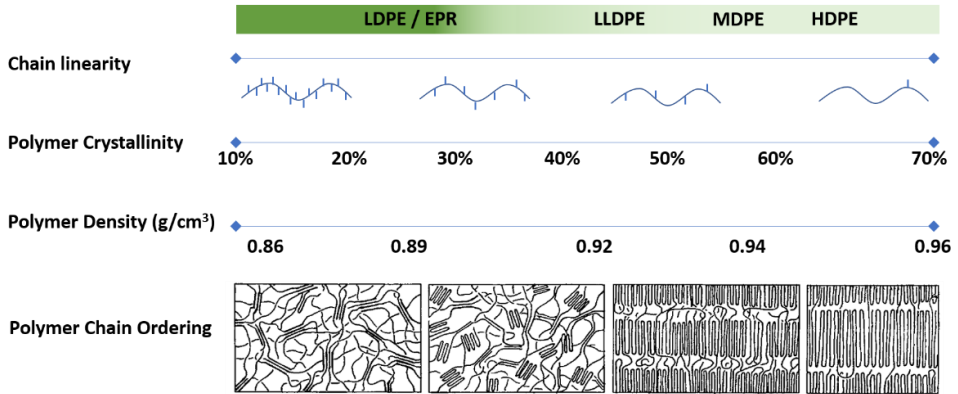
Figure 1.1 The chain linearity (number of side-chain branches), crystallinity and density and ordering of the backbone chains of different grades of polyethylene going from low-density (LDPE) and ethylene-propylene rubbers (EPR) to linear low-density (LLDPE), medium-density (MDPE) and high-density (HDPE) polyethylene. Adapted from Bensason *et al.* [11].

After polyethylene, the second most produced polyolefin is isotactic polypropylene. When propylene is inserted into a growing polymer chain, the methyl pendant group will point in a certain direction with respect to the methylene backbone and the next methyl group [13]. This leads to a variety of polypropylene methyl group orientations, as shown in Figure 1.2. These orientations of the methyl groups are referred to as I) atactic polypropylene (a-PP), in which the methyl groups have a random configuration with respect to the methylene backbone, II) syndiotactic polypropylene (s-PP) where the methyl groups have an alternating configuration with respect to the methylene backbone, III) hemi-isotactic polypropylene (hit-PP) where the first and second sets of alternating methyl groups have respectively the same and random configuration with respect to the methylene backbone and finally IV) isotactic polypropylene (i-PP) where all methyl group have the same configuration with respect to the methylene backbone [14]. The regio-and-stereospecificity control over the propylene polymerization reaction is determined by the type of catalyst used and reaction conditions [15].
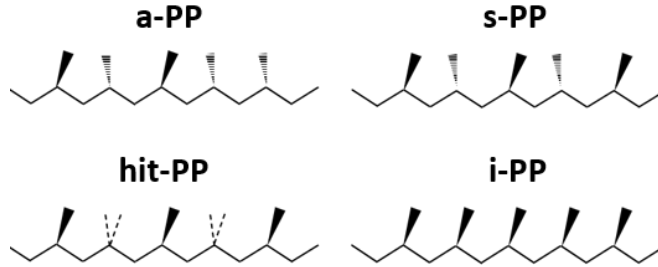
Figure 1.2 The orientation of the methyl side groups that determine the isotacticity of the polypropylene chain going from complete random orientation, called atactic (a-PP), alternating orientation, called syndiotactic (s-PP), regular orientations with random orientations in between, called hemi-isotactic (hit-PP) and finally highly regular orientations, called isotactic (i-PP). Adapted from Talarico *et al.* [14].

Besides the degree and nature of side-chain branches and the orientation of the methyl groups towards the methylene backbone, the molecular weight and molecular weight distribution (MWD) play an important role in the final physical properties of the polyolefin [16-18]. For example, a typical HDPE product will have individual polyethylene chains around a thousand repeating ethylene units, however ultra-high molecular weight polyethylene (UHMwPE), a polyethylene grade with exceptional abrasion and wear resistance as well as tensile strength, has repeating units on the order of 10^5 per polymer chain resulting in molecular weights well above 1 million g/mol [19,20] . The MWD or also called polydispersity index (PDI) is based on the ratio of the weight average molecular weight (M_w) to the number average molecular weight (M_n) as shown in Eq. 1.1-1.3, where N_x is the number of polymer chains that have the molecular weight M_x. The MWD and molecular weight have direct consequences on the processability of a material. A broader MWD will have both low molecular weight polyolefin chains that facilitate a lower-cost extrusion process for instance and high molecular weight polyolefin chains to ensure sufficient strength to maintain structural integrity of the final product [21,22].

$$M_n = \frac{\sum N_x M_x}{\sum N_x} \qquad \text{Eq. 1.1}$$

$$M_w = \frac{\sum N_x M_x^2}{\sum N_x M_x} \qquad \text{Eq. 1.2}$$

$$MWD = \frac{M_w}{M_n} \qquad \text{Eq. 1.3}$$

1.2 α-Olefin Polymerization Catalysts

To enable all of the above-mentioned polyolefin grades as well as the introduced varieties with respect to the nature of side chain branching (i.e., concentration, long versus short chains) and their molecular weight and MWD, different classes of α-olefin polymerization catalysts have been developed spanning an era of nearly 7 decades. Here a brief history on the discovery of the ethylene and propylene polymerization processes is provided.

1.2.1 Brief History on the Polymerization of α-Olefins

The serendipitous discovery of polyethylene dates back to the 1930's when Reginald Gibson and Eric Fawcett, employed by Imperial Chemical Industries (ICI), unintentionally synthesized LDPE at extreme ethylene pressures and temperature [23]. This non-catalytic, free radical polymerization process leads to a high degree of side-chain branching in the methylene backbone through chain transfer reactions. In the following decades, three different catalytic systems were discovered and subsequently improved upon. In 1951, Paul Hogan and Robert Banks who worked at *Phillips Petroleum Company* discovered that a chromium-based catalyst, now called the Phillips catalyst, could polymerize ethylene under considerably milder reaction conditions than the free-radical process, into a crystalline HDPE product [24,25]. In 1953, Karl Ziegler who worked at the *Max-Planck-Institut für Kohlenforschung* submitted a patent based on the discovery that combinations of transition metal halides with alkyl-aluminium species generated a new class of olefin polymerization catalysts [26]. Amongst these *metallorganische Mischkatalysatoren* (organometallic mixed-catalysts) as he referred to them, especially the combination of $TiCl_4$ with a diethylchloro-aluminium compound yielded a catalyst formulation similar in activity to that of the Phillips catalyst [27]. Giulio Natta caught wind of Karl Ziegler's patent application and discovered that the crystalline α-$TiCl_3$ phase together with a triethylaluminium co-catalyst was able to polymerize propylene in a mixture of i-PP and a-PP [28]. For their achievements on the discovery of the so-called Ziegler catalyst by Karl Ziegler and subsequent study on the formation of isotactic polypropylene using this Ziegler catalyst by Giulio Natta, they were jointly awarded the 1963 Nobel prize in Chemistry. Nowadays, the Ziegler and Ziegler-Natta catalyst nomenclatures are used when referring to respectively the ethylene and propylene polymerization variants of the Ziegler-type catalyst family. In this PhD Thesis, reference will be made to either to Ziegler-type catalysis in general or specifically to either the Ziegler catalyst or Ziegler-Natta catalyst. Finally, the development of the last class of polyolefin catalysts, single-center molecular catalysts, started shortly after Ziegler's discovery [29]. The initial goal here was to create a well-defined, homogeneous catalyst, titanium metallocene active site (titanocene) to study the reaction mechanism of the polymerization reaction as opposed to the original heterogeneous and highly complex Ziegler catalyst. The

major breakthrough came around the early 1980's when Hansjörg Sinn and Walter Kaminsky managed to isolate and characterize a methylaluminoxane (MAO) co-catalyst, which was able to generate a highly active metallocene catalyst for the polymerization of ethylene [30]. These single-center molecular catalysts when mixed and activated by the MAO co-catalyst are used both as homogeneous polyolefin catalysts or when immobilized on for instance a SiO_2 support matrix as heterogeneous polyolefin catalysts [29].

These three catalyst systems, the Cr active site Phillips, the Ti active site Ziegler-type and the single-centre molecular catalysts or metallocene catalysts are all used industrially to this day because of their highly different chemical nature and the tuneability this provides for the polyolefin product the customer wants.

1.2.2 The Ziegler-type Catalyst Family

The original discovery of the reduction of $TiCl_4$ with an alkylaluminium co-catalyst leads to the formation of a crystalline and solid $TiCl_3$ catalyst and is regarded as the so-called first generation Ziegler-type catalyst [31]. $TiCl_3$ is polymorphic and exists both in the brown colored, fibrillar β crystalline phase and the violet colored, layered α, γ and δ crystalline phases [32]. The overall polypropylene yield for this first-generation catalyst was on the order of 1 kg PP per g catalyst. These low yields meant that the catalyst concentration in the final polymer powder was too high. The Ti-Cl bonds of the $TiCl_3$ catalyst present in the final polymer powder are readily hydrolyzed in air to give the corrosive HCl by-product and therefore the catalyst residues had to be removed in a costly procedure called deashing [33]. The so-called second generation Ziegler-type catalyst was developed by Solvay in a process where they first generated a typical $TiCl_3/AlCl_3/AlEt_2Cl$ mixture through the reaction of $TiCl_4$ and $AlEt_2Cl$ [34]. After washing out the $AlCl_3$ with ether, a highly porous β-$TiCl_3$ catalyst was obtained that was then converted to the γ-$TiCl_3$ crystalline phase at low temperatures through the reaction with $TiCl_4$ in a slurry phase. This resulted in retaining the high porosity of the starting material and minimize crystallite growth. The Solvay process boosted the production yield from 1 kg PP per g catalyst of the first generation Ziegler-type catalysts towards 5-20 kg PP per g catalyst in this second generation.

The third generation Ziegler-type catalysts started with the discovery made by Shell in the early 1960's that δ-$MgCl_2$ could chemisorb $TiCl_4$ that after activation by a trialkylaluminium co-catalyst yields a highly dispersed Ti^{3+} active site akin to that of δ-$TiCl_3$, which is disordered along the c-axis of the crystal unit cell [35]. Through a ball-milling process, the crystallite size of $MgCl_2$ could be reduced to only a few nm. The success story of this mechanically activated δ-$MgCl_2$ over other halide metal supports is two-fold, namely i) the similar crystal structure of δ-$MgCl_2$ to that of δ-$TiCl_3$ and ii) the closely matching atomic radii of Mg^{2+} and Ti^{4+} [8,36]. This means that $TiCl_4$ can efficiently chemisorb on the epitaxially unsaturated lattices of $MgCl_2$, such as the four-coordinated (110) and five-coordinated (104), whereas the six-coordinated and fully saturated basal plane (001) remains inactive for chemisorption [37-39].

14

The reader might have noticed that the development and nomenclature of these first three generations is directly related to the desire of producing highly isotactic polypropylene, >90-95% isotacticity (I.I.). Whereas indeed the push for highly isotactic polypropylene was an adamant factor in the early development of the Ziegler-type catalysts, the discovery of MgCl$_2$ as a highly suitable support matrix to stabilize TiCl$_4$ has shaped the future of both the Ziegler ethylene polymerization and Ziegler-Natta propylene polymerization catalysts. However, it is also at this point that subsequent improvements and so-called generations in the Ziegler-type catalyst formulations have become deconvoluted with the Ziegler and Ziegler-Natta catalysts following their own separate paths.

For the Ziegler-Natta polypropylene catalysts this third generation catalyst based on the activated MgCl$_2$ support matrix took off when in the late 1960's the Montedison and Mitsui companies independently noted that adding Lewis base molecules, such as ethyl benzoate during the ball milling process stabilized and increased the number of exposed unsaturated lattices for TiCl$_4$ chemisorption [40]. These Lewis base molecules that are added during the synthesis process are typically referred to as internal donors. However, through an undesired side-reaction with the trialkylaluminium co-catalyst, these internal donors are removed from the MgCl$_2$ surface [41]. This leads to a decrease in the I.I. of the formed polypropylene as a function of exposure to the co-catalyst and polymerization activity. This was mitigated through the addition of Lewis base molecules during the polymerization reaction itself, which are referred to as external donors. Examples of third generation external donors are benzoate and methyl p-toluate. This external donor then coordinates to the vacant sites created through the desorption of the internal donor and ensures that the Ti^{3+} active site remains stereospecific for the production of iPP [42]. The subsequent fourth and fifth generation Ziegler-Natta catalysts are all based on the use of different type of internal and external donor combinations to push the polymerization activity beyond that of the 3rd generation while maintaining high I.I. values. A summary of the Ziegler-Natta catalyst generations are given in Table 1.1 with the typical activity, MWD and I.I. range they operate in. The fourth generation is based on the combination of phthalate-based internal donors (di-esters) with alkoxysilane external donors [43,44]. With the use of these phthalates, the propylene polymerization activity was boosted further, whereas the alkoxysilane external donors had the advantage of not reacting with the co-catalyst during the polymerization reaction. The fifth generation started with the discovery of di-ether based internal donors, which had the additional advantage of not requiring an external donor due to their stability with regards to the co-catalyst. Nonetheless, the addition of alkoxysilane external donors improves the I.I. value of these di-ether based Ziegler-Natta catalysts. In addition to di-ethers, this fifth generation also contains succinates and polyol ester internal donors and provide different H$_2$ response and MWD values of the resulting iPP [45].

Table 1.1 The propylene activity and resulting polypropylene isotacticity (I.I.) values for the first to fifth generation Ziegler-Natta catalysts. Adapted from [43,44].

Generation	Catalyst composition	External donor	Activity (g PP/mmol Ti · h · atm)	I.I. (%)
First	$TiCl_3$	-	~4	90
Second	Solvay-type $TiCl_3$	-	~30	95
Third	$TiCl_4/MgCl_2$/benzoate	Benzoate	~1000	92-44
Fourth	$TiCl_4/MgCl_2$/phthalate	Alkoxysilane	~1000-3000	>98
Fifth	$TiCl_4/MgCl_2$/1,3-diether	Alkoxysilane	~3000-5000	>98

For the Ziegler polyethylene catalyst there isn't a clear distinction in generations since the use of internal and external donors isn't a requirement at all. However, developments of such catalysts are mainly based to improve catalyst particle morphology, size and porosity control as well as the active site response to hydrogen (higher response means lower amount of hydrogen needed and therefore less formation of ethane through the unwanted hydrogenation of ethylene) and control over the MWD of the PE product [32].

Whereas the third generation "activated" $MgCl_2$ was based on a mechanical ball-milling process, the fourth and subsequent generations are based on chemical activation routes, which provide enhanced control over the final catalyst characteristics, such as particle morphology, size dispersion and porosity [46]. These chemical routers range from the use of Grignard reagents to $MgCl_2$ adducts with ethanol or tetrahydrofuran (THF) as well as the use of Mg alkoxides [19,47,48].

1.2.3 The Arlman-Cossee Reaction Mechanism

In Figure 1.3, the activation, initiation and chain propagation mechanisms, as proposed by Arlman and Cossee, are shown for a Ziegler-type catalyst [49]. After activation and initiation of the $TiCl_4$ precursor with a trialkylaluminium ($AlEt_3$) co-catalyst (this first step isn't shown), a Ti^{3+} active site is formed that has a vacant site for the coordination of an ethyl group from the co-catalyst, which introduces the first Ti-C bond. After inserting the ethyl group of the co-catalyst and subtraction of another chlorine ligand, a new vacant site appears to which the α-olefin monomer can coordinate. At this point, the polymer chain (at this point just the ethyl group of the initial co-catalyst) inserts itself in the coordinated α-olefin through a migratory insertion and the position of the vacant site is therefore swapped. Four chain terminating routes are possible of which three can occur without the addition of an external chain terminating reagent. Two of these routes are β-hydride eliminations where the hydride coordinates to i) the Ti active site (Ti-H bond) or ii) reacts with the coordinated α-olefin to eliminate the respective alkane. The released polyolefin chain will in this case have

16

a vinyl end group and can therefore be reinserted in a growing polyolefin chain, still coordinated to a Ti^{3+} active site. The third route is a chain transfer reaction towards the aluminium co-catalyst compound. To provide control over the molecular weight of the resulting polyolefin, H_2 can be added during the reaction as an external chain termination agent. Chain termination with H_2 leads to a methyl end-group, which can't be reinserted in a growing polyolefin chain.
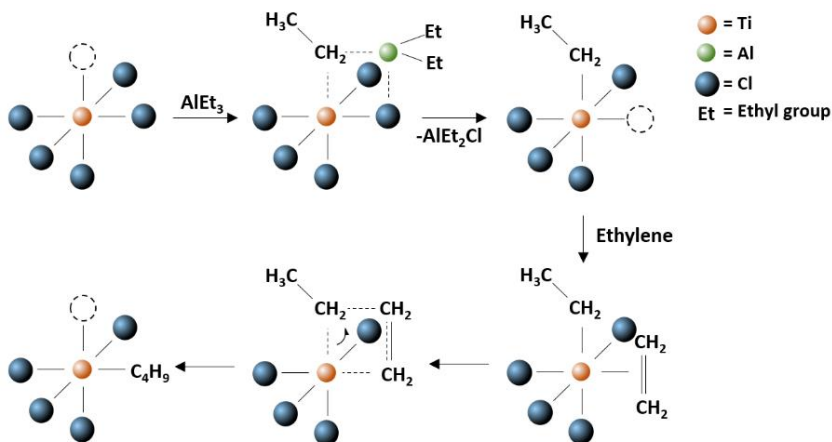
Figure 1.3 Activation, initiation and chain propagation mechanism of a Ziegler-type Ti^{3+} active site, as proposed by Arlman and Cossee. Adapted from Paulik *et al.* [9].

1.3 Polyolefin Catalyst Fragmentation Behavior

The main focus of this PhD Thesis is to study the fragmentation behavior of Ziegler-type catalysts in the early stages of α-olefin polymerization through the use of X-ray nano-tomography techniques that allow us to image the full volume of one or more particles in a non-invasive manner at high spatial resolution (sub-100 nm demonstrated over a large field-of-view).

1.3.1 From Catalyst Particle to Catalyst Fragment

Current-day Ziegler-type catalyst particles are in the range of several microns to several tens of microns in diameter and highly spherical in nature. However, these $MgCl_2$ particles are not build of a covalent framework like typical metal oxides, such as SiO_2, but formed through the ionic interactions of the constituent ions. This leads to the formation of so-called primary particles of $MgCl_2$ platelets as small as 5 nm in size [50,51]. These platelets then proceed to form the secondary building-units of up to several hundred nm or a micron in

diameter and finally agglomerate together as a particle through ionic and van der Waals interactions. A schematic representation of the typical morphological structure of activated $MgCl_2$ is given in Figure 1.4.
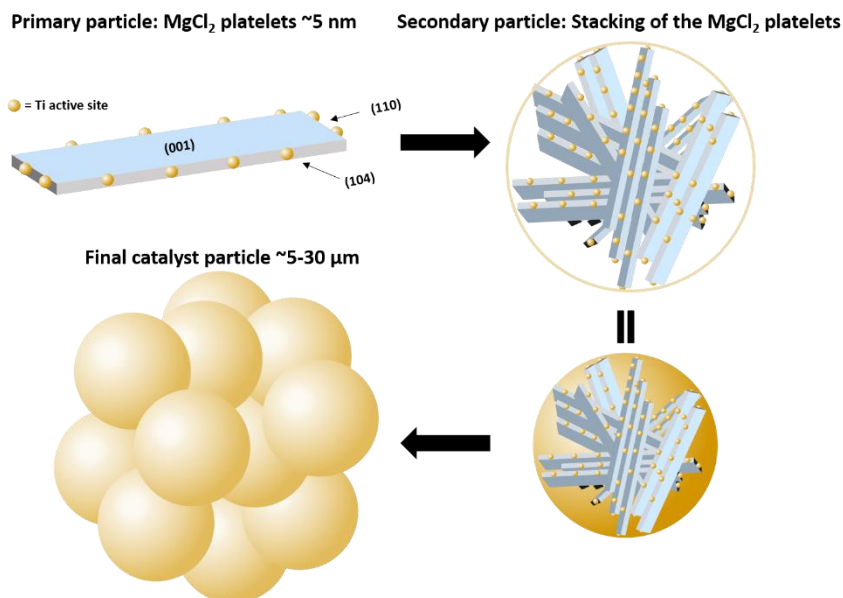
Figure 1.4 Schematic representation of the structure of a typical $MgCl_2$ support matrix Ziegler-type catalyst particle. The final catalyst particle, which is up to 5-30 microns in diameter is build-up of $MgCl_2$ platelets as small as 1-10 nm onto which the Ti pre-active sites are chemisorbed on the lateral, unsaturated lattices.

As the α-olefin comes into contact with the active site, it will become incorporated in a growing polyolefin chain. These polyolefin chains can be formed both on the external surface of the catalyst particle or inside the interior pore network. As these polyolefin chains are growing, they start to exert a stress on the framework of the catalyst particle. If the build-up exceeds the relaxation time of this stress over the local framework a threshold can be reached where the framework starts to disintegrate as a result of this stress. This disintegration is called the fragmentation of the framework [52,53]. The fragmentation of the catalyst particle is of paramount importance to prevent significant mass transfer limitations. These mass transfer limitations are mitigated by the catalyst fragmentation by facilitating shorter diffusion pathlengths for the monomer through the dense polyolefin layer to reach an active site and for the generation of newly exposed active sites that could previously have been inaccessible for the monomer. However, the fragmentation process has to be controlled to prevent for instance the formation of small catalyst fragments that become loose of the composite catalyst-polymer particle, called fines. These fines can otherwise start to migrate through the reactor on their own and cause reactor fouling both in the reactor itself or downstream equipment [54]. Such reactor fouling is a highly costly procedure due to the extensive cleaning procedure and therefore downtime introduced as well as the possible spoilage of an entire production batch that can run into the tonnes of

product. A common strategy to therefore ensure a smooth and controlled fragmentation process is by first performing a so-called pre-polymerization process under mild reaction conditions (close to ambient pressure and room temperature) to a yield of several ten g of polyolefin per g of catalyst before increasing the monomer pressure and temperature to reach orders of a hundred kg of polyolefin per g of catalyst [54-56]. Another advantage of the pre-polymerization process, besides preventing the formation of fines, is to ensure that the spherical morphology of the pristine catalyst particle is maintained in the final polymer powder morphology, which is called the replication phenomenon [57]. A spherical morphology of the resulting polymer particles is another necessary step to facilitate easier transport and post-processing into a polymer product, but also again prevent reactor fouling, since roughly shaped particles can stick to the reactor walls and break more easily into fines [53,58].

From a fundamental perspective, two limiting modes of fragmentation are described [59]. On the one hand you have the shrinking core or also called layer-by-layer fragmentation mode where the polymerization events are mainly occurring in the vicinity of the external surface of the particle. This then leads to the peeling of relatively small catalyst framework species, called fragments, of the surface by the growing polyolefin chains. This peeling continues from the external surface inwards until finely the original catalyst particle has been completely disintegrated into fine fragments that are dispersed uniformly throughout the polyolefin phase. On the other hand, you have the continuous bisection fragmentation mode where the polymerization occurs uniformly throughout the particle and the build-up of stress therefore leads to the fragmentation of the entire catalyst particle into successively smaller fragments. Both fragmentation models are visualized in Figure 1.5. This initial catalyst fragmentation process is taking place in what is typically referred to as the early stage of α-olefin polymerization [52].
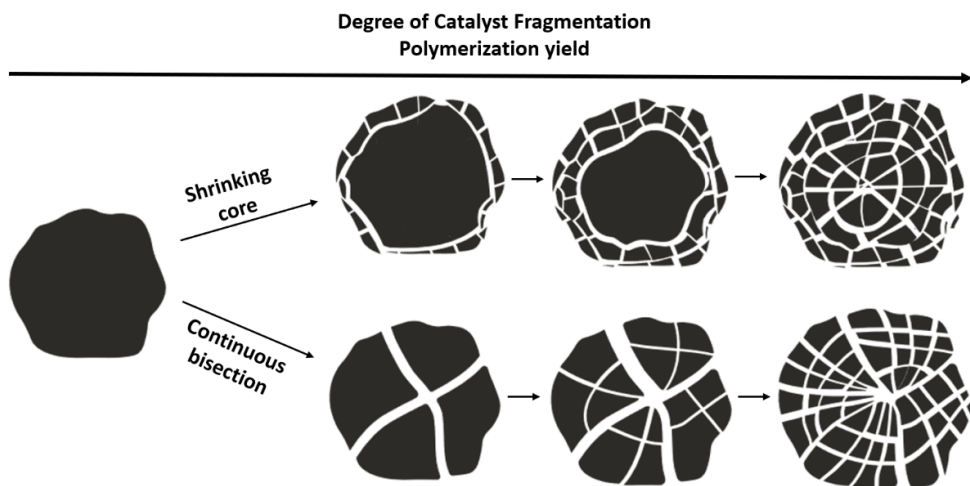
Figure 1.5 Schematic representation of the shrinking core (also called layer-by-layer) and continuous bisection fragmentation models of a catalyst particle as a function of the polymerization yield, which is directly linked to the degree of catalyst fragmentation.

These two fragmentation modes are occurring simultaneously, however depending on both reaction conditions and catalyst properties, one of the two modes can be dominating the overall fragmentation behavior [16,17,59]. Examples of reaction conditions include the reaction temperature and monomer pressure, the operating nature of the reactor, e.g. gas-phase versus slurry-phase or even liquid-phase for propylene, the type of α-olefin used and the addition of co-monomers [60-63]. Examples of catalyst properties include the chemical nature of the active site, the distribution of this active site throughout the support matrix, the degree of activation by the co-catalyst species and porosity and friability of the support matrix [64-69].

1.3.2 Studies on the Fragmentation Behavior of Polyolefin Catalysts and Polyolefin Particle Morphology Evolution

Previous studies concerning the fragmentation behavior of polyolefin catalysts and the evolution of the polyolefin particle morphology are mainly focused on the use of cross-sectional scanning electron microscopy (SEM) studies. SEM has the advantage of providing high spatial resolution down to several nm and when coupled with the collection of back-scattered electrons provides Z-contrast to discriminate between the polyolefin phase and the support matrix of the catalyst used. Additionally, energy dispersive X-ray spectroscopy (referred to as both EDS and EDX) coupled with SEM (SEM-EDX) enables one to map the elemental distribution in the region of interest and the collection of secondary electrons, which are lower in energy than the backscattered electrons, contain information on the surface topology. A few examples, with an emphasis on Ziegler-type catalysts, will be highlighted here to give the reader a feeling of how complicated the interplay of catalyst particle properties and reaction conditions can be on the evolution of the particle morphology and the underlying catalyst framework fragmentation.

Zheng and Loos for instance used cross-sectional SEM-EDX to study both Ziegler-type catalysts and immobilized metallocene catalysts at low propylene polymerization and propylene-ethylene co-polymerization yields ranging from 0.8 to 7 g polymer per g catalyst [63,66,67]. One of the most important requisites they observed to obtain a homogeneous fragmentation profile and uniform polymer particle morphology for an immobilized metallocene catalyst, was the homogeneous distribution of the catalyst and co-catalyst species throughout the particle [66]. Additionally, for a Ziegler-Natta catalyst, depending on the pore size distribution they would see either the shrinking core fragmentation model or continuous bisection fragmentation model dominating the overall fragmentation behavior at low polymer yields and under mild reaction conditions [67]. The explanation for this was that the smaller pore size and pore volume catalyst (6 nm, 0.16 cm^3/g) had considerably higher mass transfer resistance internally than the larger pore size and pore volume catalyst (9.7 nm and 0.51 cm^3/g), whereas both catalysts had a similar titanium weight loading around 2%.

Vestberg and co-authors showed how delicate the catalyst support matrix design can be to fine-tuning the final polymer particle morphology [64]. They used three different support matrixes for the liquid-phase Ziegler-Natta propylene polymerization process at 30 °C. These matrixes are two-fold $MgCl_2$ with one portraying a very low and one portraying a typical BET surface area of respectively, <5 m^2/g and 250 m^2/g and one SiO_2 matrix with 63 m^2/g. They observed with both SEM and TEM that the low porosity catalyst showed uniform fragmentation already at low yields and yielded highly spherical polymer particles with a smooth surface. The high surface area $MgCl_2$ catalyst also yielded spherical polymer particles, but with a rough surface and the SiO_2-based catalyst yielded rough cauliflower-like polymer particles.

Abboud *et al.* have made a similar comparison between $MgCl_2$ and $SiO_2/MgCl_2$ based Ziegler-Nata catalysts for propylene polymerization [65]. However, here the process was performed in the gas-phase at 50 °C and 5 bar of monomer pressure. They observed that for both support matrices the catalyst framework fragmentation occurred throughout the whole particle at early polymer yields. Cross-sectional SEM and optical video-microscopy showed that the $MgCl_2$ support matrix showed both a higher rate and more uniform fragmentation than the $SiO_2/MgCl_2$ one.

Nooijen showed the importance on the activation methodology of the Ziegler-type pre-active sites with the co-catalyst species, which can be referred to as the start-up procedure [68,69]. He found that the degree of activation of the pre-active sites both before the introduction of the α-olefin and during has a significant role on the evolution of the particle morphology. Additionally, the size of the co-catalyst (e.g., length and branching of the alkyl groups) plays a strong role in the diffusivity through the catalyst pore network and the activation rate. For example, if the contact time between the pre-active site and co-catalyst before the introduction of ethylene was short enough, a shell of active-site species close to the surface would be obtained with the Ti species at the core remaining non-activated. This then leads to a cobweb type of particle morphology evolution, where polymerization and fragmentation is only observed in a shell of a certain thickness around the surface and many polymer strings are observed at cracks around the external particle's surface. Alternatively, if the activation of the catalyst particle is uniform before the introduction of the α-olefin, polymerization was observed to occur throughout the entire particle's interior volume leading to a uniform polymer particle morphology.

Pater *et al.* showed an example where the continuous bisection fragmentation mode was seen to dominate the overall fragmentation behavior for a $MgCl_2$-based Ziegler-Natta catalyst [55]. They showed that even at extremely mild reaction conditions at low polypropylene yields ranging from 0.3-50 g PP per g catalyst the $MgCl_2$ framework was disintegrating into successively smaller fragments as a function of polymer yield, uniformly distributed throughout the polymer phase. Additionally, they observed based on the early stage polymerization kinetics that there were two regimes. In the first regime, the catalyst is the continuous phase with the polymer being formed within and a decline in the polymerization activity is observed as the polymerization yield increases until a constant polymerization activity (plateau) is obtained. At this stage, the second regime takes over where the polymer is now the continuous phase and the catalyst becomes uniformly distributed within. That is to say that the catalyst is now fully fragmented at or close to the primary particles size of the specific support matrix and the composite polymer-catalyst particle is no longer residing in the so-called early stage of α-olefin polymerization.

It should be mentioned specifically here that most studies on the interplay of reaction conditions and catalyst properties on the evolution of the particle morphology and the catalyst fragmentation process are based on (extremely) mild polymerization reaction conditions. Such

reaction conditions are typically close to 1 bar α-olefin pressures and room temperature. This is simply done to provide better control of the desired polymer yield in the range of 1-10 g polyolefin per g catalyst, whereas under industrially relevant conditions (upwards of 8 bar and 60 °C) it would be otherwise hard to quench the highly exothermic polymerization reaction at low yields. However, the group of McKenna has extensively worked on the development of so-called stopped-flow reactors and quench methods that allow industrially relevant conditions at millisecond residence times of the catalyst particles [70,71]. Using SEM, they were able to observe the initial formation of cracks at the catalyst particle's external surface and the possible formation of fines at 8 bar of ethylene pressure, 80 °C and a dwell-time of only 40 ms.

1.4 From Cross-sectional Electron Microscopy to X-ray Computed Tomography: 3-D Imaging of Entire Polyolefin Particles

The vast majority of studies concerning the fragmentation behavior of polyolefin catalyst particles and their effect on the evolution of the particle morphology focus on cross-sectional SEM techniques. However, the electron beam has a limited penetration depth on the order of several tens of nm until the incident electrons have lost their energy through the many scattering events having taking place with the material of interest [72]. To study the fragmentation behavior of a catalyst particle it is important to look not only at the exterior but especially at the interior of such said particle. For electron microscopy studies this therefore requires invasive preparation methods, either through embedding the polyolefin catalyst particles in an epoxy and subsequent (ultra)-microtoming in thin slices or the use of a focused ion beam (FIB) to mill away the outside of the material until the core is reached.

Fortunately, X-rays have a considerably higher penetration depth than electrons [73]. For example, an X-ray beam at 12 keV, which is the photon energy used in our studies in Chapters 2 and 3, can travel roughly 158 microns through an anhydrous $MgCl_2$ layer (e.g. assuming no porosity), density of 2.32 g/cm^3, before losing 1/e, ~63%, of its initial photon flux at an incident angle of 90 degrees. This distance upon which the incident X-ray beam has lost 1/e of its photon flux is called the X-ray attenuation length and is determined by a materials chemical composition, its density and the photon energy. In the case of both high-density polyethylene and isotactic polypropylene, density of 0.94 g/cm^3 used, this X-ray attenuation length is increased to over 9000 microns [74]!

In this PhD Thesis, we will demonstrate that X-ray computed nano-tomography techniques (XCNT) performed at synchrotron-based X-ray microscopes can image and visualize the entire interior volume and exterior surface of polymerized polyolefin catalyst particles in

field of views as large as 120 microns in width without requiring invasive preparation methods at sub-100 nm 3-D spatial resolution.

Tomography comes from the old Greek words of *τόμος* (tomos), which means to slice and *γράφω (*graphō), to write. The idea is to image an object by sectioning it in slices through the use a X-ray beam. In computed tomography, the object is imaged either through scanning with a parallel X-ray beam smaller than the field of view (FOV) or in a full-field modus using typically a cone X-ray beam geometry, after which the image is demagnified on a detector. The obtained image is called a 2-D projection (of the imaged object) and contains the interaction of the X-ray beam with the entire object at this angle. The next step is to rotate the object along the Z-axis perpendicular to the X-ray beam by a specified increment and collect another 2-D projection along this new rotation angle. Finally, after sufficient 2-D projections have been collected at different angles (typically between 0-180°), the 3-D volume of the object can be reconstructed using computerized (hence computed tomography) algorithms, such as the filtered back projection (FBP) and through iterative-based simultaneous algebraic reconstruction techniques (e.g. ART, SART, SIRT and more). FBP reconstruction algorithms are known to suffer from reconstructing also noise and hence iterative algorithms, such as SART have been developed, where in each iteration a reduction of artifacts and noise is achieved. However, iterative algorithms are time consuming and can additionally also remove signal intensity from real features that it approximates to be noise and the reconstruction results should always be manually inspected and validated [75,76]. A workflow of X-ray computed tomography, with an example of the X-ray microscopy setup used in Chapter 3, is shown schematically in Figure 1.6.
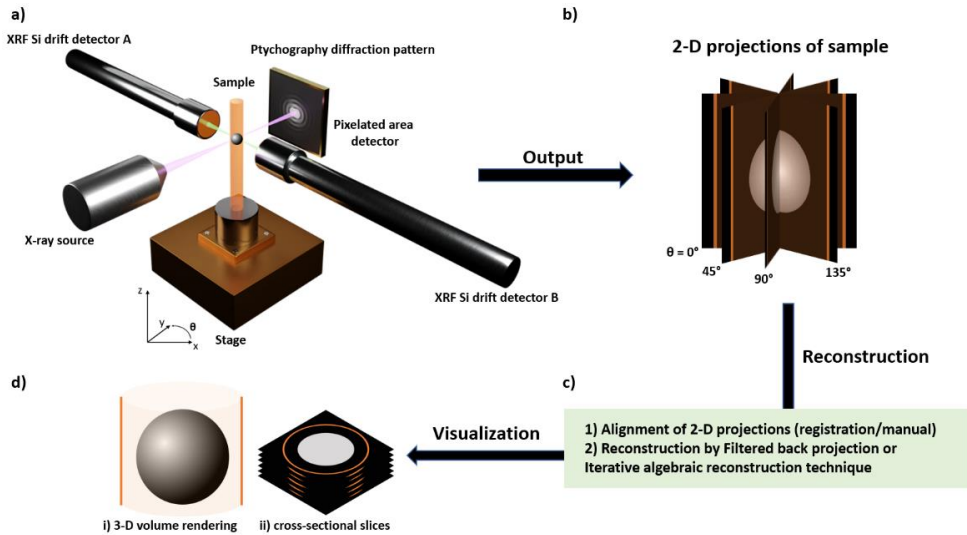
Figure 1.6 General workflow for X-ray computed tomography. (a) The correlated X-ray ptychography and fluorescence nanotomography setup used in chapter 3. The setup shown uses a parallel X-ray beam to raster-scan the sample and collects both diffracted signal in transmission mode on the pixelated area detector and X-ray fluorescent photons with two detectors at 90° and 270° angles at different rotation angles, θ. (b) The output is 2-D projections that show either the phase or electron density of the sample in the case of X-ray ptychography or the distribution of elements at each rotation angle. (c) The reconstruction toolbox based on the alignment of the 2-D projections to correct for sample drift and motor positioning inaccuracies followed by the use of a reconstruction algorithm to reconstruct the sample in 3-D. (d) Visualization of the reconstructed sample either in 3-D (the sum of all cross-sectional slices) or as individual cross-sectional slices along one of the principle planes. Adapted from O'Sullivan *et al.* [76].

The spatial resolution of the reconstructed object is defined by several factors [77,78]. The most important and limiting factor is the spatial resolution of the 2-D projections obtained, which can be either limited by the X-ray focusing optics in the case of conventional (scanning) transmission based X-ray microscopes or by the largest angle of diffraction collected in the case of coherent diffraction imaging. Additionally, the correction of positioning errors and sample drift between subsequent 2-D projections, the angular step used (which is defined by the total number projections obtained at different angles), the signal-to-noise ratio of the data and possible X-ray beam-induced morphology changes will influence the quality of the reconstructed object and therefore the achieved 3-D spatial resolution. A common approach to determine the 3-D spatial resolution is by calculating the Fourier shell correlation between two reconstructed half data-sets (typically by reconstructing the even and uneven angles of projections separately) [79].

1.4.1 X-ray Computed Micro-Tomography in the field of Polyolefin Catalysis

The use of X-ray computed microtomography (XCMT) in the field of polyolefin catalysis was explored by Ferrero, Jones and Conner [80-82]. They utilized synchrotron X-ray radiation at the Brookhaven National Laboratory in the early 1990's to study Ziegler-type and Phillips catalysts at polymerization yields as low as 11 g polyethylene per g catalyst with a pixel size down to 2 microns. With XCMT they were able to show the porosity and void space of the polymer particles as well as observe catalyst fragments within the polymer phase. However, the results given in these works are based on single reconstructed slices instead of the entire reconstructed volume due to limitations in the computational power in that era (to illustrate this: the data-sets of chapters 2 and 3 can take up to 20-40 GB of RAM memory, not even considering the computing power required from the CPU and GPU's).

Nearly two decades later, the group of Kosek resumed the work of XCMT in the field of polyolefin catalysis [83,84]. They utilized lab-based XCMT microscopes to image and reconstruct full polyolefin particles millimeters in size and study the transport rates of monomer molecules through the polyolefin phase. They showed that monomer mass transfer limitations remain important in the final polymer particles, where degassing of residual monomer molecules post-polymerization is important for safety reasons and therefore not just in the early-stage of polymerization.

However, despite the impressive pioneering works performed by the groups of Ferrero and Kosek, there is still a thousand-fold resolution gap between cross-sectional SEM studies on the fragmentation behavior of polyolefin catalysts and that of the XCMT studies demonstrated.

Therefore to bridge this resolution gap, in this PhD thesis the focus is on the development of a X-ray computed nanotomography methodology in the field of polyolefin catalysis with an emphasis on the fragmentation behavior of the catalyst framework.

1.4.2 The Correlated X-ray Computed Nano-Tomography Toolbox: X-ray Ptychography and X-ray Fluorescence Nano-Tomography

To study the fragmentation behavior of Ziegler-type polyolefin catalysts in 3-D at sub-micron spatial resolution, a synchrotron-based correlated X-ray ptychography and fluorescence nano-tomography set-up, see Figure 1.7, at the P06 beam-line at the Deutsches Elektronen-Synchrotron (DESY) was selected as the main microscopy technique of interest in this PhD Thesis. This powerful X-ray microscope is based on the simultaneous collection of ptychographic X-ray computed tomography (PXCT) and X-ray fluorescence tomography (XRF tomography or XRFT).
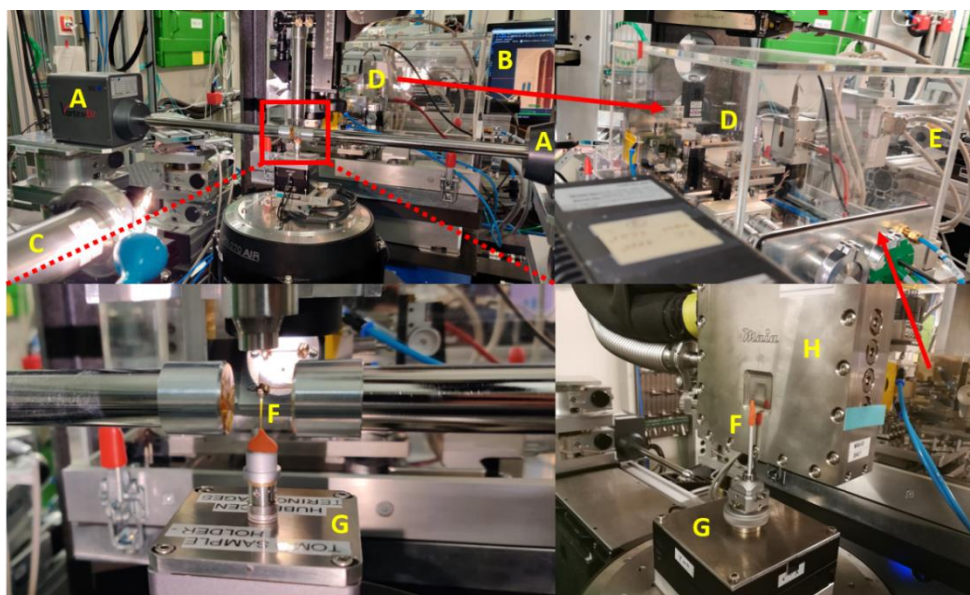
Figure 1.7 Photographs showing the experimental setup of correlated X-ray ptychography and fluorescence nano-tomography at the P06 beamline at DESY in Hamburg. In yellow letters the following parts of the setup are shown: **A** and **H** are respectively the two Si drift detectors setup used in chapter 3 and the MAIA detector used in chapter 2 to collect the fluorescent X-rays. **B** a computer inside the experimental hutch used for the sample finding and rough alignment of the rotation axis of the sample of interest. **C** is the vacuum tube that connects this first experimental hutch to a second experimental hutch where the Eiger detector resides to collect the diffraction data for X-ray ptychography. **D** is the plastic chamber that holds the Kirkpatrick-Baez mirrors to focus the incoming X-rays into a narrow beam of roughly 160x140 nm horizontal versus vertical dimensions. **E** is towards the storage ring of the synchrotron where the X-rays come from and where the X-ray optics hutch of P06 resides with the monochromators. **F** are the polymerized polyolefin catalyst samples from chapters 2 and 3 stabilized inside sealed Kapton capillaries to prevent and limit exposure to moisture, which in turn are hold onto the sample stage with a clay and magnet. **G** are the two fine sample stages used in chapters 2 and 3. The larger sample stage, which also performs the rotation of the fine stage and therefore the sample can be seen in the first photograph. The reason for the use of two different types of XRF detectors and fine stages throughout these chapters is the unfortunate service these components required for various reasons.

PXCT is a type of coherent diffraction imaging (CDI) technique where multiple and partially overlapping diffraction patterns are collected of the region of interest by scanning the sample with a focused and coherent X-ray beam [73]. Because of these multiple diffraction patterns that partially overlap either within a single 2-D projection or in subsequent rotation angles when performing computed tomography, the finite support constraint requirement of conventional CDI is bypassed [85]. The working principle behind Ptychography is highly complex and aims to iteratively update the illumination function, called the probe, and the object so that the measured coherent diffraction intensities match the calculated squared Fourier transforms of the complex exit waves [86]. Through the use of these iterative reconstruction algorithms both the phase, δ, and amplitude, β, of the object can be reconstructed with PXCT. This phase and amplitude of the object are the refraction (real) and absorption (imaginary) parts of the X-ray refractive index of this object, n, as shown in Eq. 1.4 [76].

$$n = 1 - \delta + i\beta \quad \text{Eq. 1.4}$$

At photon energies above roughly 1 keV, the phase contrast, δ, dominates over the absorption contrast, β, especially for lower Z elements, such as carbon. This has to do with the complex number of oscillator modes per atom, $(f_1 + if_2)$, which are related to respectively δ and β through Eq. 1.5-1.6 where λ is the photon wavelength, r_e is the classical electron radius and n_a is the atom number density. Whereas f_1 approaches a value close to Z (the atomic number of an element) at multi keV photon energies, f_2 will decline roughly as λ^2 with respect to f_1. In Figure 1.8, an example of the f_1 and f_2 values are shown for the low Z element carbon and high Z element gold [75]. It becomes evident that for carbon at the incident photon energy of 12 keV (~0.1 nm wavelength, red dashed line) the value of f_1 is several orders of magnitude higher than f_2, therefore making phase contrast imaging preferable for polyolefin catalysts [87].

$$\delta = \frac{r_e}{2\pi} n_a \lambda^2 f_1 \quad \text{Eq. 1.5}$$

$$\beta = \frac{r_e}{2\pi} n_a \lambda^2 f_2 \quad \text{Eq. 1.6}$$
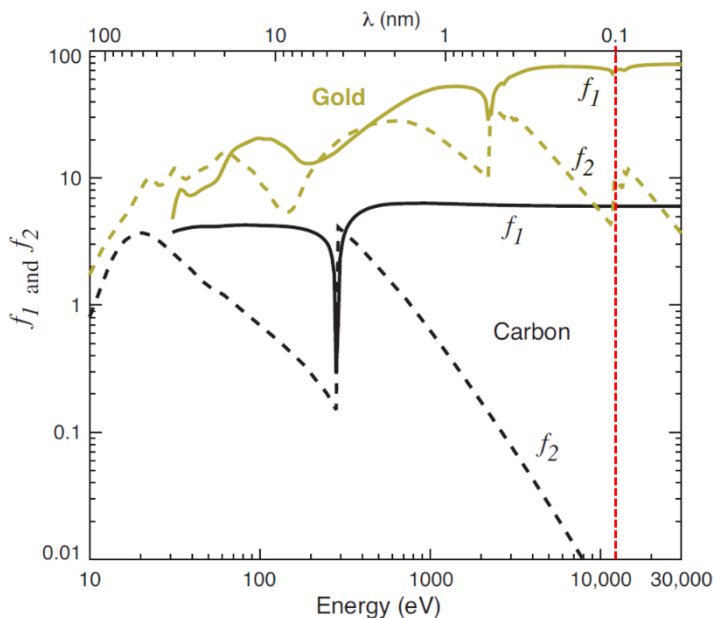
Figure 1.8 For both gold and carbon the f_1 and f_2 complex number of oscillator modes are given as a function of the X-ray photon energy. The red-dashed represents the intersection at 12 keV, the incident X-ray photon energy used in this PhD Thesis for X-ray computed nanotomography. It becomes clear that especially for lower Z elements like carbon, f_1 is orders of magnitude higher than f_2 and therefore at such high energies, phase contrast imaging becomes favorable. Reproduced from Jacobsen [75].

Reconstructing the phase, δ, part of the X-ray refractive index with PXCT has an additional advantage. That is that the real (phase) part of the refractive index, δ, is directly related to the electron density, $\rho_e(\mathbf{r})$, where $\mathbf{r}$ is the spatial coordinate as shown in Eq. 1.7 [88]. In case of computed tomography, $\mathbf{r}$ is equal to the length of a voxel and therefore by reconstructing δ, PXCT is capable of imaging the quantitative electron density contained within each voxel. Here, a voxel is the 3-D equivalent to a pixel. A requirement for quantitative PXCT is that the integral of the transmitted X-ray probe beam has to be known either in the absence of the specimen (vacuum) or through a constant phase through the beam's path with a known refractive index (for instance, air) [89]. Finally, in the case of quantitative electron density, $\rho_e(\mathbf{r})$ in g/Å^3, these obtained values can be compared to theoretical electron density, ρ_e, values calculated based on Eq. 1.8 [88]. Here N_A is Avogadro's constant, ρ_m is the mass density of a material, Z and M are respectively the number of electrons and the molar mass of the reference material. The theoretical ρ_e values of high-density polyethylene, isotactic polypropylene and anhydrous $MgCl_2$ to approximate a Ziegler-type catalyst are given in Table 1.2. In the case that a reconstructed voxel contains multiple chemical phases, then the mean electron density measured with PXCT is simply the sum of the weighted contribution of each material present. The large difference between the theoretical ρ_e values of the two polyolefins of ~0.33 e/Å^3 and that of the Ziegler-type catalysts of ~0.67 e/Å^3 shows the potential strength of using PXCT phase contrast imaging to distinguish between the two phases at high photon energies (well above the carbon K-edge).

$$\rho_e(r) = \frac{2\pi\delta(r)}{\lambda^2 r_e} \quad \text{Eq. 1.7}$$

$$\rho_e = N_A \rho_m \frac{Z}{M} \quad \text{Eq. 1.8}$$

Table 1.2 The theoretical electron density, ρ_e, values of high-density polyethylene (HDPE), isotactic polypropylene (iPP) and anhydrous $MgCl_2$ are given alongside the mass density, number of electrons, Z, and molecular weight, M, of the respective material.

Material	ρ_e (e/Å^3)	ρ_m (g/Å^3)	Z** (e)	M** (g/mol)	Z/M (e*mol/g)
HDPE	0.33	0.94e-24	16	28	0.58
iPP	0.32	0.94e-24	25	43	0.57
Anhydrous MgCl$_2$*	0.67	2.32e-24	46	95.3	0.48

Anhydrous MgCl$_2$ is chosen to represent the complex Ziegler-type catalysts that can vary significantly in terms of chemical composition (weight loading of Ti, porosity versus bulk density, internal donor additives, different support matrixes based on SiO$_2$ and clays).

** The Z and M values used are based on the repeating units of the respective polymers, -CH$_2$-CH$_2$ for HDPE and -CH$_2$-CH$_3$-CH$_2$- for iPP. However, even if one were to take the Z and M values of full polymer chains, since the ratio of Z/M is taken, virtually the same result would be obtained with a negligible difference introduced by the nature of the end-groups.*

One of the strongest aspects of PXCT is that the spatial resolution achievable isn't limited by the focusing optics used [90]. The spatial resolution obtained with PXCT is mainly limited by the largest scattering angles collected and the positioning accuracy of the motor stage. For instance, Diaz et al., have used laser interferometry to correct for random drift of the motor stage and obtained a 3-D isotropic spatial resolution of 16 nm for a 9 x 9 x 3 nm^3 field of view at 6.2 keV [91]. If one forgets for just a brief moment about computed tomography (which relaxes parameters, such as the angular step and therefore total number of unique 2-D projections collected), then Shapiro *et al.* achieved a 5 nm spatial resolution at 740 eV in 2-D images [92].

Conventional full-field and scanning transmission X-ray microscopes use a variety of X-ray focusing optics that work either on diffraction, refraction or reflection of the X-ray beam into the smallest spot-size possible [93]. Fresnel zone plates are often used in the soft X-ray to tender X-ray regimes (~100-5000 eV) and can readily achieve a spot-size down to 20-30 nm, which is nonetheless considerably higher than the associated wavelengths in this regime (100 eV = 12.4 nm, 5000 eV = 0.25 nm) [94]. In this PhD Thesis, two ellipsoidal Kirkpatrick-Baez (KB) mirrors are used to focus the monochromatic hard X-ray source (12 keV) down to roughly 160 by 140 nm (horizontal x vertical). These KB mirrors work by reflecting the incoming X-ray source at grazing incidence from a curved surface, typically made of a heavy metal layer and two subsequent mirrors are used for focusing the X-ray source both horizontally and vertically. Highly advanced, multilayer KB mirrors have achieved a spot size as small as 7 nm at 20 keV [95].

The advantage of raster-scanning the α-olefin polymerized Ziegler-type catalysts with the focused X-ray beam for PXCT, is that at the same time, the X-ray emitted photons from the sample can be collected with energy-dispersive detectors to map the distribution of the Ziegler-type catalyst specific elements [96]. The process of collecting these element characteristic emitted X-ray photons is called X-ray fluorescence and its fundamental principles are drawn schematically in Figure 1.9 [75]. Initially, a core electron is excited to a continuum (energy of a free electron in vacuum) state by an incident X-ray photon whose energy is equal to or greater than the binding energy of this core electron. This is then followed by the relaxation of a higher orbital electron to the now vacant core orbital through the emission of a fluorescent photon whose energy equals the difference between the binding energy of these two orbitals. Alternatively, instead of a fluorescent photon, the energy released upon the transition of the higher orbital electron to the vacant core orbital can also be paired with the excitation of another electron to the continuum state, which is then called an Auger electron. X-ray fluorescent photons are highly specific for each element as the binding energies of the orbitals are determined by the Z-number of the element and the interaction with other (partially) filled orbitals. Not all electron transitions are allowed due to the selection rules in quantum mechanics as shown in Eq. 1.9-1.11. For instance, a 2s to 1s transition (called $K\alpha_3$ according to Siegbahn notation and $K-L_1$ according to IUPAC) is forbidden, yet it can be weakly present in the case of multi-electron systems (since these quantum states are based on the hydrogen-like atom with a single electron) [75].
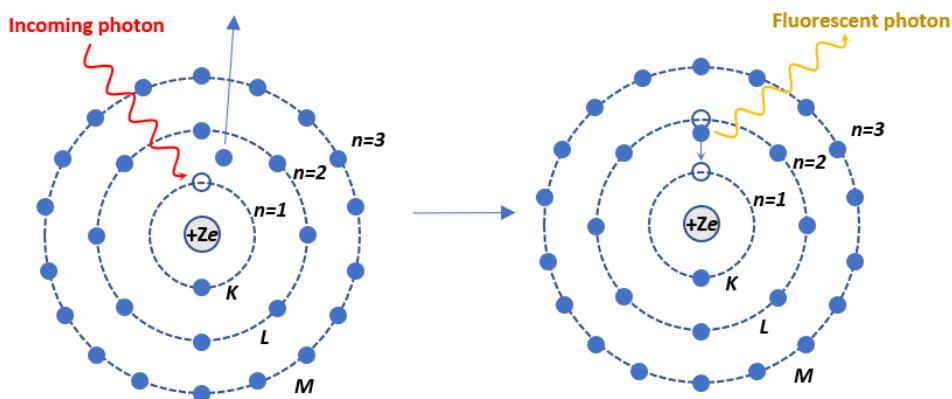
Figure 1.9 Schematic representation of the process behind X-ray fluorescence. Initially, a core electron is excited to the continuum state (ionization) through the absorption of the incoming photon who's energy is equal to or greater than the binding energy of this core electron. The now vacant orbital is then filled up by a higher orbital electron in a process that can release energy in the form of a fluorescent photon. The energy of this fluorescent photon is equal to the difference between the binding energies of the initial and final electron states. Adapted from Jacobsen [75].

$$\Delta n \neq 0 \qquad \text{Eq. 1.9}$$

$$\Delta l = \pm 1 \qquad \text{Eq. 1.10}$$

$$\Delta j = 0, \pm 1 \qquad \text{Eq. 1.11}$$

In this PhD Thesis, the elements of interest are carbon, aluminium, magnesium, chlorine and titanium as these species make up both the polyolefin, catalyst and co-catalyst phases. In Table 1.3 the characteristic emission lines based on the excitation of a 1s electron to the continuum state and subsequent relaxation of a higher shell electron are given for these elements. Additionally, the attenuation length at those energies are provided through both N_2 (to approximate air) and a polyimide capillary, which has been used in chapters 2 and 3 to seal the polyolefin samples studied and therefore prevent contact with moisture during measuring. The polyimide capillaries used in chapters 2 and 3 have a wall thickness of 10 microns (so 20 microns in total will attenuate the emitted X-ray photons).

Based on Table 1.3, it therefore becomes clear that in the case of carbon, magnesium and aluminium, the majority of the X-ray fluorescent photons will therefore be absorbed by this 10 micron thick polyimide capillary and that only the mapping of the chlorine and titanium distributions are feasible. Due to the high sensitivity of the catalyst support matrix to moisture, the only other alternative to the sealing of the sample in a polyimide tubing would be for the experimental setup to be modified and allow the measurement to be performed in a fully inert or vacuum atmosphere. Under such scenarios, it becomes in theory possible for the X-ray fluorescence detectors to detect carbon, magnesium and aluminium, all though strong self-absorption effects can occur (especially for carbon) due to the low energy of these photons with regards to the size of the (pre-polymerized) catalyst particles in the range of several microns [98,99].

Self-absorption effects refer to the emission of a X-ray photon at a certain position within the sample, where this fluorescent X-ray photon is then absorbed again by the sample itself at a position between the detector and the position of emission. Such effects typically become clear when the core of the particle shows a lower X-ray fluorescence intensity than the surface, since photons emitted from the core have to travel the longest distance through the particle and therefore have the highest probability of being absorbed again. Strategies to mitigate this effect include I) making sure that the thickness of the sample or region of interest is smaller than the attenuation length of the element characteristic X-ray emitted photon. For instance, for both the chlorine and titanium $K\alpha_{1,2}$ lines the attenuation length through pure anhydrous $MgCl_2$ (2.42 g/cm^3) is roughly 10 microns. However, the Ziegler-type polyolefin catalysts studied in this PhD Thesis have a considerable polymer phase present (9.2 g iPP per g catalyst in chapter 2 and 3.4 g PE per g catalyst in chapter 3) that disperses the catalyst phase due to the fragmentation process and therefore already helps to mitigate possible self-absorption effects as the attenuation lengths through these polyolefins are on the order of 80 and 500 microns for respectively the chlorine and titanium

K$\alpha_{1,2}$ lines. II) Collect the emitted photons over the full 0-360° rotation axis during tomography in the case of a single X-ray fluorescence detector (Chapter 2) or use 2 X-ray fluorescence detectors in opposite configuration (Chapter 3) to compensate for stronger self-absorption effects at certain rotations due to the geometry and distribution of chemical phases of the region of interest.

Table 1.3 The energy of the emission lines (X-ray fluorescent photons) of the elements of interest to Ziegler-type polyolefin catalysis are given alongside the attenuation length values[*] (1/e or ~63% of incident photons absorbed) given at that specific energy through either N_2 (as approximation of attenuation through air) or polyimide tubing. X-ray attenuation length calculations were performed with the Henke toolbox available on-line [74].

Energy (eV)	Element	Emission Line (Siegbahn // IUPAC)	Initial to final state of electron	Atten. Length N_2 (**mm**)	Atten. length polyimide tubing (**mm**)
277	C	Kα_1 // K-L$_3$	2p$_{3/2}$ to 1s	2.1	0.002
452.2	Ti	Lα_{1-2} // L$_3$-M$_{5-4}$	3d$_{5/2\&3/2}$ to 2p$_{3/2}$	0.3	0.0005[**]
458.4	Ti	Lβ_1 // L$_2$-M$_4$	3d$_{3/2}$ to 2p$_{1/2}$	0.3	0.0005[**]
1253.6	Mg	Kα_{1-2} // K-L$_{3-2}$	2p$_{3/2\&1/2}$ to 1s	4.5	0.005
1302.2	Mg	Kβ_1 // K-M$_3$	3p$_{3/2}$ to 1s	5.0	0.005
1486.3	Al	Kα_1 // K-L$_3$	2p$_{3/2}$ to 1s	7.2	0.008
1486.7	Al	Kα_2 // K-L$_2$	2p$_{1/2}$ to 1s	7.2	0.008
1557.5	Al	Kβ_1 // K-M$_3$	3p$_{3/2}$ to 1s	8.3	0.009
2620.8	Cl	Kα_1 // K-L$_3$	2p$_{3/2}$ to 1s	37.2	0.04
2622.4	Cl	Kα_2 // K-L$_2$	2p$_{1/2}$ to 1s	37.3	0.04
2815.6	Cl	Kβ_1 // K-M$_3$	3p$_{3/2}$ to 1s	46.1	0.05
4504.7	Ti	Kα_1 // K-L$_3$	2p$_{3/2}$ to 1s	190.4	0.20
4510.8	Ti	Kα_2 // K-L$_2$	2p$_{1/2}$ to 1s	191.2	0.20
4931.8	Ti	Kβ_1 // K-M$_3$	3p$_{3/2}$ to 1s	251.5	0.26

[*]note that these attenuation length values are given for the respective emission lines (fluorescent X-ray photon), which are multiple electron volts below the binding energy of the core electrons. Therefore the attenuation length of fluorescent X-ray photons is larger than for an incident X-ray photon who's energy matches the binding energy of the core electron. As example, the binding energy of 284 eV of carbon results in an attenuation length through the polyimide tubing of 0.2 microns, ten times smaller than for the Kα_1 fluorescent X-ray photon of carbon.

[**] The Lα/β emission lines of Ti are only 50 eV above the 1s binding energy of N, a major constituent of the polyimide chemical phase, hence the lower attenuation length through the polyimide tubing at this higher photon energy with respect to the Kα_1 emission line of carbon.

1.5 Scope of this PhD Thesis

The scope of this PhD Thesis is to gain a better understanding of the Ziegler-type catalyst fragmentation behavior in the early stages of α-olefin polymerization. The main microscopy technique used to study this polyolefin catalyst fragmentation behavior is synchrotron-based correlated X-ray ptychography and fluorescence tomography. An introduction towards both α-olefin polymerization and the field of X-ray (nano)tomography is given in **Chapter 1**.

In **Chapter 2** the methodology is developed to apply X-ray computed nanotomography to a single propylene polymerized Ziegler-Natta catalyst particle. There the foundations are made to study the fragmentation behavior of the moisture-sensitive Ziegler-type catalysts without exposure of the MgCl$_2$ framework to air during the measurement. In this Chapter, we show that this Ziegler-Natta catalyst particle was fragmenting according to both the continuous bisection and shrinking core fragmentation modes, but that the former was dominating the overall fragmentation behavior under the reaction conditions used. However, due to the likely presence of residual solvent molecules in the polyolefin layer only a limited amount of 2-D projections are obtained resulting in an estimated 3-D spatial resolution on the order of several hundreds of nanometer.

In **Chapter 3** this methodology is improved upon in two ways: I) after successively removing residual solvent molecules from the polymer to ensure stability under X-ray exposure a high spatial resolution of 74 nm in 3-D is achieved with ptychography X-ray computed tomography. II) instead of studying a single catalyst particle after propylene polymerization, a statistically relevant ensemble of 434 ethylene polymerized catalyst particles was imaged and analyzed. This allowed us to conclude that there is a heterogeneity in the polymerization activity and degree of fragmentation within the ensemble.

In **Chapter 4** a planar model system is developed based on the deposition of spherical caps made of a moisture-stable and high Z contrast LaOCl support matrix to replace the moisture sensitive and low Z contrast MgCl$_2$ support matrix. The chosen spherical cap morphology allows us to mimic the industrially relevant spherical catalyst morphology whilst using surface-sensitive microscopy techniques, such as photo-induced force microscopy and time-of-flight secondary ion mass spectrometry as well as the more conventional scanning electron and Raman microscopy techniques. This model system allowed us to study the fragmentation behavior of this here-introduced LaOCl support matrix under ambient transport and measuring conditions albeit based on cross-sectional microscopy.

In **Chapter 5** a summary is given on the contents of this PhD thesis as well as future persepctives. These future perspectives concern the further methodological development of X-ray nanotomography for the field of α-olefin polymerization with respect to *in-situ* imaging and exploring the other polyolefin catalyst families, namely Phillips and immobilized metallocenes. Furthermore, the initial results are shown for the synthesis of

LaOCl microspheres using ultrasonic spray pyrolysis to be used as a bulk support matrix for Ziegler-type catalysts. Finally, results towards the development of planar model systems utilizing well-defined $MgCl_2$ crystals with either non-labelled or perylene-labelled internal donors are shown.

1.6 References

1. Kaminsky, W. (Ed.), Preface. In: *Polyolefins: 50 years after Ziegler and Natta I*, Springer, Berlin, **2013**.
2. Gahleitner, M., Severn, J.R., Designing Polymer Properties. In: *Tailor-Made Polymers Via Immobilization of Alpha-Olefin Polymerization Catalysts*, Severn, J.R., Chadwick, J.C., (Eds.); Wiley-VCH, Weinheim, **2008**.
3. Gandini, A., Lacerda, T.M., From monomers to polymers from renewable resources: Recent advances, *Prog. Polym. Sci.,* **2015**, 48, 1-39.
4. Galli, P., Vecellio, G., Polyolefins: The most promising large-volume materials for the 21st century, *J. Poly. Sci. A.,* **2004**, 42, 396-415.
5. Pullukat, T.J., Patterson, R.E., Porous Silica in Transition Metal Polymerization Catalysts. In: *Handbook of Transition Metal Polymerization Catalysts*, Hoff, R., (Ed.), Jonh Wiley & Sons, Inc., Hoboken, **2010**.
6. Severn, J.R., Chadwick, J.C., (Eds.) Preface. In: *Tailor-Made Polymers Via Immobilization of Alpha-Olefin Polymerization Catalysts*, Severn, J.R., Chadwick, J.C., (Eds.); Wiley-VCH, Weinheim, **2008**.
7. Mülhaupt, R. Catalytic Polymerization and Post polymerization Catalysis Fifty Years After the Discovery of Ziegler's Catalysts, *Macromol. Chem. Phys.,* **2003**, 204, 289-327.
8. Soga, K., Shiono, T., Ziegler-Natta Catalysts for Olefin Polymerization, *Prog. Polym. Sci.*, **1997**, 22, 15-03-1546.
9. Paulik, C., Spiegel, G., Jeremic, D., Bimodal Polyethylene: Controlling Polymer Properties by Molecular Design. In: *Multimodal Polymers with Supported Catalysts*, Albunia, A.R., Prades, F., Jeremic, D., (Eds.), Springer Nature, Cham, **2019**.
10. Whiteley, K.S., Heggs, T.G., Koch, H., Mawer, R.L., Immel, W., Polyolefins. In: *Ullmann's Encyclopedia of Industrial Chemistry*, Wiley-VCH, Weinheim, **2005**.
11. Bensason, S., Minick, J., Moet, A., Chum, S., Hiltner, A., Baer, E., Classification of homogeneous ethylene-octene copolymers based on comonomer content, *J. Polym. Sci. B.,* **1996**, 34, 1301-1315.
12. Mülhaupt, R., Green polymer chemistry and bio-based plastics: Dreams and reality, *Macromol. Chem. Phys.*, 2013, 214,159-174.
13. Gahleitner, M., Paulik, C., Polypropylene and Other Polyolefins. In: *Brydson's Plastics Materials, Gilbert*, M. (Ed.), Butterworth-Heinemann, Oxford, **2017**.
14. Talarico, G., De Rosa, C., Auriemma, F., Tacticity, Regio and Stereoregularity. In: *Polypropylene Handbook*, Karger-Kocsis, J., Bárány, T., (Eds.), Springer Nature Switzerland, Cham, **2019**.
15. Severn, J.R., Chadwick, J.C., Duchateau, R., Friederichs, N., "Bound but Not Gagged"-Immobilizing Single-Site α-Olefin Polymerization Catalysts, *Chem. Rev.,* **2005**, 105, 4073-4147.
16. McKenna, T.F., Soares, J.B.P., Single particle modelling for olefin polymerization on supported catalysts: A review and proposals for future developments, *Chem. Eng. Sci.,* **2001**, 56, 3931-3949.

17. McKenna, T.F.L., Di Martino, A., Weickert, G., Soares, J.B.P., Particle Growth During the Polymerisation of Olefins on Supported Catalysts, 1 – Nascent Polymer Structures, *Macrmol. React. Eng.,* **2010**, 4, 40-64.

18. Albunia, A.R., Prades, F., Jeremic, D., (Eds.), Overview of Polyolefins - Role of Polyolefins in Our Daily Lives. In: *Multimodal Polymers with Supported Catalysts*, Springer Nature, Cham, **2019**.

19. Lafleur, S., Berthoud, R., Ensinck, R., Cordier, A., De Cremer, G., Philippaerts, A., Bastiaansen, K., Margossian, T., Severn, J.R., Tailored Bimodal Ultra-High Molecular Weight Polyethylene Particles, *J. Polym. Sci. A.,* **2018**, 56, 1646-1656.

20. Chammingkwan, P., Bando, Y., Terano, M., Taniike, T., Nano-Dispersed Ziegler-Natta, Catalysts for 1 µm-Sized Ultra-High Molecular Weight Polyethylene Particles, *Front. Chem.,* **2018**, 6, 524

21. Gahleitner, M., Melt rheology of polyolefins, *Prog. Polym. Sci.,* **2001**, 26, 895-944.

22. Beigzadeh, D., Soares, J.B.P., Hamielec, A.E., Recipes for Synthesizing Polyolefins with Tailor-Made Molecular Weight, Polydispersity Index, Long-Chain Branching Frequencies and Chemical Composition Using Combined Metallocene Catalyst Systems in a CSTR at Steady State, *J. Appl. Polym. Sci.,* **1999**, 71, 1753-1770.

23. Bett, K.E., Crossland, B., Ford, H., Gardner, A.K., Review of the engineering developments in the high pressure polyethylene process 1933-1983, *Proceedings of the Golden Jubilee Conference, Polyethylenes 1933-1983, Plastics and Rubber Institute*, London, **1983**.

24. Hogan, J.P., Banks, R.L., Polymers and production thereof, US2824721A, **1956.**

25. Hogan, J.P., Banks, R.L., Polymerization catalyst and production thereof, US2951816A, **1960**.

26. Ziegler, K., Consequences and Development of an Invention, *Angew. Chem.*, **1964**, 76, 545-553.

27. Fink, G., Contributions to the Ziegler–Natta Catalysis: An Anthology. In: *Polyolefins: 50 years after Ziegler and Natta I*, Kaminsky, W. (Ed.), Springer, Berlin, **2013**.

28. Natta, G., From stereospecific Polymerization to asymmetric autocatalytic Synthesis of Macromolecules, *Angew. Chem.*, **1964**, 76, 553-566.

29. Kaminsky, W., The discovery of metallocene catalysts and their present state of the art, *J. Polym. Sci. A.,* **2004**, 42, 3911-3921.

30. Sinn, H., Kaminsky, W., Vollmer, H-J., Woldt, R., "Living Polymers" on Polymerization with Extremely Productive Ziegler Catalysts, *Angew. Chem. Int. Ed.,* **1980**, 19, 390-392.

31. Natta, G., Corradini, P., Allegra, G., The different crystalline modifications of $TiCl_3$, a catalyst component for the polymerization of α-olefins. I: α, β-, γ-$TiCl_3$. II: δ-$TiCl_3$, *J. Pol. Sci.*, **1961**, 51, 399-410.

32. Severn, J.R., Recent Developments in Supported Polyolefin Catalysts: A Review. In: *Multimodal Polymers with Supported Catalysts*, Albunia, A.R., Prades, F., Jeremic, D., (Eds.), Springer Nature, Cham, 2019.

33. Di Pietro, J., Process for deashing polymers, US3560471A, **1969**.

34. Hermans, J., Henrioulle, P., Process for the preparation of a Ziegler-Natta type catalyst, US3769233A, **1971.**

35. Goodall, B.L., Van der Nat, A.A., Sjardijn, W., Olefin polymerization catalyst compositions and a process for the polymerization of olefins employing such compositions, EP0019312A1, **1980**.

36. Busico, V., Corradini, P., De Martino, L., Proto, A., Savino, V., Albizzati, E., Polymerization of propene in the presence of $MgCl_2$-supported Ziegler-Natta catalysts, 1. The role of ethyl benzoate as "internal" and "external" base, *Macromol. Chem. Phys.,* **1985**, 186, 1279-1288.

37. Giannini, U., Polymerization of olefins with high activity catalysts, *Macromol. Chem. Phys.*, **1981**, 5, 216-229.

38. Zannetti, R., Marega, C., Marigo, A., Martorana, A., Layer-lattices in Ziegler-Natta catalysts, *J. Polym. Sci. B.,* **1988**, 26, 2399-2412.

39. Busico, V., Causà, M., Cipullo, R., Credendino, R., Cutillo, F., Friederichs, N., Lamanna, R., Segre, A., Van Axel Castelli, V., Periodic DFT and High-Resolution Magic-Angle-Spinning (HR-MAS)^{1}H NMR investigation of the active surfaces of $MgCl_2$-supported Ziegler-Natta catalysts. The $MgCl_2$ matrix, *J. Phys. Chem. C.,* **2008**, 112, 1081-1089.
40. Kashiwa, N., The discovery and progress of $MgCl_2$-supported $TiCl_4$ catalysts, *J. Polym. Sci. A.,* **2003**, 42, 1-8.
41. Chadwick, J.C., Morini, G., Balbontin, G., Camurati, L., Heere, J.J.R., Mingozzi, I., Testoni, F., Effects of internal and external donors on the regio and stereoselectivity of active species in $MgCl_2$-supported catalysts for propene polymerization, *Macrmol. Chem. Phys.,* **2001**, 202, 1995-2002.
42. Sacchi, M.C., Tritto, I., Shan, C., Mendichi, R., Noristi, L., Role of the Pair of Internal and External Donors in $MgCl_2$-Supported Ziegler-Natta Catalyst, *Macromolecules,* **1991**, 24, 6823-6826.
43. Taniike, T., Terano, M., The Use of Donors to Increase the Isotacticity of Polypropylene, *Adv. Polym. Sci.,* **2013**, 257, 81-98.
44. Matsunaga, K., Next generation polyolefins, vol 1., p. 84, Sankeisha, Nagoya, **2008.**
45. Morini, G., Balbontin, G., Gulevich, Y.V., Kelder, R.T., Duijghuisen, H.B.P., Klusener, P.A.A., Kondorffer, F.M., Components and catalysts for the polymerization of olefins, WO2000063261, **2000**.
46. Fernandes, J.A., Girard, A-L., Support Designed for Polymerization Processes. In: *Multimodal Polymers with Supported Catalysts*, Albunia, A.R., Prades, F., Jeremic, D., (Eds.), Springer Nature, Cham, **2019**.
47. Seenivasan, K., Sommazzi, A., Bonino, F., Bordiga, S., Groppo, E., Spectroscopic Investigation of Heterogeneous Ziegler-Natta Catalysts: Ti and Mg Chloride Tetrahydrofuranates, Their Interaction Compound, and the Role of the Activator, *Chem. Eur. J.,* **2011**, 17, 8648-8656.
48. Thushara, K.S., D'Amore, M., Piovano, A., Bordiga, S., Groppo, E., The Influence of Alcohols in Driving the Morphology of Magnesium Chloride Nanocrystals, *ChemCatChem*, **2017**, 9, 1782-1787.
49. Arlman, E.J., Cossee, P., Ziegler-Natta catalysis III. Stereospecific polymerization of propene with the catalyst system $TiCl_3AlEt_3$, *J. Catal.,* **1964**, 3, 99-104.
50. Giunchi, G., Allegra, J., Structural disorder in microcrystalline $MgCl_2$, *J. Appl. Cryst.*, **1984**, 17, 172-178.
51. D'Amore, M., Thushara, K.S., Piovano, A., Causà, M., Bordiga, S., Groppo, E., Surface Investigation and Morphological Analysis of Structurally Disordered $MgCl_2$ and $MgCl_2/TiCl_4$ Ziegler-Natta Catalysts, *ACS Catal.,* **2016**, 6, 5786-5796.
52. Ferrero, M.A., Chiovetta, M.G., Catalyst fragmentation during propylene polymerization: Part I. The effects of grain size and structure, *Polym. Eng. Sci.,* **1987**, 27, 1436-1447.
53. Noristi, L., Marchetti, E., Baruzzi, G., Sgarzi, P., Investigation on the particle growth mechanism in propylene polymerization with $MgCl_2$-supported Ziegler-Natta catalysts, *J. Polym. Chem. A.,* **1994**, 32, 3047-3059.
54. Pater, J.T.M., Weickert, G., Van Swaaij, W.P.M., Polymerization of liquid propylene with a fourth-generation Ziegler-Natta catalyst: Influence of temperature, hydrogen, monomer concentration, and prepolymerization method on powder morphology, *J. Appl. Polym. Sci.,* **2003**, 87, 1421-1435.
55. Pater, J.T.M., Weickert, G., Loos, J., van Swaaij, W.P.M., High precision prepolymerization of propylene at extremely low reaction rates—kinetics and morphology, *Chem. Eng. Sci.,* **2001**, 56, 4107-4120.
56. Qi, M., Zhang, B., Fu, Z., Xu, J., Fan, Z., Millimeter-size polyethylene hollow spheres synthesized with $MgCl_2$-supported Ziegler-Natta catalyst, *J. Appl. Polym. Sci.,* **2016**, 133, 43207.

57. Simonazzi, T., Cecchin, G., Mazullo, S., An outlook on progress in polypropylene-based polymer technology, *Prog. Polym. Sci.,* **1991**, 16, 303-329.
58. Grof, Z., Kosek, J., Marek, M., Modeling of morphogenesis of growing polyolefin particles, *AIChE J.,* **2005**, 51, 2048-2067.
59. Horáčková, B., Grof, Z., Kosek, J., Dynamics of fragmentation of catalyst carriers in catalytic polymerization of olefins, *Chem. Eng. Sci.,* **2007**, 62, 5264-5270.
60. Ferrero, M.A., Chiovetta, M.G., Catalyst fragmentation during propylene polymerization: Part II. Microparticle diffusion and reaction effects, *Polym. Eng. Sci.,* **1987**, 27, 1448-1460.
61. Laurence, R.L. and Chiovetta, M.G., In: Reicher, K.H., Geisler, G. (Eds.), Polymer Reaction Engineering, Hasuer-Verlag, München, **1983**, 74-112.
62. Kittilsen, P., McKenna, T.F., Svendsen, H., Jakobsen, H.A., Fredriksen, S.B., The interaction between mass transfer effects and morphology in heterogeneous olefin polymerization, *Chem. Eng. Sci.,* **2001**, 56, 4015-4028.
63. Zheng, X., Pimplapure, M.S., Weickert, G., Loos, J., Influence of Copolymerization on Fragmentation Behavior Using Ziegler-Natta Catalysts, *Macromol. Rapid Commun.,* **2006**, 27, 15-20.
64. Vestberg, T., Denifl, P., Wilén, C-E. Porous versus novel compact Ziegler-Natta catalyst particles and their fragmentation during the early stages of bulk propylene polymerization, *J. Appl. Polym. Sci.,* **2008**, 110, 2021-2029.
65. Abboud, M., Denifl, P., Reichert, K-H., Fragmentation of Ziegler-Natta Catalyst Particles During Propylene Polymerization, *Macromol. Mater. Eng.,* **2005**, 290, 558-564.
66. Zheng, X., Smit, M., Chadwick, J.C., Loos, J., Fragmentation Behavior of Silica-Supported Metallocene/MAO Catalyst in the Early Stages of Olefin Polymerization, *Macromolecules,* **2005**, 38, 4673-4678.
67. Zheng, X., Loos, J., Morphology evolution in the early stages of olefin polymerization, *Macromol. Symp.,* **2006**, 236, 249-258.
68. Nooijen, G.A.H., Ziegler/Natta catalysts in particle form ethylene polymerization: The effect of polymerization start-up on catalyst activity and morphology of the produced polymer, *Catal. Today,* **1991**, 11, 35-46.
69. Nooijen, G.A.H., On the important of diffusion of cocatalyst molecules through heterogeneous Ziegler/Natta catalysts, *Eur. Polym. J.,* **1994**, 30, 11-15.
70. Di Martino, A., Broyer, J.P., Spitz, R., Weickert, G., McKenna, T.F., A Rapid Quenched-Flow Device for the Characterisation of the Nascent Polymerization of Ethylene under Industrial Conditions, *Macromol. Rapid Commun.,* **2005**, 26, 215-220.
71. McKenna, T.F.L., Tioni, E., Ranieri, M.M., Alizadeh, A., Boisson, C., Monteil, V., Catalytic olefin polymerisation at short times: Studies using specially adapted reactors, *Can. J. Chem. Eng.,* **2013**, 91, 669-686.
72. Kaczorowski, M., Gerberich, W.W., The "effective" penetration depth of backscattered electrons associated with electron channeling patterns (ECPs), *Mater. Lett.,* **1986**, 4, 244-248.
73. Pfeiffer, F., X-ray ptychography, *Nat. Photonics,* **2018**, 12, 9-17.
74. These calculations were performed with the "X-ray Attenuation Length" toolbox accessible at: https://henke.lbl.gov/optical_constants/atten2.html. Density values for the polyolefins were taken at 0.94 g/cm^3 (valid for both HDPE and iPP phases) and 2.32 g/cm^3 for Ziegler-type catalysts (the value of anhydrous MgCl$_2$).
75. Jacobsen, C., X-Ray Tomography in X-ray Microscopy; Cambridge University Press, Cambridge, **2020**, 321-349.
76. O'Sullivan, J.D.B., Behnsen, J., Starborg, T., MacDonald, A.S., Phythian-Adams, A.T., Else, K.J., Cruickshank, S.M., Withers, P.J., X-ray micro-computed tomography (μCT): an emerging opportunity in parasite imaging, *Parasitology*, **2018**, 145, 848-854.

77. Schneider, G., X-ray microscopy: Methods and perspectives, *Anal. Bioanal. Chem.,* **2003**, 376, 558-561.
78. Larson, B.C., Lengeler, B., High-Resolution Three-Dimensional X-ray Microscopy, *MRS Bull.,* **2004**, 29, 152-154.
79. van Heel, M., Schatz, M., Fourier shell correlation threshold criteria, *J. Struct. Biol.*, **2005**, 151, 250-262.
80. Conner, W.C., Webb, S.W., Spanne, P., Jones, K.W., Use of x-ray microscopy and synchrotron microtomography to characterize polyethylene polymerization particles, *Macromolecules,* **1990**, 23, 4742-4747.
81. Jones, K.W., Spanne, P., Lindquist, W.B., Conner, W.C., Ferrero, M.A., Determination of polymerization particle morphology using synchrotron computed microtomography, *Nucl. Instrum. Methods Phys. Res. B,* **1992**, 68, 105-110.
82. Ferrero, M.A., Sommer, R., Spanne, P., Jones, K.W., Conner, W.C., X-ray microtomography studies of nascent polyolefin particles polymerized over magnesium chloride-supported catalysts, *J. Polym. Sci. A,* **1993**, 31, 2507-2515.
83. Seda, L., Zubov, A., Bobak, M., Kosek, J., Kantzas, A., Transport and Reaction Characteristics of Reconstructed Polyolefin Particles, *Macromol. React. Eng.,* **2008**, 2, 495-512.
84. Meisterová, L., Zubov, A., Smolná, K., Štěpánek, F., Kosek, J., X-Ray Tomography Imaging of Porous Polyolefin Particles in an Electron Microscope, *Macromol. React. Eng.,* **2013**, 7, 277-288.
85. Gürsoy, D., Direct coupling of tomography and ptychography, *Opt. Lett.,* **2017**, 42, 3169-3172.
86. Dierolf, M., Menzel, A., Thibault, P., Schneider, P., Kewish, C.M., Wepf, R., Bunk, O., Pfeiffer, F., Ptychographic X-ray computed tomography at the nanoscale, *Nature*, **2010**, 467, 436-439.
87. Henke, B.L., Gullikson, E.M., Davis, J.C., X-Ray Interactions: Photoabsorption, Scattering, Transmission, and Reflection at E = 50-30,000 eV, Z = 1-92, *At. Data Nucl. Data* Tables, **1993**, 54, 181-342.
88. Diaz, A., Trtik, P., Guizar-Sicairos, M., Menzel, A., Thibault, P., Bunk, O., Quantitative x-ray phase nanotomography, *Phys. Rev. B*, **2012**, 85, 020104-1-3.
89. Rose, M., Senkbeil, T., von Gundlach, A.R., Stuhr, S., Rumancev, C., Dzhigaev, D., Besedin, I., Skopintsev, P., Loetgering, L., Viefhaus, J., Rosenhahn, A., Vartanyants, I.A., Quantitative ptychographic bio-imaging in the water window, *Opt. Express*, **2018**, 26, 1237-1254.
90. Thibault, P., Menzel, A., Reconstructing state mixtures from diffraction measurements, *Nature*, **2013**, 494, 68-71.
91. Holler, M., Diaz, A., Guizar-Sicairos, M., Karvinen, P, Färm, E., Härkönen, E., Ritala, M., Menzel, A., Raabe, J., Bunk, O., X-ray ptychographic computed tomography at 16 nm isotropic 3D resolution, *Sci. Rep.,* **2014**, 4, 3857.
92. Shapiro, D.A., Babin, S., Celestre, R.S., Chao, W., Conley, R.P., Denes, P., Enders, B., Enfedaque, P., James, S., Joseph, J.M., Krishnan, H., Marchesini, S., Muriki, K., Nowrouzi, K., Oh, S.R., Padmore, H., Warwick, T., Yang, L., Yaschuk, V.V., Yu, Y.-S., Zhao, J., *Sci. Adv.,* **2020**, 6, eabc4904.
93. Meirer, F., Weckhuysen, B.M., Spatial and temporal exploration of heterogeneous catalysts with synchrotron radiation, *Nat. Rev. Mater.,* **2018**, 3, 324-340.
94. Lider, V.V., Zone Plates for X-Ray Focusing, *J. Surf. Investig.,* **2017**, 11, 1113-1127.
95. Yamauchi, K., Mimura, H., Kimura, T., Yumoto, H., Handa, S., Matsuyama, S., Arima, K., Sano, Y., Yamamura, K., Inagaki, K., Nakamori, H., Kim, J., Tamasaku, K., Nishino, Y., Yabashi, M., Ishikawa, T., Single-nanometer focusing of hard x-rays by Kirkpatrick-Baez mirrors, *J. Phys.: Condens. Matter,* **2011**, 23, 394206.
96. De Jonge, M.D., Vogt, S., Hard X-ray fluorescence tomography-an emerging tool for structural visualization, *Curr. Opin. Struct. Biol.*, **2010**, 20, 606-614.

97. Kalirai, S., Boesenberg, U., Falkenberg, G., Meirer, F., Weckhuysen, B.M., X-ray Fluorescence Tomography of Aged Fluid-Catalytic-Cracking Catalyst Particles Reveals Insight into Metal Deposition Processes, ChemCatChem, **2015**, 7, 3674-3682.
98. Liu, Y., Meirer, F., Krest, C.M., Webb, S., Weckhuysen, B.M., Relating structure and composition with accessibility of a single catalyst particle using correlative 3-dimensional micro-spectroscopy, Nat. Comm., **2016**, 7, 12634.

Chapter 2. Correlated X-ray Ptychography and Fluorescence Nano-Tomography on the Fragmentation Behavior of an Individual Catalyst Particle During the Early Stages of Olefin Polymerization

In this Chapter a combination of ptychographic X-ray computed tomography (PXCT) and X-ray fluorescence (XRF) nano-tomography has been used to study the fragmentation behavior of an individual Ziegler-Natta catalyst particle, ~40 microns in diameter, in the early stages of propylene polymerization with sub-micron spatial resolution. The electron density signal obtained from PXCT gives the composite phases of the Ziegler-Natta catalyst particle fragments and isotactic polypropylene, while 3-D XRF visualizes multiple isolated clusters, rich in Ti, of several microns in size. The radial distribution of Ti species throughout the polymer-catalyst composite particle shows that the continuous bisection fragmentation model is the main contributor to the fragmentation pathway of the catalyst particle as a whole. Furthermore, within the largest Ti clusters the fragmentation pathway was found to occur through both the continuous bisection and layer-by-layer models. The fragmentation behavior of polyolefin catalysts was for the first time visualized in 3-D by directly imaging and correlating the distribution of the Ti species to the polymer-catalyst composite phase.

2.1 Introduction

Ziegler-Natta catalysts are considered to be the grand work horses for the production of polyolefins, such as polyethylene and isotactic polypropylene (iPP), a market of which the total volume exceeds 160 million tonnes produced annually [1]. Current generation Ziegler-Natta catalysts are typically based on a highly porous $MgCl_2$ support, chemisorbed $TiCl_4$ as the active site precursor and a trialkylaluminium co-catalyst. In the case of iPP production Lewis base molecules, such as di-esters and di-ethers, and silanes, are added to enhance the activity and stereoselectivity of the Ti active site species [1,2]. To ensure good and continuous reactor operability on such large scales, discrete polymer particle formation is crucial and therefore requires heterogeneous catalysts [2].

However, due to the formation of polymer on the catalyst particle's surface, monomer diffusion to the active site can become severely limited and a fragmentation of the catalyst particle's framework is required to sustain polymerization activity [1-5]. The formation of the polyolefin at the Ti active site within the porous framework leads to a build-up of stress and force exerted on the framework finally resulting in the fragmentation of the framework [6]. The fragmentation behavior of the catalyst particles is an interplay of the properties of the catalyst framework in terms of pore size, pore size distribution and lattice strength but also crystallinity of the polymer product [7]. The fragmentation behavior, as typically studied with cross-sectional electron microscopy techniques, is considered to be a mixture of two limiting modes of fragmentation as shown schematically in Figure 2.1. The first fragmentation model is called shrinking core or layer-by-layer, with fragmentation starting at the outer particle surface by peeling off framework species until the core is reached . The second fragmentation model is called continuous bisection where the break-up of the particle occurs through internal cleavage at the particle's core into successively smaller fragments [7-9]. These two fragmentation models are shown schematically in Figure 2.1. However, a powerful experimental toolbox for a full 3-D study on the fragmentation behavior is lacking whilst this stage in the polymerization reaction has direct consequences on the polymerization rate and more importantly the evolution of the particle morphology [7-16].

Pioneering work on the use of synchrotron radiation for the imaging of both polyethylene and polypropylene particles was done with X-ray computed microtomography (XCMT) [17-22]. However, these studies have focused on the polymer phases with 3-D voxel sizes of several microns therefore neglecting the role of the catalyst fragmentation stage occurring at significantly smaller size-scales, i.e. on the order of sub-micron to a few tens of microns.
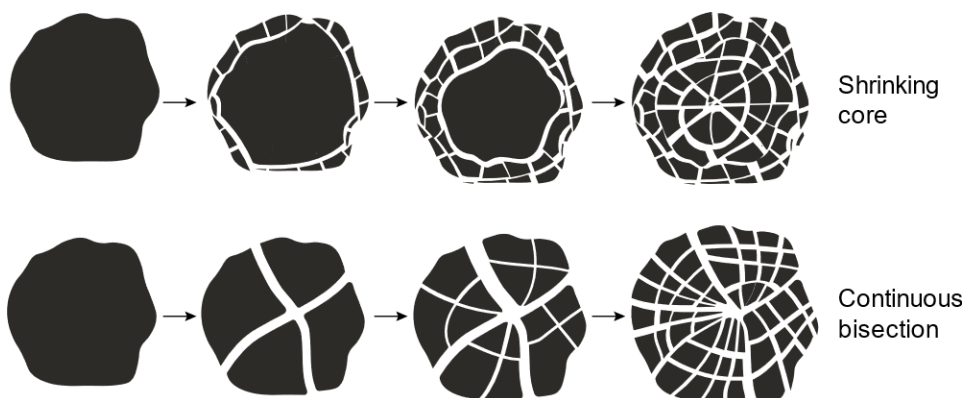
Figure 2.1 Schematic representation of the two limiting modes of fragmentation of the catalyst support matrix: shrinking core or layer-by-layer and continuous bisection. Adapted from Horácková *et al.* [8].

To tackle this length-scale gap we have focused in this Chapter on the combination of two powerful X-ray nano-tomography microscopy techniques, namely ptychographic X-ray computed tomography (PXCT) and X-ray fluorescence (XRF) nano-tomography to correlate the elemental distribution of Ti, comprising the active site species, to the fragmentation behavior of an individual Ziegler-Natta propylene polymerized catalyst particle in the early stages of polymerization. Significant progress has been made over the past years in the field of X-ray imaging full catalyst particles such as for Fluid Catalytic Cracking and Fischer-Tropsch Synthesis processes by pushing the spatial resolution into the nanometer regime. Furthermore, besides absorption-contrast based X-ray microscopy there is now also the possibility for (correlated-) 3-D chemical, elemental and diffraction imaging [23-38]. X-ray ptychography is a coherent diffraction imaging technique that can provide quantitative information about the phase changes introduced by the object [39], whereas XRF gives the spatial distribution of elements of interest, such as the Ti (Kα1 4510 eV) and Cl (Kα1 2622 eV) species for a Ziegler-Natta catalyst.

2.2 Experimental

2.2.1 Synthesis of the Ziegler-Natta Catalyst

A fourth generation Ziegler-Natta catalyst, representative for industrial propylene polymerization was prepared analogous to the procedure as described in patent EP2027164 [40]. The material made has a final catalyst formulation of $MgCl_2/TiCl_4$/Dibutyl phthalate with a Ti weight loading of 2%, as measured with inductively coupled plasma - atom emission spectroscopy (ICP-AES). Analysis of the average particle size (D_{50}), using Static Laser Scattering (SLS) and measured with a Mastersizer 3000 laser diffraction particle size analyzer instrument, showed a D_{50} of 18 µm. scanning electron microscopy (SEM) images, taken with a Phenom Pro at 15 kV accelerating voltage, of the pristine Ziegler-Natta catalyst are shown in Figure 2.2. The final catalyst has a surface area (S_{BET}) of 355 m^2/g, and pore volume (V_{pore}) of 0.279 cm^3/g with a pore size distribution mainly between 2-10 nm as determined with N_2 physisorption. The large cracks observed throughout the pristine catalyst particle, which are almost reminiscent of a smiley-face, are introduced unintentionally during the final drying step of the catalyst material.
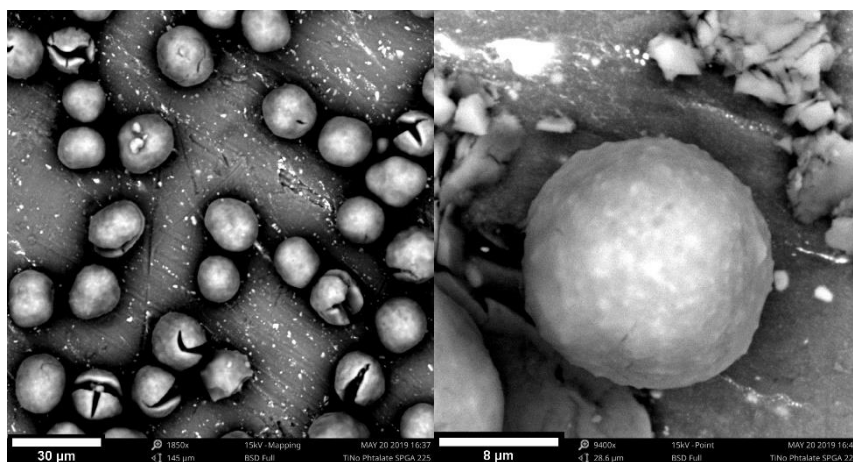
Figure 2.2 Scanning electron microscopy (SEM) images of the pristine Ziegler-Natta catalyst particles under study. A portion of the pristine catalyst particles show large cracks in the absence of α-olefin polymerization and is introduced during the final drying step of the catalyst material. SEM images were taken with a Phenom Pro SEM instrument using an accelerating voltage of 15 kV inside a N_2 filled glovebox operating at <1 ppm of H_2O and O_2.

2.2.2 Slurry-Phase Propylene Polymerization

All catalyst handling and polymerization reactions were performed under inert conditions of nitrogen at room temperature. In a dried 500 mL three-necked round-bottom flask, connected to a mechanical stirrer, 200 mL purified hexane was added. To the flask, 1 mL of a 2M solution of tri-ethyl-aluminum (TEAL) in hexane was added. Under stirring conditions subsequently using a Thermal Mass Flow meter (from Brooks) propylene and hydrogen were added at volumetric rates of respectively, 20 L/h and 5 L/h. After saturating the slurry mixture with the gasses, 900 mg of catalyst was dosed as a suspension in hexane. After 5 min, the gas feed was switched to nitrogen, which was passed through the slurry mixture for 3 min followed by stopping the mechanical stirring. After settling of the solid constituents, the top part of the clear solvent was siphoned off and replaced by hexane until a volume of 200 mL was reached. The polymerized catalyst particles were stored as a slurry in hexane. Analysis of the average particle size using SLS showed a D_{50} of ~39 µm and a relative span $\frac{D_{90}-D_{10}}{D_{50}}$ of 0,9.

The polymer yield (PY), determined to be 9.2 g iPP per g cat, was calculated indirectly based on Equation (Eq.) 2.1:

$$D_{50-polymer} = D_{50-catalyst} \cdot R_f \cdot \sqrt[3]{PY + 1} \qquad \text{Eq. 2.1}$$

Where $D_{50\text{-}polymer}$ is the average particle size of the polymerized catalyst particles and $D_{50\text{-}catalyst}$ that of the pristine catalyst particles, R_f relates to the porosity of the catalyst and polymer particles and the number of polymer particles that originate from a single catalyst particle and is assumed to be 1 here. Finally, PY is defined as the polymer yield in terms of g PP per g catalyst [41].

SEM images showing the morphology of the propylene polymerized Ziegler-Natta catalyst are shown in Figure 2.3. The particle replica effect is evident with the polymer particle taking over the shape of the pristine catalyst particle, including the still-present cracks from the catalyst drying procedure [42].
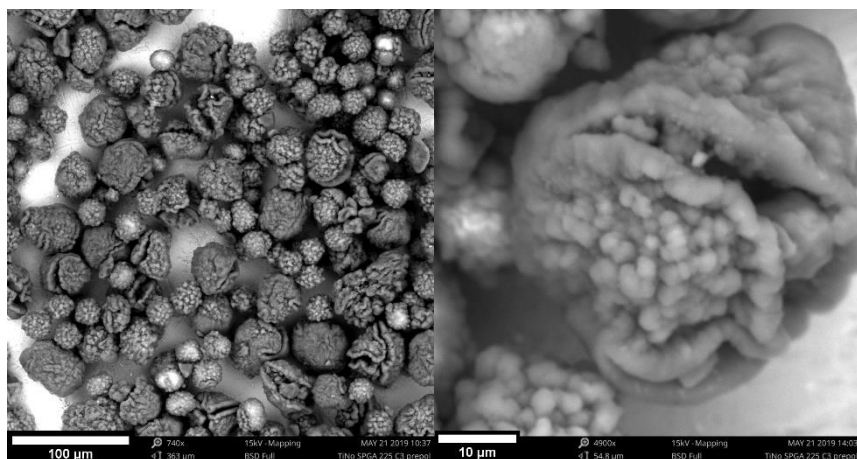
Figure 2.3 Scanning electron microscopy (SEM) images of the propylene polymerized Ziegler-Natta catalyst particles. The morphology of the cracks and the pristine catalyst particles in general is observed to be maintained as isotactic polypropylene is being formed at yields on the order of several g iPP per g cat. SEM images were taken with a Phenom Pro SEM unit and an accelerating voltage of 15 kV inside a N_2 filled glovebox operating at <1 ppm of H_2O and O_2.

2.2.3 Sample Capillary Loading

The polymerized catalyst particles, which were stored in a hexane slurry, were first allowed to settle down after which the majority of the solvent was removed followed by drying the catalyst particles under mild vacuum conditions for 30 min without applying external heat. The polymerized catalyst particles were then loaded into polyimide capillaries purchased from MicroLumen with an outer diameter of 120 µm and walls of 10 µm thick. After loading the capillaries, the ends were dipped into a two-component, low-outgassing and near-hermetic sealing epoxy, code H74, from Epotek. The epoxy was then cured at 80 °C on a hotplate for 30 min. All above mentioned actions were performed in a N_2-filled glovebox operating under 1 ppm of H_2 and O_2. After sealing of the capillaries, they were placed in glass vials sealed with Teflon tape and placed in steel vacuum tubes, sealed off with Viton O-rings suitable for transport.

2.2.4 The Correlated X-ray Nano-Tomography Setup

The PXCT and XRF datasets were collected with respectively an Eiger X 4M hybrid pixel detector (Dectris Ltd.) and a Maia 384-C X-ray fluorescence detector [43] at the Hard X-ray Micro/Nano-Probe beamline P06 at the PETRA III synchrotron facility, which is part of DESY. This correlated X-ray nanotomography setup is shown schematically in Figure 2.4. Using a golden angle collection approach, subsequent 2-D projections were collected with a constant projection angle increment of 147.5 degrees over multiple full rotations, which increases the number of different projection angles in the range from 0 to 360 degrees with every full rotation. The full range of 360 degrees (instead of just 180, which is sufficient for absorption tomography) was used to check for any possible self-absorption effects in the XRF data. Projection images were collected at 12 keV with a beam size of 160 x 140 nm^2 (h x v) focused using KB mirrors. The polymerized catalyst particle was raster-scanned over an area of 73 x 61 micron^2 using a 150 nm step-size. The elemental distribution images were obtained by fitting the obtained single pixel XRF spectra using the GeoPIXE software package [44]. For XRF the 2-D pixel size is equal to the step-size of 150 nm, which was also used for the 3-D voxel size of 150 x 150 x 150 nm^3 after reconstruction. The PXCT data-sets were reconstructed using in-house developed software. For PXCT the 2-D pixel size obtained was 43.2 nm, which was then used for the 3-D voxel size of 43.2x43.2x43.2 nm^3 after reconstruction.
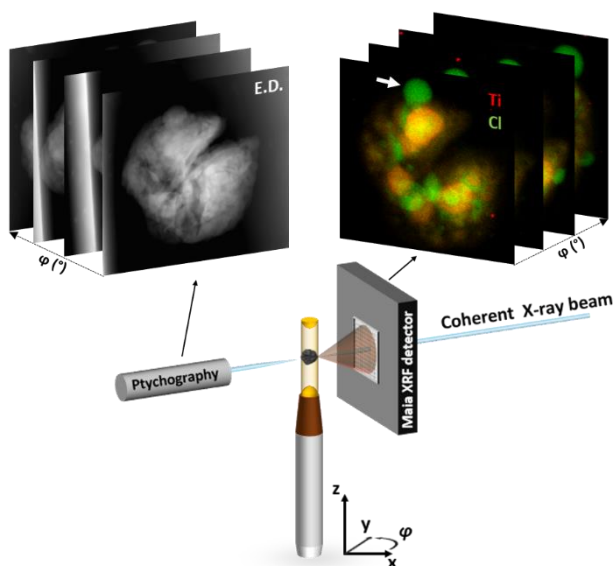
Figure 2.4 Schematic lay-out of the correlated ptychographic X-ray computed tomography (PXCT) and X-ray fluorescence (XRF) nano-tomography setup at the P06 beamline at PETRA III. The 2-D projections of electron density (E.D.) in greyscale and elemental distribution of Ti (red) and Cl (green) are obtained from respectively the X-ray ptychographic and fluorescence imaging at different angles by mounting a single polymerized Ziegler-Natta catalyst particle on a rotation stage. The white arrow indicates a region, rich in Cl and poor in Ti signal, on the particles external surface.

However, due to X-ray beam-induced morphology changes, as shown in Figure 2.5, only a limited number of 70 2-D projections collected with an average angular interval of 4.3 degrees were used for subsequent tomographic reconstructions of both the PXCT and XRF data-sets. In particular the electron density (PXCT) and chlorine (XRF) projections show severe morphology changes over time whereas the titanium (XRF) is considerably more stable. These morphology changes seem to be correlated to the presence of chlorine-rich but titanium-poor bubbles or spheres protruding the external surface of the composite particle. These bubbles are observed to collapse and spread within the composite particle as a function of X-ray beam exposure.

Our hypothesis is that these bubbles originate either from hydration of the $MgCl_2$ framework, which is highly sensitive towards any H_2O impurities, or residual slurry-phase components from an insufficient drying process. The framework hydration seems less likely due to the careful handling of both the catalyst both before and after polymerization using at all times either Schlenk-line techniques or handling inside a N_2-filled glovebox operating at <1 ppm O_2 and H_2O. Furthermore, the capillaries, which were loaded with the catalyst particles inside an inert atmosphere, were sealed with a low-outgassing and near-hermetic epoxy as discussed in sub-Chapter 2.2.3. The second hypothesis suggests that a residual phase of liquid and dissolved components such as ethyl-aluminium-chloride compounds, originating from the reaction of the triethylaluminium co-catalyst with $TiCl_4$, heptane diluent molecules and the donor molecules (a phthalate-based internal donor compound) had not been removed successfully, i.e. completely, from the composite particles during the mild vacuum drying method applied. In this scenario the chlorinated aluminium species would then be the origin of the Cl present in the bubbles and explain the absence of Ti. Unfortunately, Al XRF is not feasible with the instrumental setup used due to the low energy of the Al $K\alpha_1$ emission lines (1.48 keV), which causes strong photon attenuation through air, that is, along the path between polyimide capillary wall and the XRF detector; therefore we could not proof this hypothesis at this stage.

To mitigate these X-ray beam-induced morphology changes and therefore collect more 2-D projections and improve the achieved 3-D spatial resolution (see sub-Chapter 2.2.4) either an improvement of the drying methodology of the slurry-phase polymerized catalyst particles is required to remove residual diluent molecules from the reactor before X-ray beam exposure or through the use of cryogenic measuring conditions as demonstrated by Carzaniga *et al.* [45].
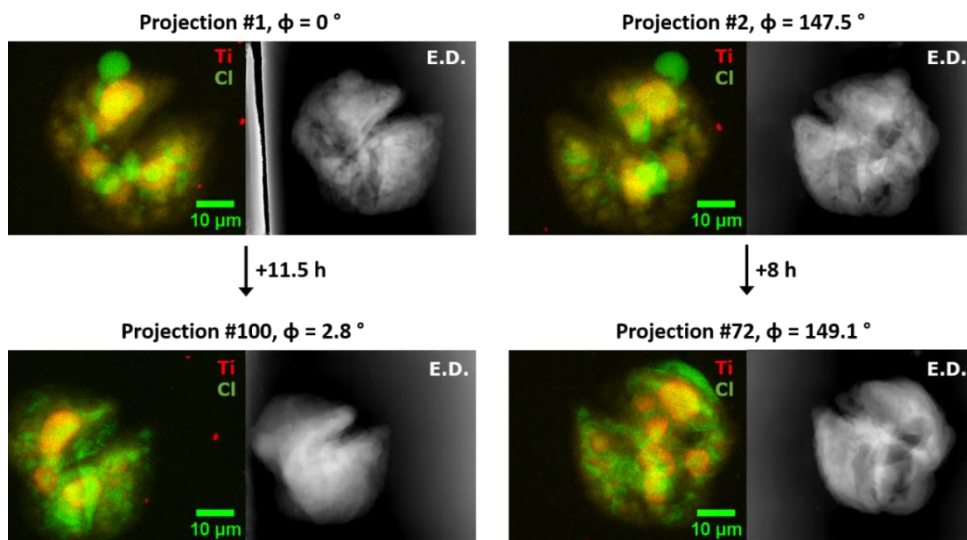
Figure 2.5 Raw 2-D projections, taken at different angles and time intervals, showing the X-ray beam-induced morphology changes as a function of exposure time. After 8 h of scanning, the Cl XRF signal is observed to be the main contributor to morphology changes, whereas the Ti XRF signal is considerably more stable. At 11.5 h of scanning (projection #100) the overall particle morphology has considerably changed in all three data-sets: the particle appears to have shrunk and the chlorine signal to have been redistributed within the composite particles volume.

2.2.5 Reconstruction of the Ptychographic X-ray Computed Tomography and X-ray Fluorescence Nano-Tomography Data-Sets

For the reconstruction of the collected PXCT and XRF tomographs the TXM-Wizard software package was used [46]. Each stack of 2-D projection images of the PXCT and XRF datasets were aligned manually to correct for motor jitter and sample movement. The 3-D tomographic slices were reconstructed with an iterative algebraic reconstruction technique (iART). The reconstruction of the above 2-D projections from both the PXCT and XRF data-sets as well as calculations based on in-house developed MATLAB scripts from subsequent sections were all performed on a consumer laptop with 16 GB of RAM and a 6 core CPU running at 2.20 GHz.

Afterwards the Avizo^{TM} software package was used for volume rendering and subsequent analysis of the obtained 3-D tomographic slices. All three data-sets (Cl XRF, Ti XRF, PXCT) were thresholded and masked to remove low intensity voxels considered to be either intrinsic noise from the raw 2-D projections or artefacts from the 3-D tomographic reconstruction. Then the data-sets were cropped in size to remove any voxels attributed to the reconstructed capillary wall. Table 2.1 and Figure 2.6 show respectively the volume, calculated spherical diameter, and histograms of the segmented images of the three data-sets before and after performing thresholding, masking and cropping operations. The correctness of the thresholding and masking was checked by comparing the diameter of virtual particle obtained after thresholding and masking of the ptychographic volume. This diameter was calculated to be 40.6 μm, i.e. very close to the experimentally found D_{50} of the polymerized particles of 39 μm. Furthermore, the calculated diameter of a sphere of the thresholded Ti XRF data volume is 21.9 μm, which is close to the D_{50} of the pristine catalyst of 18 μm, in turn confirming the applied thresholding. The larger calculated diameter for the thresholded Cl XRF volume compared to that of Ti is due to the presence of the Cl-rich bubbles on the particles external surface, which is absent in Ti signal.

Based on the following two observations this measured polymerized catalyst particle seems to be representative of the polymerized batch as a whole: 1) The close match of the equivalent spherical diameter of our measured polymer-catalyst composite particle, 40.6 μm, with that of the D_{50} of the bulk polymer batch as measured with static light scattering data, 39 μm, see sub-Chapter 2.2.2. 2) The similar morphology of the reconstructed particle with respect to those observed with SEM in Figure 2.3, where the same large cracks are observed throughout multiple polymerized catalyst particles. In future works one could establish a set of metrics as has been shown for the FCC particles with X-ray tomography [28].

Table 2.1 Volume and diameter* of the segmented ptychographic X-ray computed tomography (PXCT), Ti and Cl X-ray Fluorescence (XRF) data-sets before and after thresholding.

Data-set	Volume (µm³)	Diameter* (µm)
	Raw data-set	
PXCT	52925	46.6
Cl XRF	59666	48.5
Ti XRF	56406	47.6
	Thresholded data-set	
PXCT	34956	40.6
Cl XRF	9460	26.2
Ti XRF	5524	21.9

* The calculated diameter here is that of a sphere with the corresponding volume given in the table.
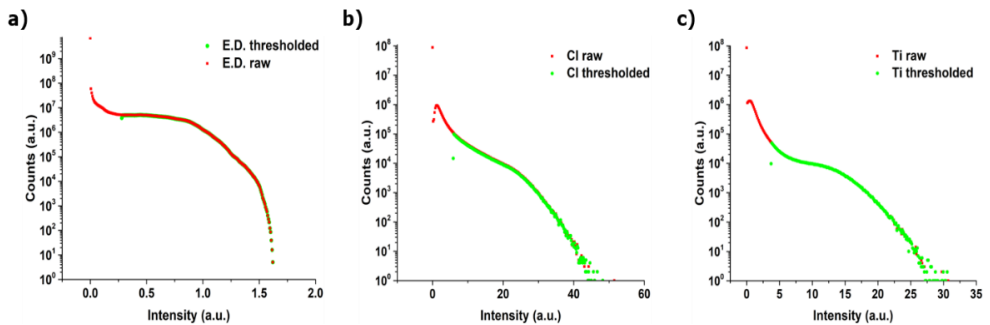
Figure 2.6 Histograms of (a) electron density obtained from ptychographic X-ray computed tomography (PXCT), (b) Cl X-ray fluorescence (XRF) intensities and (c) Ti XRF intensities of the raw data-sets in red and the thresholded data-sets in green. With the thresholding, the lowest intensity voxels are filtered out, which are considered to be noise from either the raw 2-D projections or artefacts introduced during the 3D tomographic reconstruction.

Afterwards, the thresholded XRF data-sets were aligned separately with respect to the PXCT data-set in Avizo™ using image registration via an iterative optimization algorithm that computes a transformation for the co-registration of two image data-sets [47].

For the volume rendering and subsequent operations using the Avizo™ software package, a workstation with a Nvidia® Quadro K5000, 128 GB of RAM and two Intel® XEON E5-2687W CPU units with 8 cores running at 3.10 GHz were utilized.

2.2.6 Estimation of the Achieved 3-D Resolution from Reconstructed Data-Sets

The 3-D spatial resolution of the PXCT and Ti XRF data-sets was estimated by measuring line profiles on the 2-D generated slices from the reconstructed particle [48,49]. The intensity obtained from the line profiles across the edge of the composite particle (PXCT) or clusters (Ti) were fitted with a Gaussian profile, see Eq. 2.2-2.4. Here *a* is the height of the fitted peak, *b* is the center position of the peak, and *c* is the standard deviation, related to the full width at half maximum (FWHM). The half width at half maximum value (HWHM) when corrected for the voxel size is taken as an estimate of the resolution at which this edge feature is resolved, as shown in Figures 2.7 and 2.8. Using this approach, for PXCT the 3-D resolution was estimated to be around 400 nm whereas for the Ti XRF data-set it was estimated to be around 600 nm. For the Ti XRF data-set determining the 3-D resolution with the line profile method is more difficult due to the observed layer-by-layer fragmentation of the cluster's surface as discussed in the main text, which therefore would cause broadening of the edge in a line profile.

$$f(x) = ae^{-\frac{(x-b)^2}{c^2}} \qquad \text{Eq. 2.2}$$

$$FHWM\ (voxels) = 2\sqrt{2ln2}\ c \qquad \text{Eq. 2.3}$$

$$HWHM\ (nm) = \frac{FHWM}{2} \times Voxel\ size \qquad \text{Eq. 2.4}$$

A more routinely used technique to estimate the 3-D resolution is Fourier Shell Correlation (FSC), where the original data-set is split into two half data-sets of typically alternating projection angles that are separately reconstructed and then compared after a Fourier transform [50,51]. However, in this Chapter due to X-ray beam-induced morphology changes as shown in Figure 2.8 a limited amount of 2-D projections, 70, was used for the reconstruction of both PXCT and X-ray fluorescence data-sets. This would then split the two half data-sets in a mere 35 projections with a 8.6 degree angular step and resulted in a sever underestimation of the achieved 3-D spatial resolution when using the FSC approach (order of several microns as opposed to the sub-micron resolution assessed by the 2-D line scans).
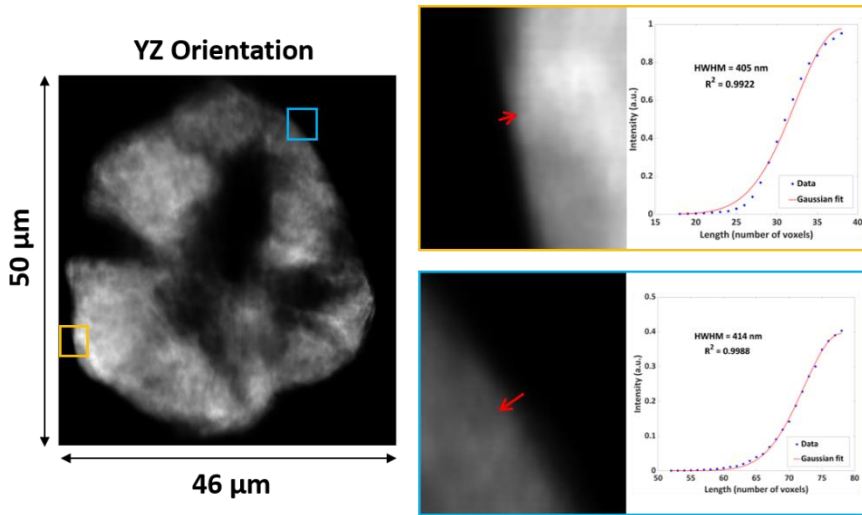
Figure 2.7 Reconstructed slice in the YZ plane of the ptychographic X-ray computed tomography data-set (**Left**). The orange and blue boxes show two edges where a line profile was measured, which gives the intensity as function of the length of the line (**Right**). The half width at half maximum value of the Gaussian fit of these line profiles is taken as an estimate of the achieved resolution at which this edge is resolved.

Figure 2.8 Reconstructed slice in the YZ plane of the Ti X-ray fluorescence nano-tomography data-set (**Left**). The orange and blue boxes show two edges where a line profile was measured, which gives the intensity as function of the length of the line (**Right**). The half width at half maximum value of the Gaussian fit of these line profiles was taken as an estimate of the resolution at which this edge is resolved.
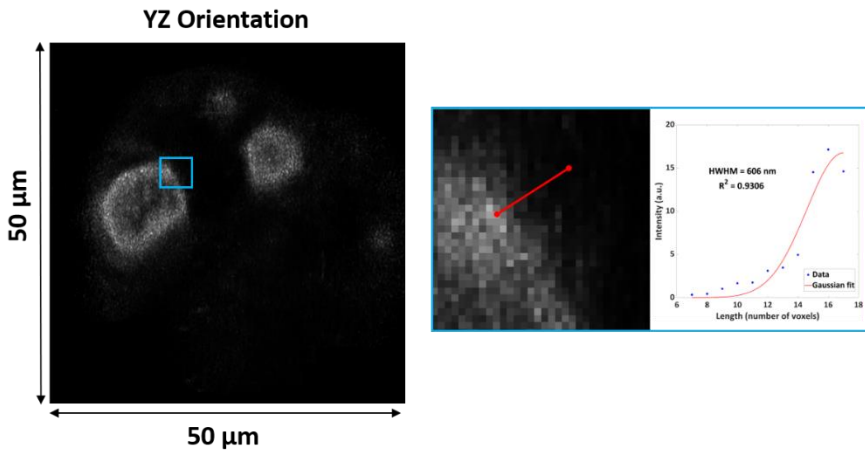
2.2.7 Calculating the Radial Distribution of Titanium

The following steps were performed to calculate the radial distribution of all the spatially-resolved titanium clusters based on the Ti XRF data-set.

First, the PXCT data-set was segmented (i.e. create binarized volume) and then resampled from its own voxel size of 43.2 x 43.2 x 43.2 nm^3 to that of the Ti XRF data-set of 150 x 150 x 150 nm^3. This step makes it easier to directly compare distance values between both data-sets and since the PXCT achieved 3-D resolution is estimated to be on the order of 400 nm, the resampling has no consequences for the data-analysis itself.

Then, the center of the polymer-catalyst composite particle was determined based on the segmented PXCT data-set by measuring the Euclidian distance of each voxel with a 1 value (since it's a binarized volume) from the surface of this composite particle. The voxel(s) with the largest distance was then taken as the center of the entire composite particle's volume.

For the Ti XRF data-set, again a segmentation step was performed followed by a labelling operating in the Avizo^{TM} software. Here labels are unique segmented volumes, which don't overlap with each other e.g. they are separated by voxels with a 0 value assigned in the original segmented Ti XRF data-set. Therefore, each label gets a unique identity value and can then be used to study the position of the label itself with respect to the center of the composite particle, the size of the label and the radial distribution of Ti within this label.

The center of each Ti label was then calculated in the same way as done for the composite particle's volume. This was done by measuring the Euclidian distance of each voxel within the label's volume towards the surface of this specific label. The voxel(s) with the largest distance was then taken as the center of this label's volume.

Now that the center of the composite particle and that of each Ti label has been calculated the following two parameters were calculated namely; The distance between the center, d_c, and surface, d_s, of each Ti label with respect to the center of the composite particle. In this case we only considered Ti labels, which were larger than 4 voxels in size due to the achieved Ti XRF 3-D resolution of 600 nm, leading to the analysis of 5571 Ti XRF labels. For small clusters the d_c and d_s values will be similar but for the largest clusters there will be a significant difference, hence why both values are provided. The distance between the surface of each label and the center of the composite particle, d_s, was calculated by expanding the volume of the label by one voxel layer until the center of the ptychographic data-set was reached. Then the shortest distance in this expanded layer was used as the distance between the label's surface and the center of the composite particle, d_s. To calculate the distance of the center of each Ti label towards the center of the composite particle, d_c, the shortest path between these two points was used.

Now that the position of each Ti label has been calculated with respect to the center of the composite particle, we can extend on this by calculating the radial distribution of titanium within such labels. In Table 2.2 the volume of the total titanium XRF segmented is given together with that of the six largest labels (with a color-coding for the name, same as used for the visualization in Figures 2.12 & 2.13). These six largest labels account for 85% of the total segmented volume with the next largest, seventh label only contributing 1.8% of the total volume (the sixth largest label contributes 6.9%). Hence, the radial distribution of titanium within the labels is only applied to the six largest labels (and therefore clusters or catalyst fragments) in this Chapter.

Table 2.2 Volume and box dimensions of the entire Ti XRF segmented volume and the sixth largest labels.

Data-set	Volume (μm^3)	Bounding box dimensions X,Y,Z (μm)
Total Ti segmented volume	5524	54,60,60
Pink label	1449	19,19,19
Green label	1155	19,19,19
Blue label	794	19,19,19
Orange label	486	12,14,15
Cyan label	411	15,13,15
Red label	380	19,19,19

To calculated the radial distribution of titanium within these six largest labels the following steps were performed. First, the distance maps were calculated for the 3-D volumes within each individual label. which provide the distance of each voxel (with a value of 1) in the label from its surface. The mean Ti intensity in a shell of one voxel thickness was then calculated for each label was then calculated going from the surface of the label towards its center.

2.3 Results and Discussion

2.3.1 Reconstructed Volume of the Isotactic Polypropylene-Catalyst Composite Particle

In Figure 2.9, the reconstructed 3-D volume rendering of the electron density showing the polymer-catalyst composite phase (a), Ti and Cl elemental distributions (b and c) and an overlay of all three (d) are visualized. The electron density tomograph shows two major cracks through the center of the catalyst particle. Complementary Scanning Electron Microscopy (SEM) data, given in Figures 2.2 and 2.3, shows that these cracks are present in both the pristine and polymerized catalyst particles, and originate from the final drying step in the catalyst synthesis. The combination of PXCT and XRF shows that there are isolated large clusters (fragments) rich in Ti and Cl, which are encapsulated by the formed iPP. The mis-match in the overlay of the Ti and Cl elemental distributions is most likely due to strong beam-induced morphology changes in the Cl signal, whereas the Ti signal is significantly more stable. For this reason, the focus for the fragmentation behavior is centered on the Ti species, which are epitaxially chemisorbed on the unsaturated lateral surfaces of the $MgCl_2$ primary crystals.

The presence of these large Ti clusters, clearly visible in Figure 2.9c, which are many microns separated from each other throughout the polymer phase visible in the PXCT electron density phase is a strong sign for the presence of the continuous bisection fragmentation model. Additionally, in Figure 2.9b, the cross-section of the large Ti cluster in the top-left shows that the core is significantly lower in Ti XRF intensity, whereas the electron density signal shows it has to be filled with i-PP (otherwise, the electron density should be dark or empty if the core of the cluster isn't filled with i-PP). This gives another strong sign that besides the presence of the continuous bisection for the catalyst particle as a whole, it is also occurring as a fragmentation pathway within this specific cluster.

However, the diffuse clouds of Ti signal that can be observed in Figure 2.9c both around this large cluster on the top-left but also around all of the other larger clusters, show that the shrinking core or layer-by-layer fragmentation model has to be occurring as well. That is to say, that this shrinking core fragmentation model would lead to the peeling off small catalyst fragments from these larger clusters and therefore leads to the formation of these observed diffuse clouds.
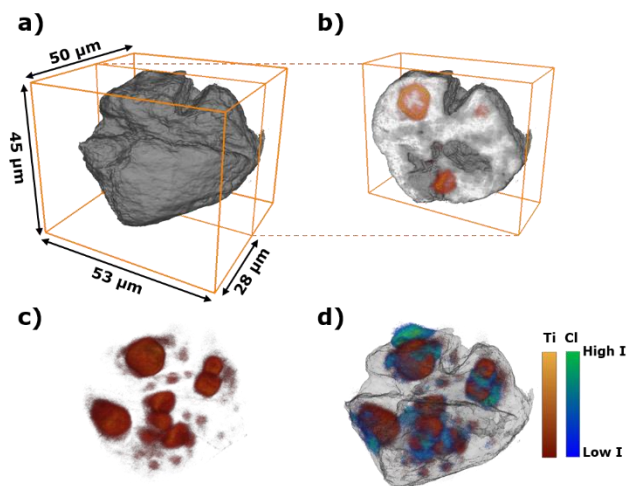
Figure 2.9 Reconstructed 3-D volume rendering of a propylene polymerized Ziegler-Natta catalyst particle, ~41 µm in diameter. (a) Electron density reconstruction (grey-scale) with a voxel size of 43.2 x 43.2 x 43.2 nm^3. (b) Extracted volume showing the position of the Ti species (in red) within the polymer-catalyst composite particle. (c) Elemental distribution of the Ti species (red colormap) with a voxel size of 150 x 150 x 150 nm^3. (d) Elemental distribution of Ti and Cl (in green) within the composite particle (only external surface rendered).

2.3.2 Radial Distribution of the Titanium Clusters Throughout the Composite Particle

As the polymerization of propylene starts, the framework begins to break up and these catalyst fragments or clusters will expand radially in conjunction with the growing polymer-phase [16]. The visualization of the PXCT and Ti XRF reconstructed volumes in sub-Chapter 2.3.1 provided strong evidence that both fragmentation models, namely the shrinking core and continuous bisection are occurring simultaneously within the composite particle. To build further upon this visualization, the radial distribution of all labelled Ti XRF clusters within the composite particle as a whole as well as the radial distribution of the Ti XRF intensities within the six largest labelled clusters were calculated as described in sub-Chapter 2.2.5.

In Figure 2.10 the histograms for both the Ti XRF label's center and surface distance to the composite particle's center called respectively, d_c and d_s, are given. The high average distance of all Ti labels from the center of the particle, 18.6 micron average from d_c and d_s, which is close to the radius of the composite particle of 20.3 micron shows that the Ti active sites are being pushed away from the center of the expanding composite particle's center due to the growth of the polymer.
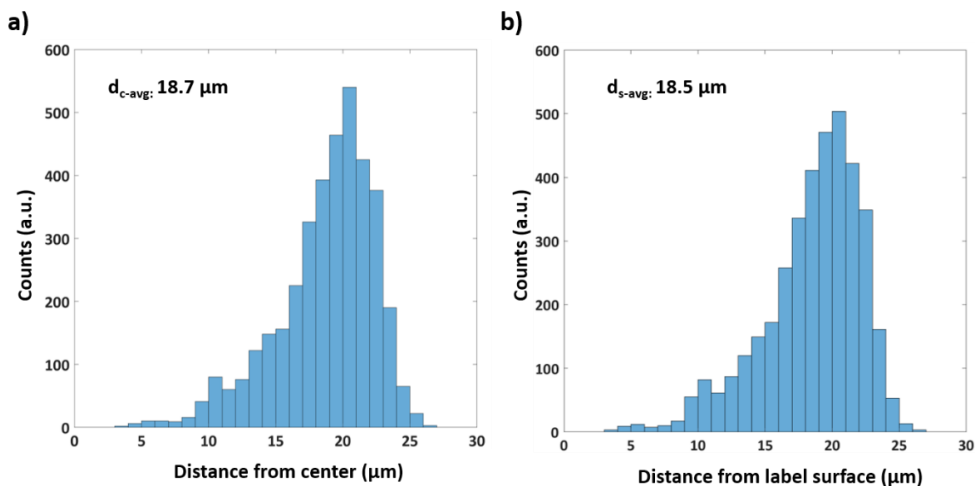
Figure 2.10 Histograms showing the frequency of the distance between the centre of the segmented Ti clusters, d_c, and that of the composite particle (a) and the frequency of the distance between the surface of the segmented Ti clusters, d_s, and that of the composite particle with a voxel size threshold 4, corresponding roughly to the estimated 3-D resolution of the Ti XRF data-set.

In Table 2.3, the distance of the six largest labels, visualized in Figure 2.10 using the same color-coding, with respect to the center of the composite particle are given. The average distances of the center, d_c, and surface, d_s, of these six labels with respect to the center of the composite particles are respectively 14.6 and 7.7 µm with the latter value correcting for the irregular size and shape of each label. These six largest Ti cluster labels are considerably closer to the core of the composite catalyst than the average d_c and d_s values given in Figure 2.10 based on all the Ti XRF labels. The separation of these six largest clusters from each other and subsequently being pushed away from the center of the composite particle, is due to the internal cleavage of the catalyst particle caused by the formed polymer as described by the continuous bisection model.

Table 2.3 The volume, V, and the distance from the center, d_c, and surface, d_s, of the six largest Ti cluster labels with respect to the center of the composite particle.

Ti cluster label	V (µm³)	d_c (µm)	d_s (µm)
1. Pink	1449	15.7	8.5
2. Green	1155	16.8	10.0
3. Blue	794	16.9	9.4
4. Orange	486	12.4	4.9
5. Cyan	411	11.6	5.3
6. Red	380	14.4	8.0

Both the large number of Ti labels smaller than 0.135 µm³ or 40 voxels in size (5443 out of 5571 meaning 97.7% of all labels) and the presence of six Ti labels larger than 380 µm³ as shown in Figure 2.11 gives additional proof that both the shrinking core and continuous bisection fragmentation models are occurring simultaneously. However, since these six largest labels correspond to the majority of the Ti segmented volume and that these labels are clearly well-separated from each other, the continuous bisection fragmentation model has to dominate the overall catalyst fragmentation behavior within the entire composite particle.
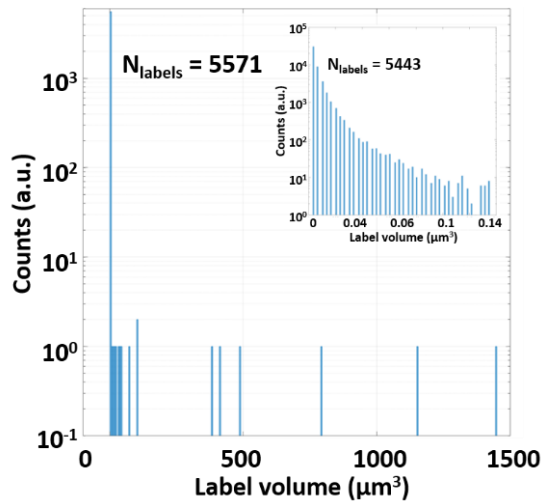
Figure 2.11 Histogram showing the frequency of the volume of all Ti labels larger than 4 voxels in size. From the 5571 Ti labels, 97.7% or 5443 Ti labels are smaller than 0.135 µm³, which corresponds to 40 voxels in size.

2.3.3 Radial Distribution of the Titanium Inside the Six Largest Cluster Labels

Now that both fragmentation models have been shown to occur in the composite particle as a whole based on the Ti XRF data-set, this can be expanded to study fragmentation behavior inside of the six largest Ti labels, which represent 85% of the total Ti segmented volume.

In Figure 2.12a these six largest labels are visualized within the isosurface volume rendering of the PXCT electron density according to their color-coding as used in Tables 2.2 and 2.3. Additionally, the radial distribution of the Ti clusters within these six largest labels are provided in Figure 2.12b. All labels, with the exception of the red label, show a similar behavior with a maximum in the mean Ti intensity at ~1 micron distance from the label's surface followed by a decay in the intensity as we go towards the center voxels. The visualized volume renderings of the Ti clusters in these six largest labels together with cut-throughs and the corresponding extracted 2-D slices are provided in Figure 2.13. For the pink label, first a diffuse cloud of Ti is observed at the label's surface followed by a clear and highly intense edge of the Ti cluster within the label and finally a lower intensity of Ti inside the core of these clusters where even clear cracks can be observed. Interestingly, there isn't one single larger cluster inside the blue label but instead two sub-clusters that are likely to have been separated from each other through internal cleavage at an earlier polymerization stage than what we captured here. The red label shows the presence of even more sub-clusters that have been pushed away from each other, due to the formation of i-PP within this cluster and subsequent internal cleavage of the framework. The reason for the increase of the mean intensity for the red label is most likely due to the calculated center of this label overlapping with one of the sub-clusters. The green, cyan and orange labels show the same behavior as the pink label. That is to say that again a lower intensity is observed at the core of the labels followed by a higher intensity at the surface and a the presence of a (but smaller, especially for orange) diffuse cloud of Ti intensity.

Both the visualized and calculated depletion of Ti at the core of these largest labels shows that also within these clusters themselves, internal cleavage of the catalyst framework is playing a significant role in the overall fragmentation behavior. The diffuse Ti clouds observed are due to the peeling-off framework species from the external surface according to the shrinking core fragmentation model.
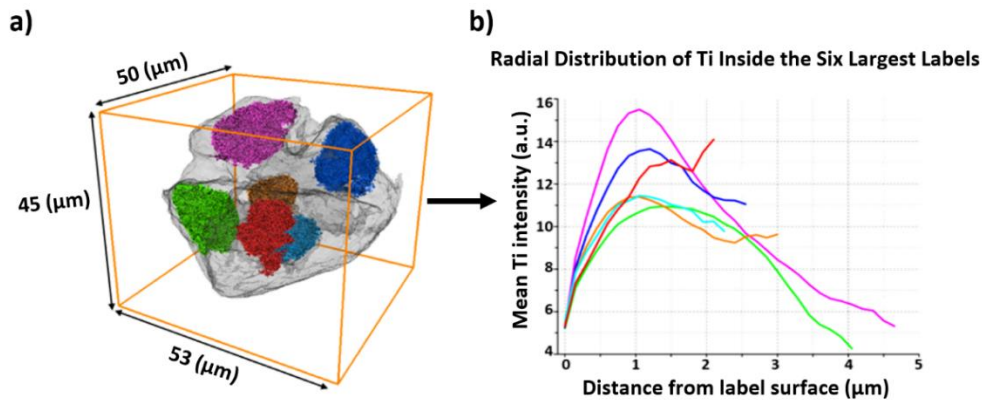
Figure 2.12 (a) The six largest Ti cluster labels (Table 2.2 color-coding) shown within the composite particle surface rendering. (b) The radial distribution of Ti within the six largest labels is calculated as a function of the mean Ti intensity from the surface of each corresponding label towards the center voxels.
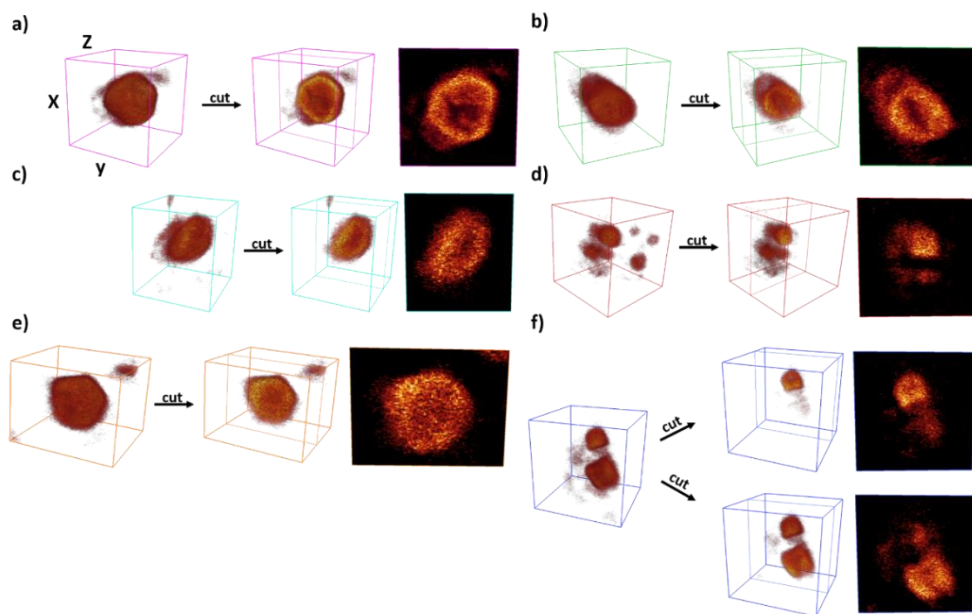
Figure 2.13 Zoom-in of the titanium clusters with and without a clipping plane shown in 3-D and the corresponding 2-D slice belonging to the six following labels from Figure 3. (a) the pink label (b) the green label (c) the cyan label (d) the red label (e) the orange label (f) the blue label with two cuts corresponding to the two sub-clusters or fragments. The dimensions of each bounding box and volume of the corresponding labels are given in Table 2.2.

The heterogeneity in the fragmentation rate observed between the different Ti clusters, especially for the blue and red labels with respect to the other labels, is likely due to a non-uniform distribution of cracks and macroporosity within the pristine catalyst particle as shown by SEM in Figure 2.2. Another explanation would be that of internal heat limitations and mass transfer limitations, however these are not expected to play a significant role in this specific situation due to the mild reaction conditions utilized as has been shown experimentally by Noristi *et al.,* for a series of propylene polymerized Ziegler-Natta catalysts at different polymer yields[52].

The lower intensity of Ti at the core of each label with respect to the edge of the label could also be due to self-absorption effects. Self-absorption occurs if significant absorption of X-rays along the pathway out of the sample takes place[22,23]. This can be the case if the pathway becomes very long for large samples or if the material through which the emitted X-ray photons have to pass is strongly absorbing at the energy of the X-ray emission line. This absorption is a function of energy, atomic number, and density and the effect is called self-absorption because the fluorescence of a part of the sample is absorbed by other parts of the sample itself.

To proof that this is not an issue in the present case to any significant extent, in Figure 2.14 the region used for the pink label is compared for both the Ti XRF and Cl XRF data. Since the fluorescent X-rays from the K shell of Cl are emitted at a much lower energy of ~2.6 keV with respect to Ti at ~4.5 keV, any self-absorption effect should be considerably larger for Cl due to the shorter penetration depth for a photon of lower energy through the same material volume. As observed based on both visualization and the line-profile the intensity of Cl is more or less constant from the edge of the cluster to the core (and even higher on average than that of Ti as expected due to the lower wt% of Ti in the catalyst with respect to Cl, which corresponds to roughly 75 wt% in pure $MgCl_2$), whereas the Ti intensity drops significantly in the core as compared to the edge. This therefore means that self-absorption effects can be ruled out as the reason for the drop of Ti intensity in the core as the same behavior should then have been observed (and even stronger) for Cl.

However, this observation is also interesting from a different perspective: the more or less constant intensity of Cl in the core of the cluster with respect to the edge would disagree with the statements made earlier that the Ti clusters are fragmenting through the core as is expected in the continuous bisection fragmentation model. This is because the same trend for the Cl intensity would then be expected. However, as mentioned in sub-Chapter 2.2.4, the bubbles observed to be rich in Cl and poor in Ti on the external particle's surface are likely residual slurry-phase components like the chlorinated Al co-catalyst, heptane diluent and silane external donor molecules. These same components are then also expected to be present within these Ti rich clusters close to the active sites and where the polymer is being formed. Thus our observation does not imply that the core of these clusters was rich in $MgCl_2$ framework species but instead of residual slurry-phase components.
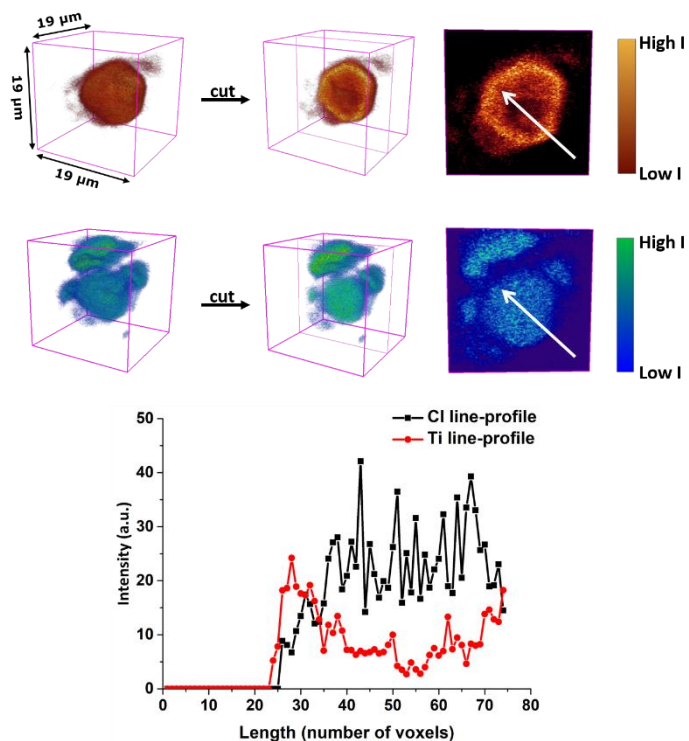
Figure 2.14 Comparison of the intensities of Ti XRF and Cl XRF in the interior of the same cluster. A line profile was obtained at the same positions and compared. It clearly shows that the Cl intensity is more or less constant throughout the centre of the cluster whereas the Ti intensity is significantly higher at the two edges than the centre of the cluster.

2.4 Conclusions

In this Chapter the strength of correlated ptychographic X-ray computed tomography and X-ray fluorescence nano-tomography to investigate the fragmentation behavior of individual polyolefin catalyst particles in the early stages of α-olefin polymerization with sub-micron 3-D spatial resolution has been shown. Both the experimental and analytical toolboxes shown here on the highly air and moisture sensitive Ziegler-Natta catalysts are directly applicable to all olefin polymerization catalyst types such as the immobilized metallocenes and provide a route for researchers to find structure-activity-polymer product relationships that could ultimately lead to rational catalyst designing for specific polymer grades. The calculated expansion of the Ti clusters from the center of the polymer-catalyst composite particle as well as the radial distribution of Ti within the six Ti largest clusters show that whilst both fragmentation models, shrinking core and continuous bisection, are present, the continuous bisection is dominating under these specific experimental conditions[3-5,7-9]. Therefore, to the best knowledge of the authors it was demonstrated for the first time in 3-D whilst directly obtaining the elemental distribution of all Ti species how this Ziegler-Natta catalyst-type behaves in the early stages of α-olefin polymerization.

2.5 References

1. Kaminsky, W. (Ed.), Polyolefins: 50 years after Ziegler and Natta I, Springer, Berlin, **2013**.
2. Severn, J. and Jones, R.J., Stereospecific α-Olefin Polymerization with Heterogeneous Catalysts In *Handbook of Transition Metal Polymerization Catalysts*; Hoff, R., (Ed.); John Wiley & Sons, Inc., Hoboken, **2018**.
3. Ferrero, M.A., Chiovetta, M.G., Catalyst fragmentation during propylene polymerization: Part I. The effects of grain size and structure, *Polym. Eng. Sci*. **1987**, 27, 1436-1447.
4. Ferrero, M.A., Chiovetta, M.G., Catalyst fragmentation during propylene polymerization: Part II. Microparticle diffusion and reaction effects, *Polym. Eng. Sci*. **1987**, 27, 1448-1460.
5. Ferrero, M.A., Chiovetta, M.G., Catalyst fragmentation during propylene polymerization: Part III. Bulk polymerization process simulation, *Polym. Eng. Sci*. **1991**, 31, 886-903.
6. Grof, Z., Kosek, J., Marke, M., Modelling of morphogenesis of growing polyolefin particles, *AIChe Journal*, **2005**, 51, 2048-2067.
7. Zheng, X., Loos, J., Morphology Evolution in the Early Stages of Olefin Polymerization, *Macromol. Symp.,* **2006**, 236, 249-258.
8. Horácková, B., Grof, Z., Kosek, J., Dynamics of fragmentation of catalyst carries in catalytic polymerization of olefins, *Chem. Eng. Sci.,* **2007**, 62, 5264-5270.
9. Pater, J.T.M., Weickert, G., Loos, J., van Swaaij, W.P.M., High precision prepolymerization of propylene at extremely low reaction rates—kinetics and morphology, *Chem. Eng. Sci.,* **2001**, 56, 4107-4120
10. Laurence, R.L. and Chiovetta, M.G., In: Reicher, K.H., Geisler, G. (Eds.), Polymer Reaction Engineering, Hasuer-Verlag, München, **1983**, 74-112.
11. Fink, G., Steinmetz, B., Zechlin, J., Przybyla, C., Tesche, B., Propylene Polymerization with Silica-Supported Metallocene/MAO Catalysts, *Chem. Rev.,* **2000**, 100, 1377-1390.
12. Weickert, G., Meier, G.B., Pater, J.T.M., Westerterp, K.R., The particle as microreactor: Catalytic propylene polymerizations with supported metallocenes and Ziegler-Natta catalysts, *Chem. Eng. Sci.*, **1999**, 54, 3291-3296.

13. Hammawa, H., Wanke, S.E., Influence of support friability and concentration of a-olefins on gas-phase ethylene polymerization over polymer-supported metallocene/methylaluminoxane catalysts, *J. Appl. Polym. Sci.,* **2007**, 104, 514-527

14. Rönkkö, H-L., Korpela, T., Knuuttila, H., Pakkanen, T.T., Denifl, P., Leinonen, T., Kemell, M., Leskelä, M., Particle growth and fragmentation of solid self-supported Ziegler-Natta-type catalysts in propylene polymerization, *J. Mol. Catal. Chem.,* **2009,** 309, 40-49.

15. Abboud, M., Denifl, P., Reichert, K-H., Fragmentation of Ziegler-Natta Catalyst Particles During Propylene Polymerization, *Macromol. Mater. Eng.,* **2005**, 290, 558-564.

16. McKenna, T.F.L., Di Martino, A., Weickert, G., Soares, J.B.P., Particle Growth During the Polymerisation of Olefins on Supported Catalysts, 1 – Nascent Polymer Structures, *Macromol. React. Eng.,* **2010**, 4, 40-64

17. Conner, W.C., Webb, S.W., Spanne, P., Jones, K.W., Use of X-ray microscopy and synchrotron microtomography to characterize polyethylene polymerization particles, *Macromolecules*, **1990**, 23, 4742-4747.

18. Ferrero, M.A., Sommer, R., Spanne, P., Jones, K.W., Conner, W.C., X-ray microtomography studies of nascent polyolefin particles polymerized over magnesium chloride-supported catalysts, *J. Polym. Sci. A,* **1993**, 31, 2507-2512.

19. Jones, K.W., Spanne, P., Lindquist, W.B., Conner, W.C., Ferrero, M., Determination of polymerization particle morphology using synchrotron computed microtomography, *Nucl. Instr. Meth. Phys. Res.*, **1992**, 68, 105-110.

20. Boden, S., Bieberle, M., Weickert, G., Hampel, U., Three-dimensional analysis of macroporosity distributions in polyolefin particles using X-ray microtomography, *Powder Technol.,* **2008**, 188, 81-88.

21. Seda, L., Zubov, A., Bobak, M., Kosek, J., Kantzas, A., Transport and Reaction Characteristics of Reconstructed Polyolefin Particles, *Macromol. React. Eng.,* **2008**, 2, 495-512.

22. Meisterová, L., Zubov, A., Smolná, K., Štěpánek, F., Kosek, X-ray Tomography Imaging of Porous Polyolefin Particles in an Electron Microscope, J., *Macromol. React. Eng.,* **2013**, 7, 277-280.

23. Cats, K.H., Gonzalez-Jimenez, I.D., Liu, Y., Nelson, J., Van Campen, D., Meirer, F., van der Eerden, A.M.J., De Groot, F.M.F., Andrews, J.C., Weckhuysen, B.M., X-ray nanoscopy of cobalt Fischer-Tropsch catalysts at work, *Chem. Comm.,* **2013**, 49, 4622-4624

24. Bare, S.R., Charochak, M.E., Kelly, S.D., Lai, B., Wang, J., Chen-Wiegart, YK., Characterization of a Fluidized Catalytic Cracking Catalyst on Ensemble and Individual Particle Level by X-ray Micro- and Nanotomography, Micro-X-ray Fluorescence, and micro-X-ray Diffraction, *ChemCatChem,* **2014**, 6, 1427-1437.

25. Beale, A.M., Jacques, S.D.M., Gibson, E.K., Di Michiel, M., Progress towards five dimensional diffraction imaging of functional materials under process conditions, *Coord. Chem. Rev.,* **2014**, 277, 208-223

26. Price, S.W.T., Ignatyev, K., Geraki, K., Basham, M., Filik, J., Vo, N.T., Witte, P.T., Beale, A.M., Mosselmans, J.F.W., Chemical imaging of single catalyst particles with scanning μ-XANES-CT and μ-XRF-CT, *Phys. Chem. Chem. Phys.,* **2015**, 17,521-529

27. Meirer, F., Morris, D.T., Kalirai, S., Yijin, L., Andrews, J.C., Weckhuysen, B.M., Mapping Metals Incorporation of a Whole Single Catalyst Particle Using Element Specific X-ray Nanotomography, *J. Am. Chem. Soc*, **2015**, 137, 102-105.

28. Meirer, F., Kalirai, S., Morris, D., Soparawalla, S., Yijin, L., Mesu, G., Andrews, J.C., Weckhuysen, B.M., Life and death of a single catalytic cracking particle, *Sci. Adv.,* **2015**, 1, e1400199.

29. Baier, S., Damsgaard, C.D., Scholz, M., Benzi, F., Rochet, A., Hoppe, R., Scherer, T., Shi, J., Wittstock, A., Weinhausen, B., Wagner, J.B., Schroer, C.G., Grunwaldt, J.-D., In-situ Ptychography of Heterogeneous Catalysts using Hard X-rays : High Resolution Imaging at Ambient Pressure and Elevated Temperature, *Microsc. Microanal.,* **2016**, 22, 178-188

30. Cats, K.H., Andrews, J.C., Stéphan, O., March, K., Karunakaran, C., Meirer, F., De Groot, F.M.F., Weckhuysen, B.M., Active phase distribution changes within a catalyst particle during Fischer-Tropsch synthesis as revealed by multi-scale microscopy, *Catal. Sci. Technol.,* **2016**, 6, 4438-4449

31. Price, S.W.T., Martin, D.J., Parsons, A.D., Sławiński, W.A., Vamvakeros, A., Keylock, S.J., Beale, A.M., Mosselmans, J.F.W., Chemical Imaging of Fischer-Tropsch catalysts under operating conditions, *Sci. Adv.,* **2017**, 3, e1602838

32. Ihli, J., Sanchez, D.F., Jacob, R.R., Cuartero, V., Mathon, O., Krumeich, F., Borca, C., Huthwelker, T., Cheng, W-C., Shu, Y., Pascarelli, S., Grolimund, D., Menzel, A., van Bokhoven, J.A., Localization and Speciation of Iron Impurities within a Fluid Catalytic Cracking Catalyst, *Angew. Chem. Int. Ed.,* **2017**, 56, 14031-14035

33. Ihli, J., Jacob, R.R., Holler, M., Guizar-Sicairos, M., Diaz, A., Da Silva, J.C., Ferreira Sanchez, D., Krumeich, F., Grolimund, D., Taddei, M., Cheng, W.-C., Shu, Y., Menzel, A., Van Bokhoven, J.A., A three-dimensional view of structural changes caused by deactivation of fluid catalytic cracking catalysts, *Nat. Comm.,* **2017**, 8, 809

34. Sheppard, T.L., Price, S.W.T., Benzi, F., Baier, S., Klumpp, M., Dittmeyer, R., Schwieger, W., Grunwaldt, J.-D., In Situ Multimodal 3D Chemical Imaging of a Hierarchically Structured Core@Shell Catalyst, *J. Am. Chem. Soc.,* **2017**, 139. 7855-7863

35. Vamvakeros, A., Jacques, S.D.M., Di Michiel, M., Matras, D., Middelkoop, V., Ismagilov, I.Z., Matus, E.V., Kuznetsov, V.V., Drnec, J., Senecal, P., Beale, A.M., 5D operando tomographic diffraction imaging of a catalyst bed, *Nat. Comm.,* **2018**, 9, 4751

36. Ihli, J., Diaz, A., Shu, Y., Guizar-Sicairos, M., Holler, M., Wakonig, K., Odstrcil, M., Li, T., Krumeich, F., Müller, E., Cheng, W-C., van Bokhoven, J.A., Menzel, A., Resonant Ptychographic Tomography Facilitates Three-Dimensional Quantitative Colocalization of Catalyst Components and Chemical Elements, *J. Phys. Chem. C.,* **2018**, 122, 22920-22929

37. Fam, Y., Sheppard, T.L., Diaz, A., Scherer, T., Holler, M., Wang, W., Wang, D., Brenner, P., Wittstock, A., Grunwaldt, J-D., Correlative Multiscale 3D Imaging of a Hierarchical Nanoporous Gold Catalyst by Electron, Ion and X-ray Nanotomography, *ChemCatChem*, **2018**, 10, 2858-2867.

38. Meirer, F., Weckhuysen, B.M., Spatial and temporal exploration of heterogeneous catalysts with synchrotron radiation, *Nat. Rev. Mater.,* **2018**, 3, 324-340.

39. (39) Pfeiffer, F., X-ray ptychography, *Nat. Photonics*, **2017**, 12, 9-17.

40. Ramjoie, Y.J.E., Vlaar, M., Friederichs, N.H., Sergeev, S.A., Zakharov, V.A., Bukatov, G.D., Taftaf, M., Aburaqabah, A., *European Patent 2027164*, **2007**.

41. Lafleur, S., Berthoud, R., Ensinck, R., Cordier, A., De Cremer, G., Philippaerts, A., Bastiaansen, K., Margossian, T., Severn, J.R., Tailored bimodal ultra-high molecular weight polyethylene particles, *J. Polym. Sci. A.,* **2018**, 56, 1645-1656.

42. McKenna, T.F.L., Di Martino, A., Weickert, G., Soares, J.B.P., Particle Growth During the Polymerisation of Olefins on Supported Catalysts, 1 – Nascent Polymer Structures, *Macromol. React. Eng.*, **2010**, 4, 40-64.

43. Ryan, C.G., Siddons, D.P., Kirkham, R., Dunn, P.A., Kuczewski, A., Moorhead, G., De Geronimo, G., Paterson, D.J., de Jonge, M.D., Hough, R.M., Lintern, M.J., Howard, D.L., Kappen, P., Cleverley, J., The New Maia Detector System: Methods For High Definition Trace Element Imaging Of Natural Material, *AIP Conf. Proc.*, **2010**, 1221, 9-17.

44. Ryan, C.G., Laird, J.S., Fisher, L.A., Kirkham, R., Moorhead, G.F., Improved Dynamic Analysis method for quantitative PIXE and SXRF element imaging of complex materials, *Nucl. Instrum. Methods Phys. Res. B*, **2015**, 363, 42-47.

45. Carzaniga, R., Domart, M.-C., Collinson, L.M., Duke, E., Cryo-soft X-ray tomography: a journey into the world of the native-state cell, Proto-plasma, **2014**, 251, 449-458.

46. Lui, Y., Meirer, F., Williams, P.A., Wang, J., Andrews, J.C., Pianetta, P., TXM-Wizard : a program for advanced data collection and evaluation in full-field transmission X-ray microscopy, *J. Synchrotron Radiat.,* **2012**, 19, 281-287.

47. Studholme, C., Hill, D.L.G., Hawkes, D.J., An overlap invariant entropy measure of 3D medical image alignment, *Pattern Recognit.,* **1999**, 32, 71-86.

48. Raabe, J., Bunk, O., X-ray ptychographic computed tomography at 16 nm isotropic 3D resolution, *Sci., Rep.,* **2004,** 4, 3857.

49. Wise, A.M., Weker, J.N., Kalirai, S., Farmand, M., Shapiro, D.A., Meirer, F., Weckhuysen, B.M., Nanoscale Chemical Imaging of an Individual Catalyst Particle with Soft X-ray Ptychography, *ACS Catal.,* **2016**, 6, 2178-2181.

50. van Heel, M., Schatz, M., Fourier shell correlation threshold criteria, *J. Struct. Biol.,* **2005**, 151, 250-262.

51. Nieuwenhuizen, R.P.J., Lidke, K.A., Bates, M., Puig, D.L., Grünwald, D., Stallinga, S., Rieger, B., Measuring image resolution in optical nanoscopy, *Nat. Methods,* **2013**, 10, 557-562.

52. Noristi, L., Marchetti, E., Baruzzi, G., Sgarzi, P., Investigation on the particle growth mechanism in propylene polymerization with MgCl2-supported ziegler–natta catalysts, *J. Polym. Sci.*, **1994**, 32, 3047-3059.

53. Kalirai, S., Boesenberg, U., Falkenberg, G., Meirer, F., Weckhuysen, B.M., X-ray Fluorescence Tomography of Aged Fluid-Catalytic-Cracking Catalyst Particles Reveals Insight into Metal Deposition Processes, *ChemCatChem,* **2015**, 7, 3674-3682.

54. Liu, Y., Meirer, F., Krest, C.M., Webb, S., Weckhuysen, B.M., Relating structure and composition with accessibility of a single catalyst particle using correlative 3-dimensional micro-spectroscopy, *Nat. Comm.,* **2016**, 7, 12634.

Chapter 3. Heterogeneity in the Fragmentation of Ziegler Catalyst Particles during Ethylene Polymerization Quantified by X-ray Nano-Tomography

Ziegler-type catalysts are the grand old workhorses of the polyolefin industry, yet their hierarchically complex nature complicates polymerization activity-catalyst structure relationships. In this Chapter, the degree of catalyst framework fragmentation of a high-density polyethylene (HDPE) Ziegler-type catalyst was studied using ptychography X-ray computed nano-tomography (PXCT) in the early stages of ethylene polymerization under mild reaction conditions. An ensemble consisting of 434 fully reconstructed ethylene pre-polymerized Ziegler catalyst particles prepared at a polymer yield of 3.4 g HDPE per g catalyst was imaged. This enabled a statistical route to study the heterogeneity in the degree of particle fragmentation and therefore local polymerization activity at an achieved 3-D spatial resolution of 74 nm with-out requiring invasive imaging tools. To study the degree of catalyst fragmentation within the ensemble, a fragmentation parameter was constructed based on a k-means clustering algorithm, that relates the quantity of polyethylene formed to the average size of the spatially resolved catalyst fragments. With this classification method, we have identified particles that exhibit weak, moderate and strong degrees of catalyst fragmentation, showing that there is a strong heterogeneity in the overall catalyst particle fragmentation and thus polymerization activity within the entire ensemble. This hints towards local mass transfer limitations or other deactivation phenomena. The methodology used here can be applied to all polyolefin catalysts including metallocene and the Phillips catalysts to gain statistically relevant fundamental insights in the fragmentation behavior of an ensemble of catalyst particles.

3.1 Introduction

After the discovery of a free radical polymerization route of ethylene into a highly branched low-density polyethylene at extreme reaction conditions in the early 1930's by Gibson and Fawcett, two different catalyst systems, based on respectively Chromium and Titanium active sites, were developed in the 1950's operating at considerably milder reaction conditions and giving a more linear and dense polyethylene product [1-3]. One of these systems was developed by Karl Ziegler based on combining a $TiCl_4$ pre-catalyst with a dialkylchloro-aluminium co-catalyst to form a Ti^{3+} active site. This discovery would ultimately result in awarding the 1963 Nobel prize to both Karl Ziegler and Giulio Natta, who discovered that the α-$TiCl_3$ form could also be used for the synthesis of stereoregular polyolefins, such as isotactic polypropylene [4,5]. Today, three different catalyst systems, namely the Ziegler catalyst, the Phillips catalyst, and molecular, single-center catalyst in homogeneous and an immobilized form as well as the non-catalytic process developed by Gibson and Fawcett are used to synthesize a wide variety of different polyethylene grades ranging from highly branched low-density (LDPE), linear low-density (LLDPE), medium-density (MDPE) to high-density (HDPE) polyethylene [6]. These polyethylene (PE) grades possess different mechanical and physicochemical properties, such as impact strength, stiffness, friction and wear resistance, melting point, and processability, leading to wide-spread applications ranging from insulating layers for electricity cables, high durability pipes for the transport of gasses and liquids, to medical appliances and protective equipment [7]. Finally, polyolefins can also be synthesized from biomass- and municipal waste-derived feedstock, such as ethylene derived from bioethanol and pyrolysis-cracking of plastic waste, and they can be implemented in a circular economy through either mechanical or chemical recycling, such as remolding and thermal decomposition to the raw feedstock [8-10].

The hierarchically complex Ziegler catalyst system remains one of the grand old workhorses of the polyethylene industry. It typically consists of a $TiCl_4$ pre-active site species epitaxially chemisorbed on a mechanically or chemically activated $MgCl_2$ support matrix and subsequently reduced and alkylated with a trialkylaluminium co-catalyst [2]. This $MgCl_2$ matrix is build-up of platelets, as small as 5 nm, referred to as the primary particles [11,12]. These primary particles stack together due to ionic interactions to form the catalyst particles in the range of 5-30 μm [13]. Depending on the synthesis routes used, the physicochemical and mechanical properties of Ziegler-type catalysts, such as the pore size distribution, can be fine-tuned [14,15]. For instance, precursors ranging from alkoxides like $Ti(OR)_4$, $Mg(OR)_2$ and $MgCl_2$ alcohol adducts to MgRCl Grignard reagents can be used [16-19]. Furthermore, spray-drying of anhydrous $MgCl_2$ in a polar solvent or the deposition of $MgCl_2$ on a spherical and porous silica support matrix are common industrial preparation routes providing high control of the catalyst particle morphology, particle size distribution and porosity [20,21].

The α-olefin polymerization process, including the growth of the polyolefin particles, starts with the fragmentation of the catalyst particle at the nanometer to micrometer scale [22-28]. Typically, this is referred to as the early stage of olefin polymerization. As the α-olefin

monomer reaches the active site it will become incorporated in a growing polymer chain. These polymers will be formed both on the external surface and internal pore structure of the polyolefin catalysts. As these polymer chains start to grow inside the pores of the catalyst particle there is a build-up of stress exerted on the framework of this respective particle. Depending on the friability of the framework, the crystallization and the growth rate of the formed polymer versus the relaxation time of the induced stress, a threshold is reached at which point the catalyst particle starts to fragment [29-31]. This fragmentation is a necessary phenomenon as it leads to the exposure of new active sites and prevents mass transfer limitations through the densely formed polyolefin layer that would otherwise inhibit catalyst activity [32,33]. However, a controlled fragmentation process is preferable to prevent the formation of fines that can lead to fouling in the reactor or downstream equipment as well as to maintain good control over the evolution of particle morphology and particle size distribution (PSD) to facilitate easier polymer powder processing [22, 34, 35]. A common approach at industrial plants is to implement a pre-polymerization step at mild reactions conditions, e.g., 0.1 MPa and close to room temperature, to facilitate a smooth fragmentation process followed by the actual polymerization conditions of 1-10 MPa and around 364 K [3, 36-39].

From a fundamental aspect, there are two limiting modes of catalyst particle fragmentation, namely the layer-by-layer or shrinking core mode and the continuous bisection mode [28]. In the first mode, the polymerization is mainly occurring near the surface of the catalyst particle and therefore the catalyst particle starts to fragment from the surface inwards until the core is reached. In the second mode, olefin polymerization occurs throughout the entire catalyst particle, which leads to an internal cleavage at the core of the catalyst particle into successively smaller fragments. Which fragmentation mode dominates the overall fragmentation behavior is determined by the type of α-olefin monomer and catalyst properties, such as pore size and pore size distribution, crystalline nature of the formed polymer, friability of the framework, distribution, nature and activation procedure of the active sites as well as heat transfer and mass transfer properties, which are influenced strongly by the operating conditions such as gas-phase versus slurry-phase [40-44].

The fragmentation behavior of polyolefin catalyst particles has been studied in the past decades mainly with the use of electron microscopy techniques [45-48]. Zheng and Loos used cross-sectional scanning electron microscopy (SEM) on both Ziegler-Natta and immobilized metallocene catalysts operating under different reaction conditions [49-51]. For a propylene polymerized Ziegler-Natta catalyst they observed that as a function of the pore size, either the shrinking core or continuous bisection mode was dominating [50]. These findings signify the crucial role that catalyst pore size and mass transfer resistance play in the fragmentation behavior. Interestingly, an immobilized metallocene catalyst showed a dominating shrinking core fragmentation behavior under ethylene polymerization conditions and the continuous bisection fragmentation behavior under propylene polymerization conditions [49]. The McKenna group showed in a series of articles the development of stopped-flow reactors and a rapid quenched-flow device that allowed the investigation of the early stages of ethylene polymerization under industrially relevant conditions both in the gas-phase and slurry-phase conditions [53-56]. These unique polymerization reactors achieved reaction times as low as 40 milliseconds at industrially

relevant reaction conditions, such as 0.8 MPa ethylene. Pater et al., on the contrary developed a reactor setup that allowed the pre-polymerization of a Ziegler-Natta catalyst with propylene under extremely low reaction rates to obtain well-defined polymerization conditions, which allowed studying the intra- and inter-particle morphologies with cross-sectional SEM [38]. Unfortunately, these electron microscopy-based studies require either invasive and destructive cutting techniques to observe a 2-D representation of the interior of the particle or are limited to information regarding exclusively the particle's exterior.

Fortunately, state-of-the-art X-ray microscopes both at synchrotron-based and lab-based facilities are able to image the interior and exterior of objects, such as catalyst and polymer particles ranging from several tens of microns to even millimeters in size with 3-D achieved spatial resolution ranging from sub-100 nm to several microns without requiring invasive preparation methods [56]. Additionally, the high beam brilliance and tuneability of the photon energy at synchrotrons has enabled chemical, elemental, and diffractive tomographic imaging, even under operando catalytical conditions [57-64]. For example, the Beale group recently demonstrated the advances made in operando X-ray tomographic imaging for both the oxidative coupling and reforming of methane [65,66]. Due to the state-of-the art photon detector and advanced on-line data-analysis the collection of each X-ray diffraction computed tomography (XRD-CT) dataset only took 117 seconds with a pixel size close to 3 microns [65]. They further demonstrated the use of a multi-modal μ-X-ray fluorescence /absorption/XRD CT toolbox [66]. Another exciting development, performed by the Grunwaldt group, has shown the strengths of correlative multimodal spectroscopy and 3D imaging techniques bridging the fields of electron, ion, and X-ray tomography [67-69]. Furthermore, they recently reported on the fabrication of two nanoreactors for *in-situ* electron and X-ray tomographic studies allowing pressures and temperatures of up to 100 kPa and 1573 K with a tilting angle of +/- 35° for a fully mounted cell [70]. The van Bokhoven group recently reported on a 3-D estimated spatial resolution between 30-40 nm for the sub-volume of several fluid catalytic cracking (FCC) catalyst particles using Ptychographic X-ray Computed Tomography (PXCT) [71-74]. They found that zeolite amorphization and structural changes are the underlying driving forces for the FCC catalyst deactivation process [73]. X-ray nano-tomography studies on FCC catalysts, performed by Bare *et al.*, [75] as well as by our group [76-83], demonstrated how the generation of a 3-D pore network for FCC catalyst particles allowed for advanced mass transport simulation studies as well as correlated localization of active sites, metal poison species, and coke species. Pioneering work on the use of computed X-ray microscopy tomography for the field of polyolefin catalysis was performed in the early 1990's at Brookhaven National Laboratory and subsequently in the late 2000's [28, 84-88] with achieved spatial resolution of several microns allowing the study of porosity of full polyolefin particles and to calculate monomer diffusion and degassing properties [33]. A recent review summarizes the field of X-ray imaging of solid catalysts, including some future perspectives [64].

In Chapter 2, we have introduced a powerful correlated 3-D X-ray ptychography and fluorescence microscopy toolbox that allowed us to directly observe in 3-D the Ti distribution, comprising the active sites, within the isotactic polypropylene phase of an individual Ziegler-Natta catalyst particle in the early stages of propylene polymerization [89]. This study showcased that for the slurry-phase propylene polymerized catalyst particle both fragmentation models were present within the same particle but furthermore that the

continuous bisection model was dominating the overall fragmentation behavior. In this Chapter, we build further upon the use of this powerful correlated 3-D X-ray microscopy toolbox, with a strong focus on the ptychographic X-ray computed tomography (PXCT) dataset that allowed us to study the heterogeneity in catalyst fragmentation and obtain geometrical parameters of many individual ethylene polymerized Ziegler-type catalyst particles from an ensemble of 434 particles within the measured field of view.

3.2 Experimental

3.2.1 Synthesis of the Ziegler Catalyst

A Ziegler catalyst, industrially relevant for the production of high molecular weight and high-density polyethylene without the addition of co-monomers was synthesized in accordance with the description in patent WO2009112254 [90]. The as-synthesized catalyst formulation resembles that of a typical $MgCl_2/TiCl_4$ Ziegler-type catalyst with a Ti weight loading of 4% obtained from Inductively Coupled Plasma- Atom Emission Spectroscopy (ICP-AES). The median particle size (D_{50}) and particle size distribution (span, defined as $\frac{D_{90}-D_{10}}{D_{50}}$) using Static Laser Scattering (SLS) were obtained using a Mastersizer 3000 laser diffraction particle size analyzer instrument. The $D_{10,50,90}$ values of the pristine catalyst are respectively 2.23, 3.64 and 6.01 μm giving a span of 1.04. Scanning electron microscopy (SEM) images of the pristine catalyst, transferred under inert conditions using a transfer module from Kammrath & Weiss, to a ThermoFischer FEI Versa 3D FEG SEM were obtained at a 2 kV accelerating voltage and are shown in Figure 3.1. Based on SEM, the pristine catalyst particles are observed to be elongated. N_2 physisorption on a typical batch of this Ziegler catalyst shows a BET surface area of 6.3 m^2/g and a pore volume of 0.026 cm^3/g. Only mesoporosity is observed for the catalyst with a pore size distribution mainly between 20 to 50 nm.
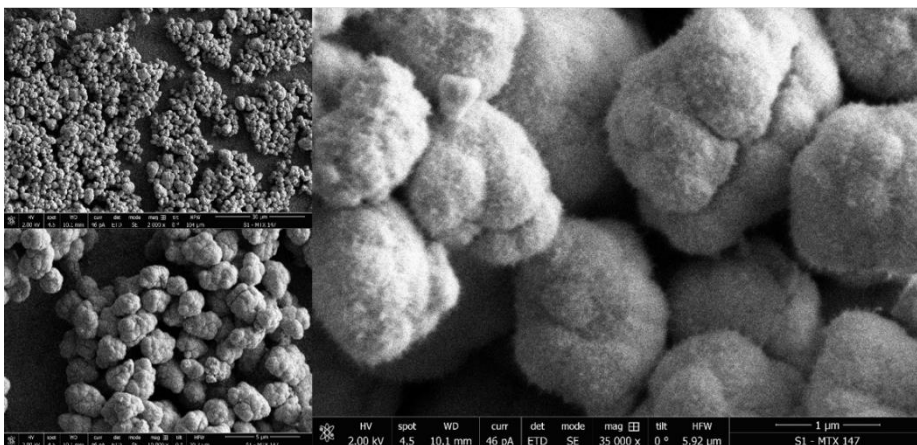

Figure 3.1 Scanning electron microscopy (SEM) images of the Ziegler catalyst used. The catalyst particles are observed to have a cauli-flower type of shape with a rough surface and cracks can be observed on the external surface, likely due to the agglomeration of smaller sub-units. A majority of the catalyst particles seems to be slightly elongated.

3.2.2 Slurry-Phase Ethylene Polymerization

Due to the high sensitivity of the as-synthesized Ziegler catalyst to moisture and oxygen all further procedures were performed inside a glovebox operating under inert conditions of N_2 with <0.3 ppm H_2O and <1 ppm O_2. A low-pressure, room-temperature polymerization set-up was designed to run from inside the glovebox, with a schematic drawing given in Figure 3.2. A cylindrical glass reactor of circa 100 mL internal volume with a single inlet can be either set under vacuo to remove the gas atmosphere inside the reactor or be filled with ethylene at a set pressure of 1.2 barg. A typical polymerization reaction was performed as follows. First, 10 mL of anhydrous (99.9% purity, dried and stored over 3Å molecular sieves, *Across Organics*) heptane was introduced in the open glass reactor equipped with a magnetic stirring bar. A 500 µL solution of triethylaluminium co-catalyst (1M in heptane, *Sigma-Aldrich*) was then added whilst stirring at 400 rpm with a ratio with regards to the catalyst of [Al]/[Ti]= 72. The co-catalyst serves two purposes here, to further purify the diluent as well as the monomer gas-feed and to activate the Ziegler pre-catalyst. Meanwhile the catalyst that was kept in a hexane slurry was dried at room temperature inside the glovebox after which 50 mg was added to the diluent mixture in the reactor whilst stirring at 400 rpm. The reactor chamber was then closed and the evacuation/feed tubing attached. The reactor was first evacuated slowly to several tens of mbar pressure to remove the N_2 atmosphere after which the ethylene (3.5N purity, Linde) was fed to the reactor. During the entire duration of the polymerization reaction the gas-feed was kept open as to ensure a constant pressure of ethylene. After five minutes of polymerization, the ethylene feed was quickly removed by switching the reactor to the vacuum pump followed by introducing N_2. The slurry was then filter dried inside the glovebox using the same vacuum pump set-up and washed successively three times with heptane and three times with pentane. Afterwards, the powder was dried for 60 minutes at room temperature followed by drying at 80 °C overnight on a hotplate inside the glovebox. The next day, the resulting dried polymer powder was weighed and gave a yield of 3.4 g HDPE per g catalyst after which it was stored until further use in a glass vial in the glovebox. The reactor set-up was designed for its simplicity in use inside a glovebox, however it should be noted that a model reactor for low polymer yields such as designed by the group of McKenna *et al.,* would allow industrially relevant polymerization conditions whilst having high control over the polymer yield [53-55].
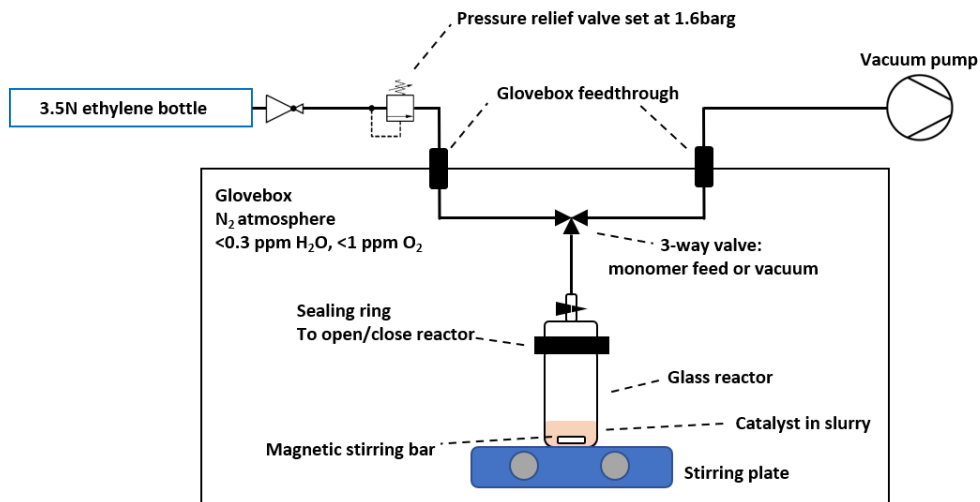
Figure 3.2 Schematic representation of the lab-based model reactor for ethylene polymerization under mild conditions (pressure up to 1.6barg and room temperature)

The polymer yield can also be estimated based on the median of the particle size distribution, D_{50}, as shown in Equation (Eq.) 3.1:

$$D_{50-polymer} = D_{50-catalyst} \cdot R_f \cdot \sqrt[3]{PY + 1} \qquad \text{Eq. 3.1}$$

Here $D_{50\text{-polymer}}$ and $D_{50\text{-catalyst}}$ are the D_{50} values of respectively the obtained polymer particles and the pristine catalyst used. R_f is a constant, which is assumed to be 1, and relates to the physical nature of the polymer and catalyst particles and that one catalyst particle is converted into one polymer particle. The polymer yield, PY, gives the yield of polymer in terms of g polymer per g catalyst and can be deduced from Eq. 3.1 if one knows the D_{50} values of polymer and catalyst [91].

The particle size distribution ($D_{10,50,90}$ and span) of the product was measured with SLS. The SLS results on these composite polymer-catalyst particles gave a D_{50} value starting at 371 µm that would decrease to 172 µm during 20 consecutive runs. The decrease in D_{50} based on the run-time is due to the constant mechanical stirring inside the SLS machine, which therefore indicates that the HDPE-Ziegler catalyst composite particles are highly agglomerated and break up due to the induced mechanical forces. SLS is able to measure such agglomerations since the working principle of SLS is based on the scattering of the laser light induced by any objects through its path towards the detector.

To confirm this agglomeration, SEM analysis was also performed of the polymerized catalyst sample and is shown below in Figure 3.3. Clearly HDPE fibers can be observed bridging multiple particles together in the right side of Figure 3.3. Whereas this catalyst yielded agglomerations at low yields, at industrially relevant yields on the order of several kg HDPE

per g catalyst spherical and isolated HDPE particles are obtained. This indicates that at some point during the polymerization process, the mechanical forces induced by the stirring in addition to the ever-increasing diameter of the particles seem to overcome the strength of the fibers bridging two or more particles together and cause a deagglomeration process.
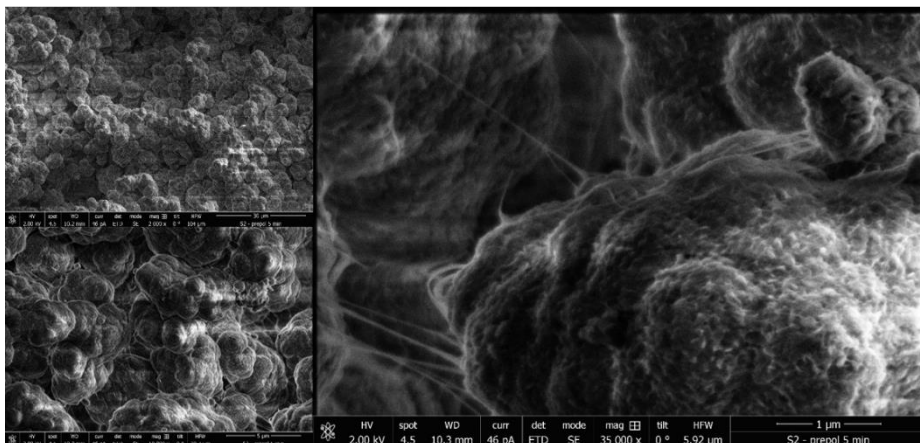
Figure 3.3 Scanning electron microscopy (SEM) images of the ethylene polymerized Ziegler catalyst. The agglomeration of the composite polymer-catalyst particles is evident in the top left and bottom left images. Furthermore, the zoom-in SEM image in the right shows the presence of polymer fibrils below 100 nm thickness bridging particles together and is likely the reason of the agglomeration of the composite particles. Furthermore, the zoom-in shows the roughness of the particle surface is maintained.

Since, the D_{50} of the composite polymer-catalyst particles from SLS are unreliable due to the strong agglomeration, the theoretical D_{50} value was calculated based on Eq. 3.1. Here the polymer yield of 3.4 g HDPE per g cat was used, which was found simply by weighing the final polymer product and correcting for the amount of catalyst injected in the reactor. With the $D_{50\text{-catalyst}}$ value of 3.6 μm, that was found reliably with SLS for the pristine catalyst, the $D_{50\text{-polymer}}$ value is estimated to be 5.9 μm.

3.2.3 Sample Capillary Loading

The sample loading inside a polyimide capillary was similar to that performed in Chapter 2 and all actions were performed inside a N_2-filled glovebox operating at <0.3 ppm H_2O and <1 ppm O_2 unless otherwise stated [89]. Polyimide capillaries obtained from MicroLumen with an inside diameter of 120 μm and wall thickness of 10 μm were used. To load the agglomerated powder, which looks like small flakes, the capillary was gently inserted into a flake and turned up-side down so that the composite powder is now at the top of the capillary. The capillary is then mildly agitated by tapping it gently from the outside with a tweezer so that the agglomerated particles drop towards the center of the capillary. Care was taken not to squeeze the center of the capillary or hit the agglomerated particles directly with the tweezer as this could cause any unwanted morphological changes to the sample unrelated to the actual polymerization process. Finally, a two-component, low-outgassing and near-hermetic sealing epoxy from Epotek©, product label H74, was used to seal the two ends of the capillary. The epoxy had to be cured at 80 °C for 30 minutes to

ensure the desired sealing effect. This was performed by placing the capillaries on a hotplate. To make sure the capillaries don't get stuck on a hotplate, small aluminium foil pieces were attached to the ends of each tubing where the epoxy was applied. Transport from the glovebox environment to the synchrotron beamline was performed by placing the loaded capillaries inside glass vials sealed with Teflon tape and placing them in steel vacuum tubes fitted with Viton O-rings and a closing ring.

3.2.4 The Correlated X-ray Nano-Tomography Setup

The correlated ptychography X-ray computed tomography (PXCT) and X-ray fluorescence (XRF) tomography experiment, see Figure 3.4, was performed at the Hard X-ray Micro/Nano-Probe beamline, P06, at the PETRA III synchrotron facility, DESY. The PXCT raw data was collected using an Eiger X 4M hybrid pixel detector (Dectris Ltd.). The main difference with respect to Chapter 2 is that the Ti XRF data-set was collected with two SII Vortex EM Si-drift detectors (internally collimated to a 50 mm^2 area) instead of the now inoperable MAIA detector. The field-of-view (FOV) of 120x20 μm (H x V) was raster-scanned with a coherent and monochromatic X-ray beam focused down to 170 x 160 nm (H x V) at 12 keV using KB mirrors with a step size of 200 nm and a dwell time of 2 ms. A total of 360 projections were obtained from 0-360°, thus a 1° interval, with a half degree off-set after 180° as to correct for any self-absorption events that might happen with XRF without duplicating collection angles. The acquisition time (including motor movement and initialization) for a single projection was 220 seconds and the total acquisition time of all projections was 22 hours. The Ti XRF raw data was fitted according to Solé *et al.,* using PyMCA [92]. The raw data collected with PXCT consists of a far-field Fraunhofer diffraction pattern collected at each scanning point [93]. Using an in-house developed iterative reconstruction algorithm the real part of the refractive index, δ(r), is then reconstructed for the object measured. Due to the absence of a stable reference in this Chapter with a known refractive index (air) in the FOV, the normalization was performed using the beam intensity without any rescaling of the real and imaginary part of the refractive index. This means that the real part of the refractive index, δ(r), measured here and therefore the local electron density, ρ_e, is in this case not quantitative. Future improvements such as upgrading to a 4th generation synchrotron leading to a higher and more coherent photon flux, e.g. Max IV, ESRF EBS or the planned Petra IV, as well as detector improvements with higher scan-rates will allow the dwell-time per pixel to be reduced to sub-ms [94-96]. This would allow for larger FOV's to be scanned without sacrificing precious allocated beam-time and thus incorporate a stable air reference for quantitative X-ray phase nano-tomography on polyolefin catalysts that require a large FOV (>140 μm in width if using these polyimide capillaries).
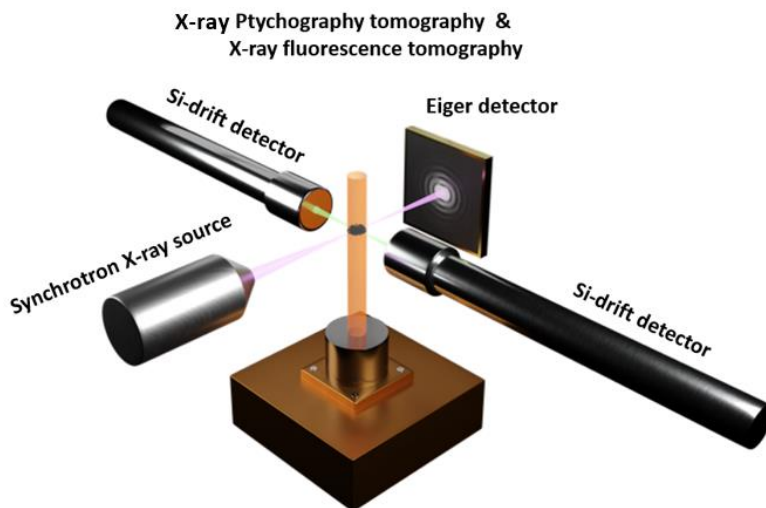
Figure 3.4 Schematic representation of the correlated ptychographic X-ray computed tomography (PXCT) and X-ray fluorescence nano-tomography set-up used at the P06 beamline at DESY. The beam was focused onto the sample by KB mirror optics and the X-Ray fluorescence signal was detected using 2 side-looking silicon drift detectors (SDDs). An Eiger X 4M detector behind the sample was used to record the diffraction data for PXCT.

In Chapter 2 significant X-ray beam-induced morphology changes were observed during the duration of the measurement and attributed to the presence of residual diluent molecules from the slurry-phase polymerization process. As described in sub-Chapter 3.2.2, this time the drying of the post-polymerization powder was done at 80 °C overnight in N_2. This proofed to be rather successful as seen in the comparison of the first and 362nd PXCT projections in Figure 3.5, which are taken 22 hours of continuous scanning and therefore exposure to the X-ray beam apart. No significant beam-damage was observed in this Chapter. It should be noted here that there is a 0.5° degree off-set between the two projections (0-180° and 180.5-360.5°).

Figure 3.5 Comparison of the first and 362nd horizontally aligned PXCT projections taken respectively at the collection angles of 0° and 360.5° (constant increment of 1° with a 0.5° off-set after 180°). No significant beam-damage is observed during the 22 hours total scanning time.
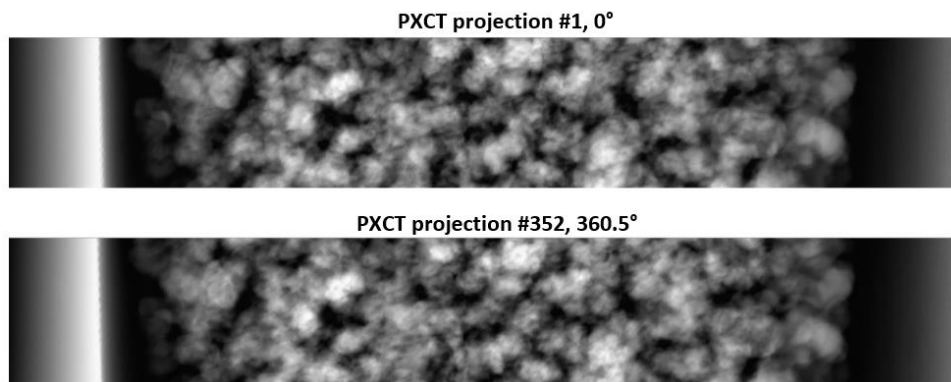
3.2.5 Reconstruction of the Ptychographic X-ray Computed Tomography and X-ray Fluorescence Nano-Tomography Data-Sets

All subsequent analytical and reconstruction procedures were performed on a workstation equipped with a Intel® Xeon® Gold 6242 CPU running at 2.80 GHz with 16 cores, 256 GB of DDR4 RAM memory running at 2933 MHz and a Nvidia® Quadra GV100 GPU. Typically around 20-50 GB of memory was occupied due to the size of the non-binned PXCT data-set and any subsequent 3-D operations. Reconstructions of the 3-D volumes of the PXCT and XRF 2-D projections were performed inside the TXM-Wizard software package [97].

After the collection of the first 180 projections a slight drift of the capillary was noticed due to mounting the capillary on the sample holder using clay and could be optimized further by switching to an epoxy glue instead. To obtain a high resolution 3-D reconstruction of the obtained data-sets, this drift together with any motor position inaccuracies has to be corrected for. Normally, in the ideal case of measuring an isolated spherical object with ample of empty space measured at all sides of the object, correcting for any movement is relatively simple. Strategies involve manually tracking the same feature(s) at each subsequent 2-D projection and using this as the center of rotation as well as the use of a registration algorithm to automatically find any displacement in both horizontal and vertical (or even tilting angle corrections) directions of the region of interest. A combination of both where at first a feature is tracked manually for a rough alignment followed by a registration algorithm for sub-pixel accuracy can be highly effective [99,998]. In this particular situation, the manual tracking isn't feasible due to the difficulty of tracking the same feature(s) over the large FOV scanned consisting of many particles.

Instead the following combination was used for the alignment of the ROI to the rotation axis (horizontal alignment) of both the PXCT and XRF data-sets. No significant drift was observed in the vertical direction. Steps B to E are visualized in Figure 3.6:

A) The first step is to flip the 180.5 to 359.5° 2-D projections horizontally. This effectively makes the second half of the data-set go from 0.5 ° to 179.5° with a 1° increment. This step proved to be crucial for good results in the final alignment used in step D. The reason to collect the angles from 0-360° was to mitigate any possible self-absorption effects while collecting the Ti XRF data.

B) Inside the Avizo™ software package (due to its ease in visualization), the raw 2-D projections of both PXCT and XRF data-sets were binarized at a threshold at 10% of the grayscale values. This means that if the histogram of pixel intensities has a theoretical range from 0-100 then all values below 10 are set equal to 0 and all values above 10 are set equal to 1. This removes low-intensity noise from the first rough alignment performed in step C. Furthermore, in the case of PXCT the capillary wall is removed from each 2-D projection manually. It should be noted here that for the Ti XRF data-sets the capillary walls are not observed.

C) A first rough alignment to bring all ROI's towards the center of image is performed as follows. For each horizontal line within the binarized image, the index of the center of the filled voxels (voxel value is 1) is found using an in-house developed Matlab© code. This is achieved by finding the index of the first and last value equal

to 1 at each horizontal line and taking the average of these indexes as the center of the respective horizontal line. The average of index of all horizontal lines is then taken to be the horizontal center of that respective 2-D projection. This is then repeated in a loop for all 2-D projections. These values give the difference of the center of the horizontal dimension of a 2-D projection with regards to the center of the ROI inside this 2-D projection. To illustrate this: for a typical PXCT 2-D projection the horizontal center of the image is at a pixel value 1250 (total size is 2500 pixels in width) and if the center of the ROI is found to be at 1240 then a horizontal translation of 1250-1240 pixels = +10 pixels within Matlab$^{©}$. The translation values necessary for each 2-D projections are then both applied to the thresholded and masked 2-D projections for the subsequent fine alignment in step D as well as saved in a text-file to perform later on the original and non-thresholded 2-D projections.

D) A registration algorithm between each thresholded and masked 2-D projection with the previous projection is then used for the fine alignment of the horizontal displacement. The Astra toolbox compatible with Matlab$^{©}$ was used for this purpose [98,99]. The translation values of the fine alignment were also saved in a text-file similar to step C.

E) The rough and fine alignment steps gave two text files of translation values. These were applied sequentially to the original 2-D projections after which the original 2-D projections were aligned successfully with respect to each other and still contain the full range of data.

F) During a typical filtered back projection (FBP) reconstruction with a Shepp-Logan filter of the central slice of each data-set, we noticed that the rotation center was still slightly off for the PXCT data-set. Using a horizontal off-set value of -20 pixels within the TXM-Wizard software package, the sharpest reconstructed central slice was obtained. This off-set value is similar to step C in the sense that it performs a horizontal translation but in this case the off-set value is equal for all 2-D projections.

G) Finally, all slices of the PXCT data-set were then reconstructed using the Shepp-Logan filter with a FBP reconstruction algorithm. Due to the low signal-to-noise ratio of the Ti XRF data-set, an iterative algebraic reconstruction algorithm (iART) was used in the TXM-Wizard software package.
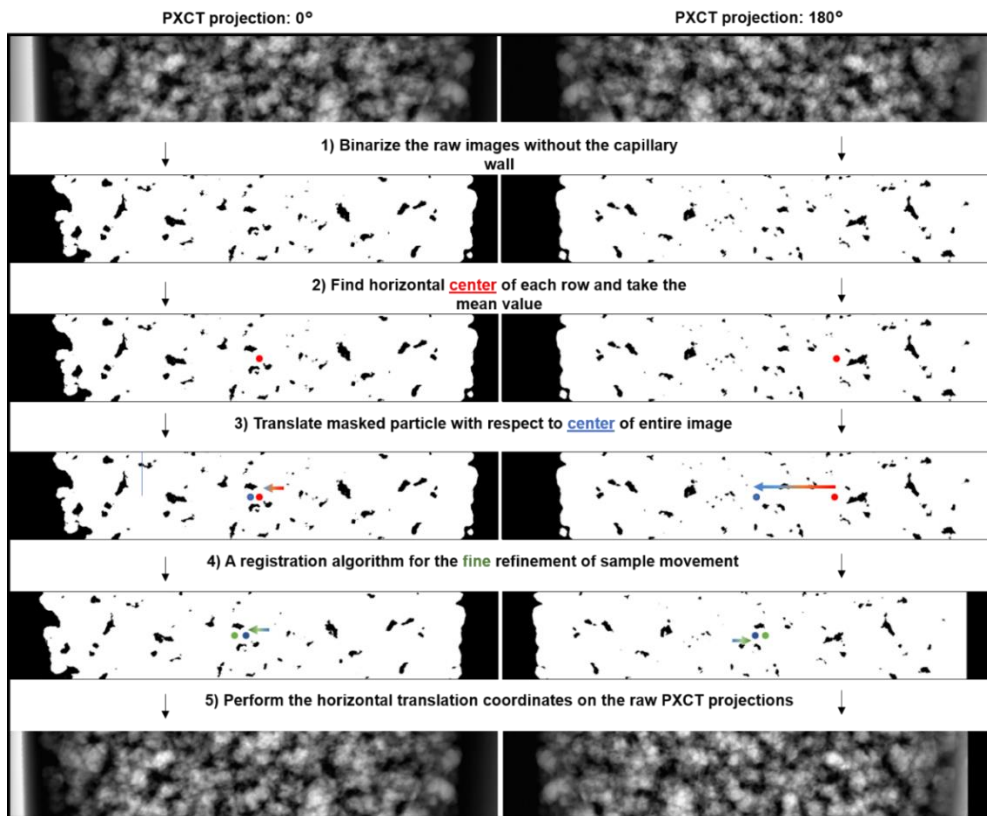
Figure 3.6 Methodology used to align and correct for any horizontal drift of the sample. The 0° and 180° PXCT projections are shown for illustration. In step 1 the raw 2-D PXCT projections are binarized with a 10% threshold and the capillary wall is removed manually. In the second step, for each horizontal line the centre position is found based on the mean value of the first and last 1-valued pixels in that horizontal line (background has a value of 0 for each pixel in a binarized image). Then the mean horizontal centre position is calculated for the entire 2-D projection. In step 3 this mean value is used to perform a first rough translation on the masked images. These translation values are meanwhile also saved in a text-file. In step 4 a registration algorithm is applied as a fine refinement step, which aligns a 2-D projection to its previous 2-D projection and these translation values are again saved in a separate text-file. In step 5, the rough and fine alignment translations are applied to the original non-masked PXCT projections sequentially to finally obtain the PXCT projections aligned with respect to each other. In a final step not shown here, corrections for the off-set of the centre of rotation are optimized within the TXM-

The voxel size of the reconstructed PXCT data-set is 45.4x45.4x45.4 nm^3 and that of the XRF data-set is 200x200x200 nm^3. All subsequent volume rendering was performed in either the Avizo^{TM} software package or within Matlab$^©$. To remove noise from the reconstruction a 3-D non-local means (NLM) filter implemented within Avizo was used. One of the main advantages of this filter is that it assumes the noise to be white-noise and preserves the sharpness of strong edges. An example of the central slice in the XY plane before and after the 3-D NLM filter is shown below in Figure 3.7. An image registration algorithm within Avizo was used to align the XRF data-set to that of the PXCT. The reconstructed PXCT data-set is originally in a 32-bit float format, which allows for storing the raw quantitative electron

density data if obtained. However, since in this Chapter the electron density isn't quantitative, most of the subsequent data-analysis was performed on a 16-bit unsigned converted data-set. This linearly scales all values into a format that can easily exported from Avizo as 2-D tiffs to be opened in Matlab$^{©}$ when using in-house developed codes, without losing information on the relative position of each chemical phase.
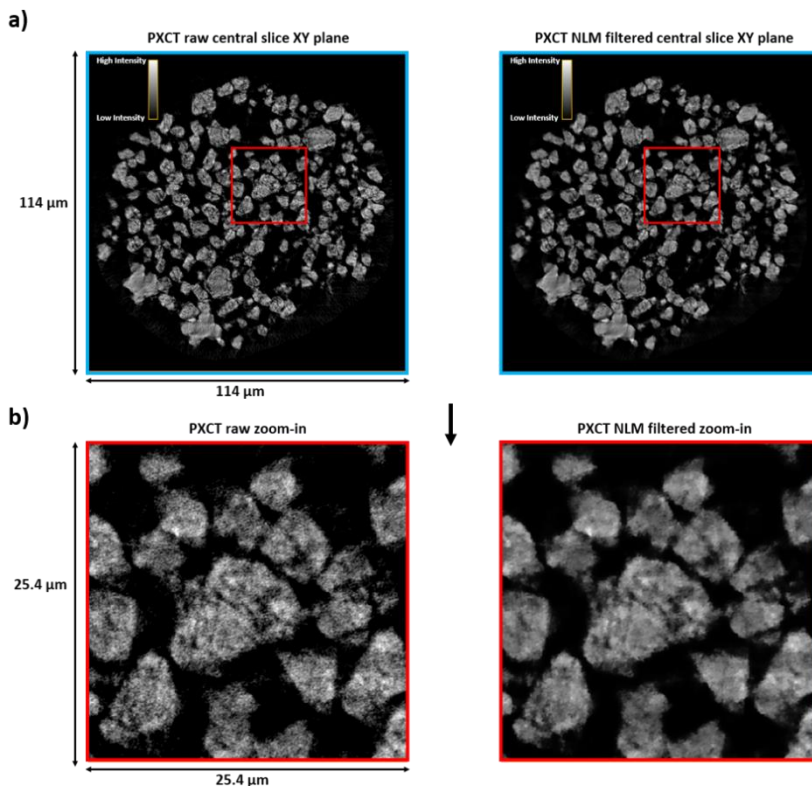
Figure 3.7 (a) In blue contour, the central slices in the XY plane are given for the PXCT data-set before (left) and after (right) applying a non-local means (NLM) filter in 3-D to eliminate white-noise. (b) In red contour, the zoom-ins are given for a detailed comparison between the raw and NLM filtered data-sets.

3.2.6 Fourier Shell Correlation Estimation of the Achieved 3-D Spatial Resolution

To estimate the achieved 3-D spatial resolution of the PXCT and XRF data-sets, the Fourier Shell Correlation (FSC) technique was used [100,101]. The FSC estimated resolution was calculated by separating the original 2-D projections (after the alignment steps from section 5) in odd and even angles and performing a FBP reconstruction on each half data-set. These two reconstructed half data-sets should theoretically contain the same spatial information. Using the Fourier transform of both 3-D reconstructed volumes, their statistical correlation

is calculated for each shell of constant spatial frequency with varying magnitude. A FSC curve plots this correlation going from low spatial frequency to high spatial frequency (1/voxel size) and the spatial resolution is then estimated as the cross-section of the correlation plot versus a chosen threshold value. Here the half-bit criterion is chosen as the value above which point the collected information can be reliably used to interpret the 3-D reconstructed volume.

In Figure 3.8 the FSC curves are given for the PXCT and XRF data-sets before any noise-reduction steps (raw reconstructions) using a Matlab©code from the Astra toolbox [98,99]. Both the 1-bit (full-bit) and ½-bit (half-bit) criterion estimated 3-D spatial resolution are given. When referred to the achieved 3-D spatial resolution in this Chapter, the ½-bit criterion value is taken. For the PXCT data-set the achieved 3-D spatial resolution is 74 nm whereas for the Ti XRF data-set this is 217 nm.
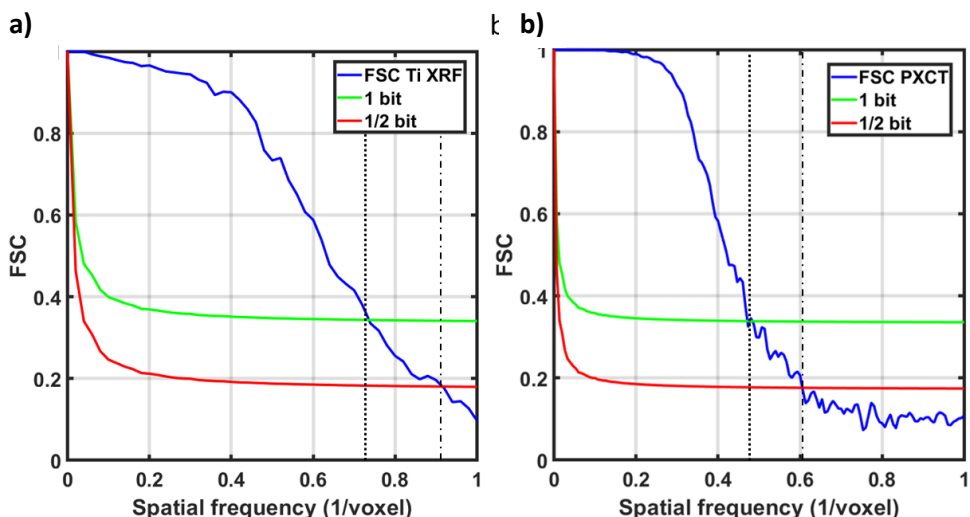
Figure 3.8 Fourier Shell Correlation (FSC) plots of (a) Ti XRF with 1/voxel size intersections of 0.74 for 1-bit and 0.92 for 1/2-bit giving estimated 3-D resolution values of respectively 270 and 217 nm and (b) PXCT with 1/voxel size intersections intersection of 0.47 for 1-bit and 0.61 for 1/2-bit giving estimated 3-D resolution values of

3.2.7 Marker-based Watershed Segmentation

From the central slices in Figure 3.7, it becomes clear that many particles are present in the scanned FOV, which opens the route to a statistical analysis of the state of fragmentation of each individual particle. A common approach would be to first binarize the 3-D volume based on a certain threshold and then use a labelling procedure to assign each particle a unique identity. However a labelling procedure performed directly on a PXCT binarized 3-D volume results in a severe underestimation of the number of composite particles imaged. The reason for this is the high connectivity between the composite particles as evidenced

also by the agglomeration of the composite particles with SEM images in Figure 3.3. Morphological operations such as erosion or selective closing (dilation followed by erosion) could be used in an attempt to remove the connectivity between adjacent particles but this didn't give satisfactory results for this PXCT data-set.

A different approach is to segment the 3-D reconstructed agglomeration into individual particles. A common approach is the so-called watershed segmentation algorithm [102]. This algorithm is based on finding the watershed ridge lines that separate catchment basins from each other. In this case, the catchment basin can be seen as the center of each particle and the watershed ridge lines would be defined at regions where the transition of low intensity voxels (background) to high intensity voxels (particle) is largest. The watershed segmentation process works best when providing some *a priori* knowledge about the position and number of particles expected through feeding the algorithm with markers. A common strategy to create these markers automatically is as follows:

A) Transform the grayscale volume into a binarized volume.
B) Calculate the distance map of the binarized volume, which gives the Euclidian distance between each voxel and the first non-zero voxel neighbors.
C) Use the inverted distance map to calculate the H-minima (ergo the position of each catchment basin), where H is a chosen value of the depth of this catchment basin from the watershed ridge lines where markers falling below this H-criterion are merged together to prevent over-segmentation.

However, despite the use of this H-criterion the non-supervised watershed segmentation algorithm is often plagued by either under-or-oversegmentation. Therefore, in this case we chose for a more time-consuming approach by manually drawing the markers so as to have a strong control over the amount of particles are generated and to prevent both under-and-over-segmentation that could otherwise occur with different H-values for the H-minima marker generation. To make a compromise between the time-consumption of drawing markers and its accuracy the following strategy was chosen (all steps performed in Avizo unless mentioned otherwise):

A) Resample the original data-set of 2500x2500x440 voxels to 625x625x110 voxels.
B) Draw the markers manually in the XY plane (110 instead of 440 slices due to the resampling step) on the resampled grayscale PXCT data-set whilst having cross-sectional views of the XZ and YZ planes open to confirm correct marker drawing. During this step it is highly important that different markers should not overlap in the 3-D volume or during the subsequent labelling procedure they will be assigned the same identity.
C) Resample the manually drawn markers back to the original size of 2500x2500x440 voxels.
D) Label the upscaled markers.
E) Binarize the original PXCT reconstructed volume using a manually found 10% threshold on the grayscale intensities. Using the near-full intensity histogram for the watershed segmentation would add too much background and noise signal to the labels and create unrealistically large particles.

F) However, the 10% thresholded binarized images underestimates the volume of each particle as we remove not only voxels belonging to the background but also part of each particle. To counter-act this, the binarized images are dilated in a ball-expansion mode (isotropic expansion). In Figure 3.9, the mean intensity of each single voxel shell added on the PXCT NLM filtered grayscale images during dilation is shown to find the dilation factor threshold that should be used. Based on these values a turnover point was observed around a dilation factor of 5, which was therefore used as the threshold for dilation. The dilation of the binarized PXCT volume was performed using in-house developed code within Matlab$^{©}$ on a 16 bit unsigned conversion of the original 32 bit float data-set.

G) The use of this dilation factor of 5 can potentially still add voxels to the binarized volume with a mean grayscale intensity value low enough that it should be assigned to a background voxel. In Figure 3.9, this background mean grayscale intensity value was obtained by looking at the plateau achieved at very large dilation factors. In this case, a plateau of a mean grayscale intensity value of 315 was found after 15 voxel dilation. All voxels from the PXCT grayscale data-set with a value equal or lower than 315 were then removed from the 5x dilated binarized volume to correct for background voxels added during dilation.

H) Create the distance map in 3-D from the corrected binarized PXCT volume in step G.

I) Invert this generated distance map.

J) Perform a marker-based watershed algorithm on the inverted distance map from step I using the upscaled labelled markers from step D. The chosen output of this algorithm is the catchment basins (meaning the separated particles).

K) The created catchment basins are automatically labelled but are still separated from each other through the calculated watershed ridge lines. The labels are therefore expanded isotropically to fill the full volume.

L) Finally, these labels are then masked by the corrected binarized volume from step G to give the separated composite polymer-catalyst particles with the entire background successfully removed.

These separated composite particles, each with its own unique label identity, can then be used for further analysis. However, from the 858 generated particles, 434 particles were partially cut-off by the lower and upper borders in the XY plane (as found by calculating the number of particles that have voxels interfacing any border). This means that these 434 particles, referred to as border particles, were not reconstructed completely due to the chosen FOV. After removal of these 434 incomplete particles, 424 completely imaged particles were obtained. These 424 separated particles were then saved as 16 bit unsigned 2-D tiff images to be opened in Matlab$^{©}$. Then in Matlab$^{©}$ each of these 424 particles was visualized in 3-D using the maximum intensity projection volume rendering from the visualization toolbox. All particles were then inspected in terms of proper segmentation and several particles were found to instead consist of multiple particles. After manually correcting these faulty markers and redoing steps H-K, the final PXCT data-set was found to contain 434 separated and completely imaged particles.
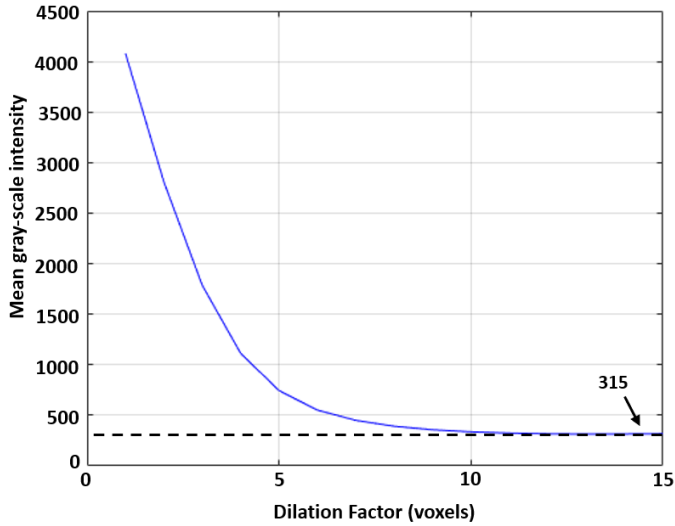
Figure 3.9 A plot of the PXCT mean grayscale intensity of each single voxel shell generated after each dilation. After 15 times dilation applied to all labelled particles, a plateau is reached of the mean grayscale intensity value of 315 (for the 16 bit unsigned converted PXCT data-set). This value was then taken as the mean grayscale intensity value of the background.

3.2.8 Calculation of the Geometrical Parameters of Each Individual Ethylene Polymerized Catalyst Particle

After the marker-based watershed segmentation and subsequent removal of the incompletely reconstructed border particles, 434 separated and completely reconstructed ethylene polymerized catalyst particles remain. For each of these particles several geometrical parameters can be calculated using the label of each particle (meaning a binarized particle with an unique identity). A short explanation on the following geometrical parameters as calculated within either the Avizo software package or Matlab© is given:

1) The volume (V, μm^3) of each particle. This is calculated by simply counting the number of non-zero voxels of each particle's binarized image and multiplying this by the volume of a single voxel (~9.4E-05 μm^3).
2) The surface area (SA, μm^2) of each particle. This is calculated in Matlab© using the Crofton formula as described by Lehmann and Legland [103].
3) The particle's equivalent spherical diameter (ESD in μm). This is calculated simply by assuming the particle to be a perfect sphere and using the following Eq. 3.2 based on the volume calculated in 1):

$$ESD = (\frac{6*V}{\pi})^{\frac{1}{3}} \quad \text{Eq. 3.2}$$

4) The <u>particle size distribution</u> (PSD, μm) of each particle. Using the ESD values, the 10, 50 and 90 percentile distribution values referred to as respectively D_{10}, D_{50} and D_{90} can be calculated as well as the span (unitless, see Eq. 3.1). These values can then be compared to other measurement techniques such as SLS or SEM as well as to the theoretically expected D_{50} based on the polymer yield as discussed in section S2.

The following particle metrics provide information about the shape of each particle and in the case of non-perfect spherical (elongated, spheroidal) also the preferred orientation of the elongation axis:

5) The <u>sphericity</u> (Ψ, unitless) of each particle. The sphericity is defined as the ratio of the surface area of a perfect sphere that encloses the same volume as the surface area of the particle, see Eq. 3.3. For a perfect sphere the ratio is therefore 1 and any object deviating from a perfect sphere will have a value lower than 1

$$\Psi = \frac{\pi^{\frac{1}{3}}*(6*V_p)^{\frac{2}{3}}}{SA_p} \quad \text{Eq. 3.3}$$

6) The <u>elongation</u> (unitless) of each particle. The elongation provides additional information on the preferred orientation of a particle's shape along a certain direction. The elongation value is calculated based on the ratio of the medium and largest eigenvalues of the covariance matrix of each particle, as explained by Meirer *et al.* [77]. A perfect sphere will have an elongation value of 1 as all eigenvalues are equal, whereas a highly elongated particle shape will have a value close to 0. In the case of values below 1, the orientation of the largest or first eigenvalue can be visualized in 3-D to show if there is any preferred orientation of the elongation axis of all the particles within the agglomeration. To do so, the classic Euler angles, i.e. yaw and pitch, were used to show the particle orientation with respect to the same fixed coordinate system used for all ethylene polymerization catalyst particles [104].

7) The <u>flatness</u> (unitless) of each particle. The flatness is calculated as the ratio of the smallest to the medium eigenvalues of the covariance matrix of each particle.

3.2.9 *k*-Means Clustering Algorithm

A *k*-means clustering algorithm was used to classify four cluster regimes for the entire PXCT data-set. This algorithm partitions each data-point, n, which is in this a PXCT grayscale intensity value, to the nearest mean position of cluster K_i. The number of clusters is chosen manually and the mean of each cluster, which is the centroid position, is initialized through the K^{++}-algorithm within Matlab[©] [105]. This initialization uses an heuristic method to find the centroid seeds for the *k*-means clustering. Four clusters, referred to in this Chapter as K_i where i=1-4, were chosen and will be discussed in sub-Chapter 3.3.4

3.2.10 Radial and Disk Analysis to Study the Fragmentation Behavior

In Figure 3.16 both the radial distribution of the all k-means clusters as well as a disk analysis on the mean grayscale intensity values is given along the XY plane. For both calculations the PXCT grayscale, PXCT labelled and k-means clustered data-sets were imported as 2-D Tiffs and analyzed with in-house developed Matlab© codes.

The radial distribution of the k-means clusters was calculated by starting at the surface of a particle and measuring the volume fraction of each k-means cluster. Then an erosion procedure of 1 voxel is initiated and the volume fraction of each k-means cluster is recalculated at this newly exposed particle surface. This is repeated until finally the center voxel(s) is reached. A detailed description of the radial distribution calculation is given by Meirer *et al.* [77]

For the disk analysis, each particle is analyzed along the XY plane starting from one end of the particle's volume to the opposite. Along this XY plane, the particle is build up from certain number of slices where the distance or step size between each slice is defined by the size of a voxel, so 45.4 nm. Then at each slice the mean grayscale intensity is calculated over all voxels present within that slice and tabulated. The final plot gives the grayscale intensity at a slice number going from one end of the particle to the next. Therefore the center of the plot corresponds to the center of the particle's respective volume.

3.3 Results and Discussion

3.3.1 Limited Information from the Ti X-ray Fluorescence Data-Set

Despite the FSC estimated 3-D spatial resolution of 217 nm for the Ti XRF data-set, assessment of the state of fragmentation within each catalyst particle didn't work as done in Chapter 2 where the system investigated was at a higher polymerization yield and therefore exhibited more pronounced and stronger catalyst support fragmentation at larger length-scales.

In Figure 3.10 a comparison of the central slice of the Ti XRF and PXCT data-sets is given as well as a zoom-in for one randomly selected particle. It becomes clear that whereas PXCT shows clear regions of different intensity values with high resolution, which are the cracks of the catalyst framework due to ethylene polymerization, these features are not clearly visible within the Ti XRF data-set. This could simply be due to the fact that the 3-D spatial resolution of the Ti XRF data-set, albeit close to the 2-D pixel value, is about 3 times larger than the PXCT data-set. Additionally to the spatial resolution gap, the Si drift XRF detectors used in this Chapter provided us with less counts in the FOV than with the now inoperable MAIA XRF detector used in Chapter 2. Nonetheless, high quality Ti and even Cl and Mg XRF data-sets could be collected with improvements in the solid collection angles of the XRF detectors, smaller X-ray beam-and-step-size and switching to a He-filled (or vacuum)

measuring chamber. This would change the attenuation length of Ti and Cl Kα photons at respectively ~4.5 keV and ~2.6 keV from several centimeters and millimeters in air towards several tens of meters in He and could allow one to measure without a polyimide capillary if transport chambers are included.
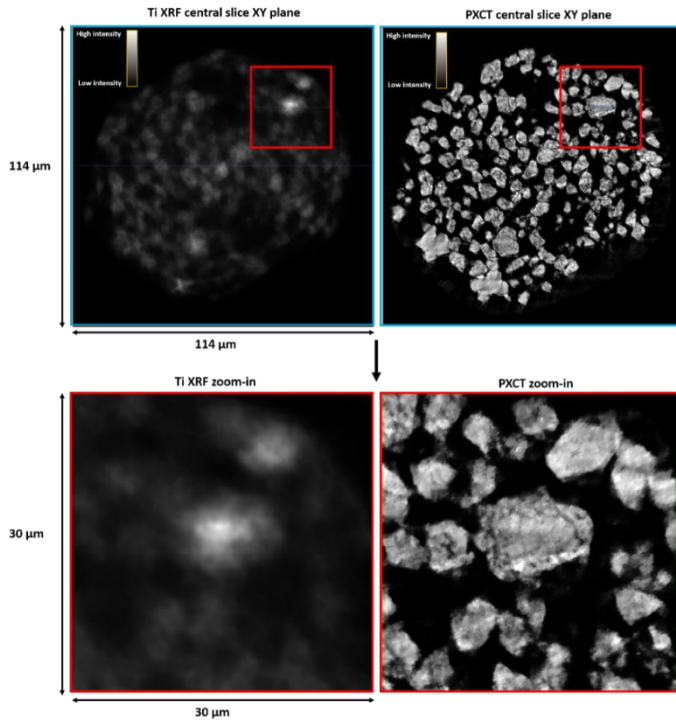
Figure 3.10 Visualizations of the reconstructed central slices in the XY plane of the Ti XRF data-set on the top-left with 200 x 200x 200 nm^3 voxel size and the PXCT data-set on the top-right with 45.4 x 45.4x 45.4 nm^3 voxel size. A zoom-in of the same 30 x 30 μm^2 area for both data-sets is given in the bottom row, which shows the clear difference in quality between the Ti XRF and PXCT data-sets.

3.3.2 Reconstructed Volume of the Polyethylene-Catalyst Particle Ensemble

Therefore, the focus of this Chapter is on the careful analysis of the high-resolution PXCT data-set, where the estimated 3-D spatial resolution has improved significantly from ~ 400 nm in Chapter 2 to 74 nm in this Chapter.

After performing the manual marker-based watershed segmentation as discussed in sub-Chapter 3.2.7, 434 fully imaged and uniquely labelled particles were obtained out of 858 particles in total. The remaining particles, which weren't fully reconstructed due to the limiting FOV are disregarded from further analysis. The result of the manual marker-based watershed segmentation in separating and classifying the particles is shown in Figure 3.11a. In Figure 3.11b, indicated by the red arrow, the advantage of using manual markers can be seen in the successful segmentation of the cyan, light-green, light-pink, and red colored particles. In Figures 3.11c, the cross-section of the segmented particles is shown as an overlay with the PXCT grayscale intensity values.
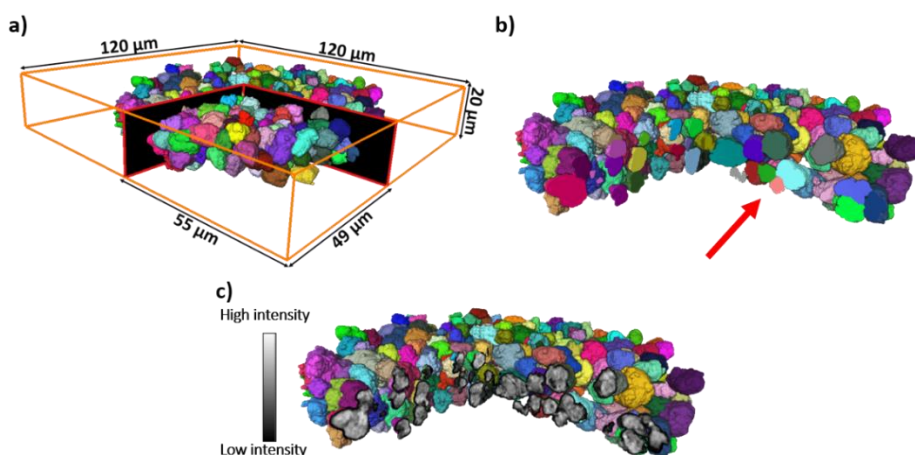
Figure 3.11 (a) 3-D volume rendering (45.4 x 45.4 x 45.4 nm³ voxel size) of the tomography data after manual marker-based watershed segmentation resulting in 434 individually labelled particles. The black planes with red outline depict the position for the visualization of the cross-sections in b-c. (b-c) Cut-out volumes showing respectively, (b) the complete particle labels and (c) the overlay of the Ptychographic X-ray Computed Tomography (PXCT) electron density grayscale intensity values within these labels.

3.3.3 Statistical Particle Metrics of the Polyethylene-Catalyst Particle Ensemble

With the successful segmentation of the highly agglomerated particle ensemble into 434 individual particles, geometrical parameters, such as the particle's volume, area, equivalent spherical diameter (ESD), PSD, sphericity, elongation and flatness could be analyzed. The calculation of these particle metrics is described in sub-Chapter 3.2.8. The mean and standard deviation values of these particle metrics are provided in Table 3.1. The geometrical parameters concerning the particle shape such as sphericity, elongation and flatness show a quite narrow distribution, especially for the sphericity with a standard deviation of 4%. This shows that the overall particle morphology within the entire ensemble is relatively homogeneous. In the case of a smooth catalyst fragmentation process, the morphology of the catalyst particle has been observed experimentally to be replicated in the final polymer particle, called the replication phenomenon [47,106]. The mean elongation of 0.60 (value = 1 for a perfect sphere) for the composite polymer-catalyst particles confirms the presence of the morphological replication phenomena as the pristine catalyst based on SEM observations given in Figure 3.1, is also slightly elongated. In Figure 3.12a both the degree and orientation of the elongation of each particle are visualized in 3-D. Additionally, in Figure 3.12b the correlation is plotted between the ψ (yaw) and ϕ (pitch) Euler angles of the major principal axis of each particle, which represent the direction of the elongation. Finally, the histograms showing the elongation and sphericity values within the entire ensemble are given in respectively Figures 3.12c,d. Based on this plot no clear preferred orientation is observed for the elongation axis within the ensemble. Therefore, although the composite particles themselves are elongated and highly agglomerated, the non-ordered orientation of the elongation direction of the particles of the ensemble shows that there is no preferred expansion direction of the agglomeration as a whole (spheroidal). Furthermore, having measured a relatively large ensemble of particles allows us to calculate the PSD, which can then be compared to both the theoretically expected D50 based on the polymer yield or bulk particle size measurement techniques such as static laser scattering (SLS). In Table 3.1, the ESD and PSD (D10,50,90 and span) of the composite particles is given. The calculated D50 of 5.61 µm of the center particles is only 5.8% smaller than that of the calculated D50 of 5.96 µm based on equation S1 (at a yield of 3.4 g HDPE per g catalyst).

Table 3.1 Overview of the mean and standard deviation values of the volume (V), surface area (SA) and equivalent spherical diameter (ESD), the 10,50,90 percentile fraction of particle size (D_x) and their span, sphericity, elongation and flatness values for the 434 completely reconstructed ethylene polymerizered catalyst particles.

V (µm³)	SA (µm²)	ESD (µm)	D_{10} (µm)	D_{50} (µm)	D_{90} (µm)	Span	Sphericity	Elongation	Flatness
109.5 ± 79.2	144.2 ± *67.0*	5.69 ± 1.17	4.40	5.61	6.87	0.44	0.74 ± 0.04	0.60 ± 0.16	0.67 ± 0.13
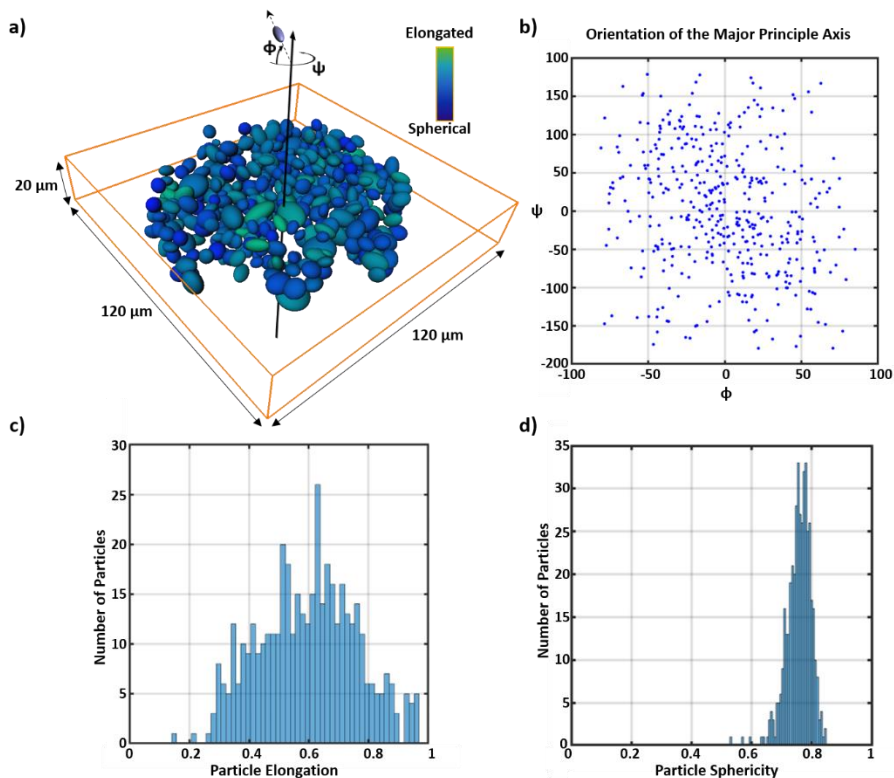
Figure 3.12 (a) 3-D volume rendering of the orientation and degree of elongation of the 434 ethylene polymerized catalyst particles. A dark blue color represents a high degree of sphericity whereas a light green color represents a high degree of elongation. (b) A plot between the ψ (yaw) and φ (pitch) Euler angles that shows the orientation of the major principle axis, the elongation direction, of a particle. (c) A histogram of the elongation values of all particles where a value of 0 means highly elongated and value of 1 highly spherical. (d) A histogram of the sphericity values of all particles where a value of 1 means a perfect sphere.

However, with respect to the span calculated for the pristine catalyst of 1.04 based on SLS results, the span and thus a measure of the width of the particle size distribution found here with PXCT of 0.44 is considerably smaller. This can be explained by the intrinsic differences between the two techniques, such as better bulk statistics with SLS, the method used to interpret the ESD values from the SLS raw data, and that SLS measures the ESD of the scattering objects in the path length of the laser-source, meaning that agglomerated objects are considered as a single particle in SLS and can thus increase and broaden the PSD determined. This last argument was indeed observed experimentally here for the agglomerated composite polymer-catalyst particles, where the SLS results gave D_{50} values going from 350 μm down to 160 μm during the collection of multiple measurements where increased stirring time was observed to cause partial deagglomeration.

3.3.4 Classification of Mixed HDPE and Catalyst Chemical Phases into Clusters

The grayscale values reported here are the real part of the refractive index, $\delta(r)$, which is linearly related to the local electron density, ρ_e (e/Å³), as shown in Eq. 3.4, where r_0 is the Thompson scattering length (alternatively known as the classical electron radius, r_e) and λ is the wavelength of the X-ray probe used in angstroms. In quantitative X-ray phase nanotomography, the local electron density measured can be directly compared to the calculated total electron density of a mixture of compounds assuming the atomic composition within a voxel is known. This formula is shown in Eq. 3.5, where N_A is Avogadro's constant, ρ_m is the total mass density, W_j, Z_j and M_j are respectively the weight percentage, number of electrons and molar mass of the j-th compound [107].

$$\rho_e(r) = \frac{2\pi\delta(r)}{r_0\lambda^2} \qquad \text{Eq. 3.4}$$

$$\rho_e = N_A\rho_m \sum_j W_j \frac{Z_j}{M_j} \qquad \text{Eq. 3.5}$$

Since in this situation the obtained real part of the refractive index and therefore local electron density are not properly scaled versus a stable reference, a comparison with a calculated total electron density from Eq. 3.5 isn't feasible. Furthermore, the histogram of the grayscale intensity values in Figure 3.13 shows a broad distribution where it is difficult to discriminate between a HDPE and Ziegler-catalyst phase. This is most likely the result of the high degree of mixing of HDPE and Ziegler catalyst phases beyond the achieved 3-D spatial resolution of 74 nm. For example, the Ziegler-catalyst shows exclusively mesoporosity with pore sizes between 20-50 nm. This means that even at the earliest stages of ethylene polymerization where HDPE is forming within the pore network but the stress exerted on the framework hasn't reach a threshold yet to cause fragmentation, considerable sub-spatial resolution mixing of two chemical phases is expected. The mass density of the HDPE and Ziegler-catalyst phases are assumed to be on the order of ~0.95 g/cm³ for HDPE and ~2.32 g/cm³ for anhydrous MgCl₂ (the framework of a Ziegler-catalyst). Therefore the high degree of mixing of both phases below the achieved spatial resolution and with a high difference in the mass density and therefore the electron density of each material is expected to be the reason for this broadening of the grayscale intensity values.

Applying a manual threshold on the grayscale intensities to what could be considered a HDPE phase and a Ziegler-catalyst phase would be subjective and open for interpretation in this difficult situation. However, the K-means clustering method provides an efficient way to partition each data-point, n, in this case a grayscale intensity value, to the nearest mean position of a cluster K_i. Alternatively, the conventional Otsu's method is expected to give

the same result for this multilevel thresholding but is computationally more exhaustive as it searches for a global optimal threshold with respect to the local optimal threshold search by the k-means algorithm [108].

Four K-clusters were chosen, where each K-cluster is expected to represent the following chemical phases in ascending order of mean electron density: K_1 should represent a chemical phase dominant in HDPE since HDPE has the lowest mass density and therefore a lower electron density according to Eq. 3.5 than the Ziegler catalyst. K_2 and K_3 both represent highly mixed phases of HDPE and the Ziegler catalyst where in K_2 and K_3 the molar fraction in a voxel are highest for respectively HDPE in K_2 and the Ziegler catalyst in K_3. Finally, K_4 has the highest mean electron density of all k-means clusters and should therefore represent a chemical phase dominant in the Ziegler catalyst. The result of the partitioning of the PXCT grayscale intensity histogram in these four different K-means clusters is shown in Figure 3.13. Furthermore, the geometrical parameters similar as to those given in Table 3.1 for the full particles are given here for each K-means cluster within each particle in Table 3.2.

The motivation for 4 k-means clusters instead of 3 k-means clusters where one could rationalize only a close-to-pure HDPE cluster, highly mixed HDPE and catalyst cluster and close-to-pure catalyst cluster is based on the calculated ESD of the clusters. As shown in Table 3.2, the ESD for the close-to-pure catalyst K_4 cluster is 3.10 µm, which is 14.8% smaller than that of the pure pristine catalyst D_{50} of 3.64 µm. With 3 instead of 4 k-means clusters, the calculated ESD of the close-to-pure catalyst cluster (K_3 in that case, since there are only 3 clusters) would be 3.66 µm and is practically equal to that of the pristine catalyst. Whereas, this might seem logical at first, this would mean that the K_1 and K_2 clusters should both represent a pure HDPE phase since all catalyst is now contained in the K_3 cluster. However, the histogram of the combined $K_{1,2}$ in the case of 4 clusters is already too broad and non-gaussian in peak-shape to describe a single chemical phase. Therefore, with 3 k-means clusters, a good portion of the highly mixed HDPE-catalyst phase is wrongfully assigned to the close-to-pure catalyst cluster K_3 and therefore overestimates the spatially-resolved catalyst.
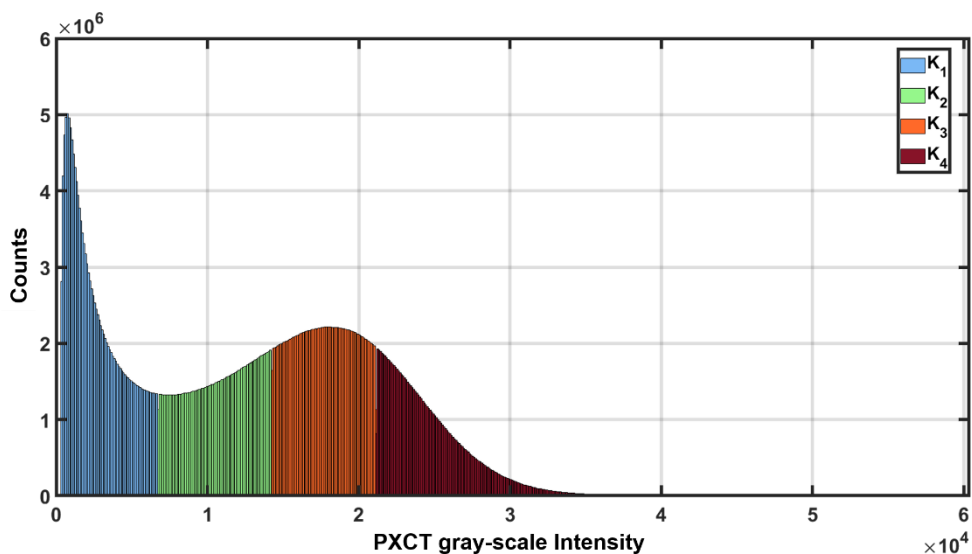
Figure 3.13 Histogram of the 16-bit unsigned converted PXCT grayscale intensity values after applying the 3-D non-local means filter. The color-coding from light blue to light green, orange and dark red correspond to the partitioning of the grayscale intensity values to four clusters (K_1 to K_4) using a *k*-means clustering algorithm. It should be noted here that the PXCT grayscale intensity values of the x-axis are of a 16-bit unsigned converted data-set (original is 32-bit float). This has no consequences for the data-analysis applied here since the raw data obtained doesn't contain the quantitative mean electron density in each voxel.

Table 3.2 Overview of the mean and standard deviation values of the volume (V), surface area (SA) and equivalent spherical diameter (ESD), the 10,50,90 percentile fraction of particle size (D_x) and their span, sphericity (Ψ) for the four *k*-means clusters of all 434 ethylene polymerized catalyst particles.

Particle Metrics	K-means cluster			
	K_1	K_2	K_3	K_4
V (µm³)	33.6 ± 18.7	24.6 ± 17.7	31.6 ± 27.3	19.7 ± 20.4
SA (µm²)	265.3 ± 145.6	304.5 ± 210.8	291.9 ± 239.4	129.2 ± 116.7
ESD (µm)	3.89 ± 0.65	3.46 ± 0.71	3.71 ± 0.89	3.10 ± 0.88
D_{10} (µm)	3.20	2.69	2.67	2.09
D_{50} (µm)	3.85	3.40	3.66	3.02
D_{90} (µm)	4.62	4.25	4.63	4.15
Span	0.37	0.46	0.53	0.68
Ψ	0.20	0.026	0.04	0.08

94

In Figure 3.14 a visual comparison is provided of the electron density grayscale intensity values and the results of the *k*-means clustering algorithm overlayed on the segmented catalyst particles. The *k*-means clustering results provide an efficient way to visualize the fragmentation behavior and will be subsequently used as the foundation to study this in-depth for the entire polyethylene-catalyst particle ensemble.
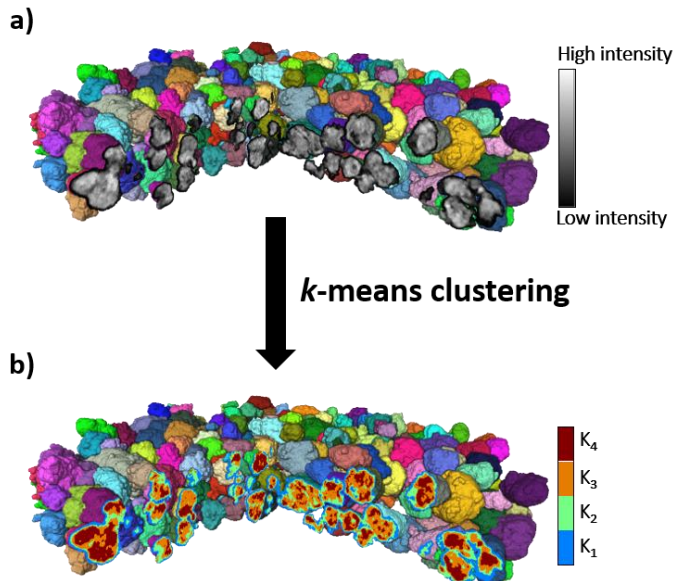
Figure 3.14 Overlay of respectively (a) the Ptychographic X-ray Computed Tomography (PXCT) grayscale intensity values and (b) the results of the *k*-means clustering algorithm performed on the PXCT data-set with 4 clusters on the segmented and labelled composite particles.

3.3.5 Determining the Degree of Catalyst Framework Fragmentation

In this Chapter, to study the degree of catalyst fragmentation within each composite particle a unitless fragmentation parameter (FP), referred to as V_r, has been designed and calculated that considers both the spatially resolved catalyst fragments (identified via K_4) and the quantity of the formed HPDE phase (via clusters K_{1-3}) directly using the k-means clusters

V_r provides a relationship between the formed HDPE phase and the fragmented catalyst phase. This is achieved by taking the ratio of the total volume of the first three k-means clusters of each particle, $K_{1,2,3}$, which constitutes both the polymer and the spatially non-resolved catalyst fragments, over the mean volume of the spatially resolved catalyst fragments in the fourth k-means cluster, K_4. These spatially resolved catalyst fragments in the K_4 cluster are referred to as the non-connected components (NCCs).

In Table 3.3 the mean, median, minimum, and maximum values as well as the standard deviation of the parameter V_r for the 434 imaged composite particles in the ensemble are reported. While the unitless values themselves have no physical meaning, the large spread of V_r, as evidenced by the standard deviation being larger than the mean, nonetheless shows that there is significant heterogeneity in the degree of catalyst fragmentation within the ensemble.

Table 3.3 Overview of the mean, median, minimum and maximum values and the standard deviation of the V_r fragmentation parameter as calculated for the 434 composite particles in the imaged ensemble to study the degree of catalyst fragmentation.

Fragmentation Parameter	Mean Value	Median Value	Minimum Value	Maximum Value	Standard Deviation
V_r	436	268	13	7180	549

Besides the here introduced fragmentation parameter, V_r, used to study the degree of catalyst fragmentation, additional fragmentation parameters could be designed and tried. These additional fragmentation parameters include standard image textural analysis techniques such as calculating the entropy, which is a measurement of the distribution of the greyscale intensity values within a particle, but also the calculation of the total number of spatially resolved catalyst fragments in the K_4 cluster, referred to as N_{NCC}, and the sum distance of these catalyst fragments to the particles center, referred to as $D_{NCC\text{-}center}$.

Fundamentally speaking both a pure catalyst particle and a pure HDPE particle will have similar low entropy and standard deviation values due to the presence of a narrow greyscale intensity distribution. Therefore, such textural analysis techniques can't distinguish between extreme cases of very low and very high degrees of catalyst fragmentation due to the complete lack of chemical information input.

Alternatively, the N_{NCC} and $D_{NCC\text{-}center}$ fragmentation parameters are fundamentally more straightforward than V_r as they directly and purely consider the catalyst fragments to study the degree of catalyst fragmentation. However, since both of these fragmentation parameters fully rely on being able to spatially resolve all catalyst fragments in the K_4 cluster to quantify the fragmentation degree it can severely underestimate the catalyst fragmentation degree in this study. The reason for this is that the smallest or also called primary particle size of the $MgCl_2$ support matrix is reported on the order of several to several tens of nm whereas the achieved spatial resolution in this Chapter is 74 nm. Therefore, both catalyst fragments smaller than 74 nm and catalyst fragments in close proximity of each other can be either assigned to a lower *k*-means cluster and thus removed from the fragmentation parameter or become assigned to a single larger fragment.

3.3.6 Family Album of the Degree of Catalyst Framework Fragmentation

To visualize this heterogeneity the central slice along the XY plane of each of the 434 composite particles is displayed in Figure 3.15. Here, the distribution of the k-means clusters is visualized as it provides a clear overview of the HPDE-rich, highly mixed, and catalyst-rich phases. It should be noted that only one central slice is visualized here for simplicity and therefore doesn't provide the 3-D overview of each particle in terms of the degree of fragmentation and fragmentation behavior (type of fragmentation model dominating). The particle at the top left has the lowest V_r value and exhibits the weakest degree of catalyst fragmentation. It therefore exhibited the lowest local ethylene polymerization activity whereas the particle on the bottom left showed the largest V_r value and thus the strongest degree of catalyst fragmentation and in turn the highest local polymerization activity. The heterogeneity in the degree of fragmentation of each particle and therefore the local polymerization activity observed are most likely the result of mass transfer limitations induced by the particle agglomeration. The particle agglomeration in turn could be caused by the high concentration of the catalyst used in the model reactor (5 g cat/ L diluent) that leads to a higher probability of catalyst particles undergoing ethylene polymerization to stick together. These agglomerations would then limit the diffusion of ethylene to all the otherwise avail-able Ti active sites within each individual particle. Other deactivation phenomena such as the presence of poisons and heat transfer limitations seem less likely due to the presence of excess triethylaluminium co-catalyst, which also acts as a scavenger for poisons and the slurry-phase operation under mild reaction conditions (2 bar ethylene, room temperature) to facilitate better heat transfer.
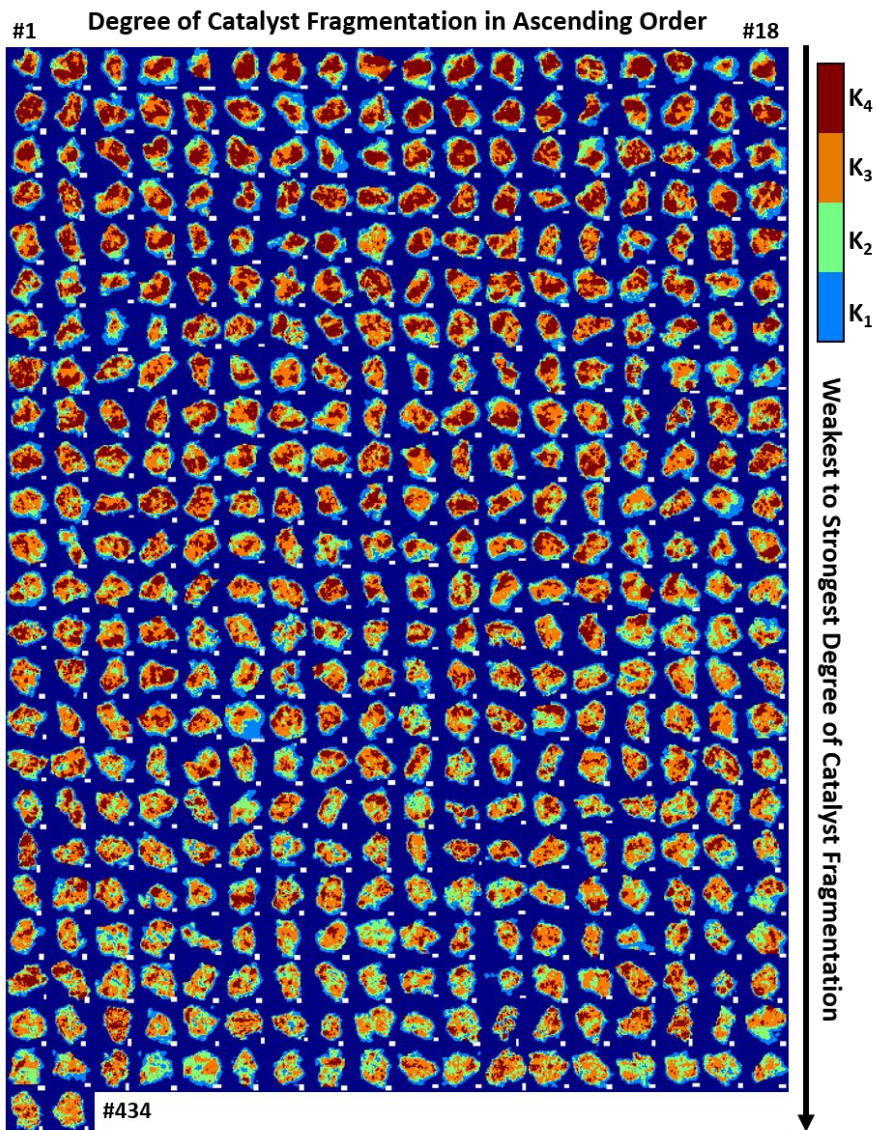
Figure 3.15 'Family album' of virtual cross-sections through all evaluated catalyst particles. The Figure shows the results of the k-means cluster analysis of the PXCT grayscale values of the central slice of each particle. Particles have been sorted by their degree of catalyst fragmentation from weakest, at the top left, to strongest, at the bottom left, fragmentation degree within the entire ensemble of 434 particles based on the unitless Vr fragmentation parameter. The white scale bar at the bottom right of each central image depicts a size of 1 micron.

3.3.7 In-Depth Fragmentation Behavior of Particles Exhibiting Different Degrees of Catalyst Framework Fragmentation

After all particles had been sorted according to their respective degree of fragmentation within the entire ensemble using the V_r fragmentation parameter, it became possible to look more in-depth into the fragmentation behavior of particles that exhibited either a weak, moderate, or strong degree of catalyst fragmentation. In Figure 5, three particles have been selected that fall in one of these three groups. The volume renderings report the 3-D distribution of the 4 k-means clusters and show how each particle is enveloped in a shell of the HDPE-dominant K_1 (blue) cluster. However, from the surface towards the core of each particle we observe a mix of K_2 (in green), K_3 (orange) and even K_4 (red), depending on the particle's fragmentation degree. In the movies available on-line at the published manuscript the 3-D volume rendering of these three particles is given for a full overview of the distribution of the clusters [109]. To complement this visualization, the radial distribution of the volume ratio of each cluster is reported in Figure 5b (see sub-Chapter 3.2.10). This radial analysis gives the volume ratio of each k-means cluster at a single voxel shell, which is normalized by the total voxel count in that shell, at a certain distance from the surface. At the core of a particle and hence the largest distances from the surface, the volume ratio can therefore show an abrupt behavior since that shell consists only of a few (central) voxels. For the first particle we observe that at the surface, the HDPE-dominant K_1 cluster has the largest volume ratio and as we go towards the core the highly mixed HDPE-catalyst K_2 and K_3 clusters sequentially dominate the volume ratio in a shell followed finally by the catalyst-dominant K_4 cluster and again a rise in the volume ratio of K_3 close to the center. In fact, this type of alternating sequence strongly fits to the shrinking-core fragmentation model where the main catalyst polymerization activity is occurring at the particle's external surface and leads to the peeling of typically small catalyst fragments of the original catalysts external surface that will become partitioned to the $K_{1,2,3}$ clusters depending on the volume ratio of HDPE to catalyst in a voxel. Additionally, the increase of K_3 at the core could point towards the formation of polyethylene also inside the core of this particle, which the visual cross-section in Figure 5a confirms. The formation of polyethylene at the core could there indicate that also the continuous bisection model is occurring for this weakly fragmented particle, albeit with a seemingly lower contribution to the overall fragmentation behavior than the shrinking core.

The external surfaces of the other two more fragmented particles are still composed of first the K_1 cluster followed by an increase of the K_2 cluster, which shows that the shrinking core model is still occurring for these more active particles. However, whereas the first particle shows a clear sequential profile between all four clusters going from the surface to the core, a change in this behavior is observed for the other two particles. For instance, the moderately fragmented particle has a second local maximum of the K_2 cluster close to the center of the particle. Furthermore, the $K_{3,4}$ clusters are more homogeneously distributed throughout this particle, with a constant higher concentration of K_3 over K_4 at each distance from the surface. This means that for this moderately fragmented particle, considerable amounts of polyethylene have now also been formed at the core of the particle in addition to the polymer layer at the surface ($K_{1,2}$), which has stayed almost constant in terms of

volume ratio width (number of voxel shells). Here the formation of polyethylene at the core of the particle has led to sufficient local fragmentation to push spatially resolved catalyst fragments (K_4) towards the surface of the particle. The dispersion of large K_4 fragments towards the surface of the particle and presence of the $K_{2,3}$ clusters at the core of the particle is also observed in the visualization of the cross-section of this moderately fragmented particle in Figure 3.16a. This shows that now besides the shrinking core fragmentation model, the continuous bisection fragmentation model is also playing a significant role in the overall fragmentation behavior of this moderately fragmented particle. Finally, for the strongest fragmented particle the most homogeneous distribution of $K_{2,3,4}$ is observed as we go from the surface towards the core of the particle. This would be expected in the scenario where the original catalyst particle keeps breaking up internally due to the formation of polyethylene within the core of the particle, which will push the smaller and smaller catalyst fragments towards the external surface. Indeed, a maximum of the K_4 volume ratio is now observed closer to the external surface than for the least and moderately fragmented particles. Additionally, the thickness of the $K_{1,2}$ cluster layers at the external surface has stayed nearly constant throughout the three particles. This means that for this strongest fragmented particle a shift towards a larger contribution of the continuous bisection fragmentation model in the fragmentation behavior is found.

Together with the central slices of all the particles given in Figure 3.15 we therefore observe that the least fragmented particles mainly consist of a dense catalyst core of the K_4 cluster followed by sequential shells of the $K_{3,2,1}$ clusters. Alternatively, the moderately and strongly fragmented particles show the presence of many K_4 fragments dispersed throughout the composite particle's volume. The combination of these findings, which is shown schematically in Figure 3.17, shows that for particles exhibiting a weak degree of catalyst fragmentation, the shrinking core fragmentation model is dominating whereas for the moderately fragmented catalyst particles a more equal contribution of both shrinking core and continuous bisection fragmentation models is observed and for the strongly fragmentated catalyst particles the continuous bisection fragmentation model is dominating the overall fragmentation behavior. The formation of polyethylene mainly at the particle's external surface as observed for the weakly fragmented particles can be explained by both internal and external mass transfer limitations or alternatively a higher concentration of active sites at the surface than the core, which can happen when the co-catalyst has not come in contact with the internally located Ti^{4+} pre-active sites upon addition of the α-olefin [38].

The disk analysis plots in Figure 3.16c report the mean grayscale intensity values per slice along the XY plane, which represents the mean electron density in a slice. The first particle shows a gradual increase of the mean electron density until a peak is reached close to the central slice along the XY plane and confirms what was observed with the radial analysis of the k-means clusters' volume ratios. That is to say that also with the disk analysis on the pure grayscale intensity values (so without a *k*-means clustering approach) a gradual change is observed from a low mean electron density phase to that of a high electron density phase. That means that there is a smooth change from a HDPE phase at the surface of the particle towards a catalyst phase at the core of the particle. The ~10 slices offset of the maximum grayscale intensity value (around slice 50) from the central slice (roughly at slice 40) also

100

confirms why the K$_3$ cluster shows a volume ratio of 1 at this first particle's center voxels. Going towards the moderately and strongly fragmented particles we see that instead of a peak a plateau is reached that maintains a rather constant mean intensity value for more than 50 slices for the moderately fragmented particle and almost 200 slices for the strongly fragmented particle. Furthermore, instead of a smooth gradient from low to high intensity as observed for the weakly fragmented particle a sharp transition is experienced especially for the strongly fragmented particle. This shows that especially for the strongly fragmented particle the catalyst phase is already highly dispersed throughout the formed HDPE phase, where local maxima can be observed even close to the edges with regards to the XY plane and is additional proof for the continuous bisection fragmentation model playing a significant role in the fragmentation behavior of these two particles.
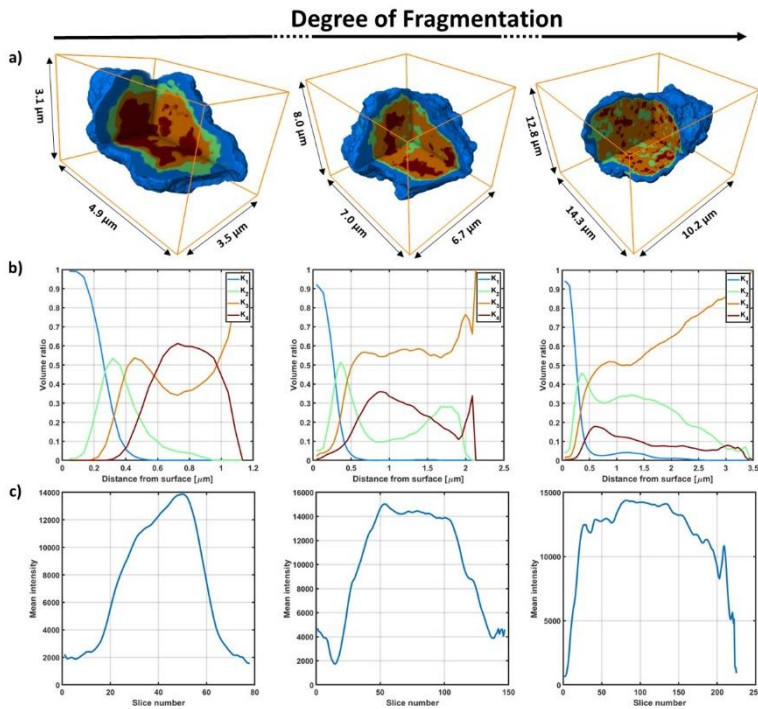
Figure 3.16 (a) Cross-sectional volume rendering of the *k*-means clustering of the grayscale intensities from three composite particles representing from left to right respectively the weakest, moderate, and strongest degrees of catalyst fragmentation as based on their sorting by the parameter V$_r$. (b) Radial analysis of the volume ratio of each *k*-means cluster going from the surface of the respective particle towards the core. (c) Disk analysis along the XY plane giving the mean grayscale intensity value of each slice going from one edge of the particle to the other.
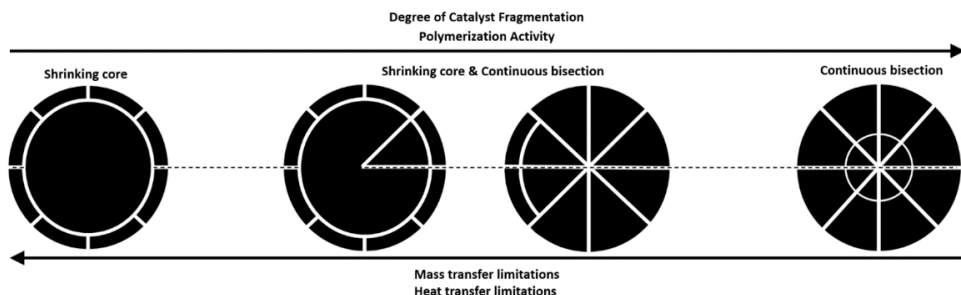
Figure 3.17 Schematic representation of the relationship between the dominating or highly mixed limiting modes of fragmentation behavior observed namely, the shrinking core and continuous bisection, versus the catalyst particle's polymerization activity and degree of catalyst fragmentation, which hints towards strong local mass and heat transfer limitations.

3.3.8 Estimating the Distribution of Particles in Fragmentation State

In sub-Chapter 3.3.3 the degree of catalyst fragmentation for the entire ensemble was assessed using the V_r fragmentation parameter and subsequently visualized for all the 434 polyethylene catalyst composite particles in sub-Chapter 3.3.4 followed by the in-depth fragmentation behavior analysis of three selected particles showing either a weak, moderate or strong degree of catalyst fragmentation in sub-Chapter 3.3.5. To build further upon this, in this sub-Chapter 3.3.6, an estimation is made on how many of these polyethylene catalyst composite particles portray either a weak, moderate or strong degree of catalyst fragmentation.

The histogram of the V_r fragmentation parameter including the *k*-means clustering analysis to partition the particles as either weak, moderate or strong degree of catalyst fragmentation is given in Figure 3.18. The methodology of this *k*-means clustering algorithm is identical to that as described in sub-Chapter 3.3.3 and here applied on the V_r fragmentation parameter values. However, caution should be taken in interpretating these values as this *k*-means clustering algorithm will define hard boundaries on whether a particle is classified as weak, moderate or strong with regards to the fragmentation degree and in reality one would rather expect a smooth transition. Keeping this in mind, the *k*-means clustering algorithm with therefore 3 clusters, estimates that respectively 274, 123 and 37 polymerized catalyst particles show a weak, moderate and strong degree of catalyst fragmentation.
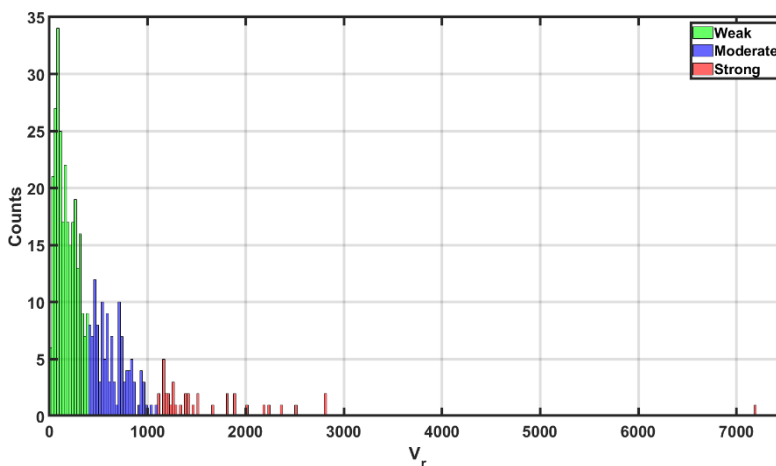
Figure 3.18 Histogram of the V_r fragmentation parameter including the partitioning of the polymerized catalyst particles into either a weak (green), moderate (purple) or strong (red) degree of catalyst fragmentation through a *k*-means clustering algorithm (3 *k*-clusters). The hard boundaries give here between these three fragmentation classes are merely an estimation as one would expect a gradual transition from a weak to a strong degree of catalyst fragmentation. 274 particles are assigned to the weak, 123 to the moderate and 37 to the strong classification.

3.4 Conclusions

Using the strength of ptychography X-ray computed nano-tomography (PXCT) to visualize the local mean electron density with an achieved 3-D spatial resolution of 74 nm over a large, scanned field of view of 120 x 120 x 20 µm³, the heterogeneity in the degree of fragmentation of 434 ethylene polymerized Ziegler-catalyst particles was analyzed and visualized in the early stages of ethylene polymerization under mild reaction conditions and with a high catalyst loading. The highly connected composite particles were successfully segmented in the reconstructed volume using a supervised marker-based watershed algorithm. This segmentation allowed for the analysis of geometrical parameters for each individual particle such as the volume, surface area, equivalent spherical diameter, sphericity and elongation. The elongation degree of the particle ensemble showed that the composite particles followed the replication phenomena of the slightly elongated pristine Ziegler catalyst particles.

Due to the high degree of mixing between the high-density polyethylene (HDPE) and catalyst phases below the achieved 3-D spatial resolution a *k*-means clustering algorithm on the PXCT grayscale intensity values was used to identify a HDPE-rich phase, two highly mixed HDPE-catalyst phases and one catalyst-rich phase. Using these clusters, a fragmentation parameter V_r was designed to study the heterogeneity in the degree of fragmentation and therefore local polymerization activity. This fragmentation parameter is based on the ratio of the summed volumes of the HDPE-rich and highly mixed HDPE-catalyst phases over that of the mean volume of the spatially resolved catalyst fragments. The advantage of this parameter is that it takes into account: i) the catalyst activity in terms of HDPE formation, ii) the loss of any catalyst fragments that have become too small to

spatially resolve them from the HDPE phase, and iii) the change in the size of the catalyst fragments as a function of polymerization activity. Using this fragmentation parameter, a strong heterogeneity was found within the entire ensemble of 434 composite particles with respect to the degree of catalyst fragmentation. Three representative particles that were categorized with respect to showing either a weak, moderate, or strong degree of catalyst fragmentation at this specific yield of 3.4 g HDPE per g catalyst were analyzed in depth. The weakly fragmented composite particle showed mainly a dominating shrinking core fragmentation model with hints to the presence of the continuous bisection fragmentation model. For the moderately and strongly fragmented composite particles the shrinking core fragmentation mode was still observed to occur, but the continuous bisection fragmentation mode had become the dominating pathway for fragmentation, which shows that monomer diffusion towards the interior of the catalyst particle was not limited with respect to the weakly fragmented composite particle; this in turn explains the higher local polymerization activity of these particles. A rough estimation was then performed on how many particles are classified as portraying either a weak, moderate or strong degree of catalyst fragmentation to give values of respectively, 274, 123 and 37 particles.

With further improvements with respect to photon flux and beam coherency, such as through the upgrading to 4th generation synchrotron facilities [93-95], as well as detector acquisition times the 3-D spatial resolution of PXCT can be pushed below the size of the primary particles of the $MgCl_2$-based framework (as small as 5 nm), while maintaining large scanning areas. This will enable a full quantitative approach to study the fragmentation degree of each individual particle with the methodology provided here and can be extended to study other polyolefin catalyst systems, such as the Phillips and metallocene catalysts.

3.5 References

1. Bett, K.E., Crossland, B., Ford, H., Gardner, A.K., Review of the engineering developments in the high pressure polyethylene process 1933-1983, *Proceedings of the Golden Jubilee Conference, Polyethylenes 1933-1983,* Plastics and Rubber Institute, London, **1983**.
2. Soga, K., Shiono, T., Ziegler-Natta Catalysts for Olefin Polymerization, *Prog. Polym. Sci.*, **1997**, 22, 15-03-1546.
3. Severn, J.R., Chadwick, J.C., Duchateau, R., Friederichs, N., „Bound but Not Gagged"-Immobilizing Single-Site α-Olefin Polymerization Catalysts, *Chem. Rev.*, **2005**, 105, 4073-4147.
4. Ziegler, K., Consequences and Development of an Invention, *Angew. Chem.,* **1964**, 76, 545-553.
5. Natta, G., From stereospecific Polymerization to asymmetric autocatalytic Synthesis of Macromolecules, *Angew. Chem.,* **1964**, 76, 553-566.
6. Kaminsky, W. (Ed.), Polyolefins: 50 years after Ziegler and Natta I, Springer, Berlin, **2013**.
7. Böhm, L.L., The Ethylene Polymerization with Ziegler Catalysts: Fifty Years after the Discovery, *Angew. Chem. Int. Ed.*, **2003**, 42, 5010-5030.
8. Mülhaupt, R., Green polymer chemistry and bio-based plastics: Dreams and reality, *Macromol. Chem. Phys.*, **2013**, 214,159-174.
9. Hees, T., Zhong, F., Stürzel, M., Mülhaupt, R., Tailoring Hydrocarbon Polymers and All-Hydrocarbon Composites for Circular Economy, *Macromol. Rapid Commun.*, **2019**, 40, 1800608.

10. Vollmer, I., Jenks, M.J.F., Roelands, M.C.P., White, R.J., van Harmelen, T., de Wild, P., van der Laan, G.P., Meirer, F., Keurentjes, J.T.F., Weckhuysen, B.M., Beyond Mechanical Recycling: Giving New Life to Plastic Waste, *Angew. Chem. Int. Ed.,* **2020**, 59, 15402-15423.

11. D'Amore, M., Thushara, K.S., Piovano, A., Causà, M., Bordiga, S., Groppo, E., Surface Investigation and Morphological Analysis of Structurally Disordered $MgCl_2$ and $MgCl_2/TiCl_4$ Ziegler-Natta Catalysts, *ACS Catal.,* **2016**, 6, 5786-5796.

12. Giunchi, G., Allegra, J., Structural disorder in microcrystalline $MgCl_2$, *J. Appl. Cryst.,* **1984**, 17, 172-178.

13. McKenna, T.F., Soares, J.B.P., Single particle modelling for olefin polymerization on supported catalysts: A review and proposals for future development, *Chem. Eng. Sci.,* **2001**, 56, 3931-3949.

14. Fernandes, J.A., Girard, A-L., Support Designed for Polymerization. In Multimodal Polymers with Supported Catalysts, Albunia, A.R., Prades, F., Jeremic, D., (Eds.); Springer Nature Switzerland, **2019**.

15. Severn, J.R., Recent Developments in Supported Polyolefin Catalysts: A Review. In Multimodal Polymers with Supported Catalysts, Albunia, A.R., Prades, F., Jeremic, D., (Eds.); Springer Nature Switzerland, **2019**.

16. Berger, E., Derroitte, J.-L., Polymerization of olefins, US Patent No. 3,901,863, **1975**.

17. Bart, J.C.J., Roovers, W., Magnesium chloride – ethanol adducts, J. *Mat. Sci.*, **1995**, 30, 2809-2820.

18. Gelus, E., Process for polymerizing olefin with a Ziegler-Natta catalyst, European Patent No. 0,703,246, **2002**.

19. Gnanakumar, E.S., Gowda, R.R., Kunjir, S., Ajithkumar, T.G., Rajamohanan, P.R., Chakraborty, D., Gopinath, C.S., $MgCl_2 \cdot 6CH_3OH$: A Simple Molecular Adduct and Its Influence as a Porous Support for Olefin Polymerization, *ACS Catal.*, **2013**, 3, 303-311.

20. Matsuura, M., Fujita, T., Catalyst component for polymerization of olefins, US Patent No. 4,703,026, **1987**.

21. Pullukat, T.J., Hoff, R.E., Silica-based Ziegler-Natta catalysts: A patent review, *Catal. Rev. Sci. Eng.*, **1999**, 41, 389-428.

22. McKenna, T.F.L., Di Martino, A., Weickert, G., Soares, J.B.P., Particle Growth During the Polymerisation of Olefins on Supported Catalysts, 1 – Nascent Polymer Structures, *Macromol. React. Eng.*, **2010**, 4, 40-64.

23. Simonazzi, T., Cecchin, G., Mazzullo, S., An outlook on progress in polypropylene-based polymer technology, *Prog. Polym. Sci.*, **1991**, 16, 303-329.

24. Ferrero, M.A., Chiovetta, M.G., Catalyst fragmentation during propylene polymerization: Part I. The effects of grain size and structure, *Polym. Eng. Sci.*, **1987**, 27, 1436-1447.

25. Ferrero, M.A., Chiovetta, M.G., Catalyst fragmentation during propylene polymerization: Part II. Microparticle diffusion and reaction effects, *Polym. Eng. Sci.*, **1987**, 27, 1448-1460.

26. Ferrero, M.A., Chiovetta, M.G., Catalyst fragmentation during propylene polymerization: Part III. Bulk polymerization process simulation, *Polym. Eng. Sci.*, **1991**, 31, 886-903.

27. Estenoz, D.A., Chiovetta, M.G., A structural model for the catalytic polymerization of ethylene using chromium catalysts. Part I: description and solution, *Polym. Eng. Sci.*, **1996**, 36, 2208-2240.

28. Horácková, B., Grof, Z., Kosek, J., Dynamics of fragmentation of catalyst carries in catalytic polymerization of olefins, *Chem. Eng. Sci.*, **2007**, 62, 5264-5270.

29. Huo, C., Ren, X.H., Liu, B.P., Yang, Y.R., Rong, S.X., Fractal Approach for Modeling the Morphology Evolution of Olefin Polymerization with Heterogeneous Catalysts, *J. Appl. Polym. Sci.*, **2003**, 90, 1463-1470.

30. Hammawa, H., Wanke, S.E., Gas phase olefin polymerization over supported metallocene/MAO catalysts: influence of support on activity and polydispersity, *Polym. Int.*, **2006**, 55, 426-434.

31. Hammawa, H., Wanke, S.E., Influence of Support Friability and Concentration of α-Olefins on Gas-Phase Ethylene Polymerization over Polymer-Supported Metallocene/Methylaluminoxane Catalysts, *J. Appl. Polym. Sci.*, **2007**, 104, 514-527.

32. Abboud, M., Denifl, P., Reichert, K.H., Fragmentation of Ziegler-Natta catalyst particles during propylene polymerization, Macromol. *Mat. Eng.*, **2005**, 290, 558-564.

33. Seda, L., Zubov, A., Bobak, M., Kosek, J., Kantzas, A., Transport and Reaction Characteristics of Reconstructed Polyolefin Particles, *Macromol. React. Eng.*, **2008**, 2, 496-512.

34. Nooijen, G.A.H., Ziegler/Natta catalysts in particle form ethylene polymerization: The effect of polymerization start-up on catalyst activity and morphology of the produced polymer, *Catal. Today*, **1991**, 11, 35-46

35. Nejad, M.H., Ferrari, P., Pennini, G., Cecchin, G., Ethylene Homo- and Copolymerization over $MgCl_2$-$TiCl_4$ Catalysts: Polymerization Kinetics and Polymer Particle Morphology, *J. Appl. Polym. Sci.*, **2006**, 108, 3388-3402.

36. Knoke, S., Ferrari, D., Tesche, B., Fink, G., Microkinetic Videomicroscopic Analysis of Olefin Polymerization with a Supported Metallocene Catalyst, *Angew. Chem., Int. Ed.*, **2003**, 42, 5090-5093.

37. Pater, J.T.M., Weickert, G., van Swaaij, W.P.M., Polymerization of Liquid Propylene with a Fourth-Generation Ziegler-Natta Catalyst: Influence of Temperature, Hydrogen, Monomer Concentration, and Prepolymerization Method on Powder Morphology, *J. Appl. Polym. Sci.*, **2003**, 87, 1421-1435.

38. Pater, J.T.M., Weickert, G., Loos, J., van Swaaij, W.P.M., High precision prepolymerization of propylene at extremely low reaction rates—kinetics and morphology, *Chem. Eng. Sci.*, **2001**, 56, 4107-4120.

39. Qi, M., Zhang, B., Zhishen, F., Xu, J., Fan, Z., Millimeter-size polyethylene hollow spheres synthesized with $MgCl_2$-supported Ziegler-Natta catalyst, *J. Appl. Polym. Sci.*, **2016**, 133, 43207-43217.

40. Laurence, R.L. and Chiovetta, M.G., In: Reicher, K.H., Geisler, G. (Eds.), Polymer Reaction Engineering, Hasuer-Verlag, München, **1983**, 74-112.

41. Nooijen, G.A.H., On the importance of diffusion of cocatalyst molecules through heterogeneous Ziegler/natta catalysts, *Eur. Polym. J.*, **1994**, 30, 11-15.

42. Weickert, G., Meier, G.B., Pater, J.T.M., Westerterp, K.R., The particle as microreactor: Catalytic propylene polymerizations with supported metallocenes and Ziegler-Natta catalysts, *Chem. Eng. Sci.*, **1999**, 54, 3291-3296.

43. Fink, G., Steinmetz, B., Zechlin, J., Przybyla, C., Tesche, B., Propylene Polymerization with Silica-Supported Metallocene/MAO Catalysts, *Chem. Rev.*, **2000**, 100, 1377-1390.

44. Rönkkö, H-L., Korpela, T., Knuuttila, H., Pakkanen, T.T., Denifl, P., Leinonen, T., Kemell, M., Leskelä, M., Particle growth and fragmentation of solid self-supported Ziegler-Natta-type catalysts in propylene polymerization, *J. Mol. Catal. Chem.*, **2009**, 309, 40-49.

45. Kakugo, M., Sadatoshi, H., Yokoyama, M., Kojima, M., Transmission electron microscopic observation of nascent polypropylene particles using a new staining method, *Macromolecules*, **1989**, 22, 547-551.

46. Kakugo, M., Sadatoshi, H., Sakai, J., Yokoyama, M., Growth of polypropylene particles in heterogeneous Ziegler-Natta polymerization, *Macromolecules*, **1989**, 22, 3172.

47. Noristi, L., Marchetti, E., Baruzzi, G., Sgarzi, P., Investigation on the Particle Growth Mechanism in Propylene Polymerization with $MgCl_2$-Supported Ziegler-Natta Catalysts, *J. Polym. Sci. A*, **1994**, 32, 3048-3059.

48. Egorov, V.M., Ivan'kova, E.M., Kulik, V.B., Lebedev, D.V., Myasnikova, L.P., Marikhin, V.A., Radovanova, E.I., Yagovkina, M.A., Seydewitz, V., Goerlitz, S., Michler, G.H., Nöchel, U., Balta-Calleja, F.J., Features of the Amorphous-Crystalline Structure of UHMWPE, *Polym. Sci.*, **2011**, 53, 75-88.

49. Zheng, X., Smit, M., Chadwick, J.C., Loos, J., Fragmentation Behavior of Silica-Supported Metallocene/MAO Catalyst in the Early Stages of Olefin Polymeriation, *Macromol.*, **2005**, 38, 4673-4678.

50. Zheng, X., Loos, J., Morphology Evolution in the Early Stages of Olefin Polymerization, *Macromol. Symp.*, **2006**, 236, 249-258.

51. Zheng, X., Pimplapure, M.S., Weickert, G., Loos, J., Influence of Copolymerization on Fragmentation Behavior Using Ziegler-Natta Catalysts, *Macromol. Rap. Commun.*, **2006**, 27, 15-20.

52. Silva, F.M., Broyer, K.P., Novat, C., Limea, E.L., Pinto, J.C., McKenna, T.F., Investigation of Catalyst Fragmentation in Gas-Phase Olefin Polymerisation: A Novel Short Stop Reactor, *Macromol. Rapid. Commun.*, **2005**, 26, 1846-1853.

53. Di Martino, A., Broyer, J., Spitz, R., Weickert, G., McKenna, T.F., A Rapid Quenched-Flow Device for the Characterisation of the Nascent Polymerisation of Ethylene under Industrial Conditions, *Macromol. Rap. Commun.*, **2005**, 26, 215-220.

54. Machado, F., Lima, E.L., Pinto, J.C., McKenna, T.F., Evolution of the Initial Stages of Gas-Phase Ethylene Polymerizations with a SiO_2-Supported Ziegler-Natta Catalyst, *Macromol. React. Eng.*, **2009**, 3, 47-57.

55. McKenna, T.F.L., Tioni, E., Ranieri, M.M., Alizadeh, A., Boisson, C., Monteil, V., Catalytic olefin polymerization at short times: Studies using specially adapted reactors, *Can. J. Chem. Eng.*, **2013**, 91, 669-686.

56. Jacobsen, C., X-Ray Tomography in X-ray Microscopy; Cambridge University Press, Cambridge, **2020**, 321-349.

57. Beale, A.M., Jacques, S.D.M., Weckhuysen, B.M., Chemical imaging of catalytic solid with synchrotron radiation, *Chem. Soc. Rev.*, **2010**, 39, 4656-4672.

58. Gonzalez-Jimenez, I.D., Cats, K., Davidian, T., Ruitenbeek, M., Meirer, F., Liu, Y., Nelson, J., Andrews, J.C., Pianetta, P., de Groot, F.M.F., Weckhuysen, B.M., Hard X-ray Nanotomography of Catalytic Solids at Work, *Angew. Chem. Int. Ed.*, **2012**, 51, 11986-11990.

59. Cats, K.H., Gonzalez-Jimenez, I.D., Liu, Y., Nelson, J., Van Campen, D., Meirer, F., van der Eerden, A.M.J., De Groot, F.M.F., Andrews, J.C., Weckhuysen, B.M., X-ray nanoscopy of cobalt Fischer-Tropsch catalysts at work, *ChemComm*, **2013**, 49, 4622-4624.

60. Beale, A.M., Jacques, S.D.M., Gibson, E.K., Di Michiel, M., Progress towards five-dimensional diffraction imaging of functional materials under process conditions, *Coord. Chem. Rev.*, **2014**, 277, 208-223.

61. Price, S.W.T., Ignatyev, K., Geraki, K., Basham, M., Filik, J., Vo, N.T., Witte, P.T., Beale, A.M., Mosselmans, J.F.W., Chemical imaging of single catalyst particles with scanning μ-XANES-CT and μ-XRF-CT, Phys. *Chem. Chem. Phys.*, **2015**, 17,521-529.

62. Cats, K.H., Andrews, J.C., Stéphan, O., March, K., Karunakaran, C., Meirer, F., de Groot, F.M.F., Weckhuysen, B.M., Active phase distribution changes within a catalyst particle during Fischer-Tropsch synthesis as revealed by multi-scale microscopy, *Catal. Sci. Tech.*, **2016**, 6, 4438-4449.

63. Price, S.W.T., Martin, D.J., Parsons, A.D., Sławiński, W.A., Vamvakeros, A., Keylock, S.J., Beale, A.M., Mosselmans, J.F.W., Chemical Imaging of Fischer-Tropsch catalysts under operating conditions, *Sci. Adv.*, **2017**, 3, e1602838.

64. Meirer, F., Weckhuysen, B.M., Spatial and temporal exploration of heterogeneous catalysts with synchrotron radiation, *Nat. Rev. Mater.*, **2018**, 3, 324-340.

65. Vamvakeros, A., Jacques, S.D.M., Di Michiel, M., Matras, D., Middelkoop, V., Ismagilov, I.Z., Matus, E.V., Kuznetsov, V.V., Drnec, J., Senecal, P., Beale, A.M., 5D operando tomographic diffraction imaging of a catalyst bed, *Nat. Commun.*, **2018**, 9, 4751.

66. Vamvakeros, A, Matras, D., Jacques, S.D.M., di Michiel, M., Price, S.W.T., Senecal, P., Aran, M.A., Middelkoop, V., Stenning, G.B.G., Mosslemans, J.F.W., Ismagilov, I.Z., Beale, A.M., Real-time multi-length scale chemical tomography of fixed bed reactors during the oxidative coupling of methane reaction, *J. Catal.*, **2020**, 386, 39-52.

67. Sheppard, T.L., Price, S.W.T., Benzi, F., Baier, S., Klumpp, M., Dittmeyer, R., Schwieger, W., Grunwaldt, J.-D., In Situ Multimodal 3D Chemical Imaging of a Hierarchically Structured Core@Shell Catalyst, *J. Am. Chem. Soc.*, **2017**, 139. 7855-7863.

68. Fam, Y., Sheppard, T.L., Diaz, A., Scherer, T., Holler, M., Wang, W., Wang, D., Brenner, P., Wittstock, A., Grunwaldt, J-D., Correlative Multiscale 3D Imaging of a Hierarchical Nanoporous Gold Catalyst by Electron, Ion and X-ray Nanotomography, *ChemCatChem*, **2018**, 10, 2858-2867.

69. Becher, J., Ferreira Sanchez, D, Doronkin, D.E., Zengel, D., Motta Meira, D, Pascarelli, S., Grunwaldt, J-D., Sheppardm T.L., Chemical gradients in automotive Cu-SSZ-13 catalysts for NOx removal revealed by operando X-ray spectrotomography. *Nat. Catal.*, **2021**, 4, 46-53.

70. Fam, Y., Sheppard, T.L., Becher, J., Scherhaufer, D., Lambach, H., Kulkarni, S., Keller, T.F., Wittstock, A., Wittwer, F., Seyrich, M., Brueckner, D., Kahnt, M., Yang, X., Schropp, A., Stierle, A., Schroer, C.G., Grunwaldt, J.-D., A versatile nanoreactor for complementary in situ X-ray and electron microscopy studies in catalysis and materials science, *J. Synchr. Rad.*, **2019**, 26, 1769-1781.

71. da Silva, J.C., Mader, K., Holler, M., Haberthür, D., Diaz, A., Guizar-Sicairos, M., Chen, W-C., Shu, Y., Raabe, J., Menzel, A., van Bokhoven, J.A., Assessment of the 3 D Pore Structure and Individual Components of the Preshaped Catalyst Bodies by X-ray Imaging, *ChemCatChem*, **2015**, 7, 413-416.

72. Ihli, J., Sanchez, D.F., Jacob, R.R., Cuartero, V., Mathon, O., Krumeich, F., Borca, C., Huthwelker, T., Cheng, W-C., Shu, Y., Pascarelli, S., Grolimund, D., Menzel, A., van Bokhoven, J.A., Localization and Speciation of Iron Impurities within a Fluid Catalytic Cracking Catalyst, Angew. *Chem. Int. Ed.*, **2017**, 56, 14031-14035.

73. Ihli, J., Jacob, R.R., Holler, M., Guizar-Sicairos, M., Diaz, A., Da Silva, J.C., Ferreira Sanchez, D., Krumeich, F., Grolimund, D., Taddei, M., Cheng, W.-C., Shu, Y., Menzel, A., Van Bokhoven, J.A., A three-dimensional view of structural changes caused by deactivation of fluid catalytic cracking catalysts, *Nat. Commun.*, **2017**, 8, 809.

74. Ihli, J., Diaz, A., Shu, Y., Guizar-Sicairos, M., Holler, M., Wakonig, K., Odstrcil, M., Li, T., Krumeich, F., Müller, E., Cheng, W-C., van Bokhoven, J.A., Menzel, A., Resonant Ptychographic Tomography Facilitates Three-Dimensional Quantitative Colocalization of Catalyst Components and Chemical Elements, *J. Phys. Chem. C.*, **2018**, 122, 22920-22929.

75. Bare, S.R., Charochak, M.E., Kelly, S.D., Lai, B., Wang, J., Chen-Wiegart, YK., Characterization of a Fluidized Catalytic Cracking Catalyst on Ensemble and Individual Particle Level by X-ray Micro- and Nanotomography, Micro-X-ray Fluorescence, and micro-X-ray Diffraction, *ChemCatChem*, **2014**, 6, 1427-1437.

76. Meirer, F., Morris, D.T., Kalirai, S., Yijin, L., Andrews, J.C., Weckhuysen, B.M., Mapping Metals Incorporation of a Whole Single Catalyst Particle Using Element Specific X-ray Nanotomography, *J. Am. Chem. Soc.*, **2015**, 137, 102-105.

77. Meirer, F., Kalirai, S., Morris, D., Soparawalla, S., Yijin, L., Mesu, G., Andrews, J.C., Weckhuysen, B.M., Life and death of a single catalytic cracking particle, *Sci. Adv.*, **2015**, 1, e1400199.

78. Meirer, F., Kalirai, S., Weker, J.N., Liu, Y., Andrews, J.C., Weckhuysen, B.M., Agglutination of single catalyst particles during fluid catalytic cracking as observed by X-ray nanotomography, *ChemComm*, **2015**, 51, 8097-8100.

79. Kalirai, S., Boesenberg, U., Falkenberg, G., Meirer, F., Weckhuysen B.M., X-ray Fluorescence Tomography of Aged Fluid-Catalytic-Cracking Catalyst Particles Reveals Insight into Metal Deposition Processes, *ChemCatChem*, **2015**, 7, 3674-3682.

80. Kalirai, S., Paalanen, P.P. Wang, J., Meirer, F., Weckhuysen, B.M., Visualizing Dealumination of a Single Zeolite Domain in a Real-Life Catalytic Cracking Particle, *Angew. Chem., Int. Ed.*, **2016**, 55, 11134-11138.

81. Wise, A.M., Weker, J.N., Kalirai, S., Farmand, M., Shapiro, D.A., Meirer, F., Weckhuysen, B.M., Nanoscale Chemical Imaging of an Individual Catalyst Particle with Soft X-ray Ptychography, *ACS Catal.*, **2016**, 2178-2181.

82. Gambino, M. Veselý, M., Filez, M., Oord, R., Ferreira Sanchez, D., Grolimund, D., Nesterenko, N., Minoux, D., Maquet, M., Meirer, F., Weckhuysen, B.M., Nickel Poisoning of a Cracking Catalyst Unravelled by Single-Particle X-ray Fluorescence-Diffraction-Absorption Tomography, Angew. *Chem., Int. Ed.*, **2020**, 59, 3922-3927.

83. Veselý, M., Valadian, R., Lohse, L.M., Toepperwien, M., Spiers, K., Garrevoet, J., Vogt, E.T.C., Salditt, T., Weckhuysen, B.M., Meirer, F., 3-D X-ray Nanotomography Reveals Different Carbon Deposition Mechanisms in a Single Catalyst Particle, *ChemCatChem.*, **2020**, 10.1002/cctc.202100276.

84. Conner, W.C., Webb, S.W., Spanne, P., Jones, K.W., Use of X-ray microscopy and synchrotron microtomography to characterize polyethylene polymerization particles, *Macromolecules*, **1990**, 23, 4742-4747.

85. Ferrero, M.A., Sommer, R., Spanne, P., Jones, K.W., Conner, W.C., X-ray microtomography studies of nascent polyolefin particles polymerized over magnesium chloride-supported catalysts, *J. Polym. Sci. A*, **1993**, 31, 2507-2512.

86. Jones, K.W., Spanne, P., Lindquist, W.B., Conner, W.C., Ferrero, M., Determination of polymerization particle morphology using synchrotron computed microtomography, *Nucl. Instr. Meth. Phys. Res.*, **1992**, 68, 105-110.

87. Boden, S., Bieberle, M., Weickert, G., Hampel, U., Three-dimensional analysis of macroporosity distributions in polyolefin particles using X-ray microtomography, *Powder Technol.*, **2008**, 188, 81-88.

88. Meisterová, L., Zubov, A., Smolná, K., Štěpánek, F., Kosek, X-ray Tomography Imaging of Porous Polyolefin Particles in an Electron Microscope, *J., Macromol. React. Eng.*, **2013**, 7, 277-280.

89. Bossers, K.W., Valadian, R., Zanoni, S., Smeets, R.., Friederichs, N., Garrevoet, J., Meirer, F., Weckhuysen, B.M., Correlated X-ray Ptychography and Fluorescence Nano-Tomography on the Fragmentation Behavior of an Individual Catalyst Particle during the Early Stages of Olefin Polymerization, *J. Am. Chem. Soc.*, **2020**, 142, 3691-3695.

90. Friederichs, N.H., Gerlofmsa, R., WO Patent 2009112254A1, **2009**.

91. Lafleur, S., Berthoud, R., Ensinck, R., Cordier, A., De Cremer, G., Philippaerts, A., Bastiaansen, K., Margossian, T., Severn, J.R., Tailored bimodal ultra-high molecular weight polyethylene particles, *J. Polym. Sci. A.*, **2018**, 56, 1645-1656.

92. Solé, V.A., Papillon, E., Cotte, M., Walter, Ph., Susini, J., A multiplatform code for the analysis of energy-dispersive X-ray fluorescence spectra, *Spectrochim. Acta Part B*, **2007**, 62, 63-68.

93. Pfeiffer, F. X-ray ptychography, *Nat. Photonics*, **2018**, 12, 9–17.

94. Johansson, U., Vogt, U., Mikkelsen, A., NanoMAX: A hard x-ray nanoprobe beamline at MAX IV, *Proc. SPIE*, **2013**, 8851, 1-10.

95. Raimondi, P., ESRF-EBS: The Extremely Brilliant Source Project, *Synchrotron Radiat. News*, **2016**, 29, 8-15.

96. Schroer, C.G., Agapov, I., Brefeld, W., Brinkmann, R., Chae, Y-C., Chao, H-C., Eriksson, M., Keil, J., Gavaldà, N., Röhlsberger, R., Seeck, O.H., Sprung, M., Tischer, M., Wanzenberg, R., Weckter, E., PETRA IV: the ultralow-emittance source project at DESY, *J. Synchrotron Radiat.*, **2018**, 25, 1277-1290.

97. Lui, Y., Meirer, F., Williams, P.A., Wang, J., Andrews, J.C., Pianetta, P., TXM-Wizard : a program for advanced data collection and evaluation in full-field transmission X-ray microscopy, *J. Synchrotron Radiat.*, **2012**, 19, 281-287.

98. van Aarle, W., Palenstijn, W.J., De Beenhouwer, J., Altantzis, T., Bals, S., Batenburg, K.J., Sijbers, J., The ASTRA Toolbox: A platform for advanced algorithm development in electron tomography, *Ultramicroscopy*, **2015**, 157, 35-47.

99. van Aarle, W., Palenstijn, W.J., Cant, J., Janssens, E., Bleichrodt, F., Dabravolski, A., De Beenhouwer, J., Batenburg, K.J., Sijber, J., Fast and Flexible X-ray Tomography Using the ASTRA Toolbox, *Optics Express*, **2016**, 24, 25129-25147.

100. van Heel, M., Schatz, M., Fourier shell correlation threshold criteria, *J. Struct. Biol.*, **2005**, 151, 250-262.

101. Nieuwenhuizen, R.P.J., Lidke, K.A., Bates, M., Puig, D.L., Grünwald, D., Stallinga, S., Rieger, B., Measuring image resolution in optical nanoscopy, *Nat. Methods*, **2013**, 10, 557-562

102. Beucher, S. and Meyer, F., The Morphological Approach to Segmentation: The Watershed Transformation. In Mathematical Morphology in Image Processing, Dougherty, E. (Ed.); Marcel Dekker Inc., New York, **1993**.

103. Lehmann, G., Legland, D., Efficient N-Dimensional surface estimation using Crofton formula and run-length encoding, *Insight J.,* **2012**, accessed online 01-12-2021: http://hdl.handle.net/10380/3342.

104. Shoemake, K., Euler Angle Conversion In Graphics Gems IV. Heckbert, P.S. (Ed.), Morgan Kaufmann, San Francisco, **1994**.

105. David, A. and Vassilvitskii, S., K-means++: The Advantages of Careful Seeding, *SODA '07: Proceedings of the 18th Annual ACM-SIAM Symposium on Discrete Algorithms,* **2007**, 1027-1035.

106. Simonazzi, T., Cecchin, G., Mazzullo, S., An outlook on progress in polypropylene-based polymer technology, *Prog. Polym. Sci.,* **1991**, 16, 303-329.

107. Diaz, A., Trtik, P., Guizar-Sicairos, M., Menzel, A., Thibault, P., Bunk, O., Quantitative x-ray phase nanotomography, *Phys. Rev. B*, **2012**, 85, 020104-1-3.

108. Liu, D., Yu, J., Otsu Method and K-means, *Proceedings of the Ninth International Conference on Hybrid Intelligent Systems*, **2009**, pp. 344-349.

109. Bossers, K.W., Valadian, R., J. Garrevoet, van Malderen, S., Chan, R., Friederichs, N., Severn, J., Wilbers, A., Zanoni, S., Jongkind, M.K., Weckhuysen, B.M., Meirer, F., *JACS Au,* **2021**, DOI: 10.1021/jacsau.1c00130.

Chapter 4. A Ziegler-type Spherical Cap Model Reveals Early Stage Ethylene Polymerization Growth Versus Catalyst Fragmentation Relationships

Polyolefin catalysts are characterized by their hierarchically complex nature, which complicates studies on the interplay between the catalyst and formed polymer phases. Here, the missing link in the morphology gap between planar model systems and industrially relevant spherical catalyst particles is introduced through the use of a spherical cap Ziegler-type catalyst model system for the polymerization of ethylene. Additionally, a moisture stable LaOCl framework with enhanced imaging contrast has been synthesized to substitute the highly hygroscopic and conventionally used $MgCl_2$ framework to support the $TiCl_4$ pre-active site. As a function of polymerization time, a change in the fragmentation behavior of the LaOCl framework was observed, which is linked to evolution of the estimated polyethylene volume and fraction of crystalline polyethylene spectral vibrational components. The combination of the spherical cap model system and the used advanced micro-spectroscopy toolbox, opens the route for high-throughput screening of catalyst functions with industrially relevant morphologies on the nano-scale.

4.1 Introduction

The Ziegler-type (e.g. Ziegler and Ziegler-Natta) catalysts discovered in the 1950's by Karl Ziegler and Giulio Natta are the dominant α-olefin polymerization catalysts for the production of different polyethylene grades, such as high-density polyethylene (HDPE) and isotactic polypropylene (i-PP) [1]. The current generation Ziegler-type catalysts are based on the chemisorption of a $TiCl_4$ pre-active site species on an activated $MgCl_2$ support matrix, followed by the reduction and alkylation with a trialkylaluminium co-catalyst [2]. In the case of propylene polymerization, additional Lewis base molecules are added either during the synthesis, which are called internal donors, or the polymerization reaction, which are called external donors, to provide local stereoregular control for the production of highly isotactic polypropylene [3].

Ziegler-type catalysts are both hierarchically complex and highly sensitive towards polar compounds, such as O_2 and H_2O, that complicate catalyst structure, polymerization activity and polymer properties studies [4-5]. One strategy to bypass the hierarchically complex nature of such a catalyst is through the design of simplified planar model systems [6]. These model systems have the additional advantage of being compatible with surface-sensitive spectroscopy and microscopy techniques, such as atomic force microscopy (AFM) and X-ray photoelectron spectroscopy (XPS) [7]. Somorjai and his group pioneered the field of using surface science techniques on planar model systems of Ziegler-type catalysts [8-12]. In one of their early works, they found experimental evidence for the $TiCl_4$ activation mechanism as proposed theoretically by Arlman and Cossee using an ultra-thin $MgCl_2$ film on a gold substrate [12,13]. Siokou and Ntais switched towards the use of a facile spin-coating technique to produce a Ziegler-type planar model system based on tetrahydrofuran (THF) adducts with $MgCl_2$ and $TiCl_4$, which is in close analogue to the chemical activation routes of $MgCl_2$ used industrially [14-18]. The effect of the type of internal donor on the stabilization of the unsaturated (110) and (104) lattices for a Ziegler-Natta planar model system was studied by the group of Niemantsverdriet by growing well-defined crystals on a $SiO_2/Si(100)$ substrate using a combined spin-coated and solvent vapor annealing approach [19-22].

For these conventional $MgCl_2$ based Ziegler-type catalyst model systems however, technical and experimental limitations are imposed due to the high moisture sensitivity of $MgCl_2$, which will lead to morphology changes under ambient conditions. Recently, Piovano et al., reported a chlorinated δ-Al_2O_3 support matrix instead of $MgCl_2$ to facilitate in-situ ethylene oligomerization at Al^{3+} sites for the production of a linear low-density polyethylene grade (LLDPE) [23,24]. The use of such non-conventional support matrixes for Ziegler-type catalysis inspired us to design a model system for ethylene polymerization using a LaOCl support matrix due to two reasons. First of all, LaOCl provides strong imaging contrast due to the high atomic weight of the lanthanide and, secondly, exceptional moisture stability to facilitate ambient measuring conditions for the selected advanced micro-spectroscopy toolbox. Whereas LaOCl has been reported as a promising catalyst material for the selective alkane activation, such as the conversion of methane to methyl chloride and ethane to vinyl chloride as well as the destruction of chlorinated hydrocarbons, it has not been reported

yet to the best of our knowledge in the field of α-olefin polymerization [25-31]. Additionally, to bridge the gap between planar model systems and the industrially relevant highly spherical catalyst particles, a spherical cap model system is introduced here to the field of catalytic α-olefin polymerization. This LaOCl-based spherical cap model system will be studied with a versatile micro-spectroscopy toolbox consisting of photo-induced force microscopy (PiFM), which provides infrared (IR) nano-spectroscopy with the spatial resolution and additional topological information of atomic force microscopy (AFM) [32], Raman microscopy, focused ion beam scanning electron microscopy energy dispersive X-ray spectroscopy (FIB-SEM-EDX). X-ray photoelectron spectroscopy (XPS) and time-of-flight secondary ion mass spectrometry (ToF-SIMS). By doing so, we were able to follow the interplay between the formation of polyethylene and fragmentation of the catalyst support matrix with high imaging contrast and under ambient ex-situ measuring conditions at different ethylene polymerization times. Both fundamental fragmentation models, namely the shrinking core and continuous bisection, were occurring simultaneously at early polymerization times, and upon sufficient fragmentation of the LaOCl framework to overcome initial mass transfer limitations, switched towards a dominating continuous bisection behavior.

4.2 Experimental

4.2.1 Synthesis of the Spherical Cap Ziegler Model Catalyst

B-doped Si(100) wafers with a thickness of 525 μm and resistivity of 0.005 Ohm*cm were purchased from Siegert Wafer. After cutting the wafers in suitable sizes (~5x5 mm^2 in size) with a diamond knife, a procedure for the grafting of the self-assembled monolayer and subsequent photo-patterning was followed as reported in literature [33]. First, the wafer pieces were cleaned with a 1:1:1 volumetric ratio of demineralized water, ethanol and acetone using an ultrasonicator for 15 min to remove surface contaminants. This step was then repeated in demineralized water for again 15 min. Then, the wafer pieces were placed in a beaker glass with a 5:1:1 volumetric ratio of demineralized water, ammonium hydroxide (28-32 wt% in H_2O, Sigma-Aldrich) and hydrogen peroxide (20 wt%, Sigma-Aldrich) and placed on a hotplate set at 65 $^\circ$C for 30 min. In this step, the native oxide surface layer on the Si(100) substrate is partially etched away and converted into surface hydroxyl groups. Afterwards, the wafers were first placed in a beaker of room-temperature demineralized water to quench this etching step and then heated to around 95 $^\circ$C in demineralized water to remove any surface absorbed ammonium species for an additional 30 min. The wafer pieces are blown-dry with a N_2 line and then placed in an oven at 120 $^\circ$C for 1 h. This is followed by the transfer of the wafer pieces to a glovebox operating at <1 ppm O_2 and H_2O, where the wafer pieces were placed in a solution of 10 mM octadecyltrichlorosilane (99%, Sigma-Aldrich) in anhydrous toluene (99.9% stored over 4Å molecular sieves, Sigma-Aldrich) for 10 min at room temperature. After the successful grafting of the self-assembled monolayer to the Si(100) surface hydroxyl groups, the wafer pieces were washed with anhydrous toluene and taken out of the glovebox. There they were blow-dried again with a

N$_2$ flow and placed at 120 °C for 5 min to anneal the ODTS layer. The wafer pieces were then placed in a UV/Ozone cleaner from Osilla Ltd with a custom-made 20x20 mm^2 copper grid photomask with a 600 mesh size and circular holes from Agar scientific placed on top of them. A piece of 5 mm thick quartz glass was finally placed on top of the photomask and the UV/Ozone treatment is performed for 30 min.

Meanwhile, a 20 mM lanthanum chloride heptahydrate (99.9%, Sigma-Aldrich) solution in ethanol (99.9%, Sigma-Aldrich) was prepared for the spin-coating step. With the wafers patterned, they were transferred to a spin-coater from Ossila Ltd that uses a recessed spin-coating chuck to hold the wafers in place. Spin-coating was performed at 3000 rpm for 30 s with an injection volume of 10 μL on the wafer surface and a loading time of 5 s. After the spin-coating, the wafer pieces were transferred into a quartz boat that was subsequently placed inside a tube oven under dry N$_2$ flow of 200 mL/min. The heat program consisted of three steps. First with a ramp of 2 °C/min to a temperature of 250 °C and dwell time of 4 h, followed by heating up to 600 °C with the same ramp and staying for an additional 4 h. Finally, the oven was cooled down 200 °C where it remained until the wafers were brought at this temperature into the glovebox.

The grafting of the TiCl$_4$ pre-active site onto the LaOCl spherical cap system has to be performed under stringent controls (<1 ppm O$_2$/H$_2$O) to prevent decomposition of TiCl$_4$ and was done inside a glovebox. In a 20 mL glass vial, a 30 vol% solution of TiCl$_4$ (99.9%, Sigma-Aldrich) in anhydrous heptane (99.9% stored over 4Å molecular sieves, Sigma-Aldrich) was prepared to which the wafer pieces were added. The vial was then closed, wrapped in aluminium foil for better heat transfer, and put on a hotplate at 95 °C for 1 h. Afterwards, the vial was cooled down to room temperature naturally, after which the wafer pieces were transferred sequentially through three glass vials filled with pure heptane to remove excess TiCl$_4$. In the last of the three washing vials, the wafers were kept for 30 min until they were transferred to a final fourth vial filled with heptane where they were kept for storage until commencing ethylene polymerization.

4.2.2 Slurry-Phase Ethylene Polymerization

A custom-made low-pressure polymerization set-up was built to run inside the glovebox. This set-up allows us to either evacuate a cylindrical glass reactor with an internal volume of roughly 100 mL using an external vacuum pump or feed ethylene (4.5N purity, Linde) at a pressure of 2 bar. The reactor was filled with a 10 mL anhydrous heptane solution containing 1 mg/mL triethylaluminium (98%, Sigma-Aldrich). The reactor was then slowly evacuated without stirring to remove the N$_2$ atmosphere followed by feeding the ethylene at 2 bar until the solution became saturated. Meanwhile, the wafer pieces that now have the TiCl$_4$ pre-active site grafted on the LaOCl surface were still stored in heptane. Two wafer pieces per polymerization time were then taken out and dried for 1 minute under a N$_2$ atmosphere. After saturating the solvent with ethylene, the reactor was slowly evacuated to atmospheric pressure, opened and quickly the two wafer pieces were placed inside the reactor followed by closing the reactor again. The reactor was then repressurized with ethylene in the absence of stirring and at this moment the timing of the polymerization

reaction was commenced. The steps from placing the wafers in the ethylene saturated solution to closing the reactor and repressurizing typically took about 10 s. Quenching of the reaction was performed by quickly evacuating the reactor after the desired time, filling the reactor with N_2, opening the reactor and place the wafer pieces in a separate vial containing several mL of pure heptane. These vials were then taken out of the glovebox and placed inside an ultrasonicator for 90 s followed by drying under a mild N_2 flow. The ultrasonicator step was found to be necessary to remove what would otherwise form a thick film originating from the hydrolysis of the co-catalyst after exposure to air. Afterwards, the polymerized wafers were dried overnight in a 60 °C oven and stored in a container labelled with the polymerization time.

4.2.3 Focused Ion Beam – Scanning Electron Microscopy

Focused ion beam scanning electron microscopy (FIB-SEM) images were collected on a FEI Helios NanoLab G3 UC scanning electron microscopy. The wafers of interest were placed on aluminium SEM stubs using a conductive carbon tape on the backside of the wafer. For SEM images, the accelerating voltage was set to 2 kV and the current to 0.10 nA and the backscattered electron images were collected with a through-lens-detector to take full advantage of the strong *Z*-contrast between LaOCl, the formed polyethylene and the Si(100) background. EDX elemental mapping was performed with a Silicon Drift Detector (SDD) X-MAX from Oxford Instruments. Prior to the milling of the region of interest with the focused ion beam a 3 μm thick Pt layer was deposited on top of the region of interest. The focus ion beam accelerating voltage was set at 30 kV and the current for both milling and cleaning at 0.43 nA. The milling was performed to create a trench perpendicularly to the surface and roughly at the center of a spherical cap. After the milling step, the cross-section was cleaned with Ga ions before collecting the backscattered electron images.

4.2.4 Photo-induced Force Microscopy

Photo-induced force microscopy (PiFM) micrographs, intensity maps and spectra were collected on a Molecular Vista Vistascope microscope equipped with a block engineering tunable quantum cascade laser (QCL), having a 1965-785 cm^{-1} range. Gold coated tips (F = 100-130 N/m, resonance frequency > 320 kHz) were used to obtain micrographs of the patterns of interest in semi-contact mode. Then, either the same ROI was scanned subsequently while changing the laser wavelength to 1471, 1461 and 1600 cm^{-1} to collect individual intensity maps, or the tip was brought to a position of choice and a full spectrum was recorded with 1 cm^{-1} resolution, 200 averages. As the signature PE peaks were found to decrease with an increasing number of averages at higher laser powers, this was prevented by setting the laser power to 2 V in all modes. The obtained height micrographs were post-processed in Gwyddion [34]. A plane background was subtracted over the Si-substrate background, and the data were treated with a line-by-line correction using a "Trimmed mean of differences" function using a Trim faction of 0.5. The IR intensity maps were only processed by a line-by-line correction, and the maps were binned using a 2 pixel mean filter. To obtain a representative "average" PiF spectrum per PE time, 9 different

patterns per time were partially mapped (~10 − 20 lines) and 2 point spectra were recorded on both the thick, spherical polyethylene regions and the highly intertwined polyethylene fiber network. These 18 spectra per time were pre-processed by applying a Whittaker baseline correction and normalization with non-negativity constraints using the PLS Toolbox of Eigenvector written in MatLab (Mathworks). Then, the individual spectra were fitted with 4 components obtained from a MCR analysis as shown in Figure 4.1.
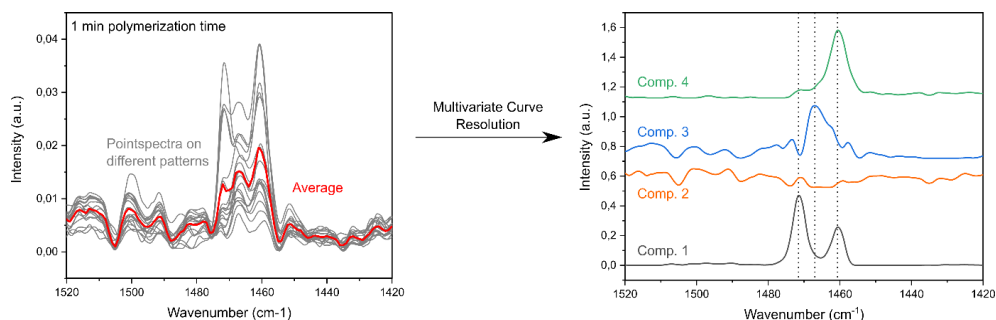

Figure 4.1 Point spectra recorded on 9 different LaOCl spherical caps after 1 min ethylene polymerization and the 4 different spectral components used in a multivariate curve resolution (MCR) analysis. The different spectral components represent the crystalline polyethylene phases (spectral components 1 and 4) as they consist purely of the -CH$_2$- bending vibrations of crystalline polyethylene in the orthorhombic phase, whereas spectral component 3 consists of a broad amorphous polyethylene -CH$_2$- bending vibration. Spectral component 2 represents interference caused by water vapor present in the system and hence on the LaOCl surface and the PiFM scanning tip.

The resulting scores, representing the contribution of different components per spectra, were then used to determine the percentage of crystalline (MCR) component present in all individual spectra per polymerization time. Using the scores of these extracted spectral components of MCR, the fraction of the crystalline components (1461 cm^{-1} and 1471 cm^{-1}) to that of the single amorphous component (1463 cm^{-1}) was calculated as shown in Eq. 4.1.

$$\text{Fraction of crystalline components} = \frac{\sum \text{crystalline polyethylene component (\#1+\#4) scores}}{\sum \text{all polyethylene component (\#1+\#3+\#4) scores}} \times 100\%$$ Eq. 4.1

4.2.5 Atomic Force Microscopy

Atomic force microscopy (AFM) was recorded on a Bruker MultiMode 8 with J Scanner in non-contact ScanAsyst HR mode, using silicon nitride ScanAsyst-HR tips (F = 0.4 N/m, frequency = 130 kHz). Per polymerization time, 6 different patterned catalysts were measured (Figure 4.12). The data was post-treated as explained before for the PiFM maps. Furthermore, x and y cross-sections were then plotted through the middle-point of the catalyst caps, and the resulting profiles were fitted using a power function on the exposed

uncovered catalyst cap (Figure 4.13). Then, the height and cap-base diameter, or chord length, were measured to obtain the catalyst volume, which could be subtracted of the total measured volume (obtained using the Gwyddion "Statistics" function) to yield the net polymer volume. More information can be found in sub-Chapter 4.3.4.

4.2.6 Raman Microscopy

Raman spectra were collected with the XploRATM PLUS Raman Spectrometer – Confocal Raman Microscope from Horiba Scientific At all times a 532nm excitation laser and a 100x objective with 0.9 NA was used together with a 1200 gr/mm grating and slit and hole sizes of respectively 200 µm and 500 µm. Knowing the NA of the objective and the wavelength of the laser, it is possible to calculate the diffraction limited lateral spatial resolution according to Eq. 4.2, which would be ~360 nm for a λ =532 nm and NA =0.9 [35].

$$\text{Spatial resolution} = \frac{0.61 \times \lambda}{NA} \qquad \text{Eq. 4.2}$$

To collect high resolution maps, a laser power of 25% maximum (15.55 mW) was used with a 50 ms dwell time, 1 accumulation per spectrum and a step size of 0.25 µm and a scan range of 2700-3100 cm^{-1}. To collect full-range, single point spectra, a laser power of 10% maximum (6.81 mW) was used with a 500 ms dwell time and 30 accumulations. Background corrections were performed within the Fityk software. No smoothing function was applied on the Raman spectra.

4.2.7 Time-of-Flight Secondary Ion Mass Spectrometry

Time-of-flight secondary ion mass spectrometry measurements (ToF-SIMS) were carried out with a M6 Hybrid SIMS (IONTOF GmbH, Münster, Germany). The machine is equipped with a 30 keV Bi nanoprobe primary ion gun, low energetic (2 kV) Cs and EI gas sputter guns as well as a 20 keV Arx/(O2)x gas cluster source. The samples were mounted with a double-sided copper tape on an electrical insulating glass slide.

Depth profiles were carried out with 30 keV Bi^{3+} primary ions in non-bunched mode (aperture 200 µm) in delayed extraction mode with topography option at negative polarity. The Bi^{3+} primary ion current was about 0.18 pA at 100 µs cycle time. The low energetic electron flood gun was used for charge compensation. Sputtering was done with a 10 keV Ar2000+ sputter beam (I $\simeq$ 8 nA). Areas of 175 x 175 µm were probed in non-interlaced mode, with 512 x 512 pixels. The raster size of the sputter gun was 300 x 300 µm² centred to the analysis area. For data evaluation Surface Lab 7.2 (ION-TOF GmbH, Münster, Germany) was used. Mass calibration was carried out with the signals C^-, OH^-, C_2^-, Cl^-, $C_3H_5^-$, $C_7H_{13}^-$, and $LaOCl^-$. calibration and comparison to literature HDPE ToF-SIMS spectra was performed with respect to the work by Kern *et al.* [36]

The mass spectra obtained from the imaged region are the convolution of the spherical caps and the Si(100) substrate. Therefore, to study if the charged mass fragments (called

secondary ions) originating from the spherical caps, a region of interest (ROI) was drawn inside the analysis software on top of the spherical caps. The resulting mass spectra of both this spherical cap ROI and the inverse ROI that represents the Si(100) substrate, are given in Figure 4.2a as well as the insets that show the drawn ROIs. Additionally, the first few sputter seconds were typically disregarded from the analysis, as shown in Figure 4.2b, due to the presence of adsorbed carbon species from the air that are removed in these first few sputter cycles. The cut-off was based on reaching a stable intensity profile for the *m/z* species.
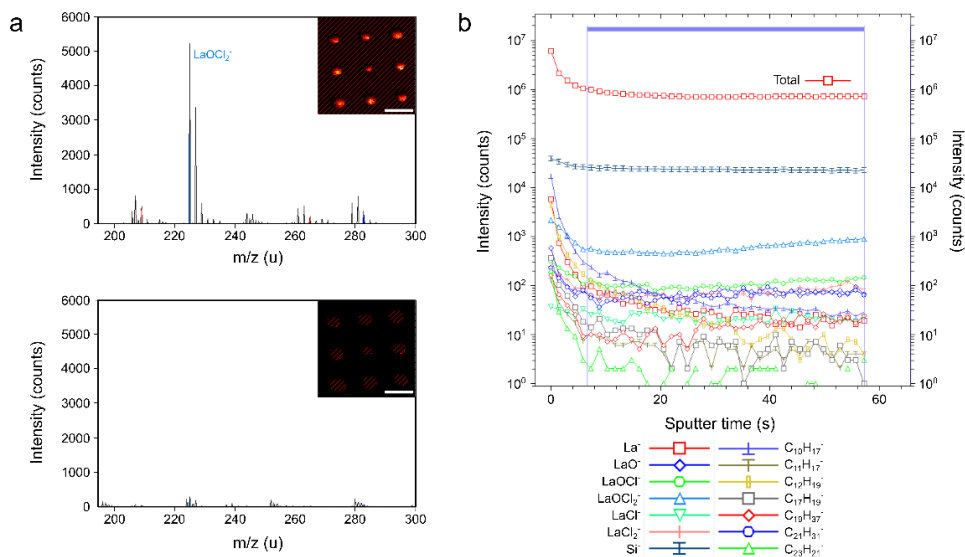

Figure 4.2 Time-of-Flight Secondary Ion Mass Spectrometry (ToF-SIMS) data and sputter profile explaining the chosen ROIs. (a) Mass spectra of the spherical cap model catalyst after 20 min polymerization time (inset map) recorded with ToF-SIMS. A ROI was picked selecting only the spherical caps, removing non-relevant mass fragments from the analysis. The ROI (top spectrum, all unmarked area in the inset map) contains the majority of the catalyst (LaOCl$_2^-$ indicated) and PE (repeating unit) compared to the substrate (bottom spectrum). (b) To avoid the interference of surface adsorbed species from the analysis, a z-ROI was chosen after the initial exponential increase/decrease of the organic fragments passed.

4.2.8 X-ray Photoelectron Spectroscopy

X-ray photoelectron spectroscopy (XPS) measurements were performed on a PHI5000 Versa Probe II system from Physical Electronics. The X-ray source was monochromatic Al Kα radiation (1486.6 eV). The pass energy for detailed spectra in the analyzer was 23.50 eV. Data evaluation was performed with CasaXPS (version 2.3.22, Casa Software Ltd.). Energy calibration was performed based on the signal of the adventitious carbon at 284.8 eV. The following three bulk reference La powders were measured: La_2O_3 (99.9%, anhydrous powder, Sigma-Aldrich), $LaCl_3$ (99.9+%, anhydrous powder, Sigma-Aldrich), LaOCl (synthesized as described by Peringer et al. [37]). The XPS samples measured are based on the synthesis of LaOCl spherical caps with a 20 mM $LaCl_3$ ∗7 H_2O in ethanol solution as described earlier. These samples were measured as both pristine and after reaction with $TiCl_4$ at 95 °C ex-situ. The in a N_2-glovebox prepared samples were stored in heptane and transported in a sealed, steel vacuum tube to an Ar-filled glovebox. There they were opened, dried under Ar atmosphere and transferred into the XPS system using a transfer vessel under Ar atmosphere.

4.3 Results and Discussion

4.3.1 Design of the Spherical Cap Model System

To bridge the morphology gap between conventional planar film model systems and the industrially relevant spherical catalyst particles, a combined photomasking and spin-coating technique was used for the synthesis of spherical caps on a suitable substrate, such as Si(100). An outline of these synthesis steps is given in Figure 4.3, starting from the hydroxylation of the Si(100) wafer towards the grafting of an octadecyltrichlorosilane (ODTS) self-assembled monolayer (SAM). This SAM is then selectively etched away using a large area (20x20 mm^2) TEM copper grid photo-mask with UV/ozone, followed by the spin-coating and calcination of the hydrated $LaCl_3$ precursor salt to finally yield the LaOCl spherical caps. The selective etching of surface anchored SAMs and subsequent coating with different metal oxides was demonstrated for the fabrication of flat square patches of TiO_2 by Masuda et al., growth of zeolite domains by Ha et al., and the synthesis of well-defined KCl single crystals by van Delft et al.[33,38,39]. In this Chapter, a LaOCl phase is chosen over a $LaCl_3$ phase to support the Ti^{3+} active site due to the high stability of LaOCl against hydration which facilitates ambient measuring conditions when applicable, whereas $LaCl_3$ is highly hygroscopic analogous to the conventional $MgCl_2$ support matrix. It should be noted that LaOCl has a tetragonal crystal structure, whereas the conventional δ-$MgCl_2$ phase, which resembles the δ-$TiCl_3$ phase, has a hexagonal crystal structure. However, all of these materials are layered with successive layers of M^{x+} and Cl^- anions (in the case of LaOCl,

LaO$^+$ layers alternating with double Cl$^-$ layers), and the primary particles of these compounds are built of platelets loosely bound together through ionic interactions [40-42]. After grafting the TiCl$_4$ active site precursor on the LaOCl spherical caps followed by the activation with a triethylaluminium (TEAL) co-catalyst and ethylene polymerization under mild conditions, e.g. 2 bar ethylene, slurry-phase at room temperature, the polyethylene-LaOCl composite spherical caps are studied in detail using a toolbox consisting of both surface-sensitive (micro)-spectroscopic and conventional micro-spectroscopic techniques.
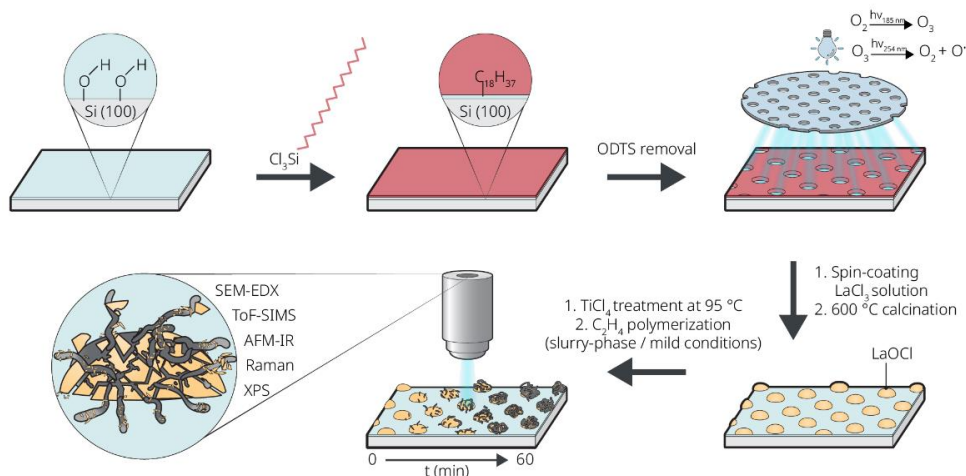

Figure 4.3 Schematic representation of the synthesis route of LaOCl spherical caps on a surface modified Si(100) wafer. Chemical modification of the Si(100) wafer surface, to generate hydrophilic circular patches (about 40 µm in diameter) separated by hydrophobic bars, is achieved through sequential grafting of the hydrophobic octadecyltrichlorosilane (ODTS) on a hydroxylated surface and selective etching with a photomask and UV/O₃. Subsequent spin-coating and calcination of a LaCl₃ ∗ 7 H₂O solution in ethanol leads to the formation of LaOCl spherical caps exclusively inside the hydrophilic regions. After grafting of TiCl₄ on the LaOCl spherical caps, ethylene polymerization was performed in slurry phase under mild conditions with a triethylaluminium co-catalyst at different reaction times. A toolbox, consisting of advanced micro-and-spectroscopic techniques, was used to follow the ethylene polymerization process ex-situ.

4.3.2 Confirmation of the LaOCl Chemical Phase

The surface-sensitive techniques, XPS and ToF-SIMS (see sub-Chapter 4.3.3) and the bulk material probing Raman microscopy were used to confirm the LaOCl chemical phase on the as-synthesized LaOCl spherical caps confirms.

Starting with XPS in Figures 4.4 and 4.5 and Table 4.1 the results are given of the pristine and TiCl$_4$ grafted spherical caps called respectively, SC-P and SC-Ti, a Si(100) reference wafer treated with TiCl$_4$ and triethylaluminium (Si-Ti/Al), and three reference powders of pure La$_2$O$_3$, LaOCl and anhydrous LaCl$_3$ chemical phases.

It should be noted here that XPS of La is not trivial for the following two reasons: i) Li et al., have shown in an in-situ study on the energy calibration of Lanthanum compounds with XPS that the component splitting (ΔE) of the La 3d$_{5/2}$ signal, which in principle can be used for chemical diagnostics, is highly prone to the measurement conditions and surface chemistry [43]. They found, for instance, that the ΔE value of an as-prepared La$_2$O$_3$ material changed from 3.6 eV to 4.3 eV after vacuum treatment at 800 °C, which basically removes carbon and oxygen adsorbates. Furthermore, they provide a literature summary of reported ΔE values for La$_2$O$_3$, La(OH)$_3$ and La$_2$O$_2$(CO)$_3$ where differences up to 0.7 eV are reported within the same materials. Therefore, although the ΔE values of the three reference materials are provided in Figure 4.4 and a trend is observed showing a decrease in the splitting value with increasing degree of surface chlorination from 4.05 eV for La$_2$O$_3$ to 3.99 eV for LaOCl and finally 3.72 eV for LaCl$_3$ the absolute values should be taken with caution. ii) Additionally, the use of the La 4p and Cl 2p XPS signals to follow the surface chemistry of the LaOCl spherical caps before and after reaction with TiCl$_4$ is highly challenging due to massive signal interference (strong overlap) of the La 4p and the Cl 2p XP signals. This prevents the determination of an accurate fitting model for the LaOCl spherical cap samples, since the individual signal features of the La 4p signal (e.g., the position of the high binding energy shoulder), which depend on the exact chemical environment (e.g., the degree of surface chlorination), cannot be properly determined. However, to provide rough trends on the degree of surface chlorination, Table 4.1 summarizes the results of a simplified fitting approach, neglecting the La 4p signal shoulder at high binding energies. Assuming that this leads to a systematic error (a systematic underestimation of the La 4p signal contribution), it should still be possible to derive trends related to the Cl fraction. Again, it should be noted here that the absolute values should be considered with caution due to the aforementioned fitting issues.

The La 3d$_{5/2}$, La 4p and Cl 2p XPS results on the LaOCl spherical caps before (SC-P) and after (SC-Ti) treatment with TiCl$_4$ at 95 °C are given in Figure 4.5. As discussed earlier, the ΔE splitting value is highly sensitive to the local chemical environment and the sample preparation steps. Since ΔE is approximately the same before and after the reaction of the LaOCl spherical cap with TiCl$_4$ (4.32 eV vs. 4.30 eV respectively) and significantly lower than the multiplet split difference between the LaOCl and the LaCl$_3$ reference powders ($\Delta(\Delta E)$ =

0.27 eV) and therefore the LaOCl surface of the spherical cap doesn't seem to be chlorinated further towards LaCl$_3$ upon treatment with TiCl$_4$ at 95 °C.

The areas of the XPS signal contributions assigned to Cl, La and Ti of the spherical cap samples are summarized in Table 4.1. As expected, the Ti 2p XP signal is only observed after the reaction of the LaOCl spherical caps with TiCl$_4$. The broadening of the Ti 2p$_{3/2}$ signal towards lower binding energies (~456-457 eV) hints clearly towards the presence of reduced Ti^{3+} species [12]. This could be due to a similar mechanism reported for the dissociative chemisorption of CCl$_4$ on the LaOCl surface, which gives rise to a CCl$^{\delta+}$-Cl$^{\delta-}$ pair coordinated to respectively the Lewis acid La^{3+} and Lewis basic O$_2^-$ surface groups [29,30]. However, it should be mentioned here that the majority of the Ti species remains in the +4 oxidation state in the absence of the co-catalyst, triethylaluminium. To exclude a dominating detrimental influence by the uncovered silicon areas on the LaOCl spherical cap sample in this context, a Si(100) substrate reference was treated with both TiCl$_4$ and the reducing triethylaluminium co-catalyst and subsequently analyzed with XPS. The corresponding Ti 2p signal is shown in blue in Figure 4.5c (denoted as Si-Ti/Al). For the Si-Ti/Al reference, the presence of reduced Ti species can also be observed, which can be attributed to the interaction with the reducing co-catalyst. However, the fraction of the reduced signal contributions is 3.4 times for the LaOCl SC-Ti sample than for the Si-Ti/Al reference. Therefore, the reduced Ti species can be mainly attributed to interactions with the LaOCl spherical caps.
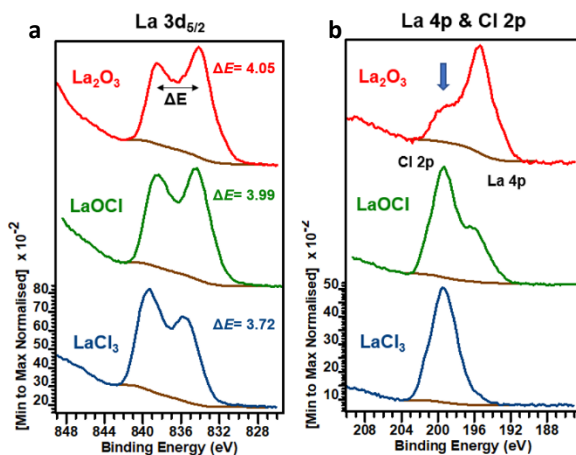

Figure 4.4 X-ray photo-electron spectroscopy (XPS) results of three Lanthanum reference materials. (a) The multiplet split of the La 3d$_{5/2}$ signals are shown for the anhydrous reference materials (La$_2$O$_3$, LaOCl and LaCl$_3$) together with the split energy, ΔE, in electron volts. (b) The La 4p and Cl 2p signals of the three reference materials. The blue arrow indicates the La 4p signal shoulder at high binding energies for La$_2$O$_3$ that overlaps with the Cl 2p signals for the chlorinated samples.
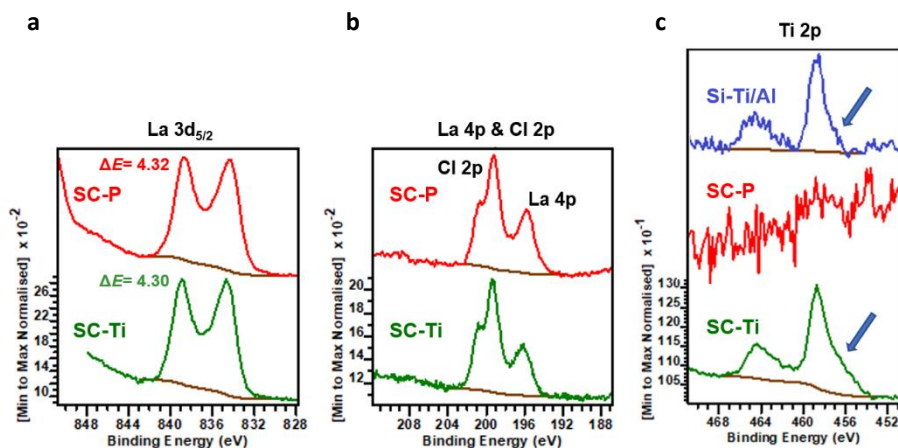
Figure 4.5 X-ray photo-electron spectroscopy (XPS) results of the LaOCl spherical cap model system before and after reaction with $TiCl_4$. (a) The multiplet split of the La $3d_{5/2}$ spectrum is given for the LaOCl spherical cap model system before (SC-P, red) and after (SC-Ti, green) reaction with $TiCl_4$. (b) The La 4p and Cl 2p spectra of SC-P and SC-Ti. (c) The Ti 2p spectrum of SC-P, SC-Ti and Si-Ti/Al (blue).

The ratios of Cl:La-related signals (Cl 2p:La $3d_{5/2}$ and Cl 2p:La 4p) of the pristine SC-P sample are slightly higher than those of the LaOCl reference, but considerably lower than those of the pure $LaCl_3$ reference. The slight deviation from the LaOCl reference might be caused by topography-related effects and the different sample geometry (spherical caps versus powder references). However, after reaction with $TiCl_4$ the Cl:La ratios increase significantly. Here, due to massive signal interference, it is not entirely clear, whether this is due to a further chlorination of LaOCl towards $LaCl_3$ with $TiCl_4$ acting as the chlorination reagent or simply due to the chemisorption of $TiCl_x$ species on the external surface of LaOCl. Since the La $3d_{5/2}$ splitting value is not affected by the reaction with $TiCl_4$ as mentioned earlier, it seems more likely that the increased ratio of the Cl:La peaks is due to the chemisorption of $TiCl_x$ species.

Table 4.1 The area under the selected La, Cl and Ti XP signals and the respective signal ratios. Values are given for the three reference materials La_2O_3, LaOCl and $LaCl_3$ as well as the pristine and $TiCl_4$ treated LaOCl spherical cap systems called SC-P and SC-Ti, respectively.

Sample	Area La $3d_{5/2}$	Area La 4p*	Area Cl 2p	Area Ti 2p	Ratio Cl 2p : La $3d_{5/2}$	Ratio Cl 2p : La 4p	Ratio Cl 2p : Ti 2p
La_2O_3	232.3	364.2	-	-	-	-	-
LaOCl	269.2	406.1	337.5	-	1.3	0.8	-
$LaCl_3$	168.3	185.0	525.1	-	3.1	2.8	-
SC-P	65.7	103.6	104.4	0.0	1.6	1.0	-
SC-Ti	38.2	61.2	79.9	81.8	2.1	1.3	1.0

* The area under the La 4p is obtained using a single signal (GL(30) line shape) and doesn't take the high binding energy shoulder observed around 200 eV into account.

Conventional Raman micro-spectroscopy (e.g. in the absence of surface-enhancement techniques) is a bulk-probing technique that nicely complements the surface-sensitivity of XPS analysis in this scenario to study the spherical cap model system. In Figure 4.6, the Raman spectra are given for the pristine LaOCl spherical cap, the Si (100) wafer background and the LaOCl powder reference material also used as the XPS reference. For the spherical cap model system, only the LaOCl chemical phase is detected. Conventional Raman micro-spectroscopy (e.g. in the absence of surface-enhancement techniques) is a bulk-probing technique that nicely complements the surface-sensitivity of XPS analysis in this scenario to study the spherical cap model system.
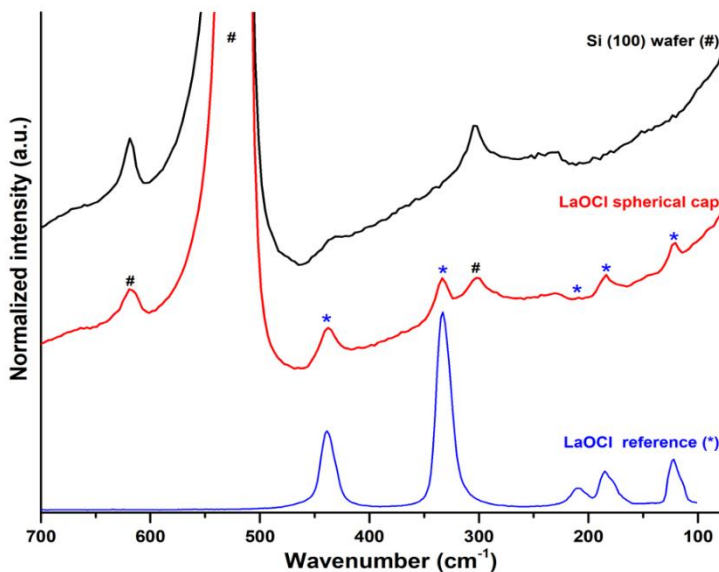

Figure 4.6 Raman micro-spectroscopy to determine the bulk chemical phase of the LaOCl spherical cap model system. In blue and black, the Raman spectra are given for respectively the LaOCl powder reference that was also used for XPS studies and a clean Si(100) wafer substrate. In red, the Raman spectrum is given for the LaOCl spherical cap model system, where the stars denote peaks belonging to the LaOCl chemical phase based on the blue spectrum and the octothorp denotes peaks belonging to the Si(100) wafer substrate.

4.3.3 The Micro-Spectroscopic Toolbox to Study the Ethylene Polymerization Versus Catalyst Fragmentation Relationships

In Figure 4.7, an overview of the utilized micro-spectroscopic toolbox is given on a 20 min ethylene polymerized LaOCl spherical caps sample. Starting with ToF-SIMS, the composition of both the surface chemistry as well as the interior through depth profiling can be obtained. Here, a secondary electron image of an ethylene polymerized LaOCl spherical cap is shown together with the distribution of the negatively charged fragments of $LaOCl^-$, $TiOCl^-$ (due to exposure to moisture), and the polyethylene characteristic $C_{21}H_{31}^-$. With the vibrational micro-spectroscopy part of the toolbox, based on Raman microscopy and PiFM, the polyethylene phase is studied in-depth as shown in Figures 4.7 and 4.9. Raman microscopy provides a time-efficient method to map the distribution of the -CH stretching vibrations in the region of 2700-3100 cm^{-1} to visualize local thickness differences of the formed polyethylene phase within the spherical caps. However, even in the best-case scenario, the diffraction-limited spatial resolution of the Raman microscope setup utilized here would be on the order of 360 nm (see Eq. 2). On the other hand, with PiFM, IR spectra with the spatial resolution of the AFM tip's apex (~ 20 nm) are obtained. This allows for the mapping and correlation of the -CH$_2$- bending vibrations of crystalline polyethylene at respectively 1461 cm^{-1}, $\delta(b_{1u})$, and 1471 cm^{-1}, $\delta(b_{2u})$ to the topological information obtained from the AFM part [44]. Finally, FIB-SEM images collected provide strong *Z*-contrast between the low atomic weight polyethylene, the intermediate atomic weight Si(100) substrate and the high atomic weight LaOCl framework with the collected backscattered electrons. Using both top-view and cross-sectional SEM images, the fragmentation of the LaOCl spherical cap as initiated by the induced stress of the polyethylene on the catalysts framework at respectively the spherical cap's exterior surface and interior volume can be observed. An in-depth study on this fragmentation behavior of the LaOCl spherical caps at different ethylene polymerization times will be given around Figures 4.19.
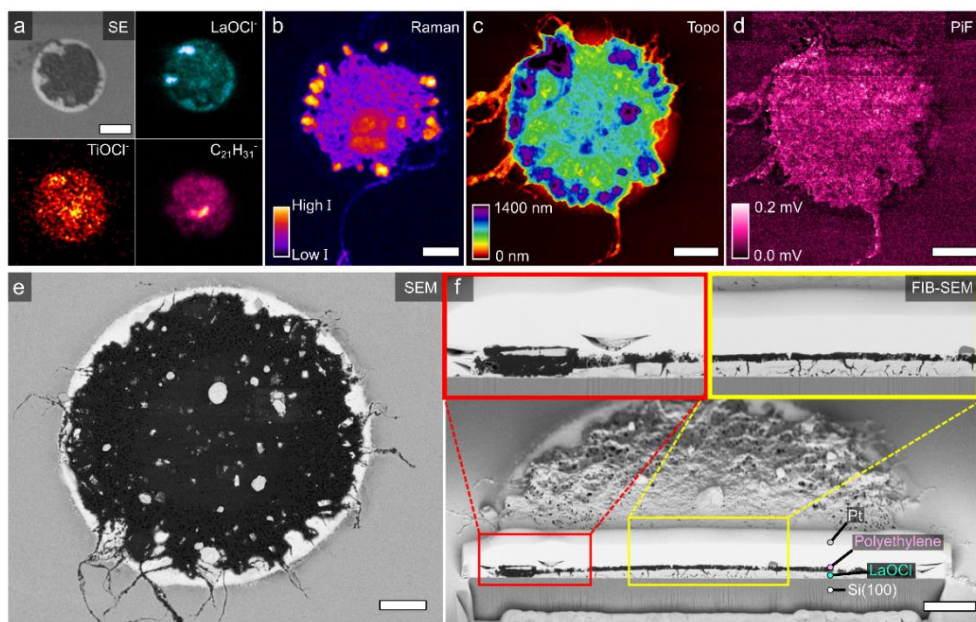
Figure 4.7 An overview of the micro-spectroscopic toolbox utilized in this Chapter to study the interplay between the formed polyethylene and the LaOCl spherical cap model system demonstrated after 20 min of ethylene polymerization. (a) Time-of-flight secondary ion mass spectrometry (ToF-SIMS) that provides a distribution of the negatively charged mass species present on the surface, such as the selected $LaOCl^-$, $TiOCl^-$ and polyethylene characteristic $C_{21}H_{31}^-$ fragments. (b) Raman microscopy map of the 2700-3100 cm^{-1} region shows the -CH stretching modes of polyethylene on a different LaOCl spherical cap. (c-d) Combined photo-induced force microscopy (PiFM) results that give both topological and morphological information in (c) and distribution of the summed $\delta(b_{1u})$ peak at 1461 cm^{-1} with the $\delta(b_{2u})$ peak at 1471 cm^{-1} of the IR spectra in (d) of the same spherical cap. (e) Top-view Scanning electron microscopy (SEM) image showing backscattered electrons that provides Z-contrast. In dark grey, polyethylene fibers are observed to grow from the LaOCl spherical cap (in bright white). (f) Focused ion beam (FIB)-SEM image of the same spherical cap, which shows a cross-section of the internal structure of the LaOCl spherical cap and the formed polyethylene phase. Zoom-ins are given in the red and yellow insets. All scale bars represent a width of 5 μm.

4.3.4 On the Formation and Characterization of the Polyethylene Phase

With the advanced micro-spectroscopy toolbox introduced for a 20 min ethylene polymerized LaOCl spherical cap, the formation and characterization of polyethylene will now be studied in-depth. In Figure 4.8, the Raman spectra are given for the LaOCl spherical caps after specified (0,1,2,5,10,20 and 60) min of ethylene polymerization, as well as the Si (100) wafer background on the 20 min ethylene polymerized sample and a HDPE reference film. All Raman spectra are normalized to the 521 cm^{-1} peak of the Si (100) substrate, which can be regarded as an internal standard. For all samples, the measured spot was optimized based on that part of the spherical cap that gave the most intense polyethylene signal. For all ethylene polymerized samples, Raman micro-spectroscopy confirms that polyethylene is formed mainly on the LaOCl spherical caps, with no observable amount detected on the background substrate and no polyethylene or other carbon phases are found on the pristine sample (0 min PE).
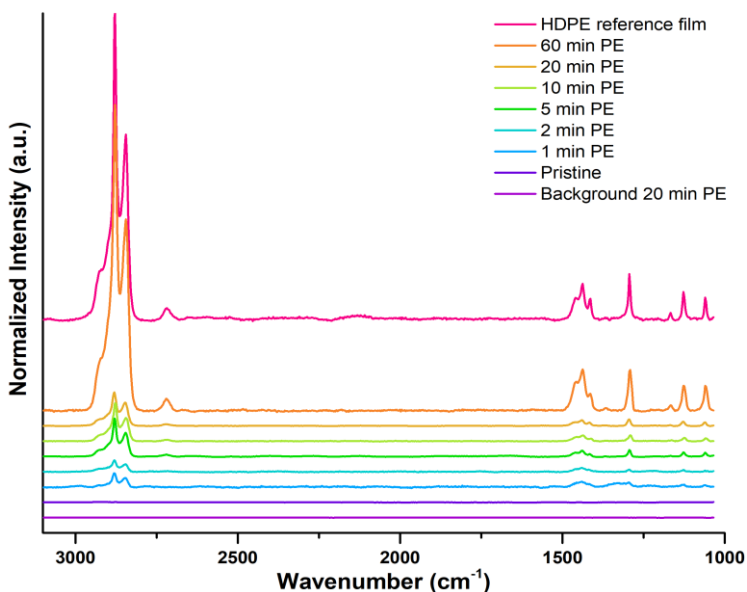

Figure 4.8 Raman spectra taken after different ethylene polymerization times on the LaOCl spherical caps as well as a HDPE reference film. Raman spectra are given from the pristine up to 60 min of ethylene polymerization on the LaOCl spherical cap model system (labelled as *x min PE*) as well as the Si (100) background of the 20 min ethylene polymerized sample (background 20 min PE) and a HDPE reference film. In all cases, normalization was performed using the Si (100) background 521 cm^{-1} peak as an internal standard.

To complement the 20 min ethylene polymerized sample showcased in Figure 4.7, in-depth Raman microscopy and PiFM analysis of three additional ethylene polymerization times of 2, 5 and 60 min are given in Figure 4.9. Additional Raman microscopy and PiFM results on the 0,1,2,5,10,20 and 60 min samples are given in Figures 4.11 and 4.11. In Figure 9a, Raman microscopy results of the -CH stretch region at 2700-3100 cm^{-1} are given to map the distribution and thickness fluctuations of the formed polyethylene. Starting at the 2 min of ethylene polymerization, two polyethylene phases are observed, namely (i) the formation of a large number of highly intertwined polyethylene fibers that create a porous polyethylene network laying on top of the spherical cap and (ii) highly intense, more spherical polyethylene regions located mainly at the edge of the spherical cap. Upon increasing the polymerization time to 5 min, both polyethylene phases increase in intensity as well as total surface coverage. At 20 min ethylene polymerization, the formation of a thicker and spheroidal polyethylene region is now also observed around the center of the spherical cap whereas at shorter polymerization times, it was observed exclusively at the outer rim. Finally, after 60 min of ethylene polymerization, the spherical cap's surface from outer rim to center is covered almost entirely in a single dense polyethylene phase, yet polyethylene fibers are still visible bridging these thicker regions together. In Figure 9b, the IR spectra obtained from PiFM are given for all the polymerization times studied. The signal-to-noise-ratio for the 1 and 2 min ethylene polymerization time are quite low, which could be explained either by the formation of the highly porous and thin polyethylene fibers at such low polymerization times or that the crystallinity of the polyethylene fibers is lower at these earlier polymerization times, leading to a higher contribution of an amorphous polyethylene phase. As the polymerization time increases, the clear doublet peaks of crystalline polyethylene appear after roughly 5 min of polymerization.

Using multivariate curve resolution (MCR), the contribution of the -CH_2- bending vibrations at 1461 cm^{-1} and 1471 cm^{-1} belonging to crystalline polyethylene in the orthorhombic phase and a broad amorphous band at 1463 cm^{-1} as well as an interference component due to adsorption of water vapor were assessed [45,46]. The scores of this MCR, which can be thought of as the concentration of a spectral component in the sum spectrum, were subsequently used to calculate the fraction of crystalline components to the overall intensity of the 1400-1500 cm^{-1} region (that is the two crystalline and one amorphous bands). This fraction as a function of ethylene polymerization time is shown in Figure 9b. Initially, this fraction increases with polymerization time up to 10 min and then decreases and stabilizes for the 20 and 60 min samples. The increase of the fraction of crystalline bands as a function of polymerization time could be related to the polymerization rate where AFM and ToF-SIMS analysis in Figures 4.12-4.16 show a decay in the increase of the estimated polyethylene on the external surface after roughly 2-5 minutes. This decrease of the polymerization rate, most likely due to internal mass transfer limitations within the LaOCl spherical caps, could then lead to a higher ratio of the rate of crystallization versus polymerization, since α-olefin polymerization is highly exothermic and can delay the crystallization of the formed polyolefin fibers. This would finally result in a higher fraction of crystalline components estimated with PiFM and subsequent MCR analysis with respect

to the amorphous component. The decrease of the crystalline fractions for the 20 and 60 min polyethylene samples as compared to the 10 min polyethylene sample could be due to the increase of the chain length of the polyethylene phase as no chain-terminating reagent, such as H_2, is employed. The increased polyethylene chain length leads to a decrease in the crystallization rate due to the increased viscosity of these longer polyolefin chains [47]. However, it should be emphasized here that no claims are made to the actual value of the crystallinity of the formed polyethylene phase, which is more conventionally assessed with bulk techniques such as differential scanning calorimetry (DSC) [48].
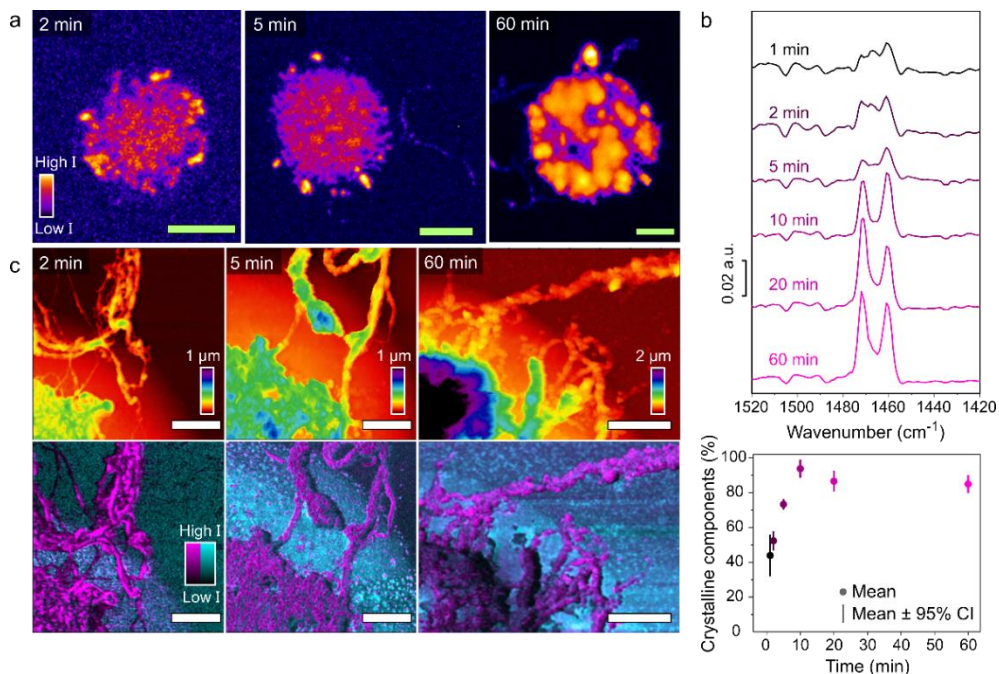

Figure 4.9 Raman microscopy and photo-induced force microscopy (PiFM) to study the crystallization of the formed polyethylene after 2, 5 and 60 min of ethylene polymerization. (a) Raman microscopy maps of the asymmetric and symmetric -CH_2- stretching vibrations in the 2700-3100 cm^{-1} region. (b) The photo-induced force (PiF) spectra that give the -CH_2- symmetric bending mode peaks of crystalline polyethylene in an orthorhombic phase are shown after different polymerization times, aver-aged of 18 spectra measured on 9 different patterned catalysts per time. Multivariate curve resolution (MCR) analysis was per-formed to fit the individual spectra on 4 different spectral components. The fraction of the two crystalline components (1461 cm^{-1} and 1471 cm^{-1} bands) versus the single amorphous component (broad band at 1463 cm^{-1}) is plotted in terms of the mean and 95% CI per time, showing a steep increase in crystallinity up until 10 min, and then a saturation as the polymer layer is grown thicker and ordered to form HDPE like PE, as seen in the spectral resemblance. (c) the topological (top) and PiF (bottom) images of zoom-ins on the spherical caps. The PiF images show the distribution of the -CH_2- symmetric bending mode peaks in magenta and LaOCl surface adsorbed carbonate species acting as markers for LaOCl in cyan. The green (Raman microscopy) and white (PiFM topology) scale bars represent a width of respectively, 10 μm and 2 μm.
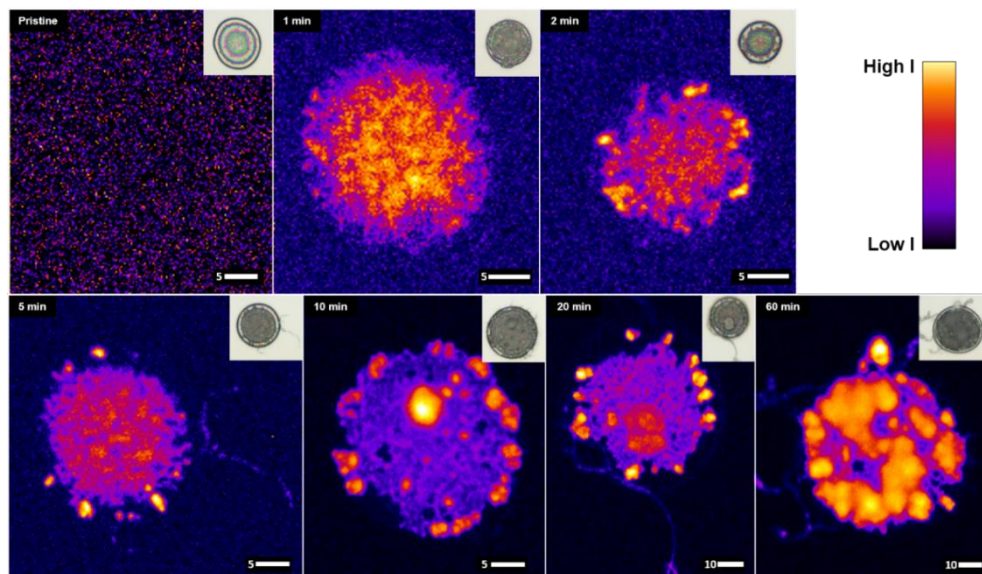
Figure 4.10 Raman micro-spectroscopy maps of the 2700-3100 cm^{-1} region on different ethylene polymerization times. The 2700-3100 cm^{-1} region imaged for each ethylene polymerization time shows the distribution of the asymmetric and symmetric -CH$_2$- stretching modes of polyethylene on a LaOCl spherical cap. The inset images show the correlated optical microscopy overview of the pristine and ethylene polymerized LaOCl spherical caps. The scale bars depict the size in microns.
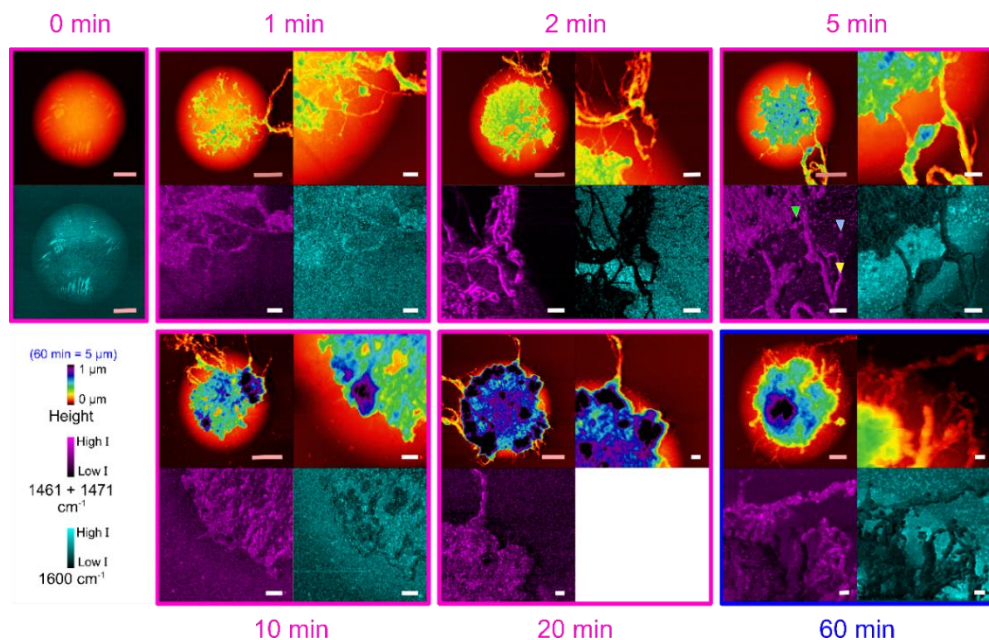
Figure 4.11 Individual Photo-induced Force micrographs of a full spherical cap, a zoom-in and the corresponding intensity maps for the 1461 + 1471 cm^{-1} and 1600 cm^{-1} vibrations on different ethylene polymerization times. Per polymerization time, the height micrographs are shown for a full spherical cap (top left) and a zoom-in (top right). The corresponding PiFM intensity maps are shown for the 1461 + 1471 cm^{-1} vibrations (magenta), and the 1600 cm^{-1} vibration (cyan) representing the PE and catalyst support, respectively. Note that the z-scale for all height micrographs is 1 μm, except for 60 min polymerization time, which has a z-scale of 5 μm. The pink inset scale bars represent 5 μm while the white scale bars represent 1 μm.

Atomic Force Microscopy (AFM) was used to investigate the topological and morphological evolution of the LaOCl spherical caps as a function of ethylene polymerization time. Figure 4.12 shows the topological images of 6 LaOCl spherical caps per ethylene polymerization time. The height contrast is set to be identical for the 0 to 20 min of polymerization time at a 0-1μm range. However, the ethylene polymerized LaOCl spherical caps of the 60 min sample were considerably thicker on average and therefore required a different height contrast as shown ranging from 0-4 μm. Purely based on the topological information provided by AFM it becomes clear that these LaOCl spherical caps become covered with polyethylene fibers of varying lengths already at ethylene polymerization times as early as 1 min. With an increase of polymerization times, thicker blobs of polyethylene start to appear (dark purple in color). It should be noted here that due to the different height scale bar in the 60 min sample, large features may appear to have a lighter (green-blue) color, which would have appeared dark purple with the height contrast used for the 0-20 min samples.
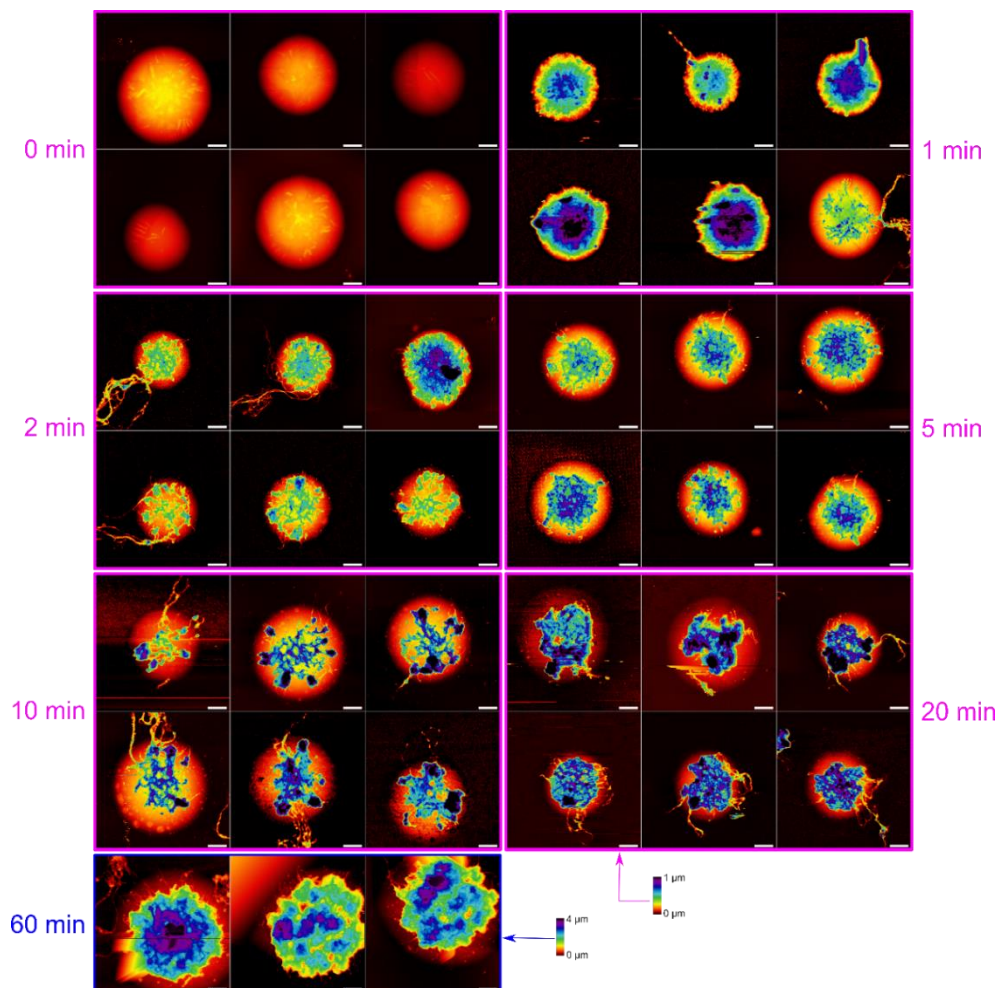
Figure 4.12 Atomic Force Microscopy (AFM) on individual catalyst caps after different ethylene polymerization times. Six LaOCl spherical caps were scanned per ethylene polymerization time, all shown using a z contrast of 1 µm, with the exception of 60 min, where only 3 viable micrographs could be obtained shown with a z contrast of 4 µm due to the excessive thickness of the polymer features which were too challenging for our scanning probe microscopy system. A general trend shows that the coverage and thickness of the formed polymer increase with increasing ethylene polymerization time. Furthermore, with the exception of 60 min, the edges of the patterned catalyst caps remain fairly visible whereas the center part of the cap gets covered by PE strings and larger features. Notes: i) At 2 min, top-right; the catalyst consisted of a non-spherical shape. ii) 5 min, bottom-left; the catalyst was measured before by SEM analysis (explaining the grid-like background) iii) 10 min, top-left and bottom-right; some noise was found only on the background, not on the formed PE. White scale bars are 5 µm.

However, using purely the height of the polymer features itself isn't accurate enough to describe the polymer yield per polymerization time, as the patterns can vary in shape (diameter or height) even within the same wafer substrate. Instead, our approach to attempt to track the polymerization yield as a function of time is shown in Figure 4.13. The individual micrographs were first flattened on the background (substrate) and then x and y cross-sectional profiles were taken from the background through the center of the spherical caps. From the resulting line profiles, the height (h) and cap base radius (a) were measured by fitting the visible parts of uncovered catalyst with a power function. From these values the catalyst caps volume were approximated with the following Eq 4.3:

$$V = \pi.h\left(a^{\frac{1}{4}} + h^{\frac{1}{3}}\right) \quad \text{Eq. 4.3}$$

where V is the cap volume in μm^3, h is the height of the cap in μm and a is the cap base radius, or chord length, in μm [49]. It should be said here that this approach does not allow us the quantify the amount of polyethylene present within the spherical cap. For such an approach, X-ray nanotomography techniques, such as ptychography X-ray computed tomography as done in Chapters 2 and 3 could offer a solution [50,51].
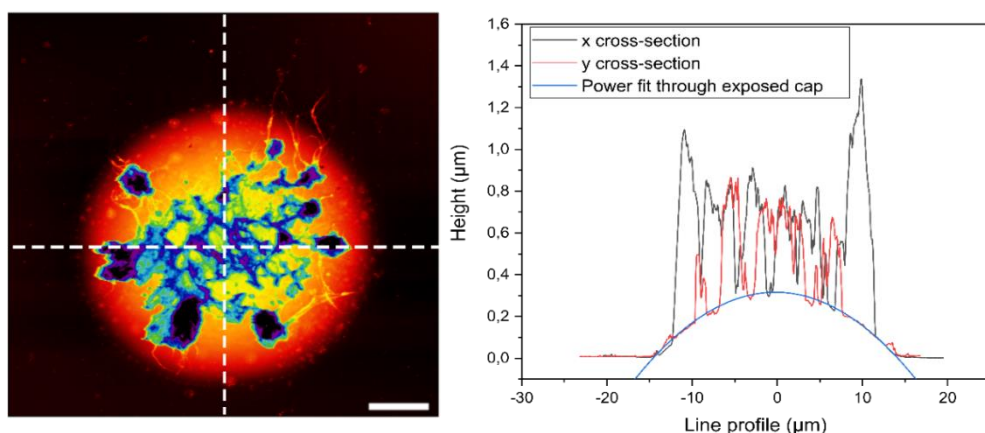
Figure 4.13 Estimation of the LaOCl spherical cap volume after ethylene polymerization. The individual micrographs shown in Figure 4.12 were each flattened on their background (substrate) around the LaOCl spherical cap and polyethylene (left). Then, a x and y cross-section was taken and the resulting height profiles were fitted with a power function over the exposed polymer-free catalyst surface. Using the software measurement tools, the cap base radius or chord length and catalyst height were measured. These were then used to estimate the volume of the catalyst, which could subsequently be subtracted from the total volume obtained in the micrograph (above the background height) to result in a net volume of polyethylene.

The total volume of all features measured, which represents the LaOCl spherical cap and polyethylene phases, minus the estimated volume of the sole LaOCl spherical cap as described above, results in the estimated volume of polyethylene (per micrograph). This volume was plotted in Figure 4.14 for all micrographs recorded as shown in Figure 4.12, and for all full micrographs recorded with PiFM as shown in Figure 4.11 (*vide infra*), to visualize the increase of polyethylene over time ignoring the initial pore volume of the catalyst which might be filled up at the early stages.

Going from 0-20 min ethylene polymerization a saturation effect of the polyethylene volume growing on the external surface of the LaOCl spherical cap is observed. This could be explained by first the formation of many extruded polyethylene fibers at early polymerization times as well as the filling of the internal pore network of the LaOCl spherical cap. As the internal pore network becomes filled with a polyethylene phase that can't be assessed with this approach (since AFM only measured topological information and not internal), these extruded polyethylene fibers will show a non-linear decaying growth rate due to mass transfer limitations. This is because new ethylene monomers will now have to diffuse through a dense polyethylene phase within the internal pore network to reach the active sites. However, at 60 min of ethylene polymerization a drastic change is observed with a considerably higher average external polyethylene volume when compared to the 5-20 min samples.

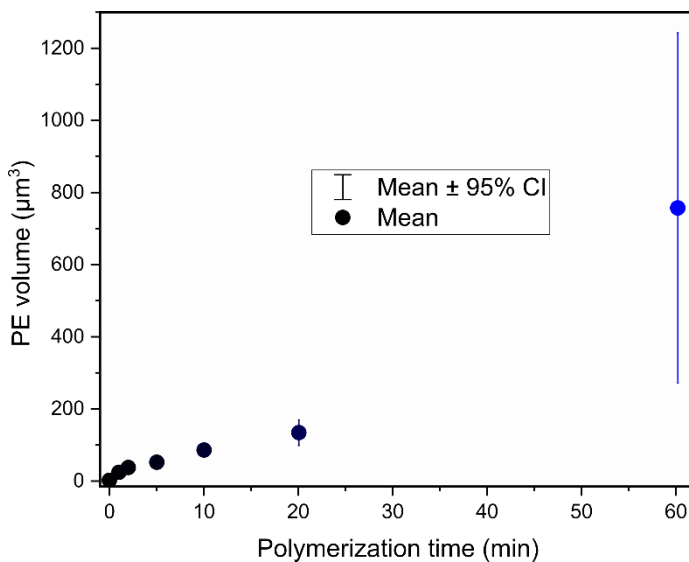**Figure 4.14** Mean volume of the polyethylene phase (PE) measured on the external LaOCl spherical caps as a function of ethylene polymerization time. The mean volume of the polyethylene phase growing on the external LaOCl spherical cap surface was calculated using the micrographs of Figure 4.12 and correction for the estimated volume of the LaOCl catalyst framework as discussed in Figure 4.13.

To complement the topological information obtained from AFM, ToF-SIMS was employed to track the surface coverage of polyethylene characteristic mass fragments such as $C_9H_{13}^-$. A selection of mass fragments is shown in Figure 4.15. Based on the ion generated SE images, the polyethylene phase can be clearly distinguished from the LaOCl spherical caps. It should be mentioned here that the ion counts for the $LaOCl^-$ fragment is typically orders of magnitude higher than for polyethylene fragments such as $C_9H_{13}^-$. This may be related to charging effects and the low ionization probability of polyolefins, making them particularly challenging to be measured with ToF-SIMS. Additionally, the sample geometry (spherical caps with rough surfaces after polymerization instead of planar systems) could also cause adverse effects here. The $C_9H_{13}^-$ mass fragment was chosen here to represent the polyethylene phase as based on the work by Kern *et al.* [36]. This polyethylene mass fragment is also found for the pristine sample, but with considerably lower ion counts or intensity and is thus more likely to be from adventitious carbon due to air exposure of the samples. Nevertheless, as is mostly visible for the 2 and 10 min maps, the $C_9H_{13}^-$ mass charge fragment shows strong correlation with the polyethylene phase visible in the SE images.

The integrated intensity for this fragment, found in the different mass spectra, is plotted in Figure 4.16. As the polymerization time increases, more of this fragment is found (note that all measurement points have the same sputter time) until after 10 min a saturation effect starts to appear. This is in line with the AFM analysis performed in Figures 4.12-4.14, where the polyethylene volume on the external surface of the LaOCl spherical caps was estimated for different ethylene polymerization times and showed a saturation of the estimated polyethylene volume at intermediate polymerization times. This could be explained by a mass transfer limitation effect occurring at such intermediate polymerization times, where the fragmentation rate is not sufficiently high yet to facilitate high enough diffusion of ethylene monomers to the active sites within the spherical cap composite phase and hence a decline in the polymerization rate is observed.
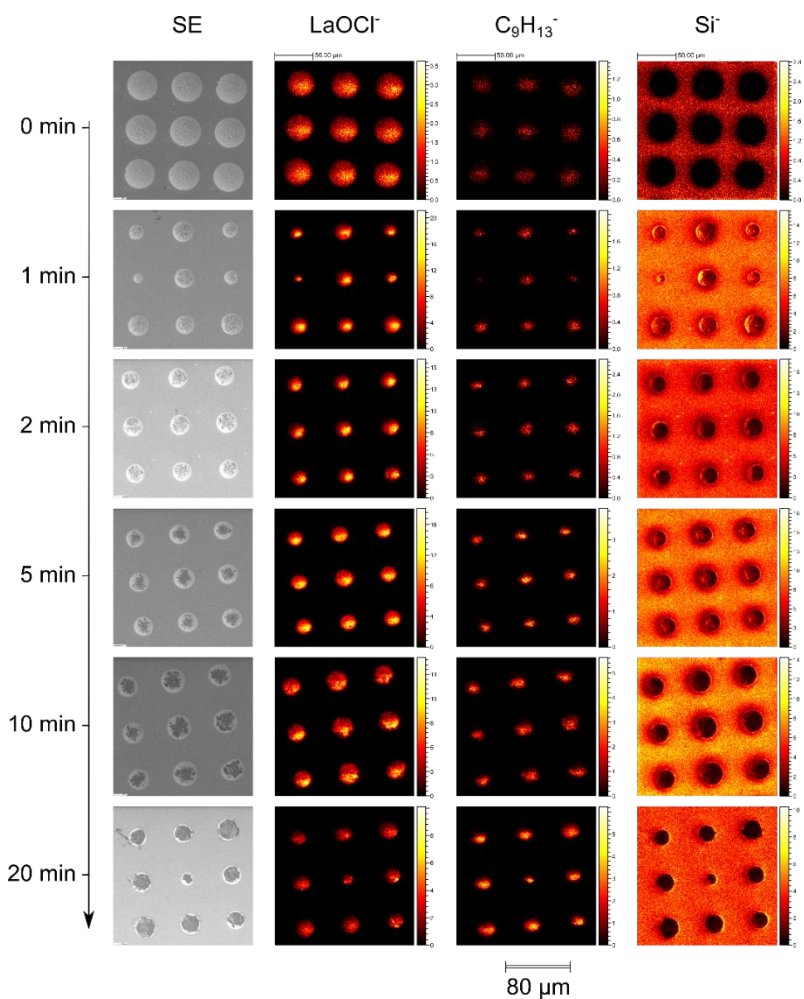
Figure 4.15 Time-of-flight secondary ion mass spectrometry (ToF-SIMS) secondary electron (SE) images, complemented by a selection of mass fragments, for different times of ethylene polymerization. The LaOCl⁻ fragment is chosen to represent the polymerization catalyst, while the $C_9H_{13}^-$ fragment is representing the polyethylene. The Si⁻ fragment is shown to highlight the substrate on which the spherical caps were synthesized, and emphasizes that the LaOCl is only present in the patterned area as intended during the synthesis.
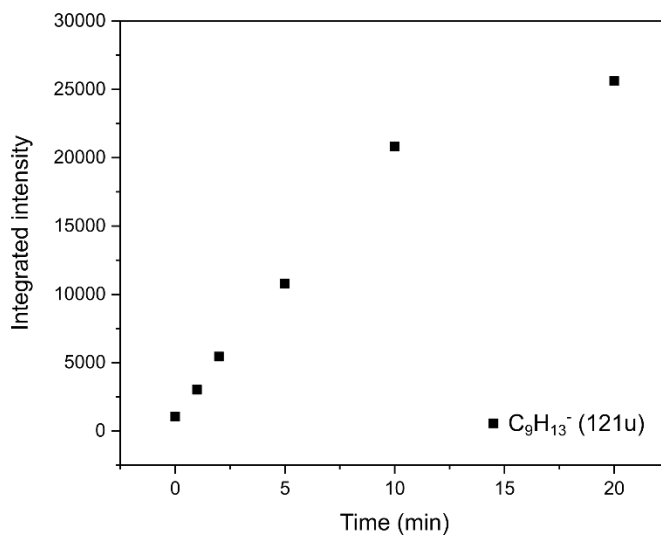
Figure 4.16 Integrated area of the $C_9H_{13}^-$ mass fragment. Representing polyethylene, the integrated area of the $C_9H_{13}^-$ mass fragment (m/z = 121 u), also shown in the mass images in Figure 4.15, is shown after increasing times of ethylene polymerization. Whereas first a linear increase is found, the integrated intensity starts to flatten out after roughly 20 min of ethylene polymerization. This indicates that the surface coverage of each island increases until a nearly full surface coverage is obtained.

4.3.5 On the Fragmentation Behavior of the LaOCl Spherical Cap

Using vibrational microscopy, AFM and ToF-SIMS the formation and evolution of the polyethylene crystallinity as a result of the ethylene polymerization reaction was studied. Additionally, two morphologically different polyethylene phases were observed, namely a highly intertwined polyethylene fiber network covering the spherical caps as well as the thick and spheroidal polyethylene regions that are initially formed at the outer rim of the spherical caps and gradually start to appear and cover most of the spherical cap. To unravel the origin of these two morphologically different polyethylene phases, top-view and cross-sectional FIB-SEM is utilized.

In Figure 4.17, an overview is given of the SEM results of all ethylene polymerization times, starting at the top with a pristine LaOCl spherical cap sample up to 60 min of ethylene polymerization at the bottom. From left to right first, an overview of multiple LaOCl spherical caps at a specific ethylene polymerization is provided, followed by a single spherical cap and finally a zoom-in on this spherical cap. Starting at the 1 min ethylene polymerized sample, it becomes clear that the polyethylene fibers that are extruded out of the spherical caps contain large amounts of small LaOCl fragments. The extrusion of the polyolefin fibers has been reported for immobilized single-site catalysts in well-defined microporous and mesoporous support matrixes for polyolefin catalysts, such as the silica-based MCM-41 and SBA-15 with pore diameters in the range of 2-25 nm [52-57]. The small LaOCl fragments must have been peeled off the internal and possibly external surface of the catalyst. This indicates the presence of the shrinking core or also called layer-by-layer fragmentation model, as illustrated in Figure 4.21. After ten min of ethylene polymerization, the external surface of the center of the spherical caps are observed to be fully covered in a polyethylene fiber network. Additionally, starting at this polymerization time, large LaOCl fragments are observed to lay intertwined with and on top of this polyethylene fiber network. The zoom-in on the 10 min ethylene polymerized sample shows one such large LaOCl fragment laying on top of the center of the spherical cap and is actually observed to already have been cleaved into several smaller fragments that are being pushed away from each other by the growing polyethylene fibers. This internal cleavage shows the presence of the continuous bisection fragmentation model, as illustrated in Figure 4.21, occurring even at the external surface of the spherical cap.
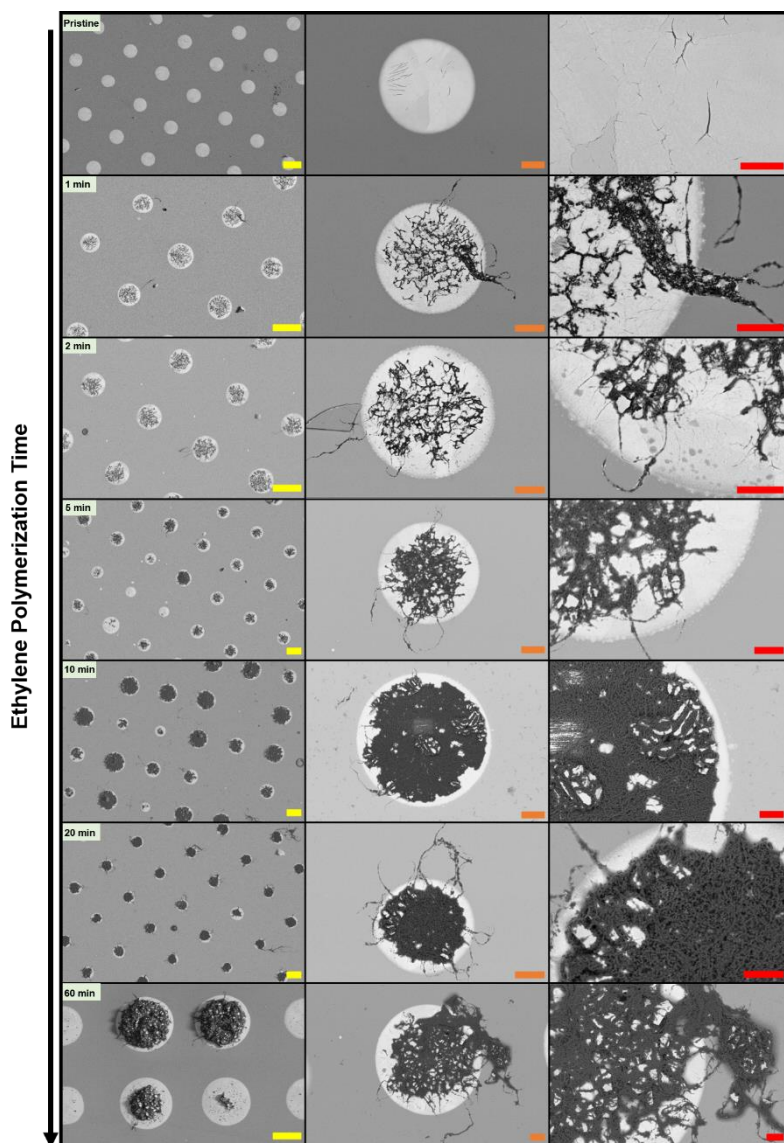
Figure 4.17 Secondary Electron Microscopy (SEM) results on the LaOCl spherical caps after different ethylene polymerization times. From left to right first, an overview consisting of multiple LaOCl spherical caps at a certain polymerization time are given followed by a single spherical cap and finally a zoom-in on that specific spherical cap. From top to bottom, an increase of ethylene polymerization time is given, starting at a pristine non-polymerized sample and going up to 60 min of ethylene polymerization. The yellow, orange and red scalebars represent a width of respectively 20, 5 and 2 microns.

EDX maps of the pristine and 20 min ethylene polymerized sample in Figure 4.18, show the presence of La, O and Cl, the constituents of LaOCl both before and after ethylene polymerization. The high photon energies of especially La at 4651 eV for the Lα_1 emission line means that the formed polyethylene phase (carbon binding energy is ~284 eV) will barely lead to attenuation of these photons and therefore cause the La phase to be easily observable through the polymer phase. For the pristine LaOCl spherical cap, only a small contribution of carbon is found, most likely due to the adsorption of carbonate species due to exposure to air during sample transfer. However, after 20 min of ethylene polymerization, the carbon signal of the formed polyethylene phase becomes clear.

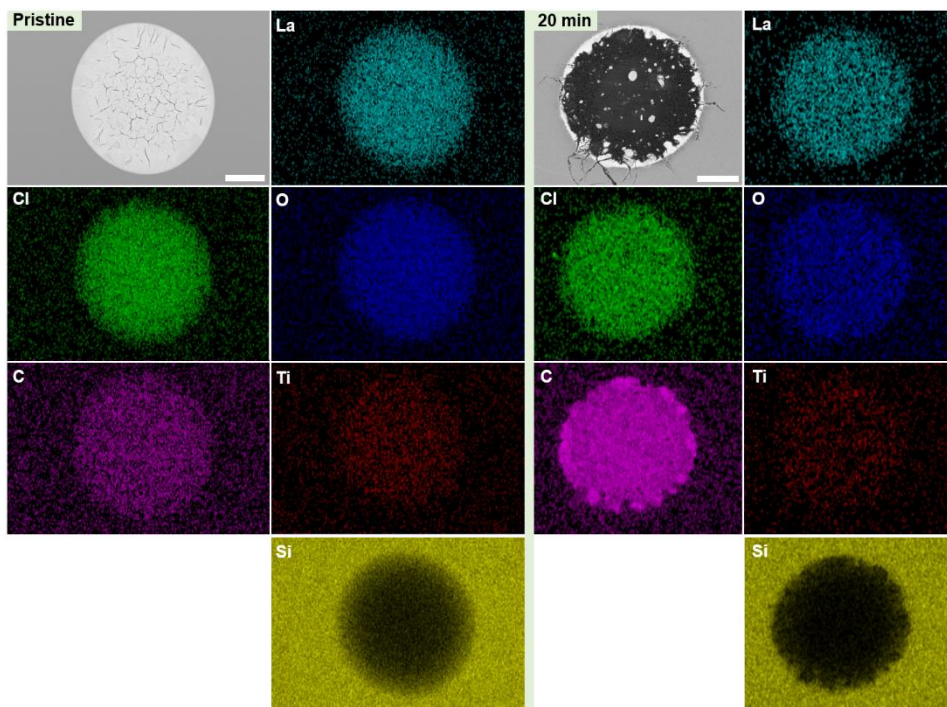**Figure 4.18** Top-view Secondary Electron Microscopy Energy Dispersive X-ray spectroscopy (SEM-EDX) results on the LaOCl spherical caps before and after ethylene polymerization. On the left and right side, the top-view back-scattered electron images of respectively the pristine and 20 min ethylene polymerized spherical caps are given alongside the EDX maps of La, Cl, O, C, Ti and Si. The scalebars depict a width of 10 microns.

The FIB-SEM results of the 20 min ethylene polymerized LaOCl spherical cap sample are extended towards pristine, 2, 5 and 60 min in Figure 4.19. The observed fragmentation behavior of these spherical caps consists of three stages as drawn schematically in Figure 4.20.

In the first stage, roughly 1 to 5 min of ethylene polymerization, the macroporous and surface-cracked LaOCl spherical cap comes in contact with ethylene that is transformed into polyethylene. Two different polymerization phenomena are observed in this first stage depending on the location within the spherical cap. Namely, i) around the center of the spherical cap, the first polyethylene fibers are extruded out of the surface exposed cracks and locally start to peel off the LaOCl framework, which becomes infused with the expanding polyethylene fibers. This peeling of small catalyst fragments belongs to the shrinking core fragmentation model (see Figure 4.21). ii) The formation of polyethylene within the internal macroporous cavities that leads to the rapid filling of such cavities. At the outer rim of the spherical caps this cavity filling is observed to lead to a significant degree of internal catalyst fragmentation already at this first stage. This type of catalyst fragmentation as described by the internal cleavage of the framework into successively smaller fragments belongs to the continuous bisection fragmentation model (see Figure 4.21) [58].

The second stage, roughly 10 to 20 min of ethylene polymerization, expands on the first phase through the steady growth of both formed polyethylene phenomena observed. That is, the porous polyethylene network formed due to the extrusion of polyethylene fibers from the exposed surface cracks increases both in total surface coverage as well as thickness and the thicker polyethylene regions observed at the outer rim, which cause a heavy local degree of framework fragmentation, increase further in thickness. Additionally, these thicker spheroidal regions, leading to a high degree of internal catalyst fragmentation, start to appear now also around the center of the spherical cap as the build-up of stress exerted on the locally thicker LaOCl framework region has now surpassed the required threshold.

Finally, in the third stage, at 60 min of ethylene polymerization, the polymerization activity has been sufficiently high to cause a full disintegration of the original spherical cap morphology in both small and large LaOCl fragments, which however still show additional internal crack lines, dispersed uniformly throughout the formed polymer stage. The presence of these small and large LaOCl fragments with internal cleavage lines that are homogeneously dispersed throughout the formed polyethylene phase show that the continuous bisection fragmentation model has become the dominant fragmentation pathway for prolonged polymerization times.
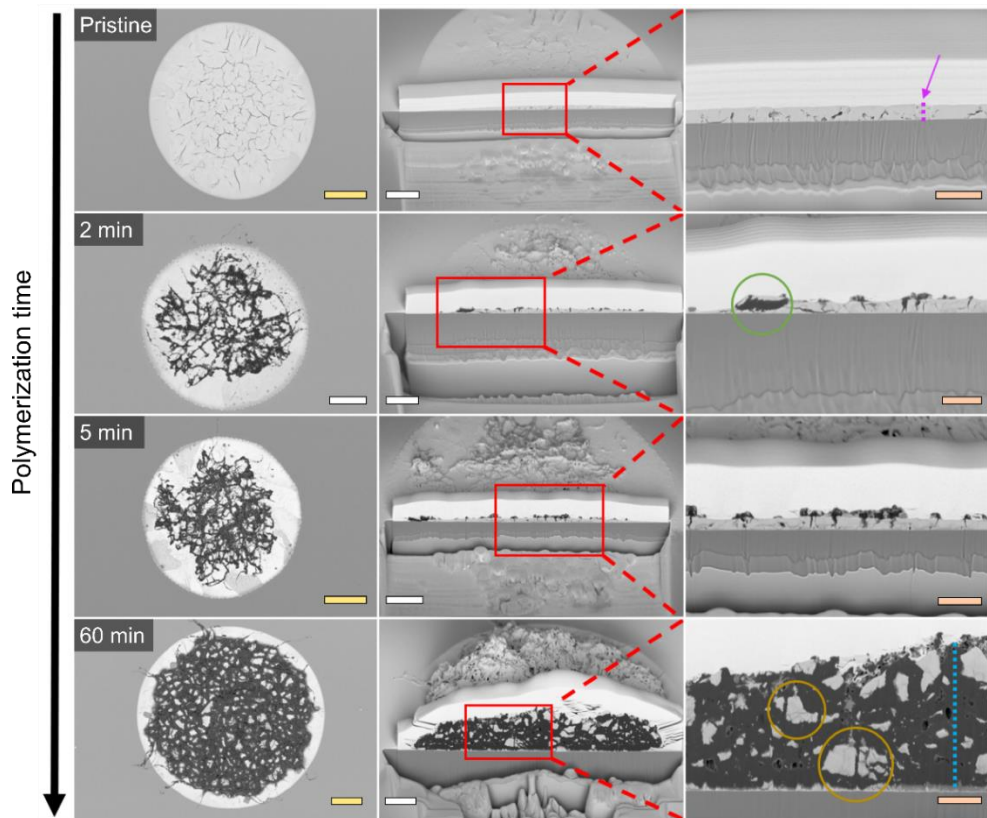
Figure 4.19 Cross-sectional scanning electron microscopy (SEM) to study the fragmentation behavior of the ethylene polymerized LaOCl spherical caps. (a) Top-down overview of the full spherical caps at respectively 0 (pristine), 2, 5 and 60 min of ethylene polymerization. (b) A cross-section of the spherical caps that shows the internal structure of the polyethylene-LaOCl spherical cap composites. (c) A zoom-in of these cross-sections to provide enhanced view of the internal structure. The pink and blue dashed lines in respectively the pristine and 60 min ethylene polymerized samples show a thickness of 600 nm for the LaOCl spherical cap and 5.7 microns for the polyethylene layer at those positions. The green circle refers to LaOCl fragments having been lifted up from the spherical cap by the polyethylene formed within the porous catalyst framework. The orange circles indicate the internal cleavage sites of the LaOCl framework. The yellow scale bars represent 10 μm, the white scale bars 5 μm and the orange scale bars 2 μm.

Figure 4.20 A schematic representation of the fragmentation behavior of the LaOCl spherical cap model system during ethylene polymerization. Three different polymerization stages are drawn, starting from the pristine spherical cap. In the first stage (i) the internal macroporous cavities and externally accessible cracks of the LaOCl spherical cap starts to be filled with polyethylene and leads to both the extrusion of polyethylene fibers from these cracks, as well as a locally heavy degree of framework fragmentation at the outer rim of the spherical caps, indicating the occurrence of both the shrinking core and continuous bisection fragmentation models in Figure 4.21. In the second stage (ii) both polymer phases, that is the extruded polyethylene fibers and the thick internal polyethylene regions at the outer rims of the spherical caps, keep growing steadily and cause the formation of additional cracking lines on the framework. Finally, in the third stage (iii) the original morphology of the spherical caps has disintegrated into both large and small LaOCl fragments that are dispersed uniformly throughout the polymer phase, showing that the continuous bisection fragmentation model has become dominant.

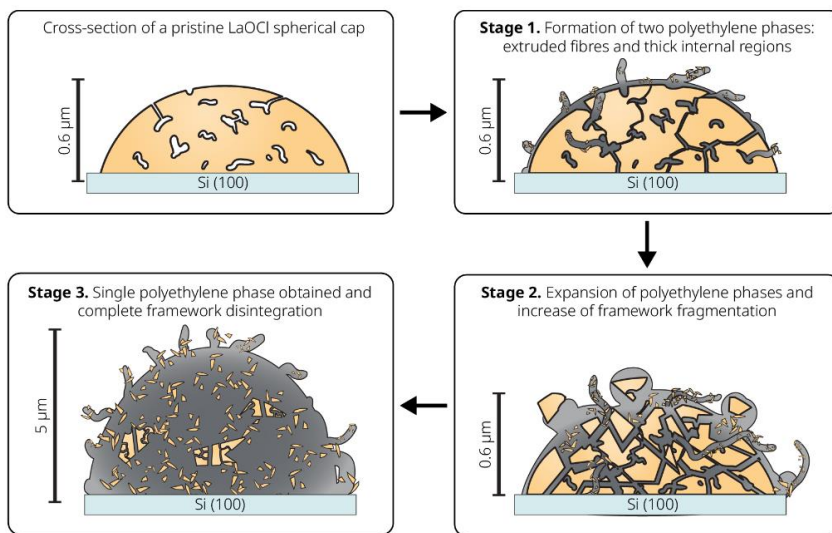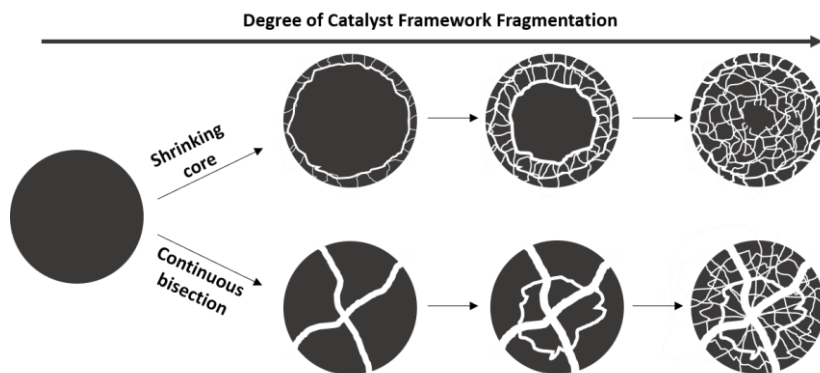**Figure 4.21** Schematic representation of the shrinking core and continuous bisection limiting modes of catalyst framework fragmentation. The shrinking core fragmentation mode starts at the surface of the catalyst particle whereas the continuous bisection fragmentation mode starts at the core outwards.

143

The SEM and EDX images, shown in Figure 4.22, belong to the cross-sectional regions of the pristine, 2 min and 60 min of ethylene polymerization, as shown in Figure 4.19. The cross-sections are taken around the center of each spherical cap. For the pristine LaOCl spherical cap, no carbon phase is observed within the cross-section, as expected, whereas for the 2 min ethylene polymerized sample a faint carbon signal can be seen, albeit difficult due to the deposition of carbon on the platinum coating above the spherical cap during the sputtering process. For the 60 min ethylene polymerization, a clear carbon phase can be observed now, as well as the LaOCl fragments dispersed within the carbon phase.
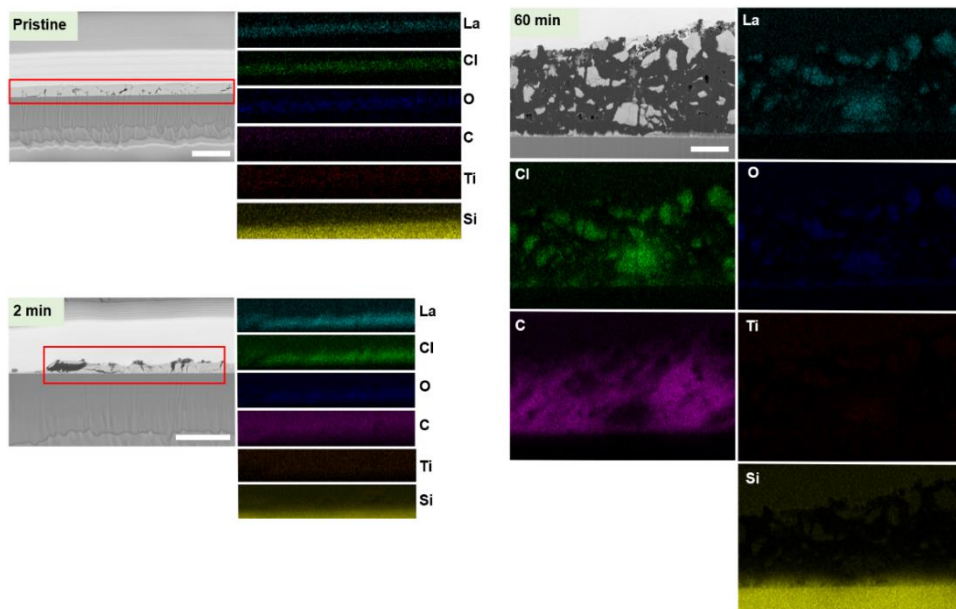
Figure 4.22 Cross-sectional Secondary Electron Microscopy Energy Dispersive X-ray spectroscopy (SEM-EDX) results on the LaOCl spherical caps before and after ethylene polymerization. The cross-sectional back-scattered electron images alongside the EDX maps of La, Cl, O, C, Ti and Si are given for the pristine, 2 min and 60 min of ethylene polymerization. The red boxes in the SEM images portray the area of the EDX maps in case it is smaller than the SEM image shown. The scalebars depict a width of 2 microns.

4.4 Conclusions

In this Chapter, a spherical cap model system has been introduced to bridge the gap between conventional planar model catalyst systems and the industrially used spherical catalyst particles in the field of α-olefin polymerization. Additionally, for this model system, LaOCl was chosen as a support matrix instead of the conventional $MgCl_2$ support matrix to support the $TiCl_4$ pre-active site. This provided both enhanced imaging contrast due to the high atomic weight of the lanthanum-based matrix and excellent moisture stability to enable the use of advanced micro-spectroscopy techniques under ambient conditions in contrast to the low atomic weight and highly hygroscopic $MgCl_2$. X-ray photoelectron spectroscopy (XPS) gave evidence for the coordination of Ti^{4+} and even a minor presence of Ti^{3+} species on the LaOCl surface before contact with the triethylaluminium co-catalyst. Time-of-flight secondary ion mass spectrometry (ToF-SIMS) and Raman microscopy confirmed the LaOCl chemical phase on the spherical cap model as well as the formation of polyethylene after ethylene polymerization. Raman microscopy and photo-induced force microscopy (PiFM) show the presence of two morphologically distinct polyethylene phases formed with i) discrete and thicker polyethylene regions starting to be formed at the outer rim of the spherical cap at early polymerization times that gradually start to cover also the center of the spherical caps and ii) a network of highly intertwined polyethylene fibers distributed more uniformly over the spherical cap. Cross-sectional scanning electron microscopy (SEM) shows that the polyethylene fibers are extruded out of crack lines already present on the pristine catalyst's surface, which are subsequently expanding further due to the stress of the polymer induced on the framework. These extruded polyethylene fibers peel off small LaOCl fragments from the surface. At the outer rim of the spherical caps, large LaOCl fragments are lifted up from the framework due to the polymerization of ethylene within the LaOCl porous framework and confirms the observations made with Raman microscopy and PiFM of locally thicker and spheroidal polyethylene regions. These findings show that both limiting modes of fragmentation, namely the shrinking core (peeling off small fragments at the surface) and continuous bisection (internal cleavage of the framework) are occurring simultaneously throughout the polymerization process at early polymerization times. However, at 60 min ethylene polymerization, a full disintegration of the spherical cap morphology is observed according to a dominating continuous bisection fragmentation model. The use of this industrially relevant spherical cap model system can be expanded further for the high-throughput testing of support matrix formulations in the field of α-olefin polymerization when combined with highly tunable deposition techniques such as inkjet printing [59].

4.5 References

1. Severn, J.R., Chadwick, J.C., (Eds.) Preface. In: *Tailor-Made Polymers Via Immobilization of Alpha-Olefin Polymerization Catalysts*, Severn, J.R., Chadwick, J.C., (Eds.); Wiley-VCH, Weinheim, **2008**.
2. Kaminsky, W. (Ed.), *Polyolefins: 50 years after Ziegler and Natta I,* Springer, Berlin, **2013**.
3. Severn, J.R., Recent Developments in Supported Polyolefin Catalysts: A Review. In: *Multimodal Polymers with Supported Catalysts*, Albunia, A.R., Prades, F., Jeremic, D., (Eds.), Springer Nature, Cham, 2019.
4. Schiffino, R., Laboratory Reactors and Procedures for Catalyst Evaluation. In: *Handbook of Transition Metal Polymerization Catalysts*, Hoff, R., (Ed.), John Wiley & Sons, Hoboken, **2018**.
5. Piovano, A., Zarupski, J., Groppo, E., Disclosing the Interaction between Carbon Monoxide and Alkylated Ti^{3+} Species: a Direct Insight into Ziegler-Natta Catalysis, *J. Phys. Chem. Lett.*, **2020**, 11, 5632-5637.
6. Sauer, J., Freund, HJ., Models in Catalysis, *Catal. Lett.*, **2015**, 145, 109-125.
7. Gao, F., Goodman, D.W., Model catalysts: Simulating the complexities of heterogeneous catalysts, *Annu. Rev. Phys. Chem.,* **2012**, 63, 265-286.
8. Kim, H.S., Tewell, C.R., Somorjai, G.A., Surface Science Studies of Ziegler-Natta Olefin Polymerization System: Correlations between Polymerization Kinetics, Polymer Structures, and Active Site Structures on Model Catalysts, *Korean J. Chem. Eng.,* **2002**, 19, 1-10.
9. Magni, E., Somorjai, G.A., Preparation of a model Ziegler-Natta catalyst Surface science studies of magnesium chloride thin film deposited on gold and its interaction with titanium chloride, *Appl. Surf. Sci*, **1995**, 89, 187-195.
10. Magni, E., Somorjai, G.A., Preparation of a model Ziegler-Natta catalyst: Electron irradiation induced titanium chloride deposition on magnesium chloride thin films grown on gold, *Surf. Sci.*, **1996**, 345, 1-16.
11. Magni, E., Somorjai, G.A., Electron irradiation induced chemical vapor deposition of titanium chloride on gold and on magnesium chloride thin films. Surface characterization by AES, XPS, and TPD, *J. Phys. Chem. B*, **1996**, 100, 14786-16793.
12. Magni, E., Somorjai, G.A., Surface science study of model Ziegler-Natta catalysts, *Surf. Sci.*, **1997**, 377, 824-827.
13. Arlman, E.J., Cossee, P., Ziegler-Natta catalysis III. Stereospecific polymerization of propene with the catalyst system TiCl$_3$lEt$_3$, *J. Catal.,* **1964**, 3, 99-104.
14. Siokou, A., Ntais, S., Towards the preparation of realistic model Ziegler-Natta catalysts: XPS study of the MgCl$_2$/TiCl$_4$ interaction with flat SiO$_2$/Si(100), *Surf. Sci.,* **2003***,* 540, 379-388.
15. Siokou, A., Ntais, S., XPS investigation of the interaction between TiCl$_4$(THF)$_2$ and AlEt$_3$ modified SiO$_x$/Si(100) surfaces *Surf. Sci.,* 2006*,* **600**, 4216-4220 (2006).
16. Giannini, U., Albizatti, E., Parodi, S., Pirinoli, F., Catalysts for polymerizing olefins, *U.S. Patent 4124532*, **1978**.
17. Fernandes, J.A., Girard, A-L., Support Designed for Polymerization. In Multimodal Polymers with Supported Catalysts, Albunia, A.R., Prades, F., Jeremic, D., (Eds.); Springer Nature Switzerland, **2019**.
18. Bart, J.C.J., Roovers, W., Magnesium chloride – ethanol adducts, *J. Mat. Sci.*, **1995**, 30, 2809-2820.
19. Andoni, A., Chadwick, J.C., Milani, S., Niemantsverdriet, H.J.W., Thüne, P.C., Introducing a new surface science model for Ziegler-Natta catalysts: Preparation, basic characterization and testing, *J. Catal.,* **2007**, 247, 129-136.

20. Andoni, A., Chadwick, J.C., Niemantsverdriet, H.J.W., Thüne, P.C., A Preparation Method for Well-Defined Crystallites of MgCl$_2$-Supported Ziegler-Natta Catalysts and their Observation by AFM and SEM, *Macromol. Rap. Comm.,* **2007**, 28, 1466-1471.

21. Andoni, A., Chadwick, J.C., Niemantsverdriet, H.J.W., Thüne, P.C., The role of electron donors on lateral surfaces of MgCl$_2$-supported Ziegler-Natta catalysts: Observation by AFM and SEM, *J. Catal.,* **2008**, 257, 81-86.

22. Andoni, A., Chadwick, J.C., Niemantsverdriet, H.J.W., Thüne, P.C., Investigation of Planar Ziegler-Natta Model Catalysts Using Attenuated Total Reflection Infrared Spectroscopy, *Catal. Lett.,* **2009**, 130, 278-285.

23. Piovano, A., Thushara, K.S., Morra, E., Chiesa, M., Groppo, E., Unraveling the Catalytic Synergy between Ti^{3+} and Al^{3+} Sites on a Chlorinated Al$_2$O$_3$: A Tandem Approach to Branched Polyethylene, *Angew. Chem.,* **2016**, 55, 11203-11206.

24. Piovano, A., Morra, E., Chiessa, M., Groppo, E., Tuning the Ti^{3+} and Al^{3+} synergy in a Al$_2$O$_3$/TiCl$_x$ catalyst to modulate the grade of the produced polyethylene, *ACS Catal.,* **2017**, 7, 4915-4921.

25. Jones, M.E., Olken, M.M., Hickman, D.A., Process for vinyl chloride manufacture from ethane and ethylene with secondary reactive consumption of reactor effluent HCl, *WO Patent 2001038273 A1*, **2001**.

26. Schweizer, A.E., Jones, M.E., Hickman, D.A., Oxidative halogenation of C1 hydrocarbons to halogenated C1 hydrocarbons and integrated processes related thereto, *U.S. Patent 6452058 B1*, **2002**.

27. Van der Avert, P., Weckhuysen, B.M., Low-temperature destruction of chlorinated hydrocarbons over lanthanide oxide based catalysts, *Angew. Chem. Int. Ed.*, **2002**, 41, 4730-4732.

28. Manoilova, O.V., *et al.*, Surface acidity and basicity of La$_2$O$_3$, LaOCl and LaCl$_3$ characterized by IR spectroscopy, TPD, and DFT calculations, *J. Phys. Chem. B,* **2004**, 108, 15770-15781.

29. Van der Heijden, *et al.*, Destructive Adsorption of CCl$_4$ over Lanthanum-Based Solids: Linking Activity to Acid-Base Properties, *J. Phys. Chem. B,* **2005**, 109, 23993-24001.

30. Podkolzin, S.G., Manoilova, O.V., Weckhuysen, B.M., Relative Activity of La$_2$O$_3$, LaOCl, and LaCl$_3$ in Reaction with CCl$_4$ Studies with Infrared Spectroscopy and Density Functional Theory Calculations, *J. Phys. Chem. B,* **2005**, 109, 11634-11642.

31. Podkolzin, S.G., Stangland, E.E., Jones, M.E., Peringer, E., Lercher, J.A., Methyl chloride production from methane over lanthanum-based catalysts, *J. Am. Chem. Soc.,* **2007**, 129, 2569-2576.

32. Nowak, D., *et al.*, Nanoscale chemical imaging by photoinduced force microscopy, *Sci. Adv.*, **2016**, 2, e1501571.

33. Masuda, Y., Sugiyama, T., Lin, H., Seo, W.S., Koumoto, K., Selective deposition and micropatterning of titanium dioxide thin film on self-assembled monolayers, *Thin Solid Films*, **2001**, 382, 153-157.

34. Nečas, D., Klapetek, P., Gwyddion: an open-source software for SPM data analysis, *Cent. Eur. J. Phys.*, **2012**, 10, 181-188.

35. Graefe, C.T., Punihaole, D., Harris, C.M., Lynch, M.J., Leighton, R., Frontiera, R.R., Far-Field Super-Resolution Vibrational Spectroscopy, *Anal. Chem.*, **2019**, 91, 8723-8731.

36. Kern, S., Kern, C., Rohnke, M., Mass spectra database of polymers for bismuth-cluster ToF-SIMS, *Surf. Sci. Spectra*, **2019**, 26, 025003.

37. Peringer, E., Tejuja, C., Salzinger, M., Lemonidou, A.A., Lercher, J.A., On the synthesis of LaCl$_3$ catalysts for oxidative chlorination of methane, *Appl. Catal. Gen.*, **2008**, 350, 178-185.

38. Ha, K., *et al.*, Photochemical Pattern Transfer and Patterning of Continuous Zeolite Films on Glass by Direct Dipping in Synthesis Gel, *Adv. Mater.,* **2001**, 13, 594-596.

39. Van Delft, F.C.M.J.M., van den Heuvel, F.C., Kuiper, A.E.T., Thüne, P.C., Niemantsverdriet, J.W., Micro-contact printing on oxide surface for model catalysts using e-beam written masters in hydrogen silsesquioxane, *Microelectron. Eng.*, **2004**, 73, 202-208.

40. Zhu, X., *et al.*, Synthesis, characterization and mechanism of formation of carbon aerogels incorporated with highly crystalline lanthanum oxychloride particles, *RSC Adv.*, **2017**, 7, 39635-39640.

41. Alizadeh, S., Mousavi-Kamazani, M., Salavati-Niasari, M., Hydrothermal Synthesis of Rod-Like LaOCl Nanoparticles from New Precursors, *J. Clust. Sci.*, **2015**, 26, 645-652.

42. Giunchi, G., Allegra, J., Structural disorder in microcrystalline $MgCl_2$, *J. Appl. Cryst.*, **1984**, 17, 172-178.

43. Li, J.P.H., *et al.*, Understanding of binding energy calibration in XPS of lanthanum oxide by *in situ* treatment, *Phys. Chem. Chem. Phys.*, **2019**, 21, 22351-22358.

44. Raff, R.A.V., Doak, K.W. (Eds.), *Crystalline Olefin Polymers Part 1*, John Wiley & Sons, Hoboken, **1965**.

45. Hagemann, H., Snyder, R.G., Peacock, A.J., Mandelkern, L., Quantitative Infrared Methods for the Measurement of Crystallinity and Its Temperature Dependence: Polyethylene, *Macromol.*, **1989**, 22, 3600-3606.

46. De Juan, A., Jaumot, J., Tauler, R., Multivariate Curve Resolution (MCR). Solving the mixture analysis problem, *Anal. Methods,* **2014**, 6, 4964-4976.

47. Whiteley, K.S., Polyolefins. In: *Ullmann's Encyclopedia of Industrial Chemistry*, Gerhartz, W., Elvers, B., (Eds.), Wiley-VCH, Weinheim, **2005**.

48. Li, D., Zhou, L., Wang, X., He, L., Yang, X., Effect of Crystallinity of Polyethylene with Different Densities on Breakdown Strength and Conductance Property, *Materials*, **2019**, 12**,** 1746-1759.

49. Oberg, E., Jones, F.D., Horton, H.L., Ryffel, H.H., *Machinery's handbook: a reference book for the mechanical engineer, designer, manufacturing engineer, draftsman, toolmaker, and machinist*, Industrial Press, New York, **1988**.

50. Bossers, K.W., Valadian, R., Zanoni, S., Smeets, R., Friederichs, Garrevoet, J., Meirer, F., Weckhuysen, B.M., Correlated X-ray Ptychography and Fluorescence Nano-Tomography on the Fragmentation Behavior of an Individual Catalyst Particle during the Early Stages of Olefin Polymerization, *J. Am. Chem. Soc.,* **2020**, 142, 3691-3695.

51. Bossers, K.W., Valadian, R., *et al.,* Heterogeneity in the Fragmentation of Ziegler Catalyst Particles during Ethylene Polymerization Quantified by X-ray Nanotomography, *JACS Au*, **2021** (10.1021/jacsau.1c00130).

52. Ko, Y.S., Woo, S.I., Polymerization with the Single-Site Catalyst Confined within the Nanospace of Mesoporous Materials or Clays. In: *Tailor-made Polymers: Via Immobilization of Alpha-Olefin Polymerization Catalysts*, (Severn, J.R., Chadwick, J.C., (Eds.), Wiley-VCH, Weinheim, **2008**.

53. Ko, Y.S., Han, T.K., Park, J.W., Woo, S.I., Propene polymerization catalyzed over MCM-41 and VPI-5 supported Et(ind)$_2$ZrCl$_2$ catalysts, *Macromol. Rapid Commun.*, **1996**, 17, 749-758.

54. Kageyama, K., Tamazawa, J., Aida, T., Extrusion polymerization: catalyzed synthesis of crystalline linear polyethylene nanofibers within a mesoporous silica, *Science*, **1999**, 285, 2113-2115.

55. Ye, Z., Zu, S., Wang, W., Alsyouri, H., Lin, Y.S., Morphological and mechanical properties of nascent polyethylene fibers produced via ethylene extrusion polymerization with a metallocene catalyst supported on MCM-41 particles, *J. Polym. Sci. Part B: Polym. Phys.*, **2003**, 41, 2433-2443.

56. Dong, X., *et al.*, Preparation of nano-polyethylene fibers and floccules using MCM-41-supported metallocene catalytic system under atmospheric pressure, *Eur. Polym. J.,* **2005**, 41, 797-803.

57. Kumkaew, P., Wanke, S.E., Parserthadam, P., Danumah, C., Kaliaguine, S., Gas-phase ethylene polymerization using zirconocene supported on mesoporous molecular sieves, *J. Appl. Polym. Sci.,* **2003**, 87, 1161-1177.
58. Horácková, B., Grof, Z., Kosek, J., Dynamics of fragmentation of catalyst carries in catalytic polymerization of olefins, *Chem. Eng. Sci.,* **2007***,* 62, 5264-5270.
59. Liu, X., *et al.*, Inkjet Printing Assisted Synthesis of Multicomponent Mesoporous Metal Oxides for Ultrafast Catalyst Exploration, *Nano Lett.,* **2012**, 12, 5733-5739.

Chapter 5. Summary and Future Perspectives

5.1 Summary

The aims of this PhD Thesis were threefold: (1) To gain a better understanding of the fragmentation behavior of industrially relevant Ziegler-type polyolefin catalysts. (2) To achieve this first aim, a methodology had to be designed and optimized to use X-ray nanotomography techniques for the highly moisture sensitive and relatively low Z-contrast polyolefin catalyst particles. (3) To fully utilize the potentials of X-ray nanotomography techniques, create a relevant Ziegler-type support matrix that provides enhanced imaging contrast with respect to the polyolefin phase.

In **Chapter 1**, the field of polyolefin catalysis is introduced with a short historic summary on the discovery and development of the non-catalytic low-density polyethylene route and subsequently the catalytic routes towards other grades of polyethylene as well as isotactic polypropylene (iPP). The Ziegler-type catalyst family is then introduced with an emphasis on the necessity of catalyst fragmentation during the α-olefin polymerization process to ensure a sufficient polymerization rate as well as the need to have good control over this process to prevent reactor fouling. A short summary is then given on several studies performed to study this catalyst fragmentation behavior with mainly scanning electron microscopy (SEM) as well as some initial results of X-ray microtomography on polyolefin (catalyst) particles. Then X-ray nanotomography techniques are introduced with an emphasis on ptychography X-ray compute tomography (PXCT) and X-ray fluorescence (XRF) nanotomography to bridge the spatial resolution gap from the initial X-ray microtomography studies into that of the field of electron microscopy.

In **Chapter 2**, X-ray nanotomography is introduced to study the fragmentation behavior polyolefin catalysts. Here the focus was on studying a ~40 micron in diameter iPP Ziegler-Natta composite particle with a polymer yield of 9.2 g iPP per g catalyst. A correlated PXCT and X-ray fluorescence nanotomography setup at the DESY p06 beamline was utilized to provide both 3-D electron density contrast from PXCT and 3-D elemental mapping from XRF nanotomography. Loading of the Ziegler-Natta propylene polymerized catalyst particles in polyimide capillaries inside a glovebox and subsequently sealing them with near-hermetic sealing epoxy glue was found crucial to prevent hydration of the $MgCl_2$ framework and therefore disintegration of the particle morphology even before exposure to the X-ray beam. Yet, severe beam-damage was observed as a function of scanning time that limited the amount of useable 2-D projections for tomographic reconstruction. Nonetheless, the 3-D volumes of the PXCT and XRF nanotomography data-sets were successfully reconstructed, albeit at non-optimal estimated 3-D spatial resolutions on the order of 500 nm. Subsequent analysis into the distribution of the Ti species, acting as markers for the catalyst phase, showed for the first time in 3-D direct evidence of the presence of both the shrinking core,

also called layer-by-layer, and continuous bisection fragmentation models. These two fundamental models describe how the catalyst particle fragments respectively, mainly at the surface due to the peeling of catalyst species due to the stress induced by the locally formed polyolefin (shrinking core) or throughout the core into successively smaller fragments (continuous bisection). Ultimately, it was found that the continuous bisection fragmentation model was dominating the overall fragmentation behavior of this specific catalyst particle studied after mild polymerization conditions. A small summary of these findings is given in Figure 5.1
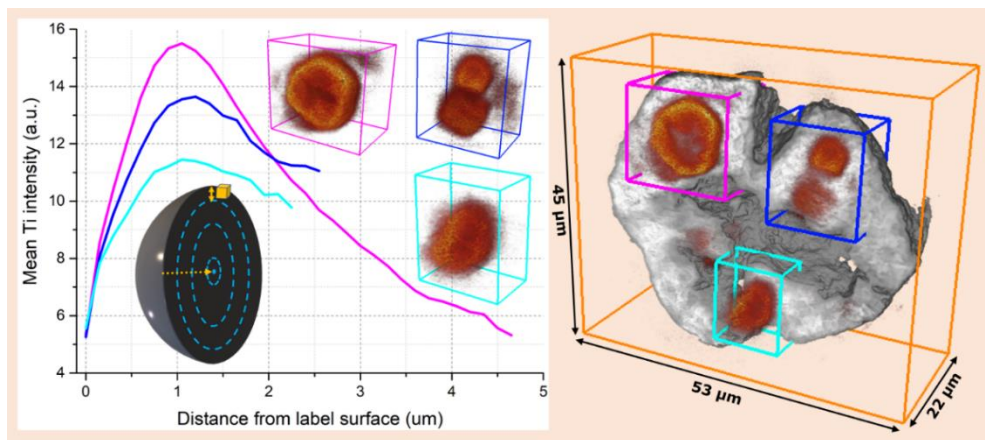

Figure 5.1 The radial distribution as well as their volume renderings using a clipping plane to visualize the interior of three selected Ti clusters in red (XRF nanotomography data-set) and the total volume showing the composite isotactic polypropylene and catalyst phases (greyscale). The radial distribution both within the largest Ti clusters as well as that of all Ti species throughout the composite particle was used to understand the fragmentation behavior of this Ziegler-Natta catalyst particle at a polymerization yield of 9.2 g iPP per g catalyst.

In **Chapter 3**, the methodology of Chapter 2 is improved upon in two ways to gain a better understanding of the fragmentation behavior of polyolefin catalyst particles. First of all, the beam-damage observed in Chapter 2 was mitigated by successfully removing residual diluent molecules that were present within the formed polyolefin shell due to carrying out the α-olefin polymerization experiments under slurry-phase conditions. This allowed the collection of 360 2-D projections with a 0.5 ° rotation angle leading to an estimated 3-D spatial resolution of 74 nm for the PXCT data-set. Additionally, by carefully selecting the Ziegler catalyst system with an average particle size around 3 microns, over 434 ethylene polymerized catalyst particles (at 3.4 g high-density polyethylene (HDPE) per g catalyst) were fully imaged and reconstructed. This opened up a route for the statistically relevant analysis of the fragmentation behavior of a large ensemble of particles. Using a marker-based watershed segmentation these 434 composite particles were successfully separated in the 3-D volume as individually labelled particles. Subsequent *k*-means clustering analysis allowed to discriminate between HDPE-rich, catalyst-rich and highly mixed HDPE-catalyst

phases and therefore study the degree of catalyst fragmentation within the ensemble. It was found that there was a large heterogeneity in the overall degree of catalyst fragmentation. Particles with a low degree of catalyst fragmentation mainly exhibited a shrinking core type of fragmentation behavior whereas for particles with a high degree of catalyst fragmentation the continuous bisection was found to be dominating the fragmentation behavior. In Figure 5.2, the volume rendering of the successfully separated 434 composite particles using the marker-based watershed segmentation algorithm as well as the results of the *k*-means clustering analysis with a zoom-in on the interior of a single composite particle are given.
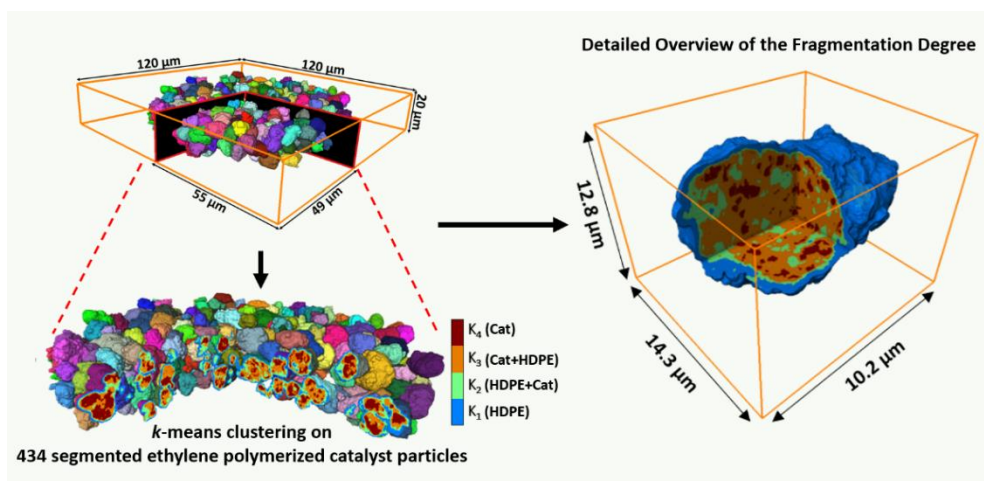

Figure 5.2 Volume rendering of the 434 ethylene polymerized catalyst particles after using a marker-based watershed segmentation algorithm to separate and label each particle. Subsequently, a *k*-means clustering algorithm was used to identify high-density polyethylene (HDPE, K_1) and catalyst (K_4) rich phases as well as mixed phases of HDPE and catalyst ($K_{2,3}$) to study the degree of catalyst fragmentation within the entire ensemble. Finally the distribution of these K-clusters are given for the interior of a single composite particle to visualize the fragmentation behavior of the catalyst particle.

In **Chapter 4**, LaOCl is introduced as a support matrix to provide enhanced imaging contrast with polyethylene as opposed to that of the conventionally used $MgCl_2$ support matrix. Additionally, whereas $MgCl_2$ is highly hygroscopic, which puts stringent limits on the measurement conditions with any imaging technique, LaOCl shows exceptional moisture stability. However, the chemistry of LaOCl and its possible precursors (chloride and nitrate salts) is vastly different from $MgCl_2$ and therefore the conventional synthesis routes for highly spherical $MgCl_2$ particles can't be directly translated to form highly spherical LaOCl particles. Instead, a new spherical cap model system is introduced that allows us to mimic the shape of a spherical particle whilst directly obtaining LaOCl from the calcination of a spin-coated $LaCl_3$ solution on a hydrophilic/hydrophobic patterned Si(100) substrate. Therefore, the introduction of this spherical cap model system for polyolefin catalysis

bridges the gap between the conventional planar thin film model systems and that of the industrially relevant spherical catalyst particles. Using a toolbox of advanced chemical imaging and spectroscopy techniques, the interplay between the formation of polyethylene within the interior porous network of the LaOCl spherical caps and the resulting fragmentation behavior of these LaOCl spherical caps is studied in detail. Using vibrational microscopy based on Raman microscopy and photo-induced force microscopy (a correlated nano-IR spectroscopy with atomic force microscopy technique), focused-ion beam scanning electron microscopy, X-ray photoelectron spectroscopy and time-of-flight secondary ion mass spectrometry, the presence of both polyethylene fibers extruded from cracks on the external surface and formation of dense polyethylene phases within the internal pore network of the LaOCl spherical caps are observed. These are then correlated to the fragmentation behavior of the LaOCl framework that shows that both the shrinking core and continuous bisection fragmentation models are occurring at early polymerization times. At prolonged polymerization times and upon the full disintegration of the original spherical cap morphology, the continuous bisection fragmentation model has become the dominating fragmentation pathway, which most likely showed that mass transfer limitations caused by a low initial fragmentation rate were overcome. In Figure 5.3, this LaOCl spherical cap model system and the advanced chemical imaging and spectroscopy toolbox utilized to study the ethylene polymerization are visualized.
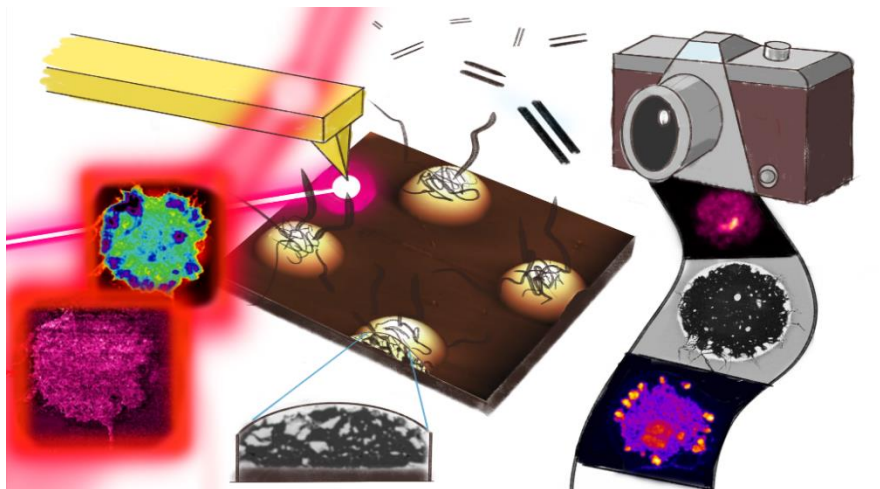
Figure 5.3 A Schematic representation of the spherical cap model system on a Si(100) wafer (dark brown) utilizing a LaOCl framework (the light brown spherical caps) as a support matrix to fabricate a Ziegler-type catalyst for the polymerization of ethylene (monomers and polyethylene fibers shown in transparent grey). The advanced chemical imaging and spectroscopy toolbox "captures" the interplay and relation between polyethylene growth and LaOCl framework fragmentation as depicted with the camera-roll.

5.2 Future Perspectives

5.2.1 A Better Understanding of the Fragmentation Behavior of Polyolefin Catalysts

Throughout this PhD Thesis, the main focus has been to study the fragmentation behavior of Ziegler-type catalysts. However, in Chapters 2, 3 and 4 the polymerization reaction conditions were performed under (very) mild reaction conditions of typically 2 bar α-olefin pressure, room temperature and without the addition of either hydrogen as a chain-terminating reagent to control the molecular weight (distribution) and co-monomers, such as 1-hexene and 1-octene, that can significantly alter polymer properties. With the currently employed reactor set-up operating inside a N_2-controlled glovebox, industrially relevant conditions such as 10 bar monomer pressure, uniform heating of the slurry to 60 °C and higher or addition of external reagents was simply not possible. Therefore, to gain a better understanding of the fragmentation behavior of polyolefin catalysts it would be beneficial to employ so-called stopped-flow reactors and rapid quenched-flow devices, such as those developed by the McKenna group [1-3]. These reactors and devices facilitate industrially relevant conditions at high pressures and temperatures, addition of hydrogen and co-monomers and low residence times of the catalyst particles down to 40 milliseconds before coming in contact with a quenching bath. Thus, low polymerization yields can be obtained at industrially relevant conditions that when paired with the in this PhD Thesis introduced PXCT and X-ray fluorescence nanotomography techniques can provide better insights into the fragmentation of polyolefin catalyst particles as they would behave inside an industrial reactor.

Another improvement to be made in parallel is that of *in-situ* X-ray nanotomography during α-olefin polymerization. Since PXCT and XRF nano-tomography are scanning techniques and even though improvements have been made recently that require less 2-D projections for instance for PXCT for high quality 3-D reconstructions, there are faster full-field alternatives that can provide phase-contrast imaging such as Zernike phase contrast and holotomography [4,5]. One should take into consideration though that one of the down-sides of these lense-based techniques is typically that their achieved 3-D resolutions are lower than that of PXCT, which is a lense-less based imaging technique. The design of such *in-situ* X-ray nanotomography experiments are especially difficult for α-olefin polymerization due to the high moisture and oxygen sensitivity even of the pre-activated catalysts and the typically high reaction rates. This means that the catalyst particles have to be transferred to the X-ray tomography set-up under inert conditions at all times as they can't be reactivated after exposure to air. Additionally, a pulsed system should be designed with two regimes. In the first regime, N_2 at a specified pressure will be flown through the capillary containing the particle and a tomograph will be collected as the starting point of the pristine catalyst morphology. In the second regime, α-olefin monomers mixed with co-

catalyst species (for Ziegler-based polyolefin catalysis) will be injected into the N_2 stream at a known concentration followed by switching back to the first regime of pure N_2 flow. In this way, short polymerization times can be ensured to limit the polymerization yield (since the concentration of monomer injected is known), whereas during the following N_2 flow regime the tomographs can be collected. This can then be repeated X number of times to collect X tomographs as a function of polymer yield. By keeping the entire system pressurized and potentially heating the capillary to 60-80 °C (can use borosilicate or quartz capillaries to this end) it should theoretically be possible to achieve industrially relevant polymerization conditions *in-situ*.

Finally, this PhD Thesis has been focused on $MgCl_2$-based Ziegler-type polyolefin catalysts for X-ray nanotomography studies. The methodologies developed in this PhD Thesis, therefore had to take into account the extreme sensitivity of the $MgCl_2$ framework for moisture, even for *ex-situ* measuring conditions (hence the motivation to develop LaOCl as a framework in Chapter 4). With these methodologies developed for the X-ray imaging of polyolefin catalyst particles (both single particle and ensembles), it would therefore be interesting to expand this research field to that of the other polyolefin catalyst families. The Phillips and immobilized metallocene based polyolefin catalysts are typically based on SiO_2 frameworks, which typically shows a lower friability than $MgCl_2$ and therefore a different fragmentation behavior and polymerization profile [6-9]. The advantage for *ex-situ* measurements on these SiO_2-based polyolefin catalysts is that sample loading will also be considerably easier. It should be mentioned here that Ziegler-type catalysts using a thin layer of $MgCl_2$ coated on SiO_2 are also industrially used and would make for a great comparison with pure $MgCl_2$ support systems when performing identical polymerization conditions [10]. Initial Cr XRF nanotomography results obtained at the Diamond Light Source (DLS) synchrotron facility, I14 beamline on a Cr/SiO_2 Phillips ethylene polymerized catalyst particle at <10 g HDPE per g catalyst is shown in Figure 5.4. It shows both an egg-yolk distribution of the Cr active site throughout the composite particle as well as a large crack from the center of the particle towards the surface, indicating that both the shrinking core and continuous bisection fragmentation models are occurring simultaneously also for the Phillips catalyst. However, additional experiments including the Cr distribution of the pristine catalyst are required to obtain a better overview.
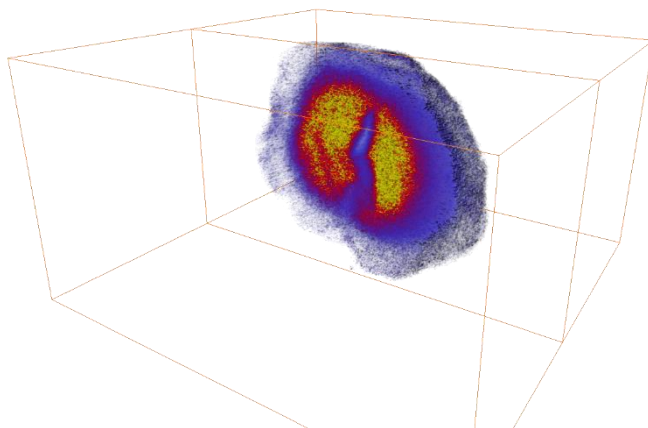
Figure 5.4 Cross-section of a reconstructed Phillips Cr/SiO_2 catalyst particle after ethylene polymerization to a yield of several g of polyethylene per g of catalyst. The reconstruction shown is of a Cr XRF data-set, therefore showing the distribution of the Cr active-site throughout the polymerized catalyst particle. An egg-yolk distribution of Cr with a major crack through the interior of the composite particle can be observed, showcasing most likely the presence of both the shrinking core and continuous bisection fragmentation models. The field of view is 67 x 67 x 55 microns. Reconstruction was performed with a filtered back projection. Achieved spatial resolution hasn't assessed for this data-set.

5.2.2 Synthesis of LaOCl Microspheres as a Ziegler-type Support Matrix

In Chapter 4, we introduced LaOCl as a moisture stable and high imaging contrast support matrix for Ziegler-type catalysis together with a spherical cap model system. This spherical cap model system had the advantage that a straightforward direct calcination of a hydrated $LaCl_3$ salt could be used to obtain the LaOCl phase whilst obtaining a model system morphology relevant to the industrially used spherical catalyst particles.

However, direct calcination of a hydrated bulk $LaCl_3$ salt will lead to large chunks of LaOCl and typically La_2O_3 due to the immense amounts of H_2O coming off that leads to further hydrolysis, even under a flow of dry air. Alternatively, we initially tried the synthesis method used by Peringer *et al.,* where an amine-base such as NH_4OH or tetraalkylaluminium hydroxide (ethyl, propyl or butyl) was added dropwise to an aqueous solution of $LaCl_3$ [11] All though this provides relatively high surface areas on the order of 100 m^2/g, scanning electron microscopy (SEM) results in Figure 5.5 show that both small and large particles are present with a non-spherical, plate-like morphology, which are the two main requisites for the development of a bulk LaOCl support matrix.
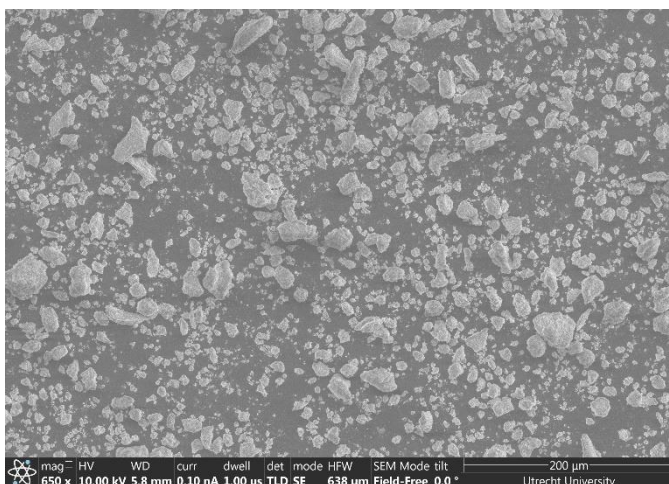

Figure 5.5 Scanning electron microscopy (SEM) image of a LaOCl batch synthesized according to the Peringer method with triethylammonium hydroxide as the precipitation base [11]. The particle size distribution ranges from particles of several microns in size to over a hundred microns as well as a rocky, non-spherical particle morphology.

Understanding that aqueous $LaCl_3$ solutions precipitate immensely fast upon the addition of a base several other routes were explored such as precipitation with urea, where hydrolysis of urea occurs above 60 °C in a homogeneous manner throughout the solvent, sugar-templated hydrothermal synthesis and ultrasonic spray-pyrolysis. The urea method yielded similar results as through the addition of the organic bases. The sugar-templated hydrothermal synthesis (StHS) route with sucrose as the sacrificial template, did provide highly spherical particles as shown in Figure 5.6 but the chemical phase obtained was either a lanthanum (oxy)carbonate intermediate or when increasing the calcination temperature to a La_2O_3 end-product instead of LaOCl.
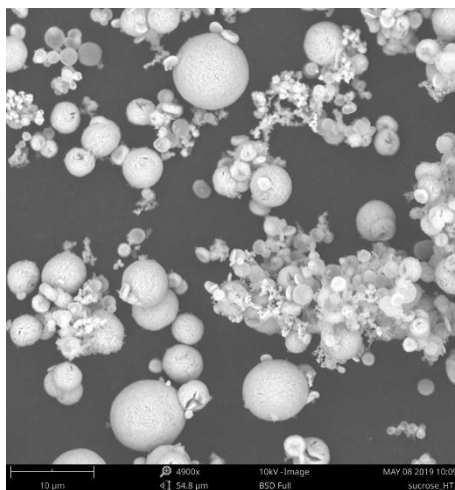

Figure 5.6 Scanning electron microscopy (SEM) image of a LaOCl batch synthesized according to the sugar-templated hydrothermal synthesis (StHS) route using sucrose as the sacrificial template. A combination of highly spherical particles of several microns in diameter as well as more hemoglobin-shaped particles were obtained through this route. Unfortunately, the chemical phase after burning off the sacrificial template was either a lanthanum (oxy)carbonate or La_2O_3.

The next step and final method developed for the synthesis of LaOCl microspheres is based on ultrasonic spray pyrolysis. In this method, the ultrasonic probe acts as a nebulizing agent to create a fine mist of H_2O droplets on the order of a few microns in diameter that contain the solute, in this case $LaCl_3 * 7H_2O$ and cetrimonium bromide (CTAB) as a templating agent to improve the porosity and surface area of the final powder. This fine mist is then pushed into the tube oven set at a certain temperature high enough to cause the chemical transformation of $LaCl_3 * 7H_2O$ to LaOCl using a carrier gas such as synthetic air or pure N_2. Finally, the products are collected in several flasks set in series containing solvents such as ethanol or H_2O and after filtration, washing steps and a drying or additional calcination procedure (if using N_2 flow to burn of the remaining and transformed CTAB template inside the pore network) the LaOCl microspheres are obtained. In Figure 5.7 the ultrasonic spray pyrolysis setup build in-house is shown.
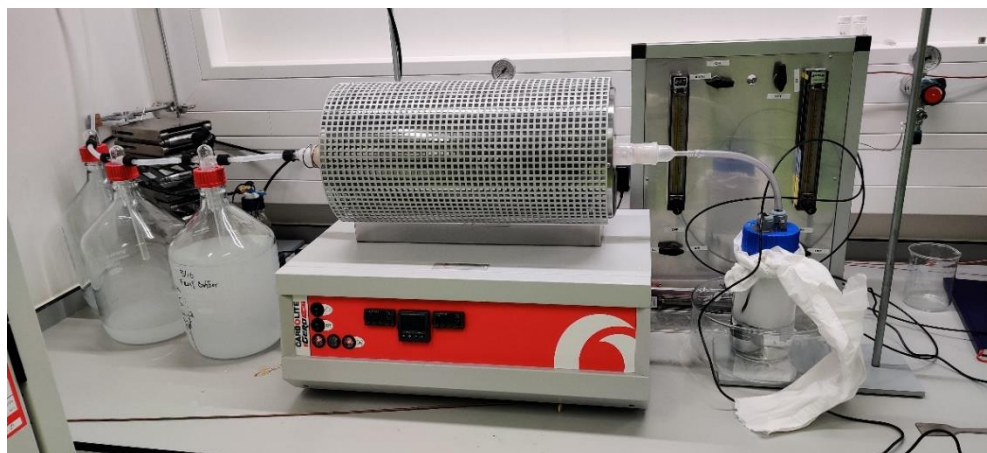
Figure 5.7 Lay-out of the ultrasonic spray-pyrolysis set-up utilized for the synthesis of LaOCl microspheres. On the right side the ultrasonic nebulizer can be seen within the aqueous LaCl$_3$ solution in the tubing for carrier gas in (black tubing) and LaCl$_3$ mist to the tube oven (transparent tubing). The tube oven is set at a temperature typically between 500-900 °C and with either a synthetic air or pure N$_2$ carrier gas. Finally, on the left side the LaOCl microspheres and by-products such as HCl are collected in several washing flasks set in series mode. Depending on the carrier gas, a final calcination step was utilized to burn off residual template (CTAB derived) molecules.

Several conditions can be played with to tune the final particle morphology as well as porosity and surface area including temperature of the tube oven, flow-rate (thus residence time), concentration of the LaCl$_3$ salt and type of carrier gas (synthetic air versus N$_2$). All though a large screening of the effect of these synthesis parameters is still ongoing, below in Figures 5.8 to 5.10 respectively SEM and TEM images as well as the X-ray diffractogram and N$_2$ physisorption derived pore size distribution are given for a LaOCl batch prepared at the following conditions: tube oven temperature of 700 °C using a pure N$_2$ carrier gas at 750 mL/min with a 10:1 molar ratio of LaCl$_3$ (0.27M) to CTAB in demineralized H$_2$O followed by a final calcination step of 500 °C with 5 °C/min ramp and 4 h hold time after the filtration and washing steps to remove the CTAB-derived template. The BET surface area and pore volumes obtained from N$_2$ physisorption for a typical batch prepared under the above-mentioned experimental conditions are on the order of 77 m^2/g and 0.3 cm^3/g, respectively.
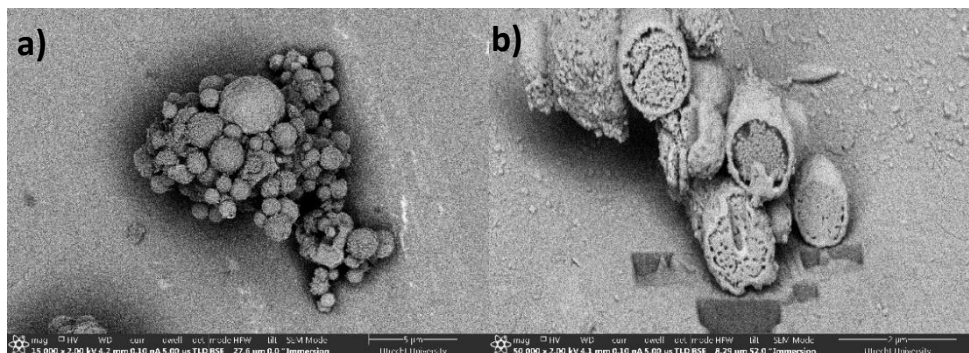
Figure 5.8 Focused-ion beam scanning electron microscopy (FIB-SEM) images showing in a) an overview of several LaOCl microspheres ranging from sub-micron up to 5 microns in diameter and in b) the cross-section of several microspheres where the highly porous interior structure can be observed.
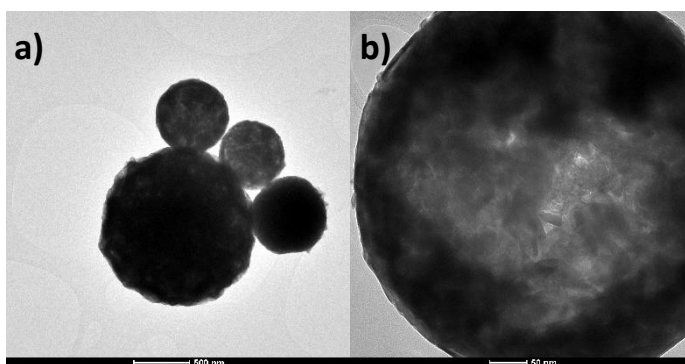
Figure 5.9 Transmission electron microscopy (TEM) images showing in a) several LaOCl microspheres and in b) zoom-in on a different single microsphere where LaOCl nano-platelets can be seen at the interior core of the particle. These microspheres were imaged without any cross-sectional preparation techniques.
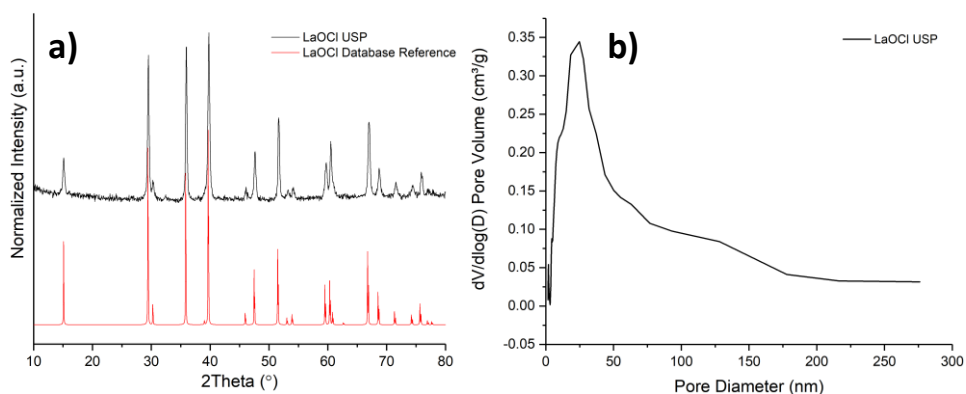
Figure 5.10 a) X-ray diffractogram showing the crystalline pure phase of LaOCl after ultrasonic spray pyrolysis (in black, LaOCl USP) at the typical experimental conditions described above versus that of a LaOCl database reference. b) N_2 physisorption data of the pore size distribution of the same LaOCl batch.

Initial SEM results of a ethylene polymerization performed on a LaOCl USP batch (without CTAB as template) is given in Figure 5.11 and shows the superb imaging contrast obtained between polymer and LaOCl phases when collecting backscattered electron signals. $TiCl_4$ grafting was performed under Schlenk-line conditions with a large excess of 30 v/v% $TiCl_4$ in heptane at 100°C for 2 hours followed by extensive washing with toluene (since $TiCl_4$ obtains a dark orange colour in toluene, which makes it an useful indicator for washing). Finally, the Ti/LaOCl catalyst was vacuum dried and stored in a N_2-filled glovebox operating at <1 ppm H_2O and O_2. Ethylene polymerization was performed at 10 bar ethylene pressure and 80 °C for roughly ten minutes using 50 mg catalyst in 10 mL heptane and a large excess of triethylaluminium (as Ti wt% isn't determined yet). The determined yield of this batch was about 30 g PE per g catalyst due to clogging of the small volume autoclave by the formed polyethylene. Benchmark ethylene polymerization testing of these Ti/LaOCl USP catalysts with conventional $MgCl_2$-based Ziegler polyethylene catalysts is ongoing.

Considerable research efforts are required to both fully optimize the LaOCl USP method for the fine-tuning of particle morphology, particle size distribution and improve the porosity towards that of the Peringer *et al.,* base precipitation method [11] and finally to study the nature of the Ti^{3+} active site on the LaOCl surface to which important questions remain: to which LaOCl crystal lattices does it preferentially coordinate? Is the nature of the active site similar to that of Ti^{3+} supported on $MgCl_2$? What is the activity of Ti/LaOCl as compared to a conventional $MgCl_2$-based Ziegler-type catalyst? Can Ti/LaOCl also polymerize propylene into isotactic polypropylene (with or without donors added)?

However, based on the superb imaging contrast observed between LaOCl and polyethylene and the excellent moisture stability, it would be highly interesting to use the ethylene polymerized LaOCl frameworks for the X-ray nanotomography techniques introduced in this PhD Thesis for α-olefin polymerization. Not only would it simplify the overall methodology since the polymerized catalyst can simply be handled under ambient conditions, it will also provide exceptional XRF data-quality due to the La Lα_1 emission energy at 4651 eV. All though this will overlap with the Ti active site, it's not a problem since Ti was used as a marker for the catalyst phase in Chapter 2 (at only a few wt% loading) and now the entire catalyst support matrix becomes a marker for XRF! Additionally, it will also help for the PXCT data-quality as the electron density of the LaOCl phase will be higher than that of $MgCl_2$ and therefore provide a stronger contrast between catalyst and polyolefin phases.
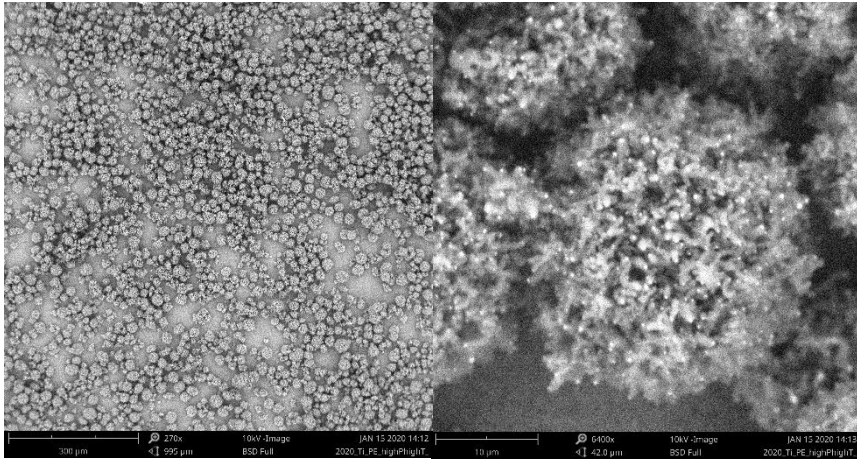
Figure 5.11 Scanning electron microscopy (SEM) images of initial ethylene polymerization results on a LaOCl USP batch (without CTAB as template to improve porosity of pristine LaOCl) on a) overview of many polyethylene-catalyst composite particles and b) zoom-in on a single particle where the white bright dots represent the fragmented catalyst phase and the long fibers observed are the formed polyethylene. The polyethylene (PE) yield is ~30 g PE per g catalyst.

5.2.3 Development of Fluorescently-Labelled Internal and External Donors MgCl$_2$ Crystals Grown on Si-based Substrates

The inspiration for Chapter 4 came from the works of Andoni *et al.,* on the synthesis of well-defined MgCl$_2$ crystals grown on SiO$_2$/Si(100) substrates using different internal donor [12-15]. They observed that diether-based donors yield exclusively 120° angles between the exposed lateral facets of these crystals whereas mono-and-diester-based donors were able to yield both 90° and 120° angles on the exposed lateral facets. This was a visual confirmation that diether-based donors coordinated most likely exclusively to the (110) lattices of MgCl$_2$ whereas ester-based donors can coordinate to both the (110) and (104) lattices as shown with theoretical calculations [16].

In parallel to the development of the LaOCl spherical cap model system to showcase a moisture stable Ziegler-type support matrix, experiments were performed towards the spin-coating and subsequent solvent vapor annealing (SVA) of a mixture of anhydrous MgCl$_2$ and different fluorescently labelled internal donors dissolved in an anhydrous alcohol inside a N$_2$-controlled glovebox on a Si(100) substrate.

AFM images of MgCl$_2$ crystals grown under varying experimental conditions with non-labelled internal donors are given in Figure 5.12. As is shown, different reaction conditions such as the SVA temperature and the use of pure or MgCl$_2$ saturated ethanol in the SVA step can have significant influences on the morphological growth of the MgCl$_2$ crystals.

With the successful growth of well-defined MgCl$_2$ crystals using non-labelled internal donors, the next step was to synthesize these well-defined MgCl$_2$ crystals with fluorescently labelled internal donors. This would then allow us a route to provide direct evidence for the coordination of fluorescently labelled diesters and diethers to the exposed lateral facets of MgCl$_2$ that exhibit a specific angle (90° versus 120°) using confocal fluorescence microscopy (CFM). The chemical structure of these fluorescently labelled donors is shown in Figure 5.13. Additionally, the interaction of these fluorescently labelled internal donors with the co-catalyst could then be studied *in-situ* with the CFM using specially adapted Linkam® cells. This would then provide visual proof that diester donors are indeed extracted from the MgCl$_2$ surface due to coordination and reaction with trialkylaluminium co-catalyst species whereas diethers are typically stable against the co-catalyst. By using mixed systems of fluorescently labelled diesters and diethers, the preferential removal of the diester could then be linked to the exposed lateral facets of the MgCl$_2$ crystal. Some initial CFM results on the coordination of fluorescently labelled internal donors to MgCl$_2$ are shown in Figure 5.14. Due to the low solubility of these fluorescently labelled internal donors in ethanol, a switch had to be made from pure ethanol as a spin-coating solvent to a 50/50 v% mixture of ethanol and iso-propanol. As can be seen especially from the AFM image in Figure 5.14, is that the morphology of these crystals are poorly defined as opposed to those shown in Figure 5.12. The most likely reason is that at these donor concentrations, a significant amount of pi-stacking occurs from the perylene tags that inhibits proper crystal growth. This

164

is also evidenced by the red-shifted CFM emission spectrum where the emission band is centered around 600 nm and in literature is around 474 nm (all though there it is measured in MeCN) [17].

Therefore, whereas this model system shows great potential to study the interplay between the internal donors and the exposed lateral facets of $MgCl_2$ crystals before (synthesis) and during propylene polymerization significant improvements are required to obtain fluorescently labelled internal donors − $MgCl_2$ crystals with the quality as those fabricated with non-labelled internal donors.
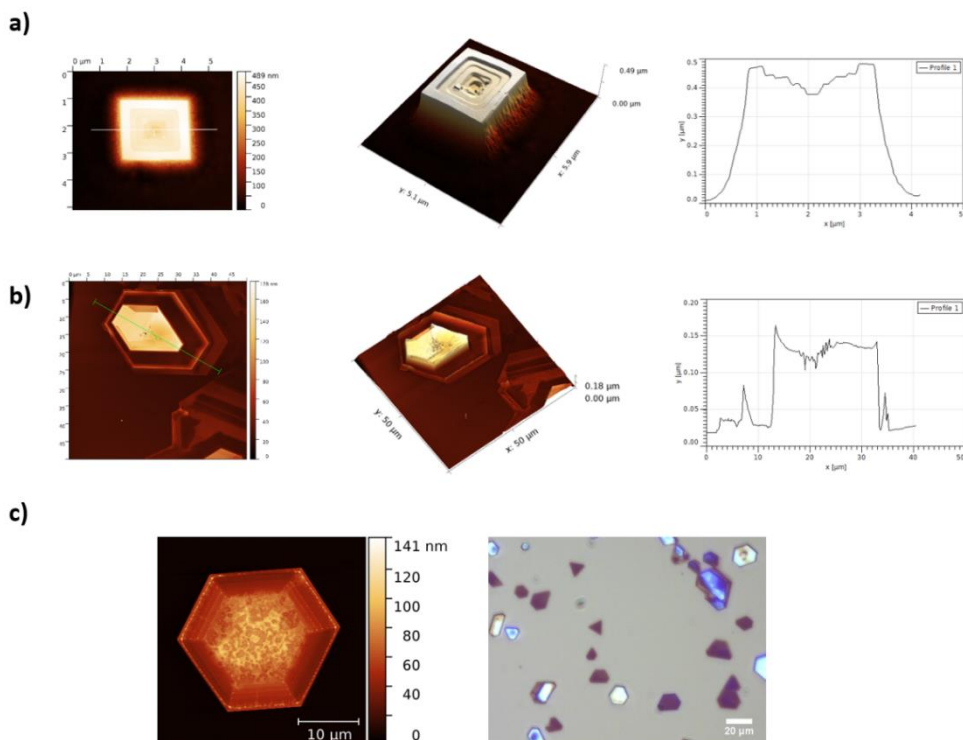
Figure 5.12 Atomic force microscopy (AFM) images of $MgCl_2$ crystals grown on a Si(100) substrate with diisobutyl phthalate (DIBP) as an internal donor from a subsequent spin-coating and solvent vapour annealing (SVA) based on Andoni *et al.* [13,14]. A) Top-view & 3-D rendered AFM images and extracted line-profile of a $MgCl_2$ crystal showing exclusively 90 ° angles between exposed lateral facets and an internal stair-case growth mechanism. Reaction conditions: 10 mM $MgCl_2$, 1 mM DIBP in ethanol spin-coated at 2800 rpm for 30 s followed by SVA at 60 °C for 3 hours using $MgCl_2$ saturated ethanol. B) Top-view & 3-D rendered AFM images and extracted line-profile of a $MgCl_2$ crystal showing exclusively 120 ° angles between exposed lateral facets. Reaction conditions: same as for **A** but pure ethanol used during the SVA step. C) Top-view AFM image of a single $MgCl_2$ crystal and optical microscope image of several $MgCl_2$ crystal showing different crystal morphologies. Reaction conditions: 10 mM $MgCl_2$, 1 mM DIBP in ethanol spin-coated at 2000 rpm for 30 s followed by SVA at 50 °C for 3 hours using $MgCl_2$ saturated ethanol.
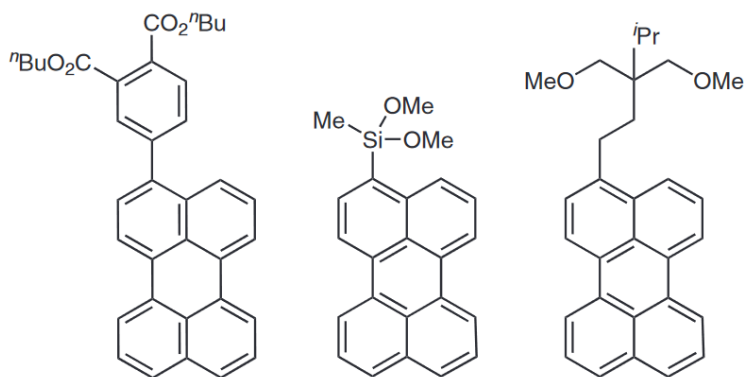
Figure 5.13 Chemical structures of the fluorescently labelled donors interesting to study with the MgCl$_2$ well-defined crystal model system of Andoni *et al.* From left to right, the diester internal, silane external and diether internal donors. The fluorescent tag is a perylene unit with a characteristic emission band typically around 400-500 nm region. Based on [17].
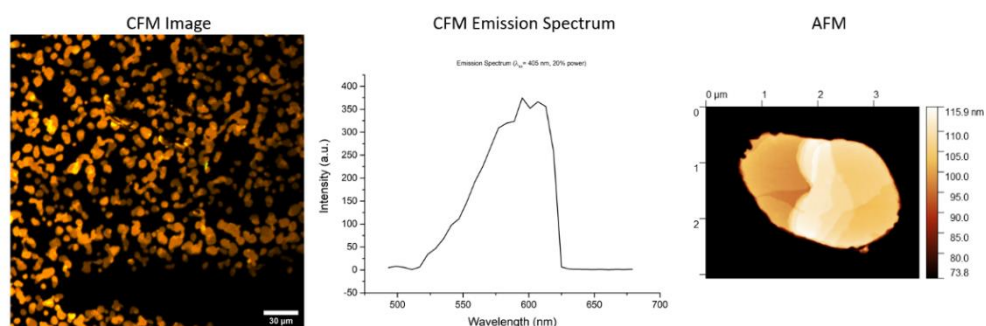
Figure 5.14 From left to right: confocal fluorescence microscopy (CFM) image with a 405 nm excitation wavelength of MgCl$_2$ crystals grown with the fluorescently labelled diester internal donor from Figure X at a 10:1 molar ratio (20 mM MgCl$_2$) in a 50/50 v% ethanol/iso-propanol mixture at 2000 rpm for 30 seconds followed by solvent vapour annealing at 60 °C for 3h using pure ethanol. Then the CFM emission spectrum is given, which shows a clear red-shifted spectrum due to pi-stacking of the perylene tags as opposed to the emission spectra given by Guzeev *et al.* [17]. Finally an atomic force microscopy image is given for one of the fluorescently labelled internal donor – MgCl$_2$ crystals, which shows that as opposed to the use of non-labelled internal donors a poorly defined MgCl$_2$ crystal is obtained under these reaction conditions.

5.3 Nederlandse Samenvatting

Het doel van deze PhD scriptie was drievoudig: (1) Het beter begrijpen van het fragmentatiegedrag van industrieel relevante Ziegler-gebaseerde polyolefine katalysatoren. (2) De ontwikkeling en optimalisatie van een methodologie voor het hanteren en meten van de zeer water-gevoelige en relatief lage *Z*-contrast gevende polyolefine katalysatoren met Röntgenstraling nanotomografie. (3) De ontwikkeling van een relevante Ziegler-gebaseerde drager materiaal met een sterker *Z*-contrast ten opzicht van het originele drager materiaal voor het beter in kaart brengen van het fragmentatiegedrag met verschillende meettechnieken.

In **Hoofdstuk 1** is het veld van polyolefine katalyse geïntroduceerd met een kort, historisch overzicht over de ontdekking en ontwikkeling van de niet-katalytische lage-dichtheid polyethylene route en daaropvolgende katalytische routes naar andere polyethyleen types en isotactisch polypropyleen (iPP). Daaropvolgend wordt de Ziegler-gebaseerde katalysatorfamilie geïntroduceerd met de nadruk op hoe belangrijk katalysatorfragmentatie is tijdens het α-olefine polymerisatieproces. Hiermee wordt zowel een minimum polymerisatiesnelheid gegarandeerd als een goede controle verkregen over het proces om reactor vervuiling te voorkomen. Een korte samenvatting is daarna gegeven over meerdere literatuur studies betreffende het bestuderen van het katalysatorfragmentatiegedrag met voornamelijk scannende elektronen microscopie (SEM) en Röntgenstraling microtomografie op polyolefine (katalysator) deeltjes. Daarna worden Röntgenstraling nanotomografie technieken geïntroduceerd met een nadruk op ptychografie Röntgenstraling berekende tomografie (PXCT) en Röntgenstraling fluorescentie (XRF) nanotomografie die de ruimtelijke resolutie tussen de reeds-gebruikte Röntgenstraling microtomografie studies verbinden met die van elektronen microscopie.

In **Hoofdstuk 2** wordt Röntgenstraling nanotomografie geïntroduceerd als analytische techniek voor het bestuderen van het fragmentatiegedrag van polyolefine katalysatoren. Hier wordt de focus gelegd op het bestuderen van een iPP Ziegler-Natta composietdeeltje van 40 micron in diameter verkregen bij een polymeer opbrengst van 9.2 g iPP per g katalysator. Een gecorreleerde PXCT en XRF nanotomografie opstelling bij de DESY P06 bundellijn werd gebruikt om zowel de elektronendichtheid (vanuit PXCT) en verschillende chemische elementen (vanuit XRF nanotomografie) in 3-D in kaart te brengen. Het laden van de Ziegler-Natta propyleen gepolymeriseerde katalysatordeeltjes in polyimide capillairen binnen inerte omstandigheden en opeenvolgend verzegelen met een epoxy lijm was cruciaal om het hydrateren van het $MgCl_2$ kader te voorkomen. Dit zou anders tot de disintegratie van de katalysatorfase leiden. Toch werd stralingsschade geconstateerd als een functie van de blootstellingstijd waardoor slechts een gelimiteerd aantal bruikbare 2-D projecties beschikbaar was voor de tomografische reconstructie. Niettemin konden de 3-D volumes van zowel de PXCT en XRF nanotomografie datasets succesvol gereconstrueerd worden. De geschatte 3-D ruimtelijke resolutie is ter grootte van 500 nm voor de

reconstructies. De daaropvolgende analyse naar de distributie van Ti soorten, die als markeringen functioneren voor de katalysatorfase, lieten voor de eerste keer in 3-D direct bewijs zien voor de aanwezigheid van zowel de krimpende kern, ook wel laag-bij-laag genoemd, en de continu doorsnijdende fragmentatiemodellen. Deze twee fundamentele fragmentatiemodellen beschrijven hoe het katalysatordeeltje kan fragmenteren. Dit gebeurt of vooral aan het oppervlak door het pellen van de katalysatorsoorten als gevolg van de stress geïnduceerd door de lokaal gevormde polyolefine (krimpende kern) of door de gehele kern in opeenvolgende kleinere fragmenten (continu doorsnijdend). Uiteindelijk, werd het continu doorsnijdende fragmentatiemodel als het dominerende model gevonden voor het totale fragmentatiegedrag van dit specifieke katalysatordeeltje na milde polymerisatie condities. Een korte samenvatting van deze bevindingen is geïllustreerd in Figuur 5.4.
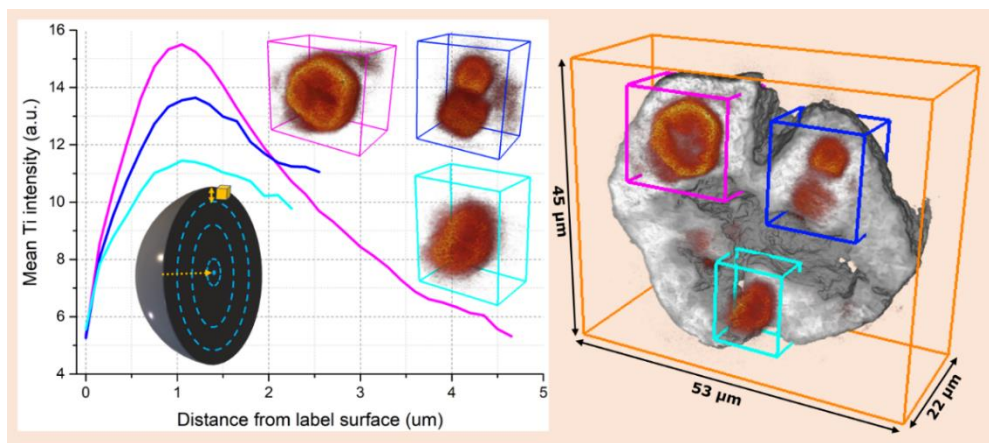
Figuur 5.4 De radiale distributie alsmede de volume weergave met een snijvlak om het binnenste te laten zien van drie geselecteerde Ti clusters in rood (XRF nanotomografie dataset) en de totale volume in grijstinten die zowel het composiet van de isotactisch polypropyleen en katalysatorfases weergeeft. De radiale distributies binnen zowel de grootste Ti clusters als die van alle Ti soorten door het composiet deeltje heen, werden gebruikt om het fragmentatiegedrag van dit Ziegler-Natta katalysatordeeltje te bestuderen.

In **Hoofdstuk 3** is via twee manieren de methodologie van Hoofdstuk 2 verbeterd om een beter begrip te krijgen van het fragmentatiegedrag van polyolefine katalysatordeeltjes. Ten eerste, werden overgebleven oplosmiddelmoleculen succesvol verwijdert. Hierdoor konden 360 2-D projecties met een 0.5 graad rotatie hoek bemachtigd worden. Dit leidde tot een geschatte 3-D ruimtelijke resolutie van 74 nm voor de gehele PXCT dataset. Bovendien kon door het zorgvuldig selecteren van het Ziegler katalysatorsysteem, met een gemiddelde deeltjes grootte van circa 3 micron, een volledige reconstructie gemaakt worden van meer dan 434 ethyleen gepolymeriseerde katalysatordeeltjes (bij een polymeer opbrengst van 3.4 g HDPE per g katalysator). Dit opende een route voor de statistisch relevante analyse van het fragmentatiegedrag van een grote groep deeltjes. Door het

gebruikmaken van een markering-gebaseerd waterscheidingssegmentatie, konden deze 434 composiet deeltjes succesvol van elkaar gescheiden worden als individueel gelabelde deeltjes in het 3-D volume. Opeenvolgende *k*-gemiddelde clusteringsanalyse stelde ons in staat om een onderscheid te maken tussen HDPE-rijke, katalysator-rijke en zeer gemixte HDPE-katalysatorfases. Hierdoor kon de mate van katalysatorfragmentatie bestudeerd worden binnen deze groep deeltjes. Hieruit bleek dat er een grote heterogeniteit is in de progressie van katalysatorfragmentatie binnen deze groep. Deeltjes met een lage progressie van katalysatorfragmentatie lieten vooral een krimpende kern type van fragmentatiegedrag zien, terwijl voor deeltjes met een hoge progressie van katalysatorfragmentatie de continu doorsnijdende type als dominerend werd bevonden voor het fragmentatiegedrag. In Figuur 5.5 zijn zowel de volume weergave van de succesvol gescheiden 434 composietdeeltjes weergegeven na het gebruik van een markering-gebaseerde waterscheidingssegmentatie en de resultaten van de *k*-gemiddelde clusteringsanalyse met een zoom-in in de interieur van een enkele composietdeeltje.
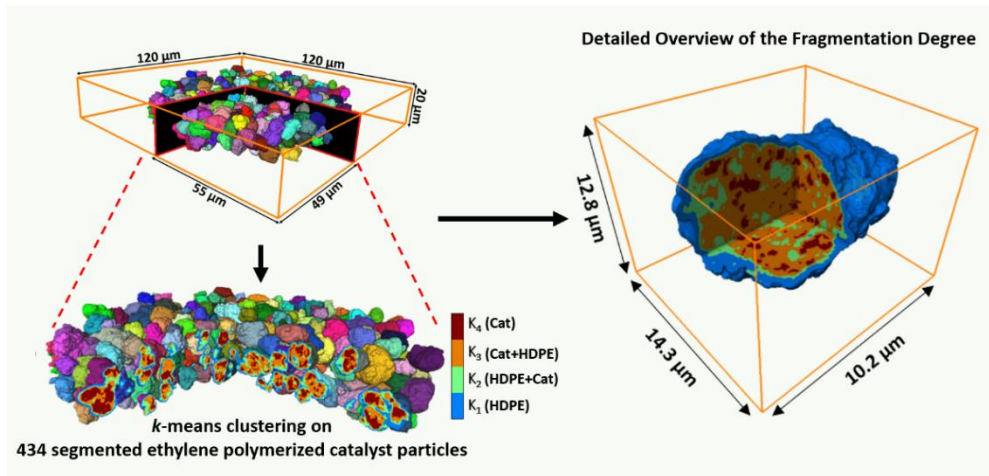
Figuur 5.5 Volume weergave van de 434 ethyleen gepolymeriseerde katalysatordeeltjes na het gebruik van een markering-gebaseerde waterscheidingssegmentatie algoritme om elke deeltje te scheiden en te labelen. Daaropvolgend, werd een *k*-gemiddelde clustering algoritme gebruikt om hoge-dichtheid polyethyleen (HDPE, K_1) en katalysator (K_4)-rijke fases te identificeren alsmede gemixte fases van HDPE en katalysator ($K_{2,3}$). Deze *k*-clusters werden gebruikt om het fragmentatiegedrag binnen de gehele groep te bestuderen. Uiteindelijk wordt de distributie van deze *k*-clusters weergegeven in het interieur van een enkele composietdeeltje om het fragmentatiegedrag van het katalysatordeeltje te laten zien.

In **Hoofdstuk 4** wordt LaOCl geïntroduceerd als een dragermateriaal om een verbeterd *Z*-contrast te geven voor het bestuderen van het katalysatorfragmentatiegedrag ten opzichte van het conventioneel gebruikte $MgCl_2$ dragermateriaal. Terwijl $MgCl_2$ zeer hygroscoop is, wat grote beperkingen met zich meebrengt voor de meetcondities van vele meettechnieken, laat LaOCl een betere stabiliteit zien tegen vocht. Echter, de chemie van LaOCl en van de mogelijke voorlopers (chloride en nitraat zouten) is enorm verschillend van $MgCl_2$. Hierdoor kunnen de reeds ontwikkelde conventionele synthese routes voor zeer sferische $MgCl_2$ deeltjes niet direct gebruikt worden om sferische LaOCl deeltjes te vormen. In plaats daarvan, is een nieuw bolkap modelsysteem door ons geïntroduceerd, die in staat is om de vorm van een sferisch deeltje na te bootsen. Daarnaast wordt de LaOCl chemische fase direct in één stap bemachtigd na het spin-coaten en calcineren van een $LaCl_3$ oplossing op een hydrofiel/hydrofoob patroonvormig Si(100) substraat. Daardoor vormt de introductie van dit bolkap modelsysteem voor polyolefine katalyse een brug tussen de conventioneel gebruikte planaire dunne laag modelsystemen en die van de industrieel relevante sferische katalysatordeeltjes. Door het gebruikmaken van een gereedschapskist van geavanceerde chemische meet-en-spectroscopie technieken, kon de wisselwerking tussen de formatie van polyethyleen binnen het porienetwerk van de LaOCl bolkappen en de daaropvolgende fragmentatiegedrag van deze LaOCl bolkappen in detail bestudeerd worden. Vibrationele microscopie technieken gebaseerd op Raman microscopie en foto-geïnduceerde kracht microscopie (een gecorreleerde nano-IR spectroscopie techniek met atoom kracht microscopie) alsmede gefocusseerde-ionen straal scannende elektronen microscopie, Röntgen foto-elektron spectroscopie en time-of-flight secundaire ionen massa spectrometrie, lieten de aanwezigheid zien van zowel polyethyleen fibers geëxtrudeerd vanuit scheuren op het externe oppervlak en de vorming van dichte polyethyleen fases binnen het poreuze netwerk van de LaOCl bolkappen. Deze bevindingen werden daarna gecorreleerd aan het fragmentatiegedrag van het LaOCl kader dat liet zien dat zowel de krimpende kern en continu doorsnijdende fragmentatiemodellen aanwezig zijn bij lagere polymerisatietijden. Bij langdurige polymerisatietijden en volledige disintegratie van de originele bolkappen morfologie, is de continu doorsnijden fragmentatiemodel dominerend geworden voor het gehele fragmentatiegedrag, wat hoogstwaarschijnlijk laat zien dat massatransport limitaties veroorzaakt door de initiële lage fragmentatiesnelheid, overwonnen werden. In Figuur 5.6, is dit LaOCl bolkappen modelsysteem weergegeven samen met de geavanceerde chemische meet-en-spectroscopie gereedschapskist, die werd gebruikt om het ethyleen polymerisatiegedrag te bestuderen.

170
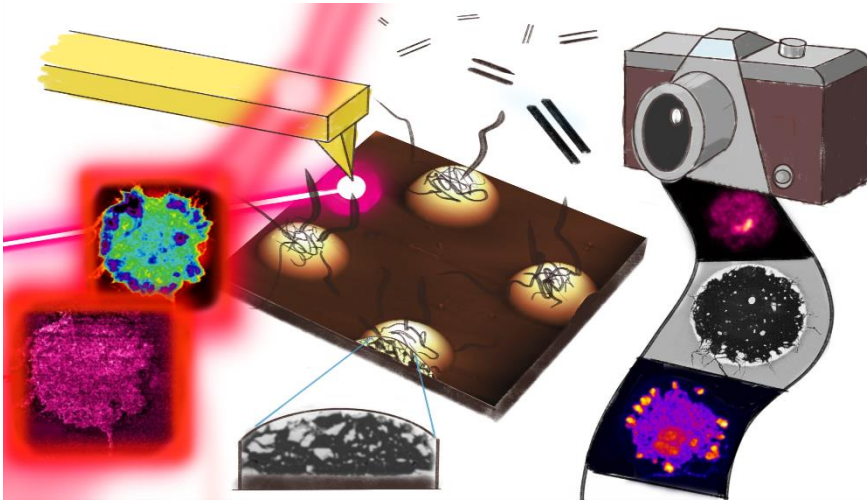
Figuur 5.6 Een schematische weergave van het bolkap modelsysteem op een Si(100) substraat (donkerbruin) door gebruikmakend van een LaOCl kader (lichtbruine bolkappen) als een drager materiaal voor een Ziegler-gebaseerde katalysator voor de polymerisatie van ethyleen (monomeren en polyethyleen fibers zijn weergegeven als donkergrijs). De geavanceerde gereedschapskist met verschillende meettechnieken "vangt" de wisselwerking en relatie tussen polyethyleen groei en LaOCl kader fragmentatie zoals weergegeven in de camera-rol.

5.4 References

1. Di Martino, A., Broyer, J., Spitz, R., Weickert, G., McKenna, T.F., A Rapid Quenched-Flow Device for the Characterisation of the Nascent Polymerisation of Ethylene under Industrial Conditions, *Macromol. Rap. Commun.*, **2005**, 26, 215-220.
2. Machado, F., Lima, E.L., Pinto, J.C., McKenna, T.F., Evolution of the Initial Stages of Gas-Phase Ethylene Polymerizations with a SiO_2-Supported Ziegler-Natta Catalyst, *Macromol. React. Eng.*, **2009**, 3, 47-57.
3. McKenna, T.F.L., Tioni, E., Ranieri, M.M., Alizadeh, A., Boisson, C., Monteil, V., Catalytic olefin polymerization at short times: Studies using specially adapted reactors, *Can. J. Chem. Eng.*, **2013**, 91, 669-686.
4. Veselý, M., Valadian, R., Lohse, L.M., Toepperwien, M., Spiers, K., Garrevoet, J., Vogt, E.T.C., Salditt, T., Weckhuysen, B.M., Meirer, F., 3-D X-ray Nanotomography Reveals Different Carbon Deposition Mechanisms in a Single Catalyst Particle, *ChemCatChem*, **2021**, 13, 2494-2507.
5. Su, Z., De Andrade, V., Cretu, S., Yin, Y., Wojcik, M.J., Franco, A.A., Demortière, A., X-ray Nanocomputed Tomography in Zernike Phase Contrast for Studying 3D Morphology of $Li-O_2$ Battery Electrode, *ACS Appl. Energy Mater.,* **2020**, 3, 4093-4102.
6. Horácková, B., Grof, Z., Kosek, J., Dynamics of fragmentation of catalyst carries in catalytic polymerization of olefins, *Chem. Eng. Sci.*, **2007**, 62, 5264-5270.
7. Huo, C., Ren, X.H., Liu, B.P., Yang, Y.R., Rong, S.X., Fractal Approach for Modeling the Morphology Evolution of Olefin Polymerization with Heterogeneous Catalysts, *J. Appl. Polym. Sci.*, **2003**, 90, 1463-1470.
8. Hammawa, H., Wanke, S.E., Gas phase olefin polymerization over supported metallocene/MAO catalysts: influence of support on activity and polydispersity, *Polym. Int.*, **2006**, 55, 426-434.
9. Hammawa, H., Wanke, S.E., Influence of Support Friability and Concentration of α-Olefins on Gas-Phase Ethylene Polymerization over Polymer-Supported Metallocene/Methylaluminoxane Catalysts, *J. Appl. Polym. Sci.*, **2007**, 104, 514-527.
10. Lu, H., Xiao, S., Structure and behaviour of $SiO_2/MgCl_2$ bisupported Ziegler-Natta catalysts for olefin polymerization, *Macromol. Chem. Phys.,* **1993**, 194, 421-429.
11. Peringer, E., Tejuja, C., Salzinger, M., Lemonidou, A.A., Lercher, J.A., On the synthesis of $LaCl_3$ catalysts for oxidative chlorination of methane, *Appl. Catal. A,* **2008**, 350, 178-185.
12. Andoni, A., Chadwick, J.C., Milani, S., Niemantsverdriet, H.J.W., Thüne, P.C., Introducing a new surface science model for Ziegler-Natta catalysts: Preparation, basic characterization and testing, *J. Catal.,* **2007**, 247, 129-136.
13. Andoni, A., Chadwick, J.C., Niemantsverdriet, H.J.W., Thüne, P.C., A Preparation Method for Well-Defined Crystallites of $MgCl_2$-Supported Ziegler-Natta Catalysts and their Observation by AFM and SEM, *Macromol. Rap. Comm.,* **2007**, 28, 1466-1471.
14. Andoni, A., Chadwick, J.C., Niemantsverdriet, H.J.W., Thüne, P.C., The role of electron donors on lateral surfaces of $MgCl_2$-supported Ziegler-Natta catalysts: Observation by AFM and SEM, *J. Catal.,* **2008**, 257, 81-86.
15. Andoni, A., Chadwick, J.C., Niemantsverdriet, H.J.W., Thüne, P.C., Investigation of Planar Ziegler-Natta Model Catalysts Using Attenuated Total Reflection Infrared Spectroscopy, *Catal. Lett.,* **2009**, 130, 278-285.
16. Busico, V., Causà, M., Cipullo, R., Credendino, R., Cutillo, F., Friederichs, N., Lamanna, R., Segre, A., Van Axel Castelli, V., Periodic DFT and High-Resolution Magic-Angle-Spinning (HR-MAS) ^1H NMR Investigation of the Active Surfaces of $MgCl_2$-Supported Ziegler-Natta Catalysts. The $MgCl_2$ Matrix, *J. Phys. Chem. C*, **2008**, 112, 1081-1089.

17. Guzeev, B.A., Mladentsev, D.Y., Sharikov, M.I., Goryunov, G.P., Uborsky, D.V., Voskoboynikov, A.Z., Synthesis of Perylene-Tagged Internal and External Electron Donors for Magnesium Dichloride Supported Ziegler-Natta Catalysts, *Synthesis*, **2019**, 51, 1399-1407.

Appendix A: List of Abbreviations

AFM	Atomic force microscopy
a-PP	Atactic polypropylene
ART	Algebraic reconstruction technique
CDI	Coherent diffraction imaging
DESY	Deutsches Elektronen-Synchrotron
DLS	Diamond Light Source
DSC	Differential scanning calorimetry
E.D.	Electron density
EDX/ED	Energy dispersive X-ray spectroscopy
EPR	Ethylene-propylene rubber
ESD	Equivalent spherical diameter
F	Force constant
FBP	Filtered back projection
FCC	Fluid catalytic cracking
FIB	Focused-ion beam
FOV	Field of view
FP	Fragmentation parameter
FSC	Fourier shell correlation
FWHM	Full width at half maximum
GL30	A line-shape definition where 70% is Gaussian and 30% is Lorentzian
H	Horizontal
HDPE	High-density polyethylene
Hit-PP	Hemi-isotactic polypropylene
HWHM	Half width at half maximum
I	Current of the sputter beam
I.I.	Isotacticity
IART	Iterative algebraic reconstruction technique
ICP-AES	Inductively coupled plasma atomic emission spectroscopy
i-PP	Isotactic polypropylene
K1	k-means cluster representing a HDPE-rich phase
K2	k-means cluster representing a highly mixed phase of HDPE and catalyst with a higher contribution of HDPE phase
K3	k-means cluster representing a highly mixed phase of HDPE and catalyst with a higher contribution of catalyst phase
K4	k-means cluster representing a catalyst-rich phase
KB	Kirkpatrick-Baez
LDPE	Low-density polyethylene
LLDPE	Linear low-density polyethylene
MAO	Methylaluminoxane
MCR	Multivariate curve resolution
MDPE	Medium-density polyethylene
MWD	Molecular weight distribution
NCCs	Non-connected components

NLM	Non-local means
ODTS	Octadecyltrichlorosilane
PE	Polyethylene
PiFM	Photo-induced force microscopy
PSD	Particle size distribution
PXCT	Ptychographic X-ray computed tomography
PY	Polymer yield
QCL	Quantum cascade laser
ROI	Region of interest
SAM	Self-assembled monolayer
SART	Simultaneous algebraic reconstruction technique
SDD	Silicon drift detector
SE	Secondary electron(s)
SEM	Scanning electron microscopy
SIRT	Simultaneous iterative reconstruction technique
SLS	Static laser scattering
s-PP	Syndiotactic polypropylene
StHS	Sugar-templated hydrothermal synthesis
TEAL	Triethylaluminium
THF	Tetrahydrofuran
ToF-SIMS	Time-of-flight secondary ion mass spectrometry
UHMwPE	Ultra-high molecular weight polyethylene
USP	Ultrasonic spray pyrolysis
V	Vertical
VLDPE	Very low-density polyethylene
Vr	A fragmentation parameter based on the ratio of the total volume of the first three k-means clusters (K1,K2,K3) to the mean volume of the catalyst-rich K4 cluster.
wt%	Weight percentage
XCMT	X-ray computed micro-tomography
XCNT	X-ray computed nano-tomography
XPS	X-ray photoelectron spectroscopy
XRF	X-ray fluorescence
XRFT	X-ray fluorescence tomography
ΔE	Component splitting value
λ	Wavelength of the X-ray probe
φ	Pitch
Ψ	Sphericity
ψ	Yaw

Appendix B: List of Scientific Publications and Presentations

B1. Scientific Publications

Bossers, K.W.[*], Mandemaker, L.D.B.[*], Nikolopoulos, N., Rohnke, M., de Peinder, P., Terlingen, B.J.P., Liu, Y., Walther, F., Weckhuysen, B.M., A Ziegler-type Ethylene Polymerization Spherical Cap Model Reveals Polymer Crystallization Versus Catalyst Fragmentation Relationships, *submitted for publication*, **2021**.
* These authors contributed equally to this work.

Bossers, K.W.[*], Valadian, R.[*], Garrevoet, J., van Malderen, S., Chan, R., Friederichs, N., Severn, J., Wilbers, A., Zanoni, S., Jongkind, M.K., Meirer, F., Weckhuysen, B.M., Heterogeneity in the State of Fragmentation Within an Ensemble of Ziegler Catalyst Particles Using X-ray Nano-Tomography, *JACS Au*, **2021,** 1, 852-864.
* These authors contributed equally to this work.

Bossers, K.W., Valadian, R., Zanoni, S., Smeets, R., Friederichs, N., Garrevoet, J., Meirer, F., Weckhuysen, B.M., Correlated X-ray Ptychography and Fluorescence Nano-Tomography on the Fragmentation Behavior of an Individual Catalyst Particle during the Early Stages of Olefin Polymerization, *J. Am. Chem. Soc.,* **2020**, 142, 3691-3695.

B2. Oral and Poster Presentations at Conferences

"Correlated X-ray Ptychography and Fluorescence Tomography on the Fragmentation Behaviour of an Individual Catalyst Particle During the Early Stages of Olefin Polymerization", Oral presentation, NCCC, Noordwijkerhout, the Netherlands, March **2020**.

"Correlated X-Ray Ptychography and Fluorescence Nano-Tomography on the Fragmentation Behavior of an Individual Catalyst Particle during the Early Stages of Olefin Polymerization", Oral presentation, 26th North American Catalysis Society Meeting, Chicago, USA, June **2019**.

"Correlated X-ray Ptychography and Fluorescence Tomography on the Fragmentation Behaviour of an Individual Catalyst Particle During the Early Stages of Olefin Polymerization", Poster presentation, NCCC, Noordwijkerhout, the Netherlands, March **2019**.

"Correlated X-Ray Ptychography and Fluorescence Nano-Tomography on the Fragmentation Behavior of an Individual Catalyst Particle during the Early Stages of Olefin Polymerization", Poster presentation, International Winter School, Bardonecchia, Italy, January **2019**.

B3. Other Publications by the Author

Mayorga-González, R., Rivera-Torrente, M., Nikolopoulos, N., Bossers, K.W., Valadian, R., Yus, J., Seoane, B., Weckhuysen, B.M., Meirer, F., Visualizing Defects and Pore Connectivity within Metal-Organic Frameworks by X-ray Transmission Tomography, *Chem. Sci.,* **2021**, 12, 8458-8467.

Jongkind, M.J., Meirer, F., Bossers, K.W., ten Have, I.C., Ohldag, H., Watts, B., van Kessel, T., Friederichs, N., Weckhuysen, B.M., Influence of Metal-Alkyls on Early-Stage Ethylene Polymerization over a Cr/SiO_2 Phillips Catalyst: A Bulk Characterization and X-ray Chemical Imaging Study, *Chem. Eur. J.,* **2021**, 27, 1688-1699.

Piovano, A., Pletcher, P., Velthoen, M.E.Z., Zanoni, S., Chung, S.-H., Bossers, K.W., Jongkind, M.K., Fiore, G., Groppo, E., Weckhuysen, B.M., Genesis of $MgCl_2$-based Ziegler-Natta Catalysts as Probed with Operando Spectroscopy, *ChemPhysChem*, **2018**, 19, 2662-2671.

Van Ravenhorst, I.K., Vogt, C., Oosterbeek, H., Bossers, K.W., Moya-Cancino, J.G., van Bavel, A.P., van der Eerden, A.M.J., Vine, D., de Groot, F.M.F., Meirer, F., Weckhuysen, B.M., Capturing the Genesis of an Active Fischer-Tropsch Synthesis Catalyst with Operando X-ray Nanospectroscopy, *Ange. Chem. Int. Ed.*, **2018**, 57, 11957-11962.

Gutterød, E.S., Øien-ØDegaard, S., Bossers, K.W., Nieuwelink, A.-E., Manzoli, M., Braglia, L., Lazzarini, A., Borfecchia, E., Ahmadigoltapeh, S., Bouchevreau, B., Lønstad-Bleken, B.T., Henry, R., Lamberti, C., Bordiga, S., Weckhuysen, B.M., Lillerud, K.P., Olsbye, U., CO_2 Hydrogenation over Pt-Containing UiO-67 Zr-MOFs-The Base Case, **2017**, 56, 13206-13218.

Acknowledgements

Alas, after 4 years and a bit, the PhD life has come to an end for me. I have been at the ICC group for what feels like a lifetime and met so many people from all over the world in these past years. It was thanks to all of these kind hearts within and outside of ICC that made this PhD Thesis possible. If anything, my PhD has shown me the importance of teamwork and especially building a fantastic team that operates on the basis of friendship. I will never forget all of the friends I made along the way, to which I would like to pay a small tribute here.

To start, I would like to thank my promotor and professor, **Bert Weckhuysen**. You have taught me a great deal of what it means to be a scientist. That is, science isn't only about concocting recipes and experiments on the lab, it is much more. To become a successful scientist you need perseverance, to take responsibility, to show initiative, create a network and become a guide and mentor for those under you. I will never forget the talk we had at the "Zwijger" , of which the name is fittingly quite ironic, that convinced me to not give up and instead keep going during hard times I endured. I can only look back now with a big smile on these last four years with what we managed to achieve and especially how we achieved this with a fantastic team of colleagues both internally at ICC and through collaborations externally. I look forward to our scientific paths crossing again hopefully soon!

Secondly, I would like to thank the Doctoral Examination Committee consisting of, **prof. Eelco Vogt**, **prof. Pieter Bruijnincx**, **dr. Florian Meirer**, **prof. Andrew Beale** and **prof. Daniel Vanmaekelbergh** for carefully going through and assessing the quality of my PhD Thesis.

I would like to thank the entire staff of the now former ICC group consisting of, **Eelco Vogt, Krijn de Jong, Petra de Jongh, Frank de Groot, Florian Meirer, Freddy Rabouw, Eline Hutter, Ward van der Stam and Pieter Bruijnincx**. A special thanks to the administrative staff, **Dymph, Ilonka**, **Iris**, **Monique**, **Belén**, **Sandra** and **Brenda**, who are simply fantastic and always ready to provide help in any way they can!

This PhD Thesis wouldn't have been possible without all of my collaborators, both internally and externally, whom I'd like to thank and acknowledge. **Laurens Mandemaker**, it all started as one of those Friday afternoon experiments after another one of our countless brainstorming experiments as we went to the Spar for lunch. A spherical cap model system to have a morphologically relevant model system for whatever we could think off! We tried countless metal oxides until finally we hit the sweet spot with LaOCl. It was a fantastic journey where we complemented each other perfectly. I couldn't be more happy and proud than to have my final experimental chapter performed in collaboration with you. **Roozbeh Valadian**, it is thanks to you that I saw the gorgeous X-ray ptychography technique and together we realized that it would be worth a try to test on my polyolefin catalysts instead of the cumbersome absorption-contrast based techniques I was using. Well, I think it is safe

to say that our little test paid off quite well in the end! You are a fantastic coder, brilliant engineer and most of all the dictionary definition of a friend. I hope that in some way we can continue our collaborations for years to come, if only in the Hofman. **Bas Terlingen**, without you we would never have tried this crazy idea about LaOCl. It was a lot of fun and headaches in trying to optimize this material to obtain the needed morphology and other material properties for polyolefin catalyst. A fantastic teamwork that lead to some very interesting results with a lot of fun! **Florian Meirer**, you have taught me a great deal about X-rays, X-ray tomography, preparing beam-line proposals and improving my writing skills, a big thank you! **Jan Garrevoet**, you were crucial for us in the planning, executing and subsequent analysis of the ptychography and X-ray fluorescence data-sets. Thank you and your colleagues at DESY for the smooth and fun beam-trips we had over the years. **Nikos Nikolopoulos**, we spent so many days at the FIB-SEM-EDX and I will never get used to the immense skills you have and keep on demonstrating with this beautiful analysis tool. I had a fantastic time collaborating with you! **Marcus Rohnke**, you were a fantastic host and superb scientist to work together with and I highly enjoyed our visits to the JLU ToF-SIMS facilities over the years, many thanks for having us! **Felix Walther**, thank you for helping us out in such a short notice with a highly challenging XPS data-set, you performed a miracle for us! **Peter de Peinder**, many thanks for the fantastic help with the PiFM data-set. If I'm not mistaken, Laurens still owes you a crate of Westvleteren. **Silvia Zanoni, Maarten Jongkind and Joren Dorresteijn**, my buddies and polymer partners-in-crime. You guys were crucial for the smooth operation of all the beam-trips we had and I will never forget the amazing trips they turned out to be (especially with the world championship). **Yuanshuai Liu**, you were one of the kindest and brilliant people I had the chance to work together with. I wish you all the best in starting your own group back in China and I hope to visit you and your family there soon! **Jiadong Xiao**, you were a great teacher and mentor to synthesize metal oxide microspheres, which I greatly enjoyed!

This PhD Thesis was part of a larger project with partners from Maastricht University, Fontys Hogeschool Eindhoven, DSM and SABIC. I would like to thank **Marc van Zandvoort and Dimitris Kapsokalyvas** for the efforts we put into confocal fluorescence microscopy. Even though it didn't work out as hoped, I highly enjoyed our meetings, conversations and the knowledge you shared with me! **Peter Thüne**, you have taught me invaluable lessons in designing and fabrication planar model systems, for which I am extremely grateful. **Sang-Ho Chun**, it is a shame we only worked together for one year but I had a blast of a time learning as much as I could from you! **Gert de Cremer**, you were a fantastic sparring partner for the polyolefin results and especially for teaching me about confocal fluorescence microscopy. **An Philippaerts, Sven Kreisig and Joachim Loos**, thank you for the meetings and discussions we had at the start of my PhD. **Arno Wilbers**, thank you for providing us with the extra knowledge and insights for the X-ray tomography reconstructions. **Remy Smeets**, I must have made you run countless pre-polymerizations for our joined X-ray nanotomography efforts but you were always motivated and happy to help us out, thank you! **Sander Janssen**, I must have wasted an immense amount of resources by clogging the needles in the PPR experiments you run for us but you remained ever-willing and friendly

to help us, thank you! **Robert Chan**, it was simply fantastic to have worked together with you on my visits to SABIC and I highly enjoyed all chatting during the small coffee breaks, will see you soon in Eindhoven! **John Severn**, you are a walking library possessing perhaps more knowledge than the famed library of Alexandria. You were always willing to help me with whatever silly questions I had and I'm extremely grateful to have had you as a mentor in these past four years, thank you! **Nic Friederichs**, I have come to realize you are a true polyolefin legend and perhaps an even better fisher! I couldn't even have imagined before starting the project that I would be able to collaborate with someone so open, friendly and welcoming. Your labs and resources were always open to me for whatever silly experiments we came up with. Together with John, your mentorship during these four years ensured my growth as a person and scientist, thank you!

I would like to thank the entire technical staff of ICC and of the EM unit for all the help provided over the years; **Ad vd E** and **Ad M**, **Marjan, Rien, Oscar, Pascal, Jan Willem, Herrick, Dennie, Joris, Jochem, Ramon, Hannie, Jules, Hans** and **Chris**.

Of course, this PhD Thesis relied on the polyolefin research sub-unit at ICC including (present and former) **Maarten Jongkind, Silvia Zanoni, Joren Dorresteijn, Alessandro Piovano, Yuanshuai Liu, Marjolein Velthoen, Peng Zhai, Paul Pletcher, Max Werny** and **Albaraa Falodah**. We all had one thing in common and that was the pain of working every day in a glovebox! Special thanks to my dear friend **Alessandro Piovano**, you were my mentor on Ziegler-Natta catalysis when you came for an internship in Utrecht during my first month as a PhD. Even though we only shared a few months, you taught me invaluable things and most of all I will never forget your kindness. I would also like to thank (our external polyolefin experts) **Elena Groppo** and **Silvia Bordiga** from the University of Torino, whom in the conferences that I have had the honor to meet on several occasions were beyond friendly and open to talk with.

One of the best things to have happened during this PhD journey was the birth of our multinational lunch group. It is thanks to you guys; **Frannie, Tota, Laurita, Seven-up, Fouadje, Abi-man**, **Illy, Nikos, Christia, Oscar, Valerio, Roman, Nathan, Livan, Remcolina, Bassie** and of course **Thee-Lau,** that I have been able to meet so many people from different nationalities and observe easy it is for us to form a coherent brotherhood, despite some of you hating pineapple pizza!

Pierre-François Vittoz, mon chéri, I will never forget our amazing nights in 't Pakhuis. With you I have made a true friend for life starting back when I was still doing my Master's in Utrecht. Will see you soon in France!

Christia "yiiiii" Jabbour, the legendary cook that manages to forget ingredients in a "only add water to this brownie recipe mixture". We must have walked to the moon and back by now as well as ate truckloads of gyros. I'm ready for the real kebab in Lebanon!

Oscar Daoura, also known as the Lebanese Sergio Ramos and my beard-brother. Now that we have tried all European Whisky's, perhaps it is time we move towards the Lebanese ones (in Lebanon!).

Francesco Mattarozzi, the man with the moustache. Thankfully, for the progress of my PhD research we were only roommates for a few months! I will never forget our evenings at Mick O'Connells and I'm afraid neither will my bank account.

Giorgio Totarella, Georgie. You were the best wrestling partner I ever had and unfortunately still haven't beat yet. Also you make some legendary limoncello.

Laura Barberis, Laurita. I don't think I have ever met such a sweet Italian soul who can erupt in absolute anger within 100 picoseconds when Francesco makes too much noise during a football match.

Savannah Turner, seven-up. You are an amazing sweetheart and an absolute TEM legend. I hope you forgive me for my Gaussian fitting skills to estimate spatial resolution.

Nikos Nikolopoulos, (*I'm quite sure I'm not allowed to put your nicknames here*). You are one fantastically and crazy Greek man. I'm still waiting for you to take me to Greece though and sample some of that real Gyros.

Silvia Zanoni, the mom of our group. You always took such great care of us on beam-trips and almost managed to make us eat healthy and exercise during those stressful days. It almost makes me want to go on a beam-trip again (all though I'm still sad I never went to Yosemite like you guys)!

Roozbeh Valadian, Illy. Our golden boy! You may have been the oldest of us but I always regarded you as a little kid brother. I will definitely miss our moments both at the beam-trips, next to each other in the office and of course at the Hofman where you showed your true potential.

Then a huge list will now appear of all the PhD and PD people I would like to thank with whom I've had some nice chats in the past years at the crappy coffee machines or on the labs; **Abishek, Ahmed, Ana, Anne-Eva, Ara, Baira, Bea M, Bea S, Carolien Vis, Caroline Versluis, Charlotte, Christa, Christine, Daan, Dmitrii, Donglong, Egor, Ellen, Erik, Fabianne, Florian, Frank, Frederique, Gang, Gareth, Guusje, Hebatalla, Hongyu, Ilse, Ina, Ioannis, Iris, Iván, Jeroen, Jessi, Joel, Jogchum, Joop, Joris, Jovana, Kai, Katarina, Katinka, Khaled, Kordula, Laura d K, Lennart, Lisette, Longfei, Luke, Mahnaz, Marianna, Marisol, Mark, Martin, Matteo, Matthias, Michael, Miguel, Nazila, Nienke, Nina, Nynke, Özgun, Pasi, Peter Bramwell, Peter Ngene, Petra, Rafael, Ramon, Robin, Rogier, Rocky, Romy, Roy, Sam, Sebastiaan, Shiyou, Shuang, Sophie, Stijn, Thomas, Tom, Wirawan, Xinwei, Yadolah, Yannick, Yaqi, Zafer, Zoran.**

Of course I would like to thank the Bachelor and Master students that I've had the honour of supervising during my time, **Livan Kort, Stefan van Vliet, Denise Pieper** and **Guido de Reijer**. I wish you all the best of luck in your on-going studies and career.

Hier moet ik dan toch even naar onze prachtige Nederlands taal over gaan om mijn dankbetuiging te geven.

Maarten Jongkind, wat ben jij toch een fantastische boer uit Amsterdam en omstreken. Gelukkig dat je besloot om je PhD in Utrecht te doen en niet in Amsterdam, want wat had ik anders toch een geweldig persoon gemist in mijn leven. Onze trips naar de U.S., waar we met 40 °C besloten om een 4 uur durende hike naar de top van Mount Diablo te doen en Bardonecchia, waar we geweldige biertap kunsten hebben laten zien, zal ik voor altijd meenemen in mijn gedachten. Nu nog samen naar Georgië!

Fouad Soulimani, je bent een ware legende. Al sinds dat Laurens en ik tijdens onze Master thesis voor je kantoor zaten, gaf je ons een warm welkom. Dat we nog vaak een bakkie pleur gaan drinken!

Joren Dorresteijn naar de maneschijn. Je bent de gedoodverfde opvolger en moet veel waar gaan maken. Geen druk maat. Wanneer gaan we tennissen?

Thomas Hartman, wat kan jij toch mooie illustraties maken! Onwijs bedankt voor het coverontwerp en alle andere plaatjes die je gemaakt hebt voor me. Nu nog samen op jacht naar ijzer.

Remco Dalebout, remmie. we lopen al sinds onze Bachelor samen rond op ICC. Jij, Lautje en ik zijn die driehoek die het al die jaren samen volgehouden hebben als een team. Ik zal nooit vergeten hoe jij op borrels en in de kroeg/club opeens willekeurig naar huis gaat zonder doei tegen ons te zeggen (en dat je dan 4 uur later ook daadwerkelijk pas thuis komt). Op naar het mannenweekend!

Bas Terlingen, bassie, de ballenman. Ik weet eerlijk gezegd niet of ik je slechte woorden grappen ga missen, maar ik geef je wel kudos voor je inzet (en vooral die legendarische Dojo van je).

Laurens Mandemaker, de maker van manden en keukens. Wat hebben wij het toch leuk en gezellig gehad deze jaren. Tot onze vreugde en waarschijnlijk spijt van de rest, werden wij in het begin van onze PhD naast elkaar gezet op de verdieping. Als ik de Master meereken, hebben we meer dan vijf jaar lang als twee rotjochies op ICC rondgelopen. Wat ik zo mooi vind, is dat wij naast herris schoppen toch ook juist zoveel samen hebben gewerkt op het lab. Want samen benutten wij onze creativiteit pas echt en hebben we ontelbare brainstorm sessies gevoerd (en nog steeds!). We vullen elkaar goed aan, jij de eeuwige optimist, ik die vervelende pessimist; en juist samen vormt dat die scherpte, passie en ambitie die je nodig hebt in een project. Ik zal nooit vergeten hoe we met roze koeken en zakken snoep in een klein hokje een strategische afweging maakte over welke AFM we wilden aanschaffen. Naast het onderzoek hebben we ook prachtige avonturen samen

beleefd. Zowel in de kroegen in Utrecht, op congressen in Noordwijkerhout en de hikes in Noorwegen. We moeten echt nog eens terug gaan naar Noorwegen en door de Lofoten kayakken. Lautje, met jou heb ik niet een vriend voor het leven gemaakt, maar een extra broer, bedankt voor alles!

Dan wil ik graag mijn familie en vrienden bedanken voor alle steun en hulp die ik de afgelopen vier jaar gekregen heb, vooral na het plotselinge overlijden van mijn vader, **Kees**, in de eerste week van mijn PhD. Ik mis je nog altijd grote vriend van me! Mijn lieve moeder, **Judith**, je stond altijd klaar en je hebt me er als een rots in de branding doorheen geholpen, bedankt! **Bas** en **Niels**, jullie zijn fantastische broers! **Cunera** en **Floor**, bedankt voor alle steun! **Jurre**, het is nu aan jou om ome **Koen** op te volgen, geen druk! **Jan**, hoewel je het PhD traject niet meer mee heb kunnen maken, ben ik trots dat ik jouw nalatenschap door heb mogen zetten als chemicus (en ook nog eens in Eindhoven nu, vlakbij het Natlab!). Natuurlijk moet ik ook **Bo, Karel**, **Bertje, Fientje** en sinds kort **Willempie** bedanken voor alle steun! Daarnaast gaat mijn dank uit naar mijn opa's, **Jan** en **Dion**, oma's, **Leny** en **Ellie,** tantes, **HannaH, Machteld, Liesbeth, Ria, Annemieke en Carla**, ooms, **Stan, Maarten, Hans, Rob** en **Ron,** neven, **Jonas, Tom, Jos, Michiel, Ben en Simon** en nichten, **Dion, Marjolein, Kitty, Dagmar** en **Maren**. Mijn goede vrienden, **Tammi** (midi midi**), Dato** (cha cha**), Henri** (worstenbroodje**), Cas, Niels, Yuri, Koen, Koen** (*ja er zijn vele Koenen*) en **Matthijs** ook zeer bedankt om mij door deze jaren heen te helpen met de goede borrels, mooie vakanties en lange avonden! **Etienne** en **Heleen**, ik heb ontzettend fijn de afgelopen jaren bij jullie een kamer kunnen huren op ook nog eens een korte afstand van zowel de Uithof als het centrum van Utrecht. Hartstikke bedankt voor jullie geweldige gastvrijheid!

About the Author

Koen Wynand Bossers was born on the 26th of August 1993 in Nieuwegein, the Netherlands. He obtained a BSc. degree in Chemistry at Utrecht University where he graduated from in 2014 with a BSc Thesis entitled "Preparation of Mesoporous Silica Confined CuS and Cu_2S Nanoparticles" under prof. Petra de Jongh. He then went on to obtain a MSc degree in Nanomaterials: Chemistry and Physics also at the Utrecht University where his MSc Thesis was entitled "Developing Novel HTM Thin Films for Hybrid Perovskite Photovoltaics" under Dr. Monica Barroso. Afterwards he performed a research internship at the University of Oslo, Catalysis Group, entitled "Studies on the Hydrogenation over CO_2 over a Metal-Organic Framework Supported Platinum Catalyst" under prof. dr. Unni Olsbye. Subsequently, he started his PhD research project under prof. dr. ir. Bert M. Weckhuysen in 2016 to study the fragmentation behavior of Ziegler-type polyolefin catalysts using advanced X-ray nano-tomography techniques at various synchrotron facilities around the world as well as develop and characterize Ziegler-type polyolefin model systems in-house. This research was funded by the Netherlands Organization for Scientific Research (NWO) in the frame of an NWO-TA grant (no. 731.015.203) with SABIC, DSM Resolve, Fontys Hogeschool Eindhoven and the University of Maastricht. Afterwards, Koen became a Junior Scientist at de Nederlandse Organisatie voor toegepast-natuurwetenschappelijk onderzoek (TNO) in Eindhoven, returning to the roots of his family. There Koen focusses on the direct utilization of solar energy to transform CO_2 into fuels and small chemical building. Besides chemistry, Koen loves to go running and hiking in nature and has a profound love for mountains and crafting beer with his brothers.